Origin of shallow, sediment-hosted 'hybrid' orogenic-epithermal/intrusion-related gold-quartz vein systems in the Menneval-Saint-Quentin district, Aroostook-Percé Anticlinorium, northwest New Brunswick, Canada

By
Glen D. Hodge

A Thesis Submitted to
Saint Mary's University, Halifax, Nova Scotia
in Partial Fulfillment of the Requirements for
the Degree of MASTER OF SCIENCE
IN APPLIED SCIENCE

December 16th, 2019, Halifax, Nova Scotia

Approved:	Dr. Jacob Hanley Supervisor
Approved:	Dr. Jim Walker Committee Member
Approved:	Dr. Jason Clyburne Committee Member
Approved:	Dr. Daniel Kontak Committee Member
Approved:	Dr. Geoff Baldwin External Examiner
Date:	December 16th, 2019

Abstract

Origin of shallow, sediment-hosted 'hybrid' orogenic-epithermal/intrusion-related gold-quartz vein systems in the Menneval-Saint-Quentin district, Aroostook-Percé Anticlinorium, northwest New Brunswick, Canada

By Glen D. Hodge
December 16th, 2019

The genetically-related Maisie and Lavoie gold occurrences, respectively located west of Menneval and east of Saint-Quentin, New Brunswick, Canada, represent a new style of non-refractory Au mineralization in the Aroostook-Percé Anticlinorium. Veins are hosted in a flysch sequence (the Whites Brook Formation), and transition from early laminated, to massive, to late bladed/vuggy quartz(-carbonate) textures. Gold in the veins has a close spatial and textural relationship to trace amounts of partially hematitized pyrite, and other base metal sulfides (galena, sphalerite, chalcopyrite) and is paragenetically late-stage, infilling crystal-lined vugs and fractures in quartz. Pyrite chemistry, S-O-C-Sr isotope systematics of vein minerals, and geochronological considerations suggest magmatic involvement, providing heat and exotic metals (Au, Bi, Te, and possibly As, Pb, Sb, Se) to the hydrothermal systems otherwise dominated by an inherited sedimentary metamorphic fluid and metal signature. The Au occurrences are classified as a hybrid gold style with characteristics of both epizonal (shallow) orogenic Au and low-sulfidation epithermal or intrusion-related Au deposits. Rapid fluid boiling ("flashing") combined with meteoric water mixing are suggested to be the primary mechanisms triggering Au precipitation. The Au occurrences are likely related to magmatic activity during the late Acadian Orogeny (<370 Ma).

Acknowledgements

I would like to thank my thesis supervisor, Dr. Jacob Hanley for his constant guidance and help navigating this study and the world of academia and science. I would also like to thank my committee members Dr. Jim Walker (Geological Surveys Branch, New Brunswick) for his help with field work, sampling, and hospitality, Dr. Jason Clyburne (Saint Mary's University) and Dr. Daniel Kontak (Laurentian University) for feedback on my progress reports and making sure I stay on task, and Dr. Geoff Baldwin (Department of Mines and Energy, Nova Scotia) for serving as my external examiner. Finally, I would like to thank Dr. Adam Sarty (Saint Mary's University) for helping me get on this path to begin with. It's been a long haul, but I'm finished now!

I would like to thank the Government of New Brunswick (Department of Natural Resources and Energy Development) for funding this project and providing me with the assistance and support needed to complete this project.

I would also like to thank all my friends and family who got me to where I am today. That particular list is a bit too long to include, but everyone who has listened to me vent, dream, and think my problems out, I thank you with all my heart. Without all of you, I would not have finished this.

Finally, I would like to thank Justin, Travis, and Griffin McElroy for your hours of support, laughter, hope, and happiness. You three really helped me get through the final push.

Table of Contents

List of Figures

Chapter 1

Chapter 2

List of Tables
Chapter 2

Chapter 1 – Thesis Introduction

1.1 Preamble

Orogenic Au deposits remain an enigmatic deposit type of interest to economic geologists. A plethora of studies have examined many aspects of this deposit type including mechanisms of formation, lithotectonic setting and structure, age, gangue and ore mineralogy, alteration, stable isotope, and fluid inclusion systematics (e.g. Groves et al., 1998; Groves et al., 2000; Ridley & Diamond, 2000; Goldfarb et al., 2001; Bierlein & Smith, 2003; Bierlein et al., 2004; Goldfarb et al., 2004; Large et al., 2009; Kontak et al., 2011; Large et al., 2011; and Goldfarb & Groves, 2015 and authors therein to name a few). Despite this large body of research, there remains significant uncertainty concerning the source of Au. Evidence for a possible genetic connection between orogenic Au endowment and Au-rich magmatic-hydrothermal (intrusion-related, epithermal) volatiles has been argued (Sillitoe and Thompson, 1998; Thompson et al., 1999; Lang and Baker, 2001; Hart and Goldfarb, 2005; Hart, 2007; and Kerr et al., 2018 and authors therein). This introductory chapter reviews both orogenic and epithermal deposit styles, including idealized mechanisms of Au precipitation from fluids. Key aspects of the relationships, and possible continuum, between orogenic and epithermal Au deposit styles are summarized in Chapter 2.

The two Au mineralized systems examined in this study are the Maisie and Lavoie Au occurrences, located in northwestern New Brunswick, Canada. Auriferous quartz veins were discovered there in 2011 (Lavoie) and 2012 (Maisie), and their discovery led to increased exploration activity in the region. . The Maisie discovery, approximately 9 km west of Menneval (lat 47^{o}-48’-59.3”; long 67^{o}-16’-23.9”) consisted of three large quartz

boulders containing visible Au with a close textural relationship to hematite. Since then extensive exploration work (trenching, drilling, and sampling) has tested both showings and identified new targets.

1.2 Epithermal Au (-Ag) deposits

Epithermal Au (-Ag) deposits (e.g. White & Hedenquist, 1995; White et al., 1995; Hedenquist et al., 1998; Hedenquist et al., 2000; Chouinard et al., 2005; Taylor, 2007; Deditius et al., 2009; Pudack et al., 2009; Deditius et al., 2014; and Franchini et al., 2015 and authors therein) are shallow-forming (< 2000 m below surface), and occur within volcanic arc terrains along convergent boundaries (Taylor, 2007 and authors therein). Epithermal deposits may be spatially associated with magmatism, which can be significant source of volatiles and metals, and also the driving (thermal) mechanism for convection-induced circulation of mineralizing hydrothermal fluids. Gold is hosted in quartz-dominated veins, stockworks, and breccias containing varying types and percentages of gangue and accessory sulfide and sulfosalt minerals, depending partly on sulfidation degree and formation depth. Epithermal deposits are divided into low- and high-sulfidation sub types with some overlap between the two. The differences between the two deposit sub-types are a function of variations in the fluid composition, ore mineral chemistry, gangue and ore mineralogy textures at a variety of scales, and alteration style resulting from differing fluid evolution and proximity to suspected magmatic-hydrothermal centres.

Low-sulfidation epithermal deposits, as summarized by White and Hedenquist (1995), comprise open space-filling, stockwork and veins of quartz, with adularia and calcite, reflecting the near-neutral pH of mineralizing fluids. Ore minerals associated with low-sulfidation deposits are native Au or Au-Ag alloy, as well as arsenopyrite, and subordinate

base metal sulfides (galena, sphalerite, pyrite, chalcopyrite), Hg and Sb sulfides, sulfosalts, and various Au and silver accessory minerals (tellurides, selenides). In deeply formed deposits, tetrahedrite-tennantite and higher base metal sulfide contents may occur. The primary alteration minerals formed are most commonly are illite, sericite, and adularia. The circulating mineralizing fluids are commonly mixtures of meteoric water and magmatic-hydrothermal fluid, in which dissolved gases, salts, and some metals are sourced from crystallizing magmas. Fluid inclusion studies (e.g. Hedenquist et al., 1994) show that fluid temperatures of ~ 160 – 240°C are typical during vein formation with salinities ≤ 1 wt% NaCl. Deep deposits (300 – 800 m) form from higher salinity fluids in the range of 3 – 10 wt% NaCl, but with similar temperature fluids and ore textures as in shallow deposits (< 300 m) (Hedenquist et al., 2000). These fluids may undergo boiling (a common mechanism for Au precipitation) which creates a vapour-rich phase (Pokrovski et al., 2005; Williams-Jones and Heinrich, 2005) sequestering CO_2 and H_2S from the mineralizing fluid, leading to the decomposition of Au hydrogen sulfide complexes. Fluid mixing may also trigger Au precipitation altering the pH and diluting the system, which will be explained in greater detail below. Vein textures preserve evidence of boiling, and may be correlated with metal grades, include lattice-bladed calcite, as well as jigsaw, plumose, and colloform textures in calcite and quartz (e.g. Moncada et al., 2012). Other common textures include vein breccias, and stockworks created by hydraulic fracturing as fluid pressures fluctuate in response to magmatic activity and tectonism.

High-sulfidation epithermal deposits, as described by White and Hedenquist (1995), present relatively lower quartz vein abundance, compared to low-sulfidation deposits, and most commonly comprise disseminated ore in acid-leached host rocks. Ores comprise some

minerals also present in low-sulfidation deposits but are differentiated by the presence of the sulfide phases enargite-luzonite and covellite rather than Hg and Sb sulfides, arsenopyrite, and tetrahedrite-tennantite that are common to low sulfidation systems. This reflects a higher sulfidation state, together with more acidic and/or oxidized conditions. The close proximity of high sulfidation systems to a volcanic edifice is linked to acidic and oxidizing fluids, relative to fluids in low sulfidation systems that contain a higher proportion of meteoric water. The alteration is advanced argillic, with vuggy silica, alunite, diaspore, kaolinite, and dickite, consistent with low pH fluids. Pyrophyllite and sericite are commonly present in deeper and/or higher T systems. Fluid inclusion studies (Shen at al., 1982; Zhang et al., 1989) report typical fluid Ts of 230 – 280°C. These hot, oxidized, and acidic fluids rise from depth, carrying metals and volatiles from magmatic bodies, and cause acid sulfate leaching of host rocks. Some textures can be similar to those in low-sulfidation deposits, but with vuggy silica (quartz) and silicified host rock predominating over quartz veining.

In high-sulfidation systems, Au is complexed by both chloride and bisulfide, with bisulfide predominating, and precipitation is triggered when acidic fluids interact with surrounding host rocks, destabilizing Au complexes (through acid neutralization), though secondary epithermal boiling (versus primary porphyry stage boiling) may also precipitate Au.

1.3 Orogenic Au deposits

Orogenic Au deposits have been historically a major economic source of Au in Canada, and many studies describe their origin and exploration potential. They are well described in major review papers by Goldfarb et al. (2001), and Groves et al. (1998, 2003). Their

geological setting, host vein and alteration mineralogy, structural features, ore mineralogy and fluid chemistry, and P-T conditions of formation have been described thoroughly (e.g. Henley et al., 1976; Phillips and Groves, 1983; Smith and Kesler, 1985; Robert and Brown, 1986a,1986b; Phillips et al., 1987; Groves et al., 1988; Mueller et al., 1988; Sibson et al., 1988; Craw and Koons, 1989; Hodgson, 1989; Marmont and Corfu, 1989; Clout et al., 1990; Cox et al., 1991; Goldfarb et al., 1991; Powell et al., 1991; Burrows et al., 1993; Seward, 1993; Couture et al., 1994; Hagemann et al., 1994; Kerrich and Cassidy, 1994; Gebre-Mariam et al., 1995; Hodgson et al., 1995; Matthaei et al., 1995; Mueller et al., 1996; Gray, 1997; Robert and Poulsen, 1997, McCuaig and Kerrich, 1998; Bateman et al., 2001; Bierlein and Crowe, 2000; Bierlein et al., 2001; Chauvet et al., 2001; Cox, 1999; Jia and Kerrich, 1999; Wyman et al., 1999; Hagemann and Cassidy, 2000; Kerrich et al., 2000; Neumayr et al., 2000; Ridley and Diamond, 2000; Ridley et al., 2000; Gray and Hutchinson, 2001; Lobato et al., 2001; Allibone et al., 2002; and Neumayr and Hagemann, 2002 and authors therein).

The formation of orogenic belts involves the compressional to transpressional accretion of continental blocks in accretionary terrains. Gold deposits in these terrains are hosted by metamorphosed rocks, usually of greenschist to amphibolite facies, and less commonly up to granulite grade. The host terrains contain metavolcanic and volcaniclastic rocks, and associated igneous intrusions, of mainly Archean age and/or metasedimentary rocks of Paleoproterozoic age. The Au-bearing veins are structurally controlled, comprising extensional and bedding parallel veins and jogs occurring in fold saddles and along fold limbs within major shear zones. Large-scale deformation may also occur in association with the emplacement of intrusive rocks sourced from deeper magmatic centres formed at

associated convergent plate boundaries. Orogenic deposits can form at depths, ranging from shallow 'epizonal' (< 6 km), to 'mesozonal' (6 – 12 km), to very deep 'hypozonal' (> 12 km). The depth at which orogenic deposits form influences the style of mineralization, although variable input from magmatic sources at depth, or meteoric (near surface) water may affect metamorphic fluid compositions. However, the dominant fluid are constituents sourced from large-scale devolatilization of crustal rocks associated with the greenschist-amphibolite transition.

Orogenic lode Au deposits are dominated by Au-bearing quartz-carbonate veins and stockworks but many deposits also show disseminated Au-rich "sulfidation" halos (in the form of sulfides or sulfarsenides) in the surrounding wall rock (Groves et al., 1998, 2003). Metal associations vary with depth from Hg and Hg-Sb (epizonal) to Au-Sb and Au-As-Te-W (mesozonal) to and Au-As (hypozonal) (Goldfarb et al., 2005; Goldfarb and Groves, 2015). Common accessory minerals in veins and mineralized wall rocks include minor (i.e. 3–5 vol %) sulfides (pyrite, pyrrhotite, arsenopyrite). Alteration comprises ankerite or dolomite as the main carbonate phase/s, with subordinate calcite, as well as the products of localized alkali metasomatism, sericitization and chloritization of host rocks (Goldfarb et al., 2005).

Fluid inclusion studies (Groves et al., 1998, 2003) show that orogenic Au mineralizing fluids were near neutral, low salinity (~3–7 wt% NaCl equiv.), single phase, $H_2O – CO_2 \pm CH_4 \pm N_2$ mixtures ranging from H_2O-dominant, to CO_2 or CH_4- dominant compositions. Fluid inclusion studies and mineral thermobarometry indicate a wide range in i the P-T conditions of ore formation (i.e. 200–600°C and from 1–5 kbar). Stable oxygen isotope data (Groves et al., 1998; Goldfarb et al., 2005) show a wide range in the estimated $\delta^{18}O_{fluid}$

from ~5 to 13‰ which is controlled by a combination of (i) the relative percent mass input of magmatic-derived fluid; (ii) the temperature of the fluid; (iii) the composition of host rocks that were metamorphosed contributing volatiles and other constituents to the fluid; (iv) modification by later fluid-rock interaction; and (v) mixing with meteoric water.

A number of different mechanisms are proposed for Au precipitation in orogenic deposits (see the review by Goldfarb et al., 2005). For example, Au may be precipitating during mixing of fluids (e.g. dilution and cooling by meteoric water), or via pH changes resulting from fluid-wall rock interaction. . For example, wall rock "sulfidation" (reaction of fluid derived S and As with wall-rock Fe to form sulfides) will cause bisulfide complexes of Au to destabilize. Rapid fluctuations in P may destabilize bisulfide complexes of Au in fluids through boiling, a process linked to pressure "throttling" in veins (i.e., rapid transitions in confining pressure) during repeated fault movements (Sibson et al., 1988).

1.4 Au solubility and precipitation controls

The factors influencing Au solubility, and mechanisms for Au precipitation are critical to delineate as these determine, in part, the amount of Au that may accumulate in a mineralizing system. If Au is not initially put in to solution, or cannot be precipitated from a Au-rich solution, an economic deposit will not form. Despite a diverse range of characteristics among deposits, there are common chemical processes responsible for Au transport and precipitation.

The primary mass action expressions for Au solubility and precipitation via bisulfide complexing (Seward, 1993; Williams-Jones et al., 2009 and authors therein) are:

$$Au_{(s)} + HS^-_{(aq)} + H^+_{(aq)} + ¼\ O_{2(aq)} = Au(HS)°_{(aq)} + ½\ H_2O_{(aq)} \qquad \text{equation (1)}$$

$Au_{(s)} + 2HS^-_{(aq)} + H^+_{(aq)} + ¼\ O_{2(aq)} = Au(HS)^-_{2(aq)} + ½\ H_2O_{(aq)}$ equation (2)

Au can also complex with chloride in solution as follows:

$Au_{(s)} + 2Cl^-_{(aq)} + H^+_{(aq)} + ¼\ O_{2(aq)} = AuCl_{2(aq)} + ½\ H_2O_{(aq)}$ equation (3)

In both low-sulfidation epithermal and orogenic Au systems, boiling (i.e. phase separation) in ore fluids can be a key process controlling Au precipitation. a As the mineralizing fluid undergoes rapid boiling, H_2S (and/or SO_2) will fractionate into the vapour phase, causing a decrease in $HS^-_{(aq)}$ and pH. In accordance with Le Chatelier's Principle, the loss in HS^- and H^+ (to form H_2S or SO_2 gas) results in a shift of the mass action equations (1) and (2) to the left, precipitating Au via decomposition of bisulfide complexes. Boiling can be caused by repeated isothermal shifts in pressure, during hydraulic fracturing when fluid pressure exceeds lithostatic (confining) pressure (i.e. the "fault-valve" model; Sibson et al., 1988), thereby facilitating Au mineralization that may produce an economically viable deposit.

In high-sulfidation epithermal deposits changes in pH and oxidation are the primary mechanisms for Au precipitation. At low pH, Au is highly soluble (Williams-Jones et al., 2009) as both a bisulfide or chloride complexes. Conversely, a decrease in H^+ (i.e. during wall rock alteration) to produce phyllic alteration will shift equations (1) – (3) to the left, resulting in Au bisulfide or chloride decomposition and subsequent Au precipitation. Dilution of the acidic Au transporting fluid with neutral pH meteoric, can also trigger Au precipitation due to net fluid pH increase as well as diluting the dissolved complexing ligand activity.

In equations (1) – (3) an increase in f_{O2} increases the solubility of Au (see also Fig. 1); however, once f_{O2} increases significantly, bisulfide will ultimately oxidize to sulfate, and Au will become insoluble and precipitate:

$Au(HS)^{0}_{(aq)} + 2O_{2(aq)} = H^{+}_{(aq)} + SO_4^{2-}{}_{(aq)} + Au_{(s)}$ equation (4)

$Au(HS)^{-}{}_{2(aq)} + 4O_{2(aq)} = 2H^{+}_{(aq)} + 2SO_4^{2-}{}_{(aq)} + 2Au_{(s)}$ equation (5)

If mineralizing fluids undergo boiling, as described previously, H_2S and/or SO_2 will partition into the vapour phase, resulting in a decrease in $HS^{-}_{(aq)}$ in the fluid. . In addition, $H_{2(aq)}$ will be lost from the fluid as it partitions into the vapour more rapidly than H_2S during boiling (McKibben and Eldridge, 1990). When this happens $O_{2(aq)}$ increases in solution (from the decomposition of H_2O in solution) driving equations (4) and (5) to the right.

Sulfidation reactions in veins and wall rocks, involve the formation of pyrite or arsenopyrite (common in both epithermal and orogenic deposits), and lead to Au mineralization. The formation of pyrite and arsenopyrite from S-rich fluids occurs via equations 6 and 7.

$Fe_2O_{3(s)} + 4\ HS^{-}{}_{(aq)} = 2FeS_{2(s)} + ½\ O_{2(aq)} + 2H_2O_{(l)}$ equation (6)

$2Fe_2O_{3(s)} + 4\ HS^{-}{}_{(aq)} + 4As_{(aq)} = 4FeAsS_{(s)} + 2\ O_{2(aq)} + 2H_2O_{(l)}$ equation (7)

Once again, according to Le Chatelier's Principle the formation of pyrite or arsenopyrite will consume bisulfide, shifting equation (1) to the left, favouring Au precipitation, as shown in the combined reaction (equation 8).

$2\ Au(HS)^{o}_{(aq)} + H_2O_{(l)} + Fe^{2+}$ (wall rock) $\leftrightarrow 2\ Au_{(s)} + FeS_2 + 4\ H^{+}_{(aq)} + ½\ O_{2(aq)}$ equation (8)

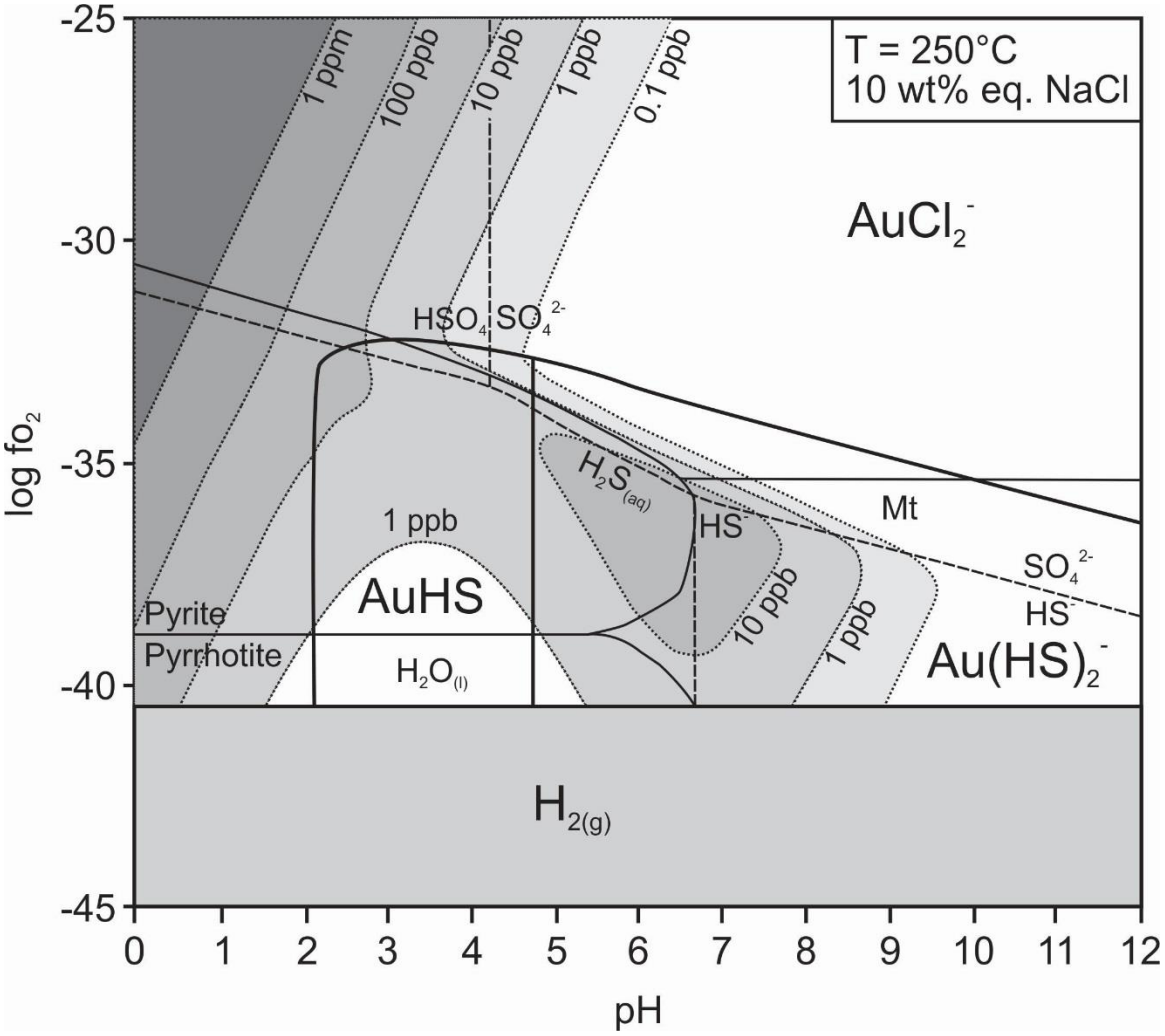

Figure 1.1 – Log fO_2-pH diagram showing stability fields for dominant S species in aqueous Au systems at 250°C and 10 wt% equiv. NaCl. Stability fields for dominant soluble Au complexes and Fe-S-O phases are also shown, as well as contours of Au solubility. Diagram modified from Barnes and Czamanske (1967) and drawn at $\sum S = 0.1$.

Finally, Au mineralization may occur through fluid cooling. At moderate f_{O2}, over a wide range in pH, Au will be complexed with bisulfide [equations (1), (2), (4) – (8)], and transported at concentrations up to several hundred ppb (Fig. 1), but at low pH and high f_{O2} Au can form complexes with Cl^- (equation 3), with chloride replacing the bisulfide anion. The amount of Au that can be carried by chloride may be much higher than bisulfide at such conditions. However, with decreasing pH and increasing fO_2, changing the predominant Au complex to a chloride alters the complexes' stability with respect to T, as Au chloride complexes are less stable over the same T range as bisulfide. By cooling the system over a few hundred degrees, Au will precipitate as chloride complexes decomposes (e.g. Williams-Jones, et al., 2009). Decomposing Au chloride complexes can be further complicated if there is still S in the system, as Au will remobilize/respeciate as Au-bisulfide, which is stable over a wider range to much lower temperatures compared to chloride Au complexes. When chloride complexes predominate, the system must be completely buffered with respect to Cl^- or have minimal bisulfide present to optimize Au precipitation from decomposing chloride complexes. This is the case in extremely acidic fluid conditions, or at high f_{O2} (Fig. 1).

1.5 Conclusion

Epithermal and orogenic Au deposits show contrasting geological attributes, but they share similar physicochemical controls with respect to Au solubility and mechanisms of Au deposition. As described, processes common to the formation of economic Au deposits include: boiling of Au-bearing fluids, shifts in the T, pH, S content, and/or f_{O2} of these fluids in response to mixing, wall rock reactions, etc. Identifying the exact processes that formed an economic Au deposit can be challenging, as several processes likely apply in

tandem. Given the overlap of many genetic characteristics in orogenic and epithermal deposits, it can be equally as difficult to distinguish one type from another. These deposit types, while already widely studied, require further investigation to improve working genetic models for exploration.

1.6 References

Allibone AH, McCuaig TC, Harris D, Etheridge M, Munroe S, Byrne D, Amanor J, Gyapong W (2002) Structural controls on gold mineralization at the Ashanti deposit, Obuasi, Ghana. Society of Economic Geologists Special Publication. 9, p 65-93

Barnes HL, Czamanske GK (1967) Solubilities and transport of ore minerals. Geochemistry of hydrothermal ore deposits. p 334-381

Bateman RJ, Hagemann SG, McCuaig TC, Swager CP (2001) Protracted gold mineralization throughout Archaean orogenesis in the Kalgoorlie camp, Yilgarn Craton, Western Australia: structural, mineralogical, and geochemical evolution. Geological Survey of Western Australia. Record, 17, p 63-98

Bierlein FP, Crowe DE (2000) Phanerozoic orogenic lode gold deposits: Reviews in Economic Geology. 13, p 103-139

Bierlein FP, Smith PK (2003) The Touquoy Zone deposit: an example of "unusual" orogenic gold mineralisation in the Meguma Terrane, Nova Scotia, Canada. Canadian Journal of Earth Sciences. 40(3), p 447-466

Bierlein FP, Arne DC, Foster DA, Reynolds P (2001) A geochronological framework for orogenic gold mineralisation in central Victoria, Australia. Mineralium Deposita. 36(8), p 741-767

Bierlein FP, Arne DC, Cartwright I (2004) Stable isotope (C, O, S) systematics in alteration haloes associated with orogenic gold mineralization in the Victorian gold province, SE Australia. Geochemistry: Exploration, Environment, Analysis. 4(3), p 191-211

Burrows DR, Spooner ET, Wood PC, Jemielita RA (1993) Structural controls on formation of the Hollinger-McIntyre gold quartz vein system in the Hollinger shear zone, Timmins, southern Abitibi greenstone belt, Ontario. Economic Geology. 88(6), p 1643-1663

Chauvet A, Piantone P, Barbanson L, Nehlig P, Pedroletti I (2001) Gold Deposit Formation during Collapse Tectonics: Structural, Mineralogical, Geochronological, and Fluid Inclusion Constraints in the Ouro Preto gold Mines, Quadril átero Ferrífero, Brazil. Economic Geology. 96(1), p 25-48

Chouinard A, Williams-Jones AE, Leonardson RW, Hodgson CJ, Silva P, Téllez C, Vega J, Rojas F (2005) Geology and genesis of the multistage high-sulfidation epithermal Pascua Au-Ag-Cu deposit, Chile and Argentina. Economic Geology. 100(3), p 463-490

Clout JM, Cleghorn JH, Eaton PC (1990) Geology of the Kalgoorlie gold field. In: Geology of the mineral deposits of Australia and Papua New Guinea (14, p 411-431). The Australasian Institute of Mining and Metallurgy, Melbourne

Couture JF, Pilote P, Machado N, Desrochers JP (1994) Timing of gold mineralization in the Val-d'Or District, southern Abitibi Belt; evidence for two distinct mineralizing events. Economic Geology. 89(7), p 1542-1551

Cox SF (1999) Deformational controls on the dynamics of fluid flow in mesothermal gold systems. Geological Society, London, Special Publications. 155(1), p 123-140

Cox SF, Wall VJ, Etheridge MA, Potter TF (1991) Deformational and metamorphic processes in the formation of mesothermal vein-hosted gold deposits—examples from the Lachlan Fold Belt in central Victoria, Australia. Ore geology reviews. 6(5), p 391-423

Craw D, Koons PO (1989) Tectonically induced hydrothermal activity and gold mineralization adjacent to major fault zones. In: The geology of gold deposits. Economic Geology Monograph. 6, p 463-470

Deditius AP, Utsunomiya S, Ewing RC, Chryssoulis SL, Venter D, Kesler SE (2009) Decoupled geochemical behavior of As and Cu in hydrothermal systems. Geology. 37(8), p 707-710

Deditius AP, Reich M, Kesler SE, Utsunomiya S, Chryssoulis SL, Walshe J, Ewing RC (2014) The coupled geochemistry of gold and As in pyrite from hydrothermal ore deposits. Geochimica et Cosmochimica Acta. 140, p 644-670

Franchini M, McFarlane C, Maydagán L, Reich M, Lentz DR, Meinert L, Bouhier V (2015) Trace metals in pyrite and marcasite from the Agua Rica porphyry-high sulfidation epithermal deposit, Catamarca, Argentina: Textural features and metal zoning at the porphyry to epithermal transition. Ore Geology Reviews. 66, p 366-387

Gebre-Mariam M, Hagemann SG, Groves DI (1995) A classification scheme for epigenetic Archaean lode-gold deposits. Mineralium Deposita. 30(5), p 408-410

Goldfarb RJ, Groves DI (2015) Orogenic gold: Common or evolving fluid and metal sources through time. Lithos. 233, p 2-6

Goldfarb RJ, Snee LW, Miller LD, Newberry RJ (1991) Rapid dewatering of the crust deduced from ages of mesothermal gold deposits. Nature. 354(6351), p 296-298

Goldfarb RJ, Groves DI, Gardoll S (2001) Orogenic gold and geologic time: a global synthesis. Ore geology reviews. 18(1), p 1-75

Goldfarb RJ, Ayuso R, Miller ML, Ebert SW, Marsh EE, Petsel SA, Miller LD, Bradley D, Johnson C, McClelland W (2004) The late Cretaceous Donlin Creek gold deposit,

Southwestern Alaska: Controls on epizonal ore formation. Economic geology. 99(4), p 643-671

Goldfarb R, Baker T, Dube B, Groves DI, Hart CJ, Gosselin P (2005) Distribution, character and genesis of gold deposits in metamorphic terranes. Society of Economic Geologists. p 407-450

Gray DR (1997) Tectonics of the southeastern Australian Lachlan Fold Belt: structural and thermal aspects. Geological Society, London, Special Publications. 121(1), p 149-177

Gray MD, Hutchinson RW (2001) New evidence for multiple periods of gold emplacement in the Porcupine mining district, Timmins area, Ontario, Canada. Economic Geology. 96(3), p 453-475

Groves DI, Phillips GN, Ho SE, Houstoun SM, Standing CA (1988) Craton-scale distribution of Archean greenstone Au deposits; predictive capacity of the metamorphic model. Economic Geology. 82(8), p 2045-2058

Groves DI, Goldfarb RJ, Gebre-Mariam M, Hagemann SG, Robert F (1998) Orogenic Au deposits: a proposed classification in the context of their crustal distribution and relationship to other Au deposit types. Ore geology reviews. 13(1-5), p 7-27

Groves DI, Goldfarb RJ, Knox-Robinson CM, Ojala J, Gardoll S, Yun GY, Holyland P (2000) Late-kinematic timing of orogenic Au deposits and significance for computer-based exploration techniques with emphasis on the Yilgarn Block, Western Australia. Ore Geology Reviews. 17(1-2), p 1-38

Groves DI, Goldfarb RJ, Robert F, Hart CJR (2003) Au deposits in metamorphic belts: overview of current understanding, outstanding problems, future research, and exploration significance. Economic Geology. 98, p 1-29

Hagemann SG, Cassidy KF (2000) Archean orogenic lode Au deposits: Reviews in Economic Geology. 13, p 9 -68

Hagemann SG, Gebre-Mariam M, Groves DI (1994) Surface-water influx in shallow-level Archean lode-Au deposits in Western, Australia. Geology. 22(12), p 1067-1070

Hart CJ (2007) Reduced intrusion-related Au systems. Geological Association of Canada, Mineral Deposits Division. 5, p 95-112

Hart CJ, Goldfarb RJ (2005) Distinguishing intrusion-related from orogenic Au systems. In: New Zealand Minerals Conference Proceedings. 2005, p 125-133

Hedenquist JW, Matsuhisa Y, Izawa E, White NC, Giggenbach WF, Aoki M (1994) Geology, geochemistry, and origin of high sulfidation Cu-Au mineralization in the Nansatsu District, Japan. Economic Geology. 89(1), p 1-30

Hedenquist JW, Arribas A, Reynolds TJ (1998) Evolution of an intrusion-centered hydrothermal system; Far Southeast-Lepanto porphyry and epithermal Cu-Au deposits, Philippines. Economic Geology. 93(4), p 373-404

Hedenquist JW, Arribas AN, Gonzalez-Urien E (2000) Exploration for epithermal Au deposits. Reviews in Economic Geology. 13(2), p 45-77

Henley RW, Norris RJ, Paterson CJ (1976) Multistage ore genesis in the New Zealand geosyncline a history of post-metamorphic lode emplacement. Mineralium deposita. 11(2), p 180-196

Hodgson CJ (1989). The structure of shear-related, vein-type Au deposits: a review. Ore Geology Reviews. 4(3), p 231-273

Hodgson CJ, Love DA, Hamilton JV (1995) Giant mesothermal Au deposit: descriptive characteristics, genetic model and exploration are selection criteria. Giant ore deposits. SEG SP-2, p 157-206

Jia Y, Kerrich R (1999) Nitrogen isotope systematics of mesothermal lode Au deposits: Metamorphic, granitic, meteoric water, or mantle origin? Geology. 27(11), p 1051-1054

Kerr MJ, Hanley JJ, Kontak DJ, Morrison GG, Petrus J, Fayek M, Zajacz Z (2018) Evidence of upgrading of Au tenor in an orogenic quartz-carbonate vein system by late magmatic-hydrothermal fluids at the Madrid Deposit, Hope Bay Greenstone Belt, Nunavut, Canada. Geochimica et Cosmochimica Acta. 241, p 180-218

Kerrich R, Cassidy KF (1994) Temporal relationships of lode Au mineralization to accretion, magmatism, metamorphism and deformation—Archean to present: A review. Ore Geology Reviews. 9(4), p 263-310

Kerrich R, Goldfarb RJ, Groves DI, Garwin S (2000) The geodynamics of world class Au deposits: Characteristics, space-time distribution, and origins. Reviews in Economic Geology. 13, p 501-551

Kontak DJ, Horne RJ, Kyser K (2011) An oxygen isotope study of two contrasting orogenic vein Au systems in the Meguma Terrane, Nova Scotia, Canada, with implications for fluid sources and genetic models. Mineralium Deposita. 46(3), p 289-304

Lang JR, Baker T (2001) Intrusion-related Au systems: the present level of understanding. Mineralium Deposita. 36(6), p 477-489

Large RR, Danyushevsky L, Hollit C, Maslennikov V, Meffre S, Gilbert S, Bull S, Scott R, Emsbo P, Thomas H, Singh B (2009) Au and trace element zonation in pyrite using a laser imaging technique: Implications for the timing of Au in orogenic and Carlin-style sediment-hosted deposits. Economic Geology. 104(5), p 635-668

Large RR, Bull SW, Maslennikov VV (2011) A carbonaceous sedimentary source-rock model for Carlin-type and orogenic gold deposits. Economic Geology. 106(3), p 331-58

Lobato L, Ribeiro-Rodrigues L, Vieira F (2001) Brazil's premier gold province. Part II: geology and genesis of gold deposits in the Archean Rio das Velhas greenstone belt, Quadrilátero Ferrífero. Mineralium Deposita. 36(3-4), p 249-277

Marmont S, Corfu F (1989) Timing of gold introduction in the Late Archean tectonic framework of the Canadian Shield: Evidence from U-Pb zircon geochronology of the Abitibi subprovince. Econ. Geol. Monogr. 6, p 101-111

Matthaei SK, Henley RW, Bacigalupo-Rose S, Binns RA, Andrew AS, Carr GR, French DH, McAndrew J, Kananagh ME (1995) Intrusion-related, high-temperature gold quartz veining in the Cosmopolitan Howley metasedimentary rock-hosted gold deposit, Northern Territory, Australia. Economic Geology. 90(5), p 1012-1045

McCuaig TC, Kerrich R (1998) P—T—t—deformation—fluid characteristics of lode gold deposits: evidence from alteration systematics. Ore Geology Reviews. 12(6), p 381-453

McKibben MA, Eldridge CS (1990) Radical sulfur isotope zonation of pyrite accompanying boiling and epithermal gold deposition; a SHRIMP study of the Valles Caldera, New Mexico. Economic Geology. 85(8), p 1917-1925

Moncada D, Mutchler S, Nieto A, Reynolds TJ, Rimstidt JD, Bodnar RJ (2012) Mineral textures and fluid inclusion petrography of the epithermal Ag-Au deposits at Guanajuato, Mexico: Application to exploration. Journal of Geochemical Exploration. (114), p 20-35

Mueller AG, Harris LB, Lungan A (1988) Structural control of greenstone-hosted gold mineralization by transcurrent shearing: A new interpretation of the Kalgoorlie mining district, Western Australia. Ore Geology Reviews. 3(4), p 359-387

Mueller AG, Campbell IH, Schiotte L, Sevigny JH, Layer PW (1996) Constraints on the age of granitoid emplacement, metamorphism, gold mineralization, and subsequent cooling of the Archean greenstone terrane at Big Bell, Western Australia. Economic Geology. 91(5), p 896-915

Neumayr P, Hagemann SG (2002). Hydrothermal fluid evolution within the Cadillac tectonic zone, Abitibi greenstone belt, Canada: relationship to auriferous fluids in adjacent second-and third-order shear zones. Economic Geology. 97(6), p 1203-1225

Neumayr P, Hagemann SG, Couture JF (2000) Structural setting, textures, and timing of hydrothermal vein systems in the Val d'Or camp, Abitibi, Canada: implications for the evolution of transcrustal, second-and third-order fault zones and gold mineralization. Canadian Journal of Earth Sciences. 37(1), p 95-114

Phillips GN, Groves DI (1983) The nature of Archaean gold-bearing fluids as deduced from gold deposits of Western Australia. Journal of the Geological Society of Australia. 30(1-2), p 25-39

Phillips GN, Groves DI, Brown IJ (1987) Source requirements for the Golden Mile, Kalgoorlie: Significance to the metamorphic replacement model for Archean gold deposits. Canadian Journal of Earth Sciences. 24(8), p 1643-1651

Pokrovski GS, Roux J, Harrichoury JC (2005) Fluid density control on vapor-liquid partitioning of metals in hydrothermal systems. Geology. 33(8), p 657-660

Powell R, Will TM, Phillips GN (1991) Metamorphism in Archaean greenstone belts: calculated fluid compositions and implications for gold mineralization. Journal of Metamorphic Geology. 9(2), p 141-150

Pudack C, Halter WE, Heinrich CA, Pettke T (2009) Evolution of magmatic vapor to gold-rich epithermal liquid: The porphyry to epithermal transition at Nevados de Famatina, northwest Argentina. Economic Geology. 104(4), p 449-477

Ridley JR, Diamond LW (2000) Fluid chemistry of orogenic lode-gold deposits and implications for genetic models: Reviews in Economic Geology. 13, p 141-162

Ridley JR, Groves DI, Knight JT (2000) Gold deposits in amphibolite and granulite facies terranes of the Archean Yilgarn craton, Western Australia: evidence and implications of synmetamorphic mineralization. Reviews in Economic Geology. 11, p 265-290

Robert F, Brown AC (1986a) Archean gold-bearing quartz veins at the Sigma Mine, Abitibi greenstone belt, Quebec; Part I, Geologic relations and formation of the vein system. Economic Geology. 81(3), p 578-592

Robert F, Brown AC (1986b) Archean gold-bearing quartz veins at the Sigma Mine, Abitibi greenstone belt, Quebec; Part II, Vein paragenesis and hydrothermal alteration. Economic Geology. 81(3), p 593-616

Robert F, Poulsen KH (1997) World-class Archaean gold deposits in Canada: An overview. Australian Journal of Earth Sciences. 44(3), p 329-351

Seward TM (1993) The hydrothermal geochemistry of gold. In: Gold metallogeny and exploration. p 37-62. Springer, Dordrecht

Shen K, Champigny N, Sinclair AJ (1982) Fluid inclusion and sulphur isotope data in relation to genesis of the Cinola Gold deposit, Queen Charlotte Islands, B.C., in: Geology of Canadian Gold Deposits, The Canadian Institute of Mining and Metallurgy, Special Volume 24, p 255-257

Sibson RH, Robert F, Poulsen KH (1988) High-angle reverse faults, fluid-pressure cycling, and mesothermal gold-quartz deposits. Geology. 16(6), p 551-555

Sillitoe RH, Thompson JF (1998) Intrusion–Related Vein Gold Deposits: Types, Tectono-Magmatic Settings and Difficulties of Distinction from Orogenic Gold Deposits. Resource Geology. 48(4), p 237-250

Smith TJ, Kesler SE (1985) Relation of fluid inclusion geochemistry to wall rock alteration and lithogeochemical zonation at the Hollinger-McIntyre gold deposit, Timmins, Ontario, Canada. CIM bulletin. 78(876), p 35-46

Taylor BE (2007) Epithermal gold deposits. Mineral deposits of Canada: a synthesis of major deposit-types, district metallogeny, the evolution of geological provinces, and exploration methods. Edited by WD Goodfellow. Geological Association of Canada, Mineral Deposits Division, Special Publication. 5, p 113-139

Thompson JF, Sillitoe RH, Baker T, Lang JR, Mortensen JK (1999) Intrusion-related gold deposits associated with tungsten-tin provinces. Mineralium Deposita. 34(4), p 323-334

White NC, Hedenquist JW (1995) Epithermal gold deposits: styles, characteristics and exploration. SEG newsletter. 23(1), p 9-13

White NC, Leake MJ, McCaughey SN, Parris BW (1995) Epithermal gold deposits of the southwest Pacific. Journal of geochemical exploration. 54(2), p 87-136

Williams-Jones AE, Heinrich CA (2005) 100th Anniversary special paper: vapor transport of metals and the formation of magmatic-hydrothermal ore deposits. Economic Geology. 100(7), p 1287-1312

Williams-Jones AE, Bowell RJ, Migdisov AA (2009) Gold in solution. Elements. 5(5), p 281-287

Wyman DA, Kerrich R, Groves DI (1999) Lode gold deposits and Archean mantle plume–island arc interaction, Abitibi subprovince, Canada. The Journal of geology. 107(6), p 715-725

Zhang X, Nesbitt BE, Muehlenbachs K (1989) Gold mineralization in the Okanagan Valley, southern British Columbia; fluid inclusion and stable isotope studies. Economic Geology. 84(2), p 410-424

Chapter 2 – Origin of shallow, sediment-hosted 'hybrid' orogenic-epithermal/intrusion-related gold-quartz vein systems in the Menneval-Saint-Quentin district, Aroostook-Percé Anticlinorium, northwest New Brunswick, Canada

[*]Glen Hodge[1], Jacob Hanley[1], James Walker[2], Brandon Boucher[3], Zoltán Zajacz[4], Ryan Sharpe[5], and Mostafa Fayek[5]

[1]*Department of Geology, Saint Mary's University, 923 Robie Street, Halifax, NS, B3H3C3*
[2]*Energy and Resource Development, Government of New Brunswick, 2574 Route 180, South Tetagouche, NB, E2A7B8*
[3]*Department of Earth Sciences, University of New Brunswick, 2 Bailey Drive, Fredericton, NB, E3B5A3*
[4]*Department of Earth Sciences, University of Toronto, 22 Russell Street, Toronto, ON, M5S3B1*
[5]*Department of Geological Sciences, University of Manitoba, 125 Dysart Road, Winnipeg, MB, R3T2N2*

[*]corresponding author email: ghodge.physics@gmail.com

For submission to Ore Geology Reviews

Abstract

The Maisie and Lavoie gold vein systems, located in the Menneval – Saint-Quentin region of New Brunswick, Canada, lie within the Aroostook–Percé Anticlinorium (Restigouche Zone, Appalachian Orogen). They are hosted in Middle to Late Ordovician, calcareous and siliciclastic (deep-water flysch) sedimentary rocks of the Whites Brook Formation (Grog Brook Group). Native gold (Au:Ag=93:7) is hosted in quartz(-calcite) veins consisting of three distinct quartz(-calcite) textural stages (early laminated "Q1" → massive "Q2-C2" → late vuggy/lattice-bladed "Q3-C3"). Gold in the veins has a close spatial and textural relationship to trace amounts of partially hematitized pyrite, and other trace base metal sulfides (galena, sphalerite, chalcopyrite), and is paragenetically late-stage, infilling crystal-lined vugs in Q3 and fractures in Q1-Q2.

Fluid inclusions consist of three assemblage types (petrography based on observations at 20°C). Type 1 FIA (dominantly secondary, rarely indeterminate origin) consist of L_{aq}-rich, two-phase (L_{aq}+V) inclusions with optically homogeneous phase ratios. Type 2 FIA (dominantly secondary, rarely indeterminate origin) consist of variably L_{aq}-rich to V-rich to V-dominant, two-phase (L_{aq}+V) inclusions with widely variable L_{aq}:V ratios within

single FIA indicating heterogeneous entrapment. Type 3 FIA (indeterminate or secondary origin) consist of rare, L_{aq}-rich, two-phase (L_{aq}+V) inclusions amidst groups of dominantly V-rich to V-dominant, two-phase (L_{aq}+V) inclusions, interpreted to have entrapped a rapidly boiling ("flashing") fluid. Fluid inclusions in type 1 FIA have an average salinity (determined from final ice melting T) of ~2.2 ± 1.0 wt.% NaCl equiv. (1σ; n=66) and T_h values of ~174 ± 22°C (1σ; n=66). L_{aq}-rich inclusions in type 2 FIA have similar average salinities (~3.0 ± 1.6 wt.% NaCl equiv; 1σ; n=7) and T_h values (~215 ± 36°C; 1σ; n=7), as do L_{aq}-rich inclusions in type 3 FIA (salinity = ~2.2 ± 1.0 wt.% NaCl equiv; 1σ; n=14; T_h = ~190 ± 30°C; 1σ; n=14), and single L_{aq}-rich inclusions not associated with FIA (salinity = ~2.5 ± 2.0 wt.% NaCl equiv; 1σ; n=134; T_h = ~185 ± 25°C; 1σ; n=134). Individual FIA have much smaller intra-FIA ranges in fluid inclusion T_h and salinity. Anomalously high T_h values measured in some L_{aq}-rich inclusions, in particular in types 2 and 3 FIA, are attributed to accidental entrapment of small amounts of immiscible V in inclusions that optically appear to be end-member L_{aq} inclusions in these boiling/flashing FIA. In contrast, variability in T_h in type 1 FIA may be related to minor post-entrapment modification or real variations in P and T. Raman spectroscopy data shows that the fluids at Maisie and Lavoie carried trace amounts of CH_4 and N_2 but no detectable CO_2. Fluid inclusions at Maisie and Lavoie are interpreted to reflect trapping low salinity fluids that underwent boiling/flashing at very low confining P. Meteoric water mixing explains the fluid salinity values (as low as ~ 0 wt% equiv. NaCl) recorded in some samples/FIA.

Pyrite chemistry, determined by laser ablation inductively-coupled plasma mass spectrometry (LA-ICP-MS) spot analysis and mapping, reveals two generations of pyrite growth and trace metal association. Early pyrite I (coeval with Q2-C2) is enriched in Zn,

Cu, Sn and Ag and contains low Au (10^{-1} to 10^{0} ppm), whereas later pyrite II (coeval with Q3) is and overprints pyrite I ("island-mainland" and fracture-controlled replacement textures) is Au-enriched (10^{1} to 10^{2} ppm) and shows co-enrichment in Te, As, Bi, Sb, Pb, and Se with Au. In comparison, sedimentary (diagenetic) pyrite in the sulfidic Boland Brook Formation, that underlies the Maisie and Lavoie areas at depth , is a possible source of some metals (Cu, Zn, Sn, Mo) but has very low concentrations of Au (< 0.01 ppm; routine detection limits). An inherited sedimentary source of Cu, Zn, Sn, and Mo is suggested, whereas Au and associated elements are exotic to the host rocks.

Values of $\delta^{18}O_{V\text{-}SMOW}$ for quartz at Maisie and Lavoie obtained with secondary ion mass spectrometry (SIMS) range from ~ +12 to +25‰ overall, with a minor increase in the overall range of values from Q1 and Q2 (pre-gold; ~ +12 to +19‰) to Q3 (gold-coeval; ~ +18 to +25‰). Values of $\delta^{18}O_{V\text{-}SMOW}$ in Q3 at Maisie reach slightly higher maximum values than at Lavoie (by ~ 5‰). The ranges in $\delta^{18}O_{V\text{-}SMOW}$ in C3 calcite are similar to those of Q3, but extend to lower values of $\delta^{18}O_{V\text{-}SMOW}$ (~+15 to +25‰ at Maisie; ~+16 to +20‰ at Lavoie). The increase in $\delta^{18}O_{V\text{-}SMOW}$ values in the quartz with time, which corresponds to an estimated decrease in $\delta^{18}O_{V\text{-}SMOW}$ range for the equilibrium fluid from ~ +10 to +18‰ (Q1) to ~ +2 to +12‰ (vuggy Q3) and ~ +3 to +16‰ (bladed Q3) may have resulted from mixing of low-grade metamorphic fluids derived from partial dissolution/devolatilization of the host marine sediments, with cooler meteoric waters leading up to, and during, the main Au-mineralizing stage of vein development.

Bulk $\delta^{34}S_{V\text{-}CDT}$ values of vein sulfides (pyrite, chalcopyrite, galena, and sphalerite) obtained from SIMS range from -2.0 to 8.8 ‰. These values are typical of sulfides formed from the hydrothermal decomposition of sedimentary S-rich organic compounds, and

inconsistent with the range measured in the Boland Brook Formation pyrite ($\delta^{34}S_{V\text{-}CDT}$ = -17.2 to -13.0 ‰), precluding the dissolution of Boland Brook Formation pyrite as the main S source for sulfides in the veins. This is further supported by $\delta^{13}C_{V\text{-}PDB}$ values (bulk analyses) of vein calcite, ranging from -8.3 to -6.5 ‰ at Maisie, and -6.1 to -5.8 ‰ at Lavoie suggesting the influence of organic C. Likewise, at both locations, $^{87}Sr/^{86}Sr_o$ values of vein calcite range from 0.708610 to 0.709735. These values are very similar to hydrothermally modified marine carbonates within MVT settings in similar sediments regionally, reinforcing the influence of host sediments on fluid composition.

Cumulatively, the S-O-C-Sr isotope, fluid inclusion and pyrite compositional data indicate that the host sedimentary rocks had a major compositional impact on fluid chemistry (dissolution of marine carbonate cement, detrital feldspar, S derived from organic matter and some metals derived from sedimentary sulfides) but that late meteoric and "magmatic" (intrusion-related, epithermal?) contributions were likely. Gold mineralization at Maisie and Lavoie represent the same style of mineralization, sharing the following key genetic characteristics: (i) gold is *late-stage* (vug- and fracture-hosted; post-dating laminated and massive vein stages) and is coeval with trace pyrite and Zn-Pb-Cu sulfides; (ii) no disseminated sulfides related to mineralization are found in the wall rocks (wall-rock sulfidation is lacking); (iii) Au deposition involved meteoric water mixing with, and decompression-induced boiling ('flashing') of, a low salinity (< ~4-6 wt% equiv. NaCl), CO_2-poor fluid of sedimentary metamorphic origin (± a magmatic contribution?) at a T between ~150-250^oC and P < 50 bar; and (iv) later remobilization of gold (locally) during shallow oxidation of the veins.

The Maisie and Lavoie auriferous veins have features consistent with both shallow (epizonal) orogenic Au deposits hosted in sedimentary rocks, and low-sulfidation epithermal or intrusion-related Au deposits. Some of the exotic metals elevated in pyrite II (Au, Bi, Te, and As?) may be linked to magmas which also sourced a porphyry dike adjacent to the Maisie vein. Semi-quantitative mineral thermometry of wall-rock chlorite (Al-in-chlorite) adjacent to the main quartz vein at Maisie, and early brookite (Zr-in-brookite) and quartz (Ti-in-quartz) from the vein itself suggests that local conditions early in vein development (prior to Q3 and associated Au deposition) were much hotter (i.e., by several hundred degrees) than published regional metamorphic conditions interpreted from vitrinite reflectance data. Preliminary geochronology (ID-TIMS) for inherited magmatic zircon from the main quartz vein at Maisie returned a maximum mineralization age of 370.03 ± 0.20 Ma, whereas the porphyry dike adjacent to the vein contains zircons that returned distinct age populations of 367.12 ± 0.11 Ma (crystallization age) and 368.15 ± 0.25 Ma (inherited). While the age of an inherited zircon from the Au vein at Maisie constrains only the maximum age of mineralization to near the end of the Acadian orogeny (Late Devonian), the overall population of magmatic zircons highlights a previously unrecognized ~ 3 Ma period of magmatic activity in the area that began prior to vein formation, and does not preclude the possibility that this activity contributed to the Au endowment in the hydrothermal systems.

2.1 Introduction

Despite exhaustive investigations of the mineralogy and paragenesis, fluid evolution (through fluid inclusion and stable isotope studies), alteration, structure, and timing of vein formation in orogenic gold systems (e.g. Groves et al., 1998; Goldfarb et al., 2005;

Lambeck et al., 2011; Large et al., 2011; Bodnar et al., 2014; and Goldfarb and Groves, 2015 and authors therein), ambiguity concerning Au source and the relative importance (if any) of magmas as heat and fluid and/or metal sources still persists. This is commonly a key theme in orogenic Au studies (Homestake, South Dakota, USA: Rye & Rye, 1974; Dolaucothi, Wales, United Kingdom: Annels & Roberts, 1989; Bendigo-Ballarat, Australia: Kerrich and Wyman, 1990; Natalka, Russia: Eremin et al., 1994; Carlin and Jerritt Canyon, Nevada, USA: Groves et al, 1998; Ramsay et al, 1998; Meguma terrain of Nova Scotia, Canada: Ryan and Smith, 1998; Goldfarb et al., 2001; Muruntau, Uzbekistan: Wilde et al, 2001; Kumtor, Kyrgyzstan: Mao et al., 2004; and Saint-André-de-Restigouche, Québec: Garnier et al, 2007). The potential role played by magmas in the formation of orogenic Au systems is difficult to assess for many reasons; some key aspects of this challenge: (i) identifying the causative magmatic sources – are they temporally, spatially, and are structurally available to contribute volatiles and metals?; (ii) quantifying the Au fertility of available magmas – what is the mass of magma and associated magmatic Au-rich fluid needed (and how Au-rich), relative to metamorphic fluid extracting Au from potentially exotic, variably Au-enriched protoliths in the host terrane?; (iii) detecting a minor but potentially Au-rich magmatic fluid component from a mass-dominant metamorphic fluid signature – can a combination of high resolution analytical techniques discriminate a small but potentially critical magmatic fluid (and Au) source?

The largest orogenic Au deposits in Canada are associated with Archean greenstone belts; however, smaller but economically significant deposits occur in the northern Appalachian Orogen, including the sediment (flysch)-hosted deposits of the Meguma terrane (Kontak et al., 1990; Ryan and Smith, 1998; Sangster et al., 2007) of Nova Scotia,

Canada. Further north, in New Brunswick, within the Miramichi and Elmtree terranes, and adjacent Matapédia Basin, Au occurrences (and metallic mineral deposits in general) are relatively sparse with few discoveries in the last few decades outside of the Bathurst and Gaspé districts (Tremblay and Dube, 1991; Malo et al., 2000; McClenaghan et al., 2003; Garnier et al., 2007; Thorne, 2011). These include Fe-Cu ± Au skarns at McKenzie Gulch (Lentz et al., 1995), and occurrences of refractory Au in orogenic and polymetallic sulfides at the Elmtree property (West Gabbro Zone, Discovery Zone, and South Gold Zone) (Ruitenberg et al., 1989; Bustard and Lentz, 2019) and Middle River Au occurrence (Schwarz & Lentz, 2009) occurrences.

Geological studies in northern New Brunswick, Canada (Carroll, 2003a,b; Wilson et al., 2004; Parkhill, 2005; and Wilson and Kamo, 2012) established a lithogeochemical frame work for evaluating the genetic relationship between Au mineralization and potentially causative magmatic systems. For example, Siluro-Devonian sedimentary and volcanic rocks hosting Au mineralization in the Upsalquitch Forks area, were penetratively-deformed during the Acadian orogeny. McCutcheon and Bevier (1990) suggested that major structural features (i.e. McKenzie Gulch, Rocky Brook–Millstream, and Restigouche–Grand Pabos faults) were not the only controls on Au mineralization. They suggested that an ~ 18 Ma duration of bimodal magmatism in the Late Silurian to Early Devonian (Wilson, 2017) likely played an equally important role. Justification for this relationship includes the presence of small intrusions that are spatially and genetically linked to the Simpsons Field, McCormack Brook, Dalhousie Road, and Mulligan Gulch Au occurrences but that were emplaced remote from the major faults, or that clearly postdate faulting. Such magmas may have supplied metals, or at least provided heat to drive

the convective systems responsible for the re-distribution of metals from another source via hydrothermal activity.

Recently discovered non-refractory Au quartz vein occurrences in subgreenschist-facies flysch sequences of the Matapédia Basin (Restigouche Zone) may represent a new style of Au mineralization in the region, highlighting the importance of continued exploration in atypical terranes. In this study, two occurrences, the Maisie and Lavoie showings, will be investigated and compared in order to accomplish the following objectives: (i) to provide mineral identification and a means to evaluate paragenetic relations through petrography (microscopy, Raman spectroscopy, and SEM); (ii) to constrain the conditions of vein formation through mineral chemistry and thermometry, hot cathodoluminescence, and fluid inclusion microthermometry and chemistry; (iii) to constrain fluid and metal source through investigation of the trace element chemistry, stable isotope (C, S, and O) and radiogenic isotope (Sr) systematics of vein minerals; (iv) to constrain the timing of vein formation relative to magmatic activity, locally, through preliminary U-Pb geochronology; and (v) to classify the style of Au mineralization at both occurrences. Finally, the results of this work are used to develop a model to describe the genesis of the previously unknown style of Au mineralization in northwest New Brunswick.

2.2 Geology

2.2.1 – Regional geology of the Saint-Quentin and Menneval area

The rocks of northwestern New Brunswick and adjacent southeastern Québec comprise Late Ordovician to Early Devonian siliceous and carbonaceous sedimentary rocks. The region is divided into three, northeast-southwest striking tectono-stratigraphic belts (Fig. 1): the Connecticut Valley–Gaspé Synclinorium (CVGS), the Aroostook-Percé

Anticlinorium (APA), and the Chaleurs Bay Synclinorium (CB). In Québec, these belts are collectively included in the Gaspé Belt (Malo and Bourque, 1993). In New Brunswick the CVGS and APA are included in the Restigouche Zone, whereas the CBS is included in the Tobique-Chaleur Zone (Davies, 1977).

Within the region, Au deposits of varying type exist (Fig. 1), with occurrences of three prominent styles of Au mineralization reported in literature (Ruitenberg et al. (1989); Malo et al. (2000); Garnier et al. (2007); Thorne (2011); and Bustard and Lentz (2019)):

1. *Orogenic Au* – Elmtree (West Gabbro and South Gold Zone), Rocky Brook, Upsalquitch, McCormack Brook, Dalhousie Road, Simpson Field, and Manzer Giberson
2. *Skarn related Au* – Saint-Andre-de-Restigouche, Patapedia, Stephens Brook, McKenzie Gulch, and Reggie Brook
3. *Gold-rich VMS* – Murray Brook
4. *Polymetallic "epithermal"* – Elmtree (Discovery Zone)

In New Brunswick the APA is separated from adjacent belts by the Restigouche Fault in the west and the McKenzie Gulch Fault in the east. The Restigouche Fault is the southwestern extension of the Grand Pabos Fault. In Québec, this fault is thought to account for up to ~85 km of past dextral strike slip movement (Malo and Béland, 1989). In the Gaspé Peninsula there are several Au and base metal skarn occurrences within rocks of the APA, most of which are associated with strike-slip movement along the Grand Pabos Fault system during the Acadian orogeny (Malo et al., 2000). In the eastern Gaspé Peninsula the Grand Pabos Fault marks the boundary between the APA and the Chaleur Bay

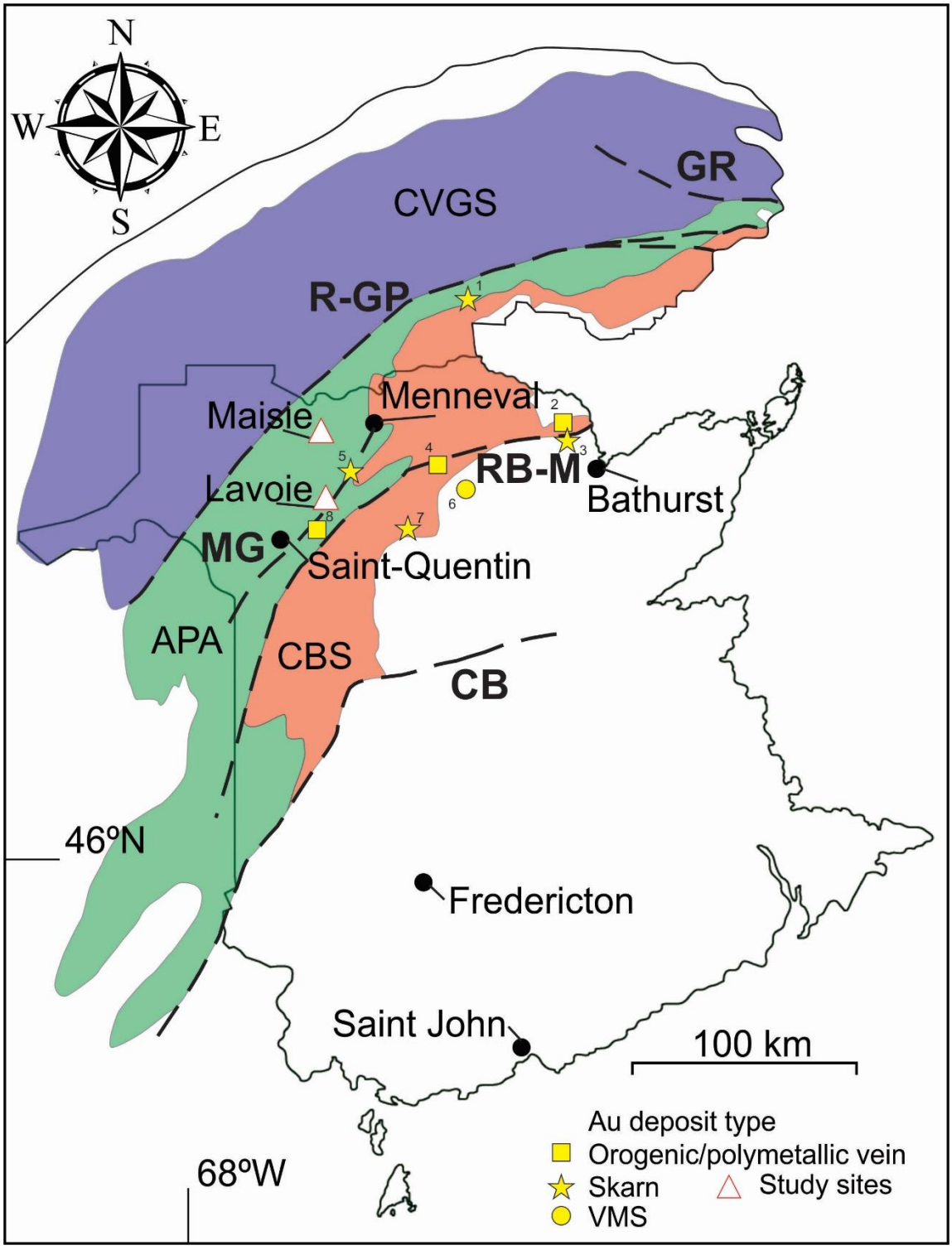
N
W
E
S
CVGS
GR
R-GP
Maisie
Menneval
Lavoie
RB-M
Bathurst
MG
Saint-Quentin
APA
CBS
CB
46ºN
Fredericton
Saint John
100 km
68ºW
Au deposit type
Orogenic/polymetallic vein
Skarn
Study sites
VMS
1
2
3
4
5
6
7
8

Figure 2.1 previous page- Map of northern New Brunswick and Québec showing major faults and structural trends. Study area of the Maisie and Lavoie Au occurrences marked by red/white triangles. Map modified after Wilson et al. (2004), with additional Au deposits/occurrences compiled from Ruitenberg et al. (1989), Malo et al. (2000), Garnier et al. (2007), and Thorne (2011). Numbered Au deposits and occurrences are: 1 – Saint-André-de-Restigouche/Patapédia; 2 –Elmtree (West Gabbro, South Gold, and Discovery Zones); 3 – Stephens Brook; 4 – Rocky Brook/Upsqualch/McKormic Brook/Dalhousie/Simpson Field; 5 – McKenzie Gulch; 6 – Murray Brook; 7 – Reggie Brook; 8 – Manzer Giberson. Major structures: CVGS – Connecticut Valley - Gaspé Synclinorium; APA – Aroostook-Percé Anticlinorium; CBS – Chaleur Bay Synclinorium; GR – Grande Riviere Fault; R-GP – Restigouche – Grand Pabos Fault; MG – McKenzie Gulch Fault; RB-M – Rocky Brook - Millstream Fault; CB – Catamaran Brook Fault.

Synclinorium to the south, whereas to the west the Grand Pabos Fault crosses the APA to become the Restigouche Fault. The APA contains a middle Paleozoic succession of clastic and calcareous marine sedimentary rocks of the Grog Brook Group, and conformably overlying Matapédia Group.

The Maisie and Lavoie Au veins are hosted by the Grog Brook Group, which is subdivided into the Boland Brook and Whites Brook Formations. The Boland Brook Formation is dominated by dark greenish-grey, thinly-bedded, non-calcareous mudstone, siltstone, and fine-grained sandstone (Carroll 2003a; Wilson, 2003; Wilson et al., 2004). Medium- to coarse-grained sandstone, and conglomerate compose the lowest exposed parts of the Boland Brook Formation. The Boland Brook Formation is conformably overlain by the Whites Brook Formation and consists of light to medium greenish grey, medium- to thick-bedded, medium- to coarse-grained, calcareous to non-calcareous sandstone and conglomerate, with thin interbeds of dark grey non-calcareous shale and siltstone. Although thickness varies considerably, the Whites Brook Formation may be up to 4000 m thick in the study area (Carroll 2003a and Wilson et. al. 2004). The Whites Brook Formation has yielded graptolites of late Caradocian to early Ashgillian age (~449 Ma; Riva and Malo, 1988). The Whites Brook Formation is conformably overlain by the Pabos Formation (Matapédia Group).

The Matapédia Group, which conformably overlies the Grog Brook Group, is divided into the Pabos Formation and the conformably overlying White Head Formation. In New Brunswick, the Pabos Formation is at least 1000 m thick and consists mainly of thinly-bedded, dark greenish-grey calcareous siltstone with thin sandstone laminae, intercalated with thin beds of grey carbonate-rich mudstone and minor fine-grained sandstone (Carroll,

2003a; Wilson, 2003; Wilson et al., 2004). A lower member, locally exposed at Squaw Cap on Route 17 and on the Restigouche River, downstream from its confluence with the Upsalquitch River, is transitional between the underlying Whites Brook Formation and more typical Pabos lithotypes. It consists of light grey, weakly to strongly calcareous, medium-bedded, medium- to coarse-grained sandstone, siltstone and minor conglomerate, intercalated with dark grey calcareous shale (Wilson, 2003).

Igneous rocks are rare in the APA; however, few small mafic intrusions including north-northeast striking lamprophyre and diabase dikes have been recognized. . The largest of these, located just west of Kedgwick, NB, can be traced for over 12 km along a northwest strike (anomalously large compared to other dikes), and is offset by east-northeast trending faults. Another large mafic dike located just west of the Lavoie occurrence, strikes east-northeast, and has returned an Ar-Ar age of 409 ± 5.9 Ma (Carroll, 2003a). Two other mafic intrusions in the Kedgwick–St. Quentin area, (lamprophyre and diabase), have returned ages of 376.5 ± 1.9 Ma and 391.8 ± 1.8Ma, respectively (Carroll, 2003a). Felsic intrusions, composed of granodiorites, felsites, and dacites, are somewhat more common but tend to be spatially associated with the margins of the APA, i.e. with the major northeast striking faults such as the McKenzie Gulch, Rocky Brook-Millstream, and Restigouche–Grand Pabos faults. The only ages available for felsic intrusions comes from a biotite granodiorite dike within a metamorphic aureole of the Patapedia River intrusion, which gives a U-Pb date of 364.4 ± 0.4Ma (Carroll, 2003a), and the McKenzie Gulch quartz-plagioclase/plagioclase-hornblende porphyry dikes, which give U-Pb dates of 386.4 ± 3.3 Ma and 386.2 ± 3.1 Ma, respectively (Massawe and Lentz, 2020). Other felsic intrusions (Jerry Ferguson Porphyry, Red Brook Granodiorite, McKenzie Gulch Porphyry, Landry

Brook Quartz Monzonite) in the Restigouche and Charlo-Jacquet River areas yielded ages between ~401 Ma and ~383 Ma, spanning the duration of the Acadian orogeny (McCutcheon and Bevier, 1990; Wilson et al., 2004, after V. McNicoll, communication, 2001).

2.2.2 – Bedrock geology and description of the Maisie and Lavoie occurrences

2.2.2.1 – Geology of Maisie and Lavoie

The Whites Brook Formation, which hosts both the Maisie and Lavoie occurrences (Fig. 2), consists of up to 4000 m of light to medium greenish grey, medium- to thick-bedded, medium- to coarse-grained, calcareous to non-calcareous sandstone and conglomerate, with thin interbeds of dark grey, non-calcareous shale and siltstone (Carroll 2003a, b).

Host rocks to Au mineralization belong to the Ordovician Whites Brook Formation (Fig. 2) and consist of light grey, fine-grained sandstones interbedded with dark greenish grey mudstone and siltstone. The light green mudstone is similar to that included in the Boland Brook Formation that underlies the Whites Brook Formation and crops out approximately 2.5 km to the south and south east of the Maisie showing and approximately the same distance east of the Lavoie showing. The Boland Brook Formation (Fig. 2) is characterized by millimetre-scale laminations, and bed thicknesses on the order of 4 to 5 cm.

A fine-grained plagioclase-biotite dacite porphyry intrusion occurs immediately northwest of the Maisie showing. Drill core intersections of this unit suggest that it has a NE-SW strike; however, at present cross-cutting and genetic relationships to the quartz veins and Au mineralization at Maisie are unknown.

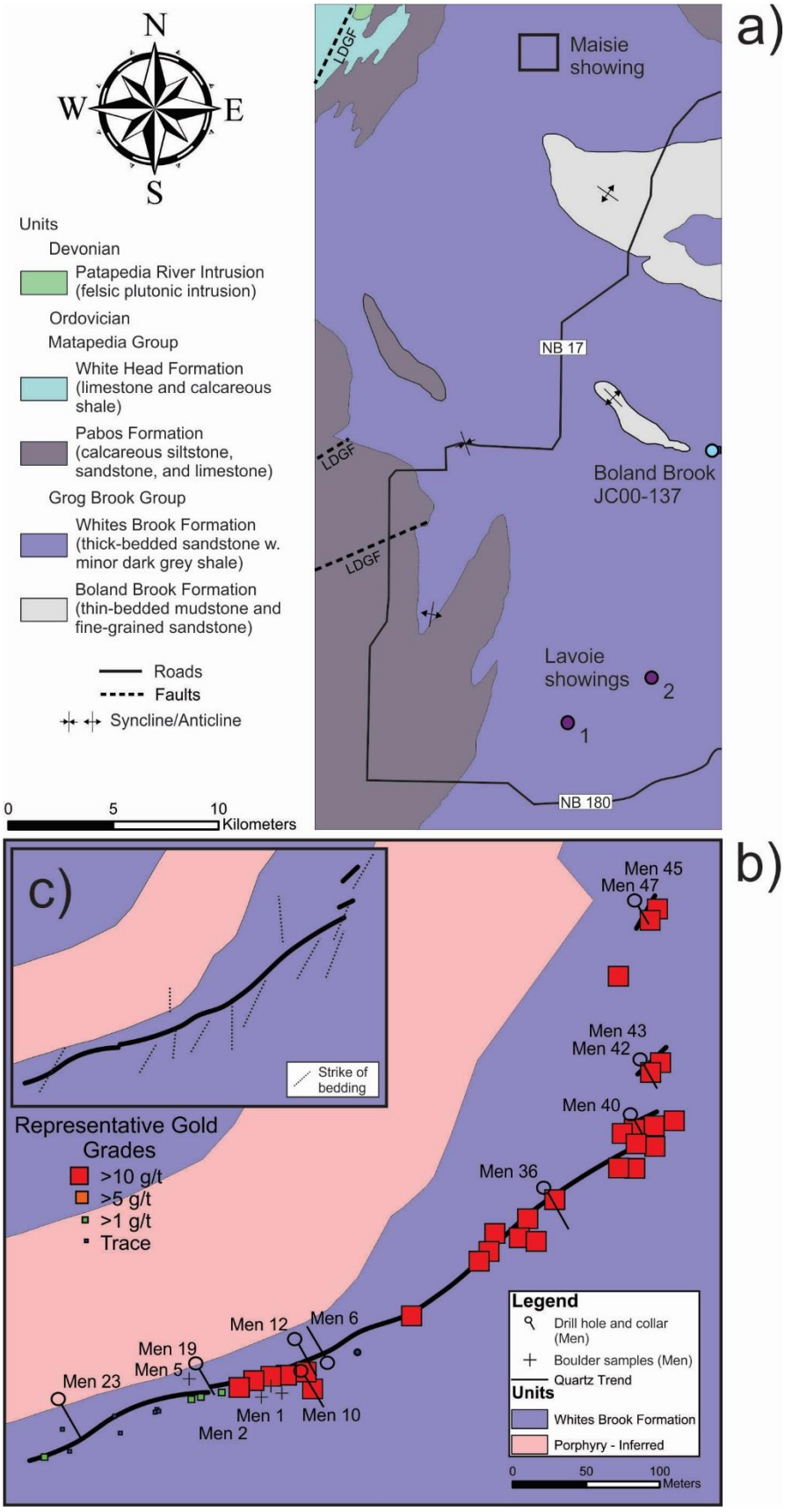
a)
N
W
E
S
Units
Devonian
Patapedia River Intrusion (felsic plutonic intrusion)
Ordovician
Matapedia Group
White Head Formation (limestone and calcareous shale)
Pabos Formation (calcareous siltstone, sandstone, and limestone)
Grog Brook Group
Whites Brook Formation (thick-bedded sandstone w. minor dark grey shale)
Boland Brook Formation (thin-bedded mudstone and fine-grained sandstone)
Roads
Faults
Syncline/Anticline
0
5
10
Kilometers
LDGF
Maisie showing
NB 17
Boland Brook JC00-137
Lavoie showings
2
1
NB 180
b)
c)
Strike of bedding
Representative Gold Grades
>10 g/t
>5 g/t
>1 g/t
Trace
Men 45
Men 47
Men 43
Men 42
Men 40
Men 36
Men 12
Men 6
Men 19
Men 5
Men 23
Men 1
Men 10
Men 2
Legend
Drill hole and collar (Men)
Boulder samples (Men)
Quartz Trend
Units
Whites Brook Formation
Porphyry - Inferred
0
50
100
Meters

Figure 2.2 previous page – Geological maps of the study area. a) Simplified regional geological map of the Saint-Quentin (Lavoie) and Menneval (Maisie) study areas, New Brunswick, displaying bedrock geology and major regional faults. LDGF = Lower Downs Gulch Fault. b) Local map of Maisie Au showing, including representative Au grades, drill hole collar locations and horizontal projections, the location of a porphyry dike adjacent to the vein (based on SLAM Exploration publication), and soil sample sites along trench walls. Inset depicts bedding trend based on drill core logs. c) Inset shows bedding orientation based on drill core logs. Bedding trend is shown to be sub-orthogonal to vein strike.

The metamorphic grade of the rocks hosting the Lavoie and Maisie Au occurrences is not high, revealed by vitrinite reflectance values collected ~5 km from the Lavoie showing (5.8 %) and ~2 km from the Maisie showing (4.4 %). Based on the vitrinite data, host rocks have been metamorphosed beyond the oil window, to a maximum temperature of ~ 265 °C (regionally; Bertrand et al., 2005).

2.2.2 – Sample site and trench location descriptions

At both Maisie and Lavoie there was limited exposure of the auriferous veins in trenches and outcrop limiting the opportunity to gather structural data and to map at outcrop-scale.

At the Maisie (47°48'56"N, +67°16'17"W) Au occurrence (Fig. 2), a large auriferous quartz(-carbonate) vein has been traced almost continuously over a strike length of ~700 m and vein widths ranging from 30 cm to > 2 m on surface. At its western end, drill intersects infer that the vein strikes east-northeast but becomes more northeast–striking towards the east (Fig. 2b). The eastern–most 100 m of the vein is segmented by at least three north-northwest trending, sinistral, brittle faults that offset and reorient vein segments to a more north-northeast strike (20^{o}-25^{o}) (Fig. 2b). Additional auriferous veins have also been identified to the southeast of this largest vein. Bulk rock Au grades in the vein are low where the vein is close and tangential to the porphyry dike contact in the southwest map area, but increase from <1 gm/t to >10 gm/t over a very short distance toward the northeast end of the vein. The Au grades remain high (>10 gm/t) for the remaining length of the vein (see Fig. 2b).

The Lavoie (47°31'20"N, +67°15'40"W) Au occurrence consists of northeast–striking auriferous quartz veins that are semi-continuous over a minimum strike length of 220 m

and widths up to 1.5 m. Float samples in the vicinity indicate that the mineralized zone may extend over a strike length of up to ~580 m.

Trench exposures of the host sedimentary rocks at Maisie and Lavoie show mainly sub-horizontal primary bedding, with gentle folding of this bedding (Fig. 3a, b). Locally, quartz(-carbonate) veins (with some minor extensional jogs), breccia, and spur veins formed along parted bedding planes (i.e. sheeted veins, Figure 3d). Within small isoclinal, disharmonic folds where there has been buckling of the host rocks, small quartz veinlets part the folded bedding in these areas and appear to be folded quartz veins, but they are only mimicking the shape of the folds (Fig. 3e), being syn- to post-deformational. Exposed quartz-carbonate veins range from massive single veins (Fig. 3c) to sheeted veins (Fig. 3d). At Maisie, with the exception of localized bedding parallel vein structures, the main quartz vein cross-cuts primary bedding suborthogonally (Fig. 2c) and pencil cleavage (Acadian; Wilson et al., 2004) in the wall rocks (Fig. 3f), indicates that the vein formed in a fault that postdates host deposition and post-dates or is late-syngenetic with regional Acadian deformation.

2.2.3 – Gold exploration history at the Maisie and Lavoie occurrences

At the Maisie Au showing, a program of shallow drilling in 2012 and early 2013 was successful in proving the extension of mineralization to depths of ~25 m (Slam Exploration Ltd., communication). The drilling program initially consisted of 27 diamond drill holes totaling ~4850 m. To date, the highest grade is from a 4 m-wide quartz vein interval, at 8.5 gm/t Au that includes a 0.3 m-wide interval grading 104 gm/t (drill hole MG-12-26) (Lloyd, 2013).

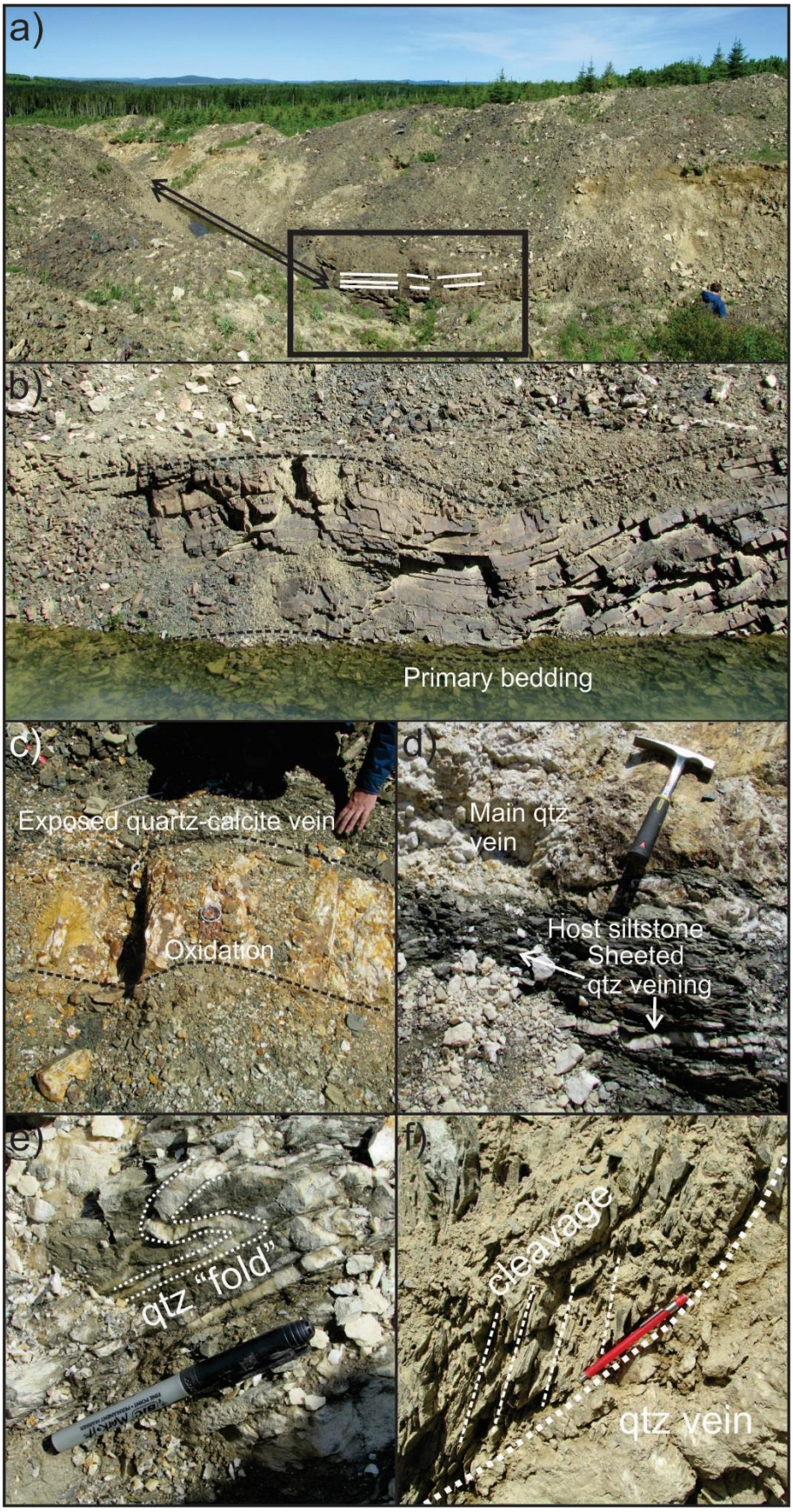
a)
b)
Primary bedding
c)
Exposed quartz-calcite vein
Oxidation
d)
Main qtz vein
Host siltstone
Sheeted qtz veining
e)
qtz "fold"
f)
cleavage
qtz vein

Figure 2.3 previous page – Photos of field relations showing representative host rock and vein relationships, and structures, at the Maisie and Lavoie gold showings. a) Overview of a segment of the exposed vein trench showing the scale of trenching and preserved bedding (Maisie). b) Magnified in image of boxed region in 2a showing gently folded, primary sedimentary bedding, trending northeast (Maisie). c) Exposed quartz-calcite vein (in floor of trench), showing oxidation (gossan) of sulfides (Maisie). d) Vein exposure showing sheeted veining in host sedimentary rock (Maisie). e) Quartz vein contained within (mimicking) pre-existing folded sediments (Lavoie). f) Host rocks showing pencil cleavage cross-cut by a Au-mineralized quartz vein (Lavoie).

The Lavoie Au showing, discovered in 2011 by Tim Lavoie, is a 650 m long, north-northeast striking quartz vein, with grab samples of quartz vein material from the Discovery Zone (Lavoie showing, Fig. 2) containing free Au and yielding assays of up to 493 gm/t Au (Klaussen & Lloyd, 2012). A small drill program, consisting of 4 diamond drill holes totalling 240 m explored the vein over a short strike length. Follow up exploration was then carried out in 2017, further northeast of the Lavoie property (Lavoie showing 2, Fig. 2). While no drilling was performed at the time, there is trenching of the vein, and till samples were collected. Of the two Lavoie Au showings, trenching has identified seven individual quartz veins over a distance of ~ 50 m, with widths ranging from 0.10 to 1.0 m. Grab samples have yielded Au values up to 154 ppb. The trenching of the RIM vein (Lavoie showing 2, Fig. 2), strikes north-east for >60 m. Grab samples from the RIM vein returned assays of up to 677 gm/t Au (Flanagan, 2015). X-terra Resources Inc. recently acquired the property and conducted ground geophysics, trenching, and geochemical till sampling in 2019, results of this work are confidential at the time of writing.

2.3 Methodology

The primary objectives for this study are to characterize the Maisie and Lavoie Au occurrences and to form a genetic model, which can be achieved through; (i) host rock and vein petrography; (ii) vein formation constraints; (iii) fluid and metal source; and (iv) determining the age of vein mineralization. These objectives were met by using the following analytical methods.

2.3.1 – Scanning electron microscopy (SEM)

Quantitative analysis of mineral phases hosting Au and vein accessory minerals, and characterization of paragenetic relationships, was done using SEM back-scattered electron

(BSE) imaging and energy dispersive spectroscopy (EDS) at Saint Mary's University. The instrument used was a TESCAN MIRA 3 LMU VPS field emission SEM equipped with a solid-state EDS detector (Oxford Instruments X-max 80mm^2). The SEM was operated at an accelerating voltage between 20 and 30 kV, a beam current of 2 nA, and a working distance of 17 mm. The desktop computer software used for EDS spectrum collection and analysis was the INCA platform (ETAS GmbH). Gold composition was determined by SEM-EDS analysis.

2.3.2 – "Hot cathode" cathodoluminescence imaging

Qualitative "hot cathode" cathodoluminescence (CL) emission imaging, which provides textural information related to quartz vein formation, was conducted at Saint Mary's University, Halifax, Nova Scotia, using a Lumic HC4-LM cathodoluminescence microscope coupled to an Olympus BXFM focusing mount. Images were captured by a Kappa DX40C Peltier-cooled camera operated using the DX40C-285FW software package (Lumic). The hot CL was operated at an acceleration voltage between 12.4-13.1 kV, a beam current of 0.35 mA, a filament current of 2.3 A, a deflection of 10 V and a focus of 5.5 V.

2.3.3 – Electron microprobe (EMPA)

To obtain analysis of chlorite for semi quantitative thermometry, electron microprobe analysis (EMPA-WDS) was carried out at the Regional Electron Microprobe Center at Dalhousie University, Halifax, Nova Scotia. The instrument used was a JEOL-8200 EMP which uses a Noran 133 eV energy dispersive spectrometer. The EMP was operated at an accelerating voltage of 15 kV, a beam current of 20 nA, and a spot size of 1 µm. For calibration and peak Kα positioning, the following standards were used: (i) sanidine for K, Al, and Si; (ii) kaersutite for Ca, Ti, and Mg; (iii) Cr-metal for Cr; (iv) jadeite for Na; (v)

garnet for Fe; and (vi) pyrolusite for Mn. Count times were 20 s on peak, and 10 s on backgrounds. An in-house chlorite standard (SB53 chlorite) was used to monitor analytical accuracy. Chlorite compositions were recast from major and minor oxides to cations per formula unit (p.f.u.) using the program WinCcac (Yavuz et al., 2015)

2.3.4 – Fluid inclusion microthermometry

Microthermometry was performed on 160 inclusions in 9 samples from the Maisie occurrence, and 59 inclusions in 6 samples from the Lavoie occurrence using a Linkham FTIR600 heating-freezing stage mounted on an Olympus BX51 microscope at Saint Mary's University, Halifax, Nova Scotia. Where possible the FIA method (Goldstein and Reynolds, 1994) was used to group inclusions of common temporal origin. Quartz- and calcite-hosted fluid inclusions were mapped out in 15 doubly-polished thin sections, and 1cm x 1cm representative wafers were cut out with a fine diamond saw, and removed from glass slides in an acetone bath. Calibration of the stage was done using synthetic fluid inclusion standards consisting of pure CO_2 (melting at -56.6 °C) and pure H_2O (melting at 0˚C and homogenizing at critical T of 374.1 °C). Using these constraints, a correction for stage bias was applied to data. Uncertainties for the microthermometric measurements are ± 0.2 °C for measurements around 0 °C, and ± 0.5 °C for measurements over 300 °C at a heating rate of 1°C/min . Fluid inclusions were modelled in the NaCl – H_2O system using the program SOWAT (Driesner, 2007; Driesner and Heinrich, 2007), with salinities and isochores determined using T_m^{ICE} and T_h values.

2.3.5 – Major, minor, and trace element analysis by LA-ICP-MS

2.3.5.1 – Trace element analysis of pyrite

Trace element (precious, transition, semi-metals concentrations) in pyrite were determined by laser ablation inductively-coupled plasma mass spectrometry (LA-ICP-MS) at the Department of Earth Sciences, University of New Brunswick. Spot ablations of pyrite were conducted using a 24 μm beam diameter at a 3 Hz repetition rate with the laser fluence regulated at ~3 J/cm^2. Spot ablations involved 30 s of transient signal collected from pyrite followed by 30 s of gas background collection. Pyrite trace element mapping used a 17 μm beam diameter, a stage scan speed of 6 μm/s, and a 10 Hz repetition with the laser fluence regulated at ~3 J/cm^2. Oxide production rates were maintained below 0.3 %. Dwell times for all elements was 10 ms except for Au, Pt, and Pd which were 50 ms. For spot analyses, a 'squid' smoothing device was used to ensure low %RSD signals; the 'squid' was removed for trace element mapping to ensure fastest possible washout duration from the cell (~3 orders of magnitude decrease in signal intensity in 1 s). Trace element concentrations in unknowns were calibrated against sulfide reference material MASS-1 (to calibrate analyte sensitivities) and an internal standard of 46.5 wt % Fe for ideal pyrite. At the end of the ablation sequence, the laser log file and ICP-MS intensity data file were synchronized using Iolite™ (Paton et al., 2011) running as a plug in for Wave metrics Igor Pro 6.22™. Individual ablation signals were inspected offline and adjusted when necessary to avoid artifacts related to ablating through thin grains or from the beam ablating another mineral (e.g., silicates). Spikes in the data were automatically filtered using the default 2σ outlier rejection in the Iolite internally- standardized trace-element data reduction scheme. For trace element maps, non-pyrite phases were removed using the Fe CPS elemental map as a

guide; concentration scales for each map portray internally standardized absolute ppm levels. Data were collected from the continuous line scans by integrating counts over a selected time interval, which converts a portion of the line scan analysis into a point-type analysis.

2.3.5.2 – Major, minor, and trace element analysis of brookite and quartz

Major and trace element analysis of brookite and quartz were determined by LA-ICP-MS at the Department of Earth Sciences, University of New Brunswick. The measurements were acquired using a pulsed (20 ns) 193 nm ArF Excimer laser ablation system (Resonetics RESOlution M-50) coupled to an Ar^- plasma quadrupole ICP-MS (Thermo Scientific X Series II). The ablation system employs a two-volume Laurin Technic sample cell. Measurements were conducted with a 10 ms dwell time for each analyte isotope, a forward torch power of 1450 W, gas flow rates of 0.8 l/min, 0.65 l/min and 6 ml/min for Ar, He and N_2, respectively, and laser fluence of 6 J/cm^2. The raw data (in cps vs. time) were quantified using the Iolite software package (Paton et al. 2011), with synthetic NIST SRM 610 glass used as an external reference material to calibrate analyte sensitivities, Ti (59.9 wt. %) as the internal standard for brookite, and Si (~100 wt.%) as the internal standard for quartz. The BHVO-2G reference glass was used as a QC monitor.

2.3.5.3 – Major and trace element analysis of fluid inclusions and zircon

The major and trace element compositions of fluid inclusions and trace element chemistry of zircon were determined by LA-ICP-MS at the University of Toronto, Department of Earth Sciences, Toronto, Ontario and Boise State University, Idaho. At the University of Toronto, the instrument used was NWR 193 UC laser ablation system coupled to an Agilent 7900 inductively coupled plasma quadruple mass spectrometer. Gas

flow rates used were 1.0 L/min for He and 0.85 L/min for Ar. Dwell times were set to 10 ms for all elements measured, except for Ag and Au, which were 30 ms and 100 ms respectively. Ablation pit diameter was set to 5 µm larger than the inclusion being ablated, and 30 µm for calcite. Trace element quantification of fluid inclusions was performed using the software platform SILLS (Guillong et al., 2008). Analyte sensitivities were calibrated using the reference standard NIST610, ablated at the beginning and end of each block of inclusions or zircon spots. The salinity of the inclusions (in wt.% equiv. NaCl) determined by microthermometry was used for internal standardization. The Zr (wt%) content of ideal zircon were used as internal standard for calcite and zircon quantification. Values for quartz host were used to correct fluid inclusion data, by removing background values in average quartz.

At Boise State University, zircon was analyzed by LA-ICP-MS using a ThermoElectron X-Series II quadrupole IC-PMS and New Wave Research UP-213 Nd:YAG UV (213 nm) laser ablation system. Zircon was ablated with a laser spot of 30 µm wide using fluence and pulse rates of 5 J/cm^2 and 5 Hz, respectively, during a 45 second analysis (15 sec gas blank, 30 sec ablation) that excavated a pit ~25 µm deep. Ablated material was carried by a 1.2 L/min He gas stream to the nebulizer flow of the plasma. Quadrupole dwell times were 5 ms for Si and Zr, and 10 ms for REE; total sweep duration was 950 ms. Background count rates for each analyte were obtained prior to each spot analysis and subtracted from the raw count rate for each analyte. For concentration calculations, background-subtracted count rates for each analyte were internally normalized to ^{29}Si and calibrated with respect to NIST SRM-610 and -612 glasses as the primary standards.

2.3.6 – Bulk O, C, and Sr isotope of vein calcite

Approximately 30–60 μg of carbonate powder was excavated from each sample using a tungsten carbide microdrill bur (Komet Dental; 0.4 mm diameter) mounted on a dremel tool, and weighed into glass vials (Saint Mary's University). Carbon and oxygen isotope ratios of carbonates were measured on a Nu Perspective dual-inlet isotope ratio mass spectrometer connected to a NuCarb carbonate preparation system at McGill University Stable Isotope Laboratory (Montréal, Canada). The powdered carbonates were then reacted individually with H_3PO_4 after heating to 90 ºC for 1 hour (McGill University). The released CO_2 was collected cryogenically and isotope ratios were measured against an in-house reference gas in dual inlet mode. Samples were calibrated to VPDB using house standards. For the purpose of reporting data in this study, $\delta^{18}O$ values reported from the McGill facility relative to VPDB were converted to VSMOW. Uncertainties are ±0.05 ‰ (1σ) for both $\delta^{13}C$ and $\delta^{18}O$.

For Sr isotope analyses, approximately 15 mg of sample powder was collected for each sample using a tungsten carbide dental drill. Strontium isotope ratios were measured on a Thermo Scientific Triton™ thermal ionization mass spectrometer (TIMS) at the Université de Québec à Montréal/Geotop. Powders were first leached three times in 0.2M ammonium acetate, and then rinsed three times in MQH_2O. The calcite fraction of the samples was then dissolved in 0.5M acetic acid, which was then separated from the insoluble fraction by centrifugation, dried down, and taken up in 3N HNO_3. Sr was separated from the matrix following standard Sr chromatography procedures using EICHROM Sr Spec™ resin. Internal mass bias was corrected based on the ratio $^{86}Sr/^{88}Sr = 0.1194$. Analyses of NBS SRM 987 yielded a long-term average of 0.710245, compared to the accepted value of

0.710250. Values of $(^{87}Sr/^{86}Sr)_o$ were corrected for a negligible amount of radioactive ingrowth resulting from trace Rb content.

2.3.7 – SIMS O and S isotope analysis of vein quartz, calcite, and sulfide accessory minerals

Stable oxygen isotope ratios of vein quartz and calcite, and sulfur isotope ratio of pyrite, chalcopyrite, galena, and sphalerite were collected using a CAMECA IMS 7f secondary ion mass spectrometer (SIMS) at the Department of Geology, University of Manitoba. The conditions for sulfur and oxygen isotope analysis by SIMS are similar. A cesium (Cs+) primary beam with a 6.5 nA current for oxygen and 3 nA current for sulfur was accelerated (+10 kV) onto the sample surface with a sputtering diameter of ~25 μm. The instrument operated with a 200 V offset for sulfur and for oxygen, –9 kV secondary accelerating voltage, and a mass resolving power of 350. For a detailed description of operating conditions and strategy for correction of instrumental mass fractionation and matrix effects, see Riciputi et al. (1998) for S isotope analysis and Fayek et al. (2002) for O isotope analysis.

2.3.8 – Laser confocal Raman spectroscopy

Raman spectroscopy was performed on fluid inclusions at Saint Mary's University (Halifax, Nova Scotia), to characterize the volatile composition of vapour bubbles in the fluid inclusions as well as identification of a birefringent solid phase in the inclusions. The instrument used was a Jobin-Yvon Horiba LabRam HR confocal Raman microscope with an 800 mm spectrograph and Synapse 1024 x 256 pixel CCD detector. A 600 grooves/mm grating and 25–40 μm confocal hole size were used during routine spectrum collection. A 532 nm (green) Nd-YAG laser (105 mW laser power at source) was used for excitation.

The laser beam was directed through a 100x objective. Spectrum collection (single window) over the range 200-4200 cm^{-1} was done using an acquisition time of 40 s per accumulation and 3 accumulations per analysis.

2.3.9 – CA-ID-TIMS U-Pb geochronology

U-Pb dates were obtained from Boise State University, Idaho, USA, by the chemical abrasion isotope dilution thermal ionization mass spectrometry (CA-ID-TIMS) method from analyses of single zircon grains, modified after Mattinson (2005). Zircon grains were separated from a rock using standard techniques. Zircon was annealed in a muffle furnace at 900 °C for 60 hours in quartz beakers.

Zircon was put into 3 ml Teflon PFA beakers and loaded into 300 µl Teflon PFA microcapsules. Fifteen microcapsules were placed in a large-capacity Parr vessel and the zircon partially dissolved in 120 µl of 29 M HF for 12 hours at 190 °C. Zircon was returned to 3 ml Teflon PFA beakers, HF was removed, and zircon was immersed in 3.5 M HNO_3, ultrasonically cleaned for an hour, and fluxed on a hotplate at 80 °C for an hour. The HNO_3 was removed and zircon was rinsed twice in ultrapure H_2O before being reloaded into the 300 µl Teflon PFA microcapsules (rinsed and fluxed in 6 M HCl during sonication and washing of the zircon) and spiked with the Boise State University mixed ^{233}U-^{235}U-^{205}Pb tracer solution. Zircon was dissolved in Parr vessels in 120 µl of 29 M HF with a trace of 3.5 M HNO_3 at 220 °C for 48 hours, dried to fluorides, and re-dissolved in 6 M HCl at 180 °C overnight. U and Pb were separated from the zircon matrix using an HCl-based anion-exchange chromatographic procedure (Krogh, 1973), eluted together and dried with 2 µl of 0.05 N H_3PO_4.

Pb and U were loaded on a single outgassed Re filament in 5 µl of a silica-gel/phosphoric acid mixture (Gerstenberger and Haase, 1997), and U and Pb isotopic measurements made on a GV Isoprobe-T multicollector thermal ionization mass spectrometer equipped with an ion-counting Daly detector. Pb isotopes were measured by peak-jumping all isotopes on the Daly detector for 100 to 160 cycles, and corrected for 0.16 ± 0.03%/a.m.u. (1 sigma error) mass fractionation. Transitory isobaric interferences due to high-molecular weight organics, particularly on ^{204}Pb and ^{207}Pb, disappeared within approximately 60 cycles, while ionization efficiency averaged 10^4 cps/pg of each Pb isotope. Linearity (to ≥1.4 x 10^6 cps) and the associated deadtime correction of the Daly detector were determined by analysis of NBS982. Uranium was analyzed as UO_2^+ ions in static Faraday mode on 10^{12} ohm resistors for 300 cycles, and corrected for isobaric interference of $^{233}U^{18}O^{16}O$ on $^{235}U^{16}O^{16}O$ with an $^{18}O/^{16}O$ of 0.00206. Ionization efficiency averaged 20 mV/ng of each U isotope. U mass fractionation was corrected using the known $^{233}U/^{235}U$ ratio of the Boise State University tracer solution.

U-Pb dates and uncertainties were calculated using the algorithms of Schmitz and Schoene (2007), $^{235}U/^{205}Pb$ of 77.93 and $^{233}U/^{235}U$ of 1.007066 for the Boise State University tracer solution, and U decay constants recommended by Jaffey et al. (1971) and $^{238}U/^{235}U$ of 137.818 from (Heiss et al., 2012). $^{206}Pb/^{238}$ U ratios and dates were corrected for initial ^{230}Th disequilibrium using $D_{Th/U} = 0.20 \pm 0.05$ (1σ) and the algorithms of Crowley et al. (2007), resulting in an increase in the $^{206}Pb/^{238}U$ dates of ~0.09 Ma. All common Pb in analyses was attributed to laboratory blank and subtracted based on the measured laboratory Pb isotopic composition and associated uncertainty. Uranium blanks are estimated at 0.013 ± 0.009 pg (1σ).

Weighted mean $^{206}Pb/^{238}U$ dates were calculated from equivalent dates (probability of fit >0.05) using Isoplot 3.0 (Ludwig, 2003). Errors on the weighted mean dates are given as ± x / y / z, where x is the internal error based on analytical uncertainties only, including counting statistics, subtraction of tracer solution, and blank and initial common Pb subtraction, y includes the tracer calibration uncertainty propagated in quadrature, and z includes the ^{238}U decay constant uncertainty propagated in quadrature. Internal errors should be considered when comparing these dates with $^{206}Pb/^{238}U$ dates from other laboratories that used the same Boise State University tracer solution or a tracer solution that was cross-calibrated using EARTHTIME gravimetric standards. Errors including the uncertainty in the tracer calibration should be considered when comparing our dates with those derived from other geochronological methods using the U-Pb decay scheme (e.g., laser ablation ICPMS). Errors including uncertainties in the tracer calibration and ^{238}U decay constant (Jaffey et al., 1971) should be considered when comparing our dates with those derived from other decay schemes (e.g., $^{40}Ar/^{39}Ar$, ^{187}Re-^{187}Os). Errors for weighted mean dates and dates from individual grains are given at 2σ. Errors typically approach 0.03 to 0.02 % and can be as good as 0.01 %, resulting from the utilization of the double spike method for Pb using ^{202}Pb and ^{205}Pb (J. Crowley, Boise State University, communication, 2019).

2.4 Results

2.4.1 – Petrography of the host rocks, porphyry, and quartz(-carbonate) veins

Outcrop in the immediate vicinity of the veins at Maisie and Lavoie is limited, and observations were limited to rocks accessible in shallow drill core sections and trench and pit exposures with rubbly walls obscuring vein-wall rock contacts (Fig. 3a, b, f).

2.4.1.1 – Description of the host rocks and an associated porphyry dike

The main host rock siltstone at both showings preserves primary bedding, or trough bedding, with regional folding observed in outcrop (Figs. 3a and b) and in some core samples (Fig. 4a), and contains an assemblage of quartz, albite, relict phlogopite (with chlorite after phlogopite), and rare muscovite (Fig. 4b). Chlorite grains occur as 20 to 50 µm laths (Fig. 4d inset). At vein-wall rock contacts a weak hornfels has developed (Fig. 4c) showing a greater abundance of phlogopite and muscovite (Fig. 4d), a coarser grain size, and a more consolidated (less fissile) nature (Fig. 4c,e), in contrast to brittle pencil cleavage seen distally (> 10 – 20 cm) to large vein contacts at trench sites (Fig. 3d,f).

The porphyry dike at Maisie is a, beige, plagioclase-phyric (< 5 vol. %, < 5mm diameter phenocrysts) dacite (Fig. 2b/Fig. 4g, h). The porphyry contains millimetre-sized albite laths, as well anhedral quartz phenocrysts (~ 50 µm grains) hosted in a fine-grained quartz-plagioclase groundmass. The dike lies approximately 15 m NW of the discovery outcrop (Sample Men19) and has an inferred strike of N-NE based on DDH intersections. The porphyry is estimated to be ~ 100 - 150m wide and has a strike length at least equal to the length of the gold-bearing vein. In areas proximal to both the dike and adjacent quartz veins, the host siltstone also shows evidence of hornfelsing (Fig. 4f).

Igneous rocks are not spatially associated with the Lavoie occurrence.

2.4.1.2 – Quartz(-carbonate) veins

At the scale of the occurrences (i.e. 100s of meters) the Lavoie and Maisie quartz(-carbonate) veins show similar vein dimensions and form. At Maisie, the main auriferous quartz(-carbonate) vein has an observable strike length of at least 700 m with multiple fault offsets of the vein towards its northeast end (Fig. 2b). At Lavoie, auriferous quartz(-

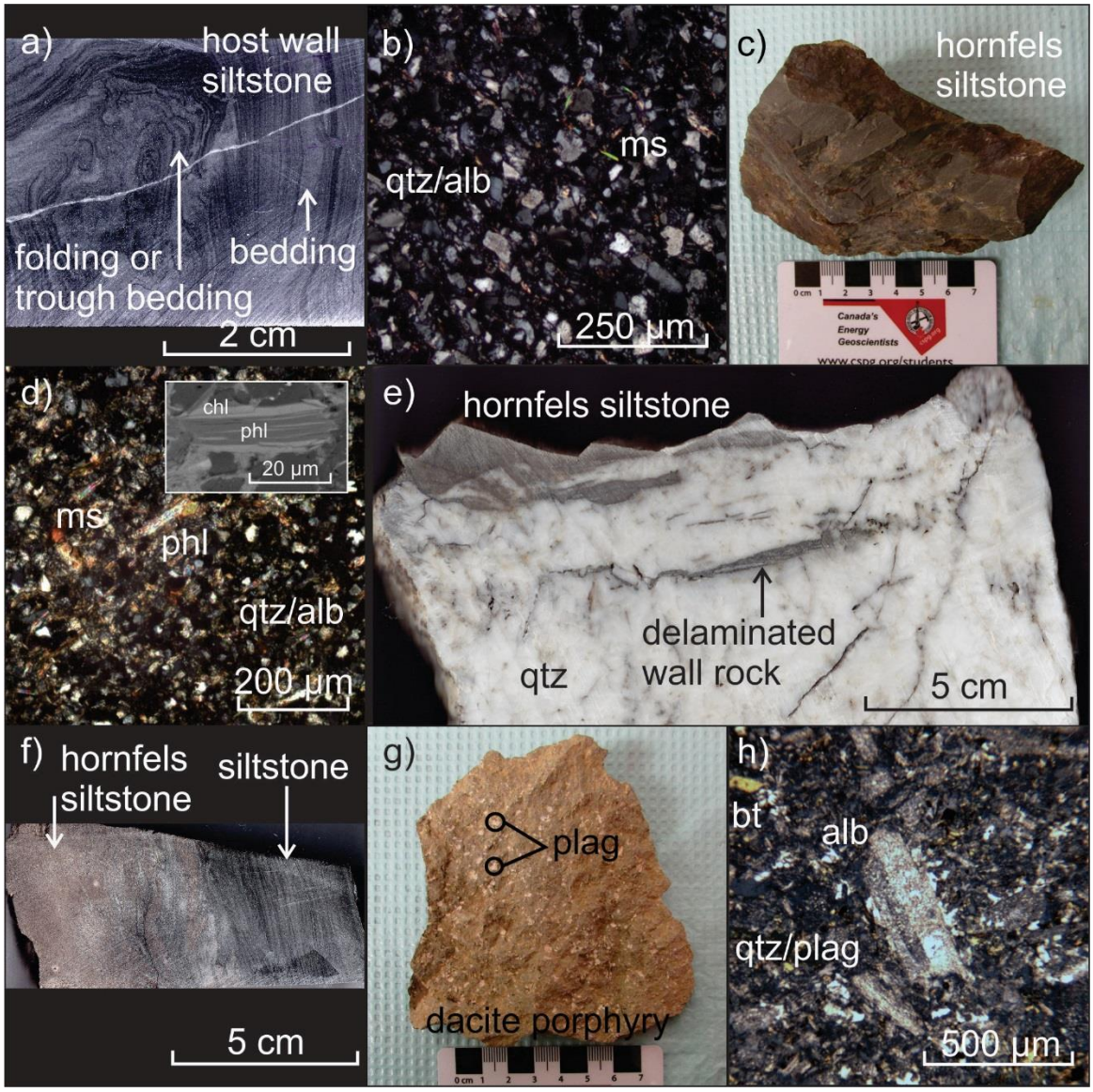
a)
host wall siltstone
folding or trough bedding
bedding
2 cm
b)
ms
qtz/alb
250 µm
c)
hornfels siltstone
Canada's Energy Geoscientists
www.cspg.org/students
d)
chl
phl
20 µm
ms
phl
qtz/alb
200 µm
e)
hornfels siltstone
delaminated wall rock
qtz
5 cm
f)
hornfels siltstone
siltstone
5 cm
g)
plag
dacite porphyry
h)
bt
alb
qtz/plag
500 µm

Figure 2.4 previous page – Hand sample, BSE, and transmitted light microscopy images from host sedimentary and spatially associated igneous rocks at Maisie. a) Host siltstone displaying folded bedding or trough bedding. b) Transmitted light image (cross polarized) of siltstone host rock to mineralized veins. c) Hand sample of host siltstone metamorphosed to hornfels facies. Siltstone is more consolidated and does not display pencil cleavage (Fig. 3d-f) seen more than ~ 10 cm from the mineralized vein and porphyry dike contacts with host siltstone. d) Cross polarized light image and BSE image (insert) of siltstone hornfels showing the same matrix as host siltstone, but in areas phlogopite is present. Larger muscovite grains (~ 50 to 70 µm) are also present. Inset shows BSE image of a phlogopite grain with chlorite rims. BSE inset shows chloritization of wall rock phlogopite. e) Wall rock vein contact showing delaminated, hornfelsed host siltstone. f) Drill core section of host siltstone. Drill core section was recovered from a hole running between the porphyry dike and mineralized vein. Hornfels metamorphism observed (brown colour, obliterated layering associated with recrystallization. g) Beige plagioclase-biotite dacite porphyry hand sample. h) Transmitted light image of the adjacent dacite porphyry. Mineral abbreviations: qtz=quartz; alb=albite; ms=muscovite; phl=phlogopite; plag=plagioclase; bt=biotite; chl=chlorite.

carbonate) veins occur over a minimum strike length of 220 m but continuity (structural) is not observed between individual exposures. Vein widths at both locations vary from 10s of cm up to 4.5 m. At both locations (Figs. 2b and 3c) veins range from a single aperture to multiple apertures having a "sheeted" morphology (Fig. 3d). Where this occurs individual subparallel vein apertures are separated by thick (centimeter-scale) wall rock septae.

At both locations the veins show three different macroscopic textural styles. The first is laminated veining in which quartz occurs in mm to tens of cm-scale bands hosted between wall rock septae (Fig. 4e; Fig. 5a, b). These laminations can be traced for centimeter- to up to a few meters in length along the veins. The second textural style is massive quartz. This is the most dominant style of quartz mineralization at Maisie and Lavoie, forming massive, milky, translucent domains throughout the veins. Massive quartz domains range from 10s of centimeter to meter-scale in maximum dimension (Fig. 3c; Fig. 5c, h, i), and occurs over the entire length of the veins. The third textural style is vuggy or bladed quartz. Vugs range from millimeter- to centimeter-scale, commonly lined with millimeter- to centimeter-scale euhedral quartz crystals and infilled by pyrite, hematite, or gold (Fig. 5c, g, h, j). Quartz blades are mm-to cm-scale in length, and occur in close proximity to vugs (Fig. 5d, e, i). Quartz blades often occur in clusters, of forming groups of 20-30 blades, though not exclusively.

At both locations quartz is the primary vein mineral and occurs with minor amounts of calcite. As described, quartz shows several textural generations, each tied to a different vein formation stage. Herein, these shall be referred to as types Q1 through Q3, as follows: (i) Q1 – early-stage laminated quartz (~10 % of vein quartz). Quartz that formed in this stage

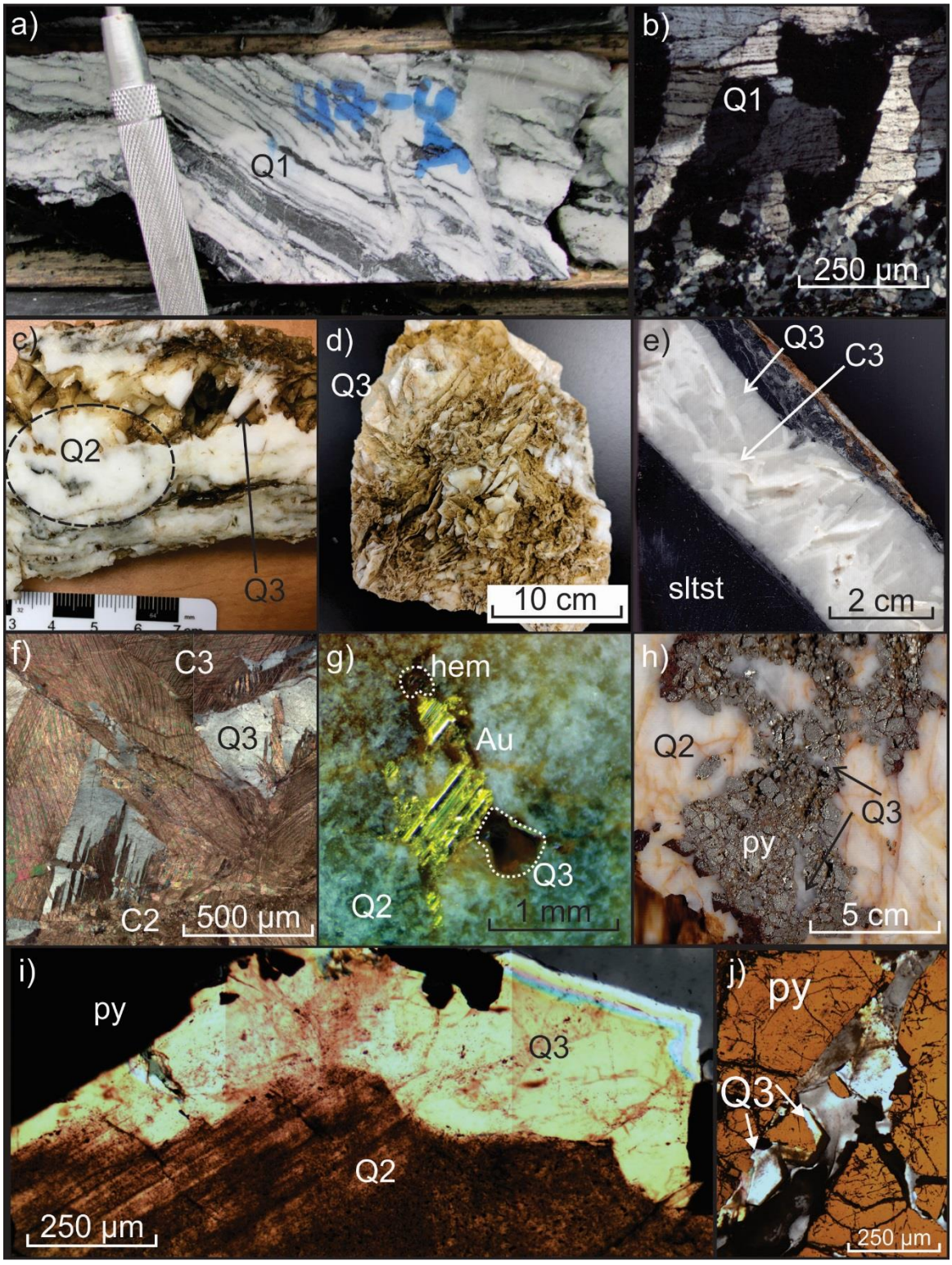
a)
Q1
b)
Q1
250 µm
c)
Q2
Q3
d)
Q3
10 cm
e)
Q3
C3
sltst
2 cm
f)
C3
Q3
C2
500 µm
g)
hem
Au
Q3
Q2
1 mm
h)
Q2
Q3
py
5 cm
i)
py
Q3
Q2
250 µm
j)
py
Q3
250 µm

Figure 2.5 previous page – Hand sample and transmitted/reflected light microscope images of quartz(-carbonate) veins. Samples shown were collected from Maisie, but mirror mineralization at Lavoie. a) Quartz vein drill core sample displaying multiple lamellae of wall rock, related to crack-seal events. b) Cross polarized light image of early-stage fine-to medium-grained quartz bridges. c) Quartz hand sample from trenching, showing massive Q2 quartz and vuggy Q3 quartz crystals. d) Bladed Q3 quartz boulder from trench site, as calcite has corroded. e) Drill core sample showing lattice-bladed C3 calcite intergrown with Q3 quartz. Core samples preserve C3 at their centres, whereas surface samples from trenches show cavities from dissolved calcite, which is depicted in the previous panel. f) Cross polarized light image of lattice-bladed C3 calcite crosscutting Q3 quartz, with variable C3 calcite lattice blade size. g) Massive Q2 quartz hand sample with visible Au (VG). Vugs (Q3) show partial infilling of visible Au and hematite. h) Massive Q2 quartz hand sample from trenched vein. Vugs containing pyrite are preserved. i) Cross polarized light image of massive Q2 quartz forming alongside pyrite, and vuggy Q3 infilling free space. j) Reflected light image of vuggy Q3 quartz overgrowths on pyrite. Mineral abbreviations: Q1=laminated quartz; Q2=massive quartz; Q3=vuggy/lattice-bladed quartz; py=pyrite; Au=gold; hem=hematite; C2=massive/polycrystalline calcite; C3=lattice-bladed calcite.

of veining occurs as grain aggregates (Fig. 5a, b), mm-to cm-size (width) and up to ~ 10 cm in length, forming laminations isolated between wall rock septae (dark). Quartz "bridges", resulting from incremental opening of quartz veins during periods of over-pressure (Fig. 5b; Henderson et al., 1990), ranging from 10s to a few 100s of microns in size are present near vein margins; (ii) Q2 – mid-stage, massive aggregates of quartz crystals (~95 % of vein quartz) not in laminations (up to ~3 mm) (Fig. 5c,g-i). Rarely, massive quartz contains brecciated clasts of Q1 (Fig. 6) providing evidence of the Q1-Q2 relative timing relationship. (iii) Q3 – late-stage, vuggy (euhedral) to quartz intergrowths with calcite (~5 % of vein quartz; Fig. 5c-j), with crystals ranging from ~ 100s of microns in length to a couple millimetres, and commonly occurring as overgrowths on Q2 and pyrite (Fig. 5i,j).

Calcite occurs as a minor phase (up to ~ 10 vol% of vein mineralogy, locally), and comprises two textural generations, namely: : (i) C2 – early-stage calcite, (coeval, and intergrown with, Q2), consisting of aggregates of crystals, with individual crystals ranging from 10 – 200 μm; and (ii) C3 – late-stage, lattice-bladed calcite (coeval, and intergrown with, Q3), with crystals mm- to cm in size (Fig. 5e, f). Dolomite occurs as rare (< 1 vol%), grain aggregates (20 – 35 μm crystals) and is likely secondary, related to late alteration.

A cathodoluminescence image mosaic of a section of a typical quartz vein in thin section, along with a corresponding image in transmitted, plane-polarized light is shown in Figure 6. The CL image shows variations in the CL intensity and a red luminescence (Fig. 6a), consistent with the CL colour reported in low grade metamorphic quartz (Boggs et al., 2002). Figure 6b shows clearly the timing relationship between Q1 and Q2. Specifically, it shows a clast of brecciated Q1 (containing laminations) hosted in Q2.

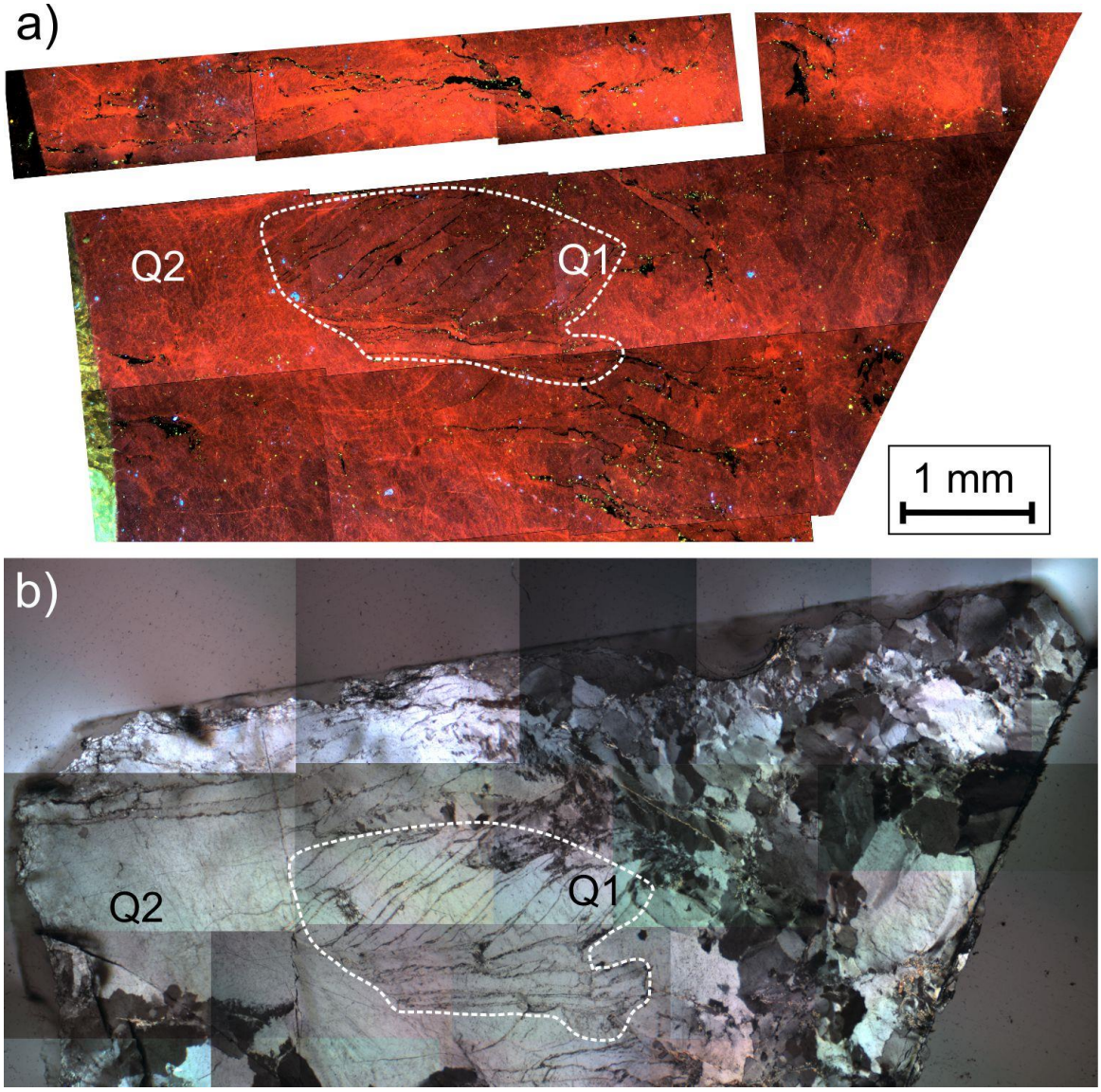

Figure 2.6 – Massive (Q2) quartz from Maisie and containing a fragment of earlier brecciated laminated (Q1) quartz. a) CL image of a chip of Q2, displaying CL colour (red) typical of low metamorphic grade (cf. Boggs et al., 2002). b) Transmitted, cross-polarized light image of the same Q2-Q1 relationship. The Q1 clast is outlined by white dashed border in both frames.

2.4.2 – Ore and accessory mineral petrology and chemistry

2.4.2.1 - Gold

Native gold (± minor Ag) at both Maisie and Lavoie is hosted in all stages of quartz. Gold is present along fractures in Q1 and Q2 (Fig. 7a, k) and as infilling of vugs in Q3, along with euhedral to subhedral quartz crystals (Fig. 7g, h). Gold is most commonly hosted in Q2 and Q3 at both locations. Gold does not appear to be hosted in C2 or C3 carbonate. Gold shows a close textural and spatial relationship with pyrite and hematitized pyrite (Fig. 7h, k), commonly sharing grain boundaries with hematitized pyrite (Fig. 7f, i). In a few examples, gold was observed as inclusions within galena (Fig. 7b), or in close proximity to covellite at the Lavoie occurrence.

The ratio of Au:Ag at Lavoie range from 92.8:7.2 to 93.4:6.6 (n=3), and at Maisie from 91.9:8.1 to 95.6:4.4 (n=32) (Table 1).

Gold grains isolated from heavy mineral quartz-carbonate vein separates (7014 g of vein sample) were counted and measured at Overburden Drilling Management Ltd., to determine grain size distribution at the two showings. Of the gold grains characterized from Maisie (n= 26,023), the grain size distribution is as follows: 58.49 % of grains up to 625 μm^2; 31.15 % of grains up to 2500 μm^2; 6.78 % up to 20,000 μm^2; 2.78 % up to 100,000 μm^2; 0.69 % up to 500,000 μm^2, and 0.12 % up to 1,000,000 μm^2 (Fig. 8a).

Gold grains recovered from heavy mineral separates (1422 g of vein sample) from a quartz-carbonate vein at Lavoie (n= 25,865) showed very similar grain size distributions, as follows: 58.15 % of grains up to 625 μm^2; 38.78 % of grains up to 2500 μm^2; 2.03 % up to 20,000 μm^2; 0.77 % up to 100,000 μm^2; and 0.27 % up to 500,000 μm^2 (Fig. 8b).

Table 1 - Gold grain compositions and ratios

Sample/ Grain	Au (%)	Ag (%	Au:Ag Ratio	Sample/ Grain	Au (%)	Ag (%	Au:Ag Ratio
Men1				Men2			
1	93.1	6.9	13.5	1	93.2	6.8	13.6
2	93.6	6.4	14.6	2	93.4	6.6	14.2
3	93.7	6.3	14.9	3	93.2	6.8	13.8
4	93.3	6.7	14.0	4	93.7	6.4	14.7
5	92.5	7.5	12.4	5	94.7	5.3	17.8
6	92.3	7.7	12.0	6	94.4	5.6	16.8
7	93.4	6.6	14.1	7	93.5	6.5	14.5
8	93.8	6.2	15.2	8	94.0	6.0	15.7
9	93.6	6.4	14.5	9	93.7	6.4	14.7
10	92.8	7.2	13.0	10	95.6	4.4	21.9
11	92.9	7.1	13.1	11	93.8	6.2	15.1
12	93.2	6.8	13.7	12	92.7	7.3	12.7
13	92.7	7.3	12.6	13	93.5	6.5	14.4
14	92.8	7.2	12.9	14	93.7	6.3	14.8
				15	92.9	7.1	13.1
				16	91.9	8.1	11.4
				17	93.3	6.7	13.9
				18	92.9	7.1	13.2
				NW4			
				1	93.4	6.6	14.1
				2	92.8	7.2	12.9
				3	93.2	6.8	13.7

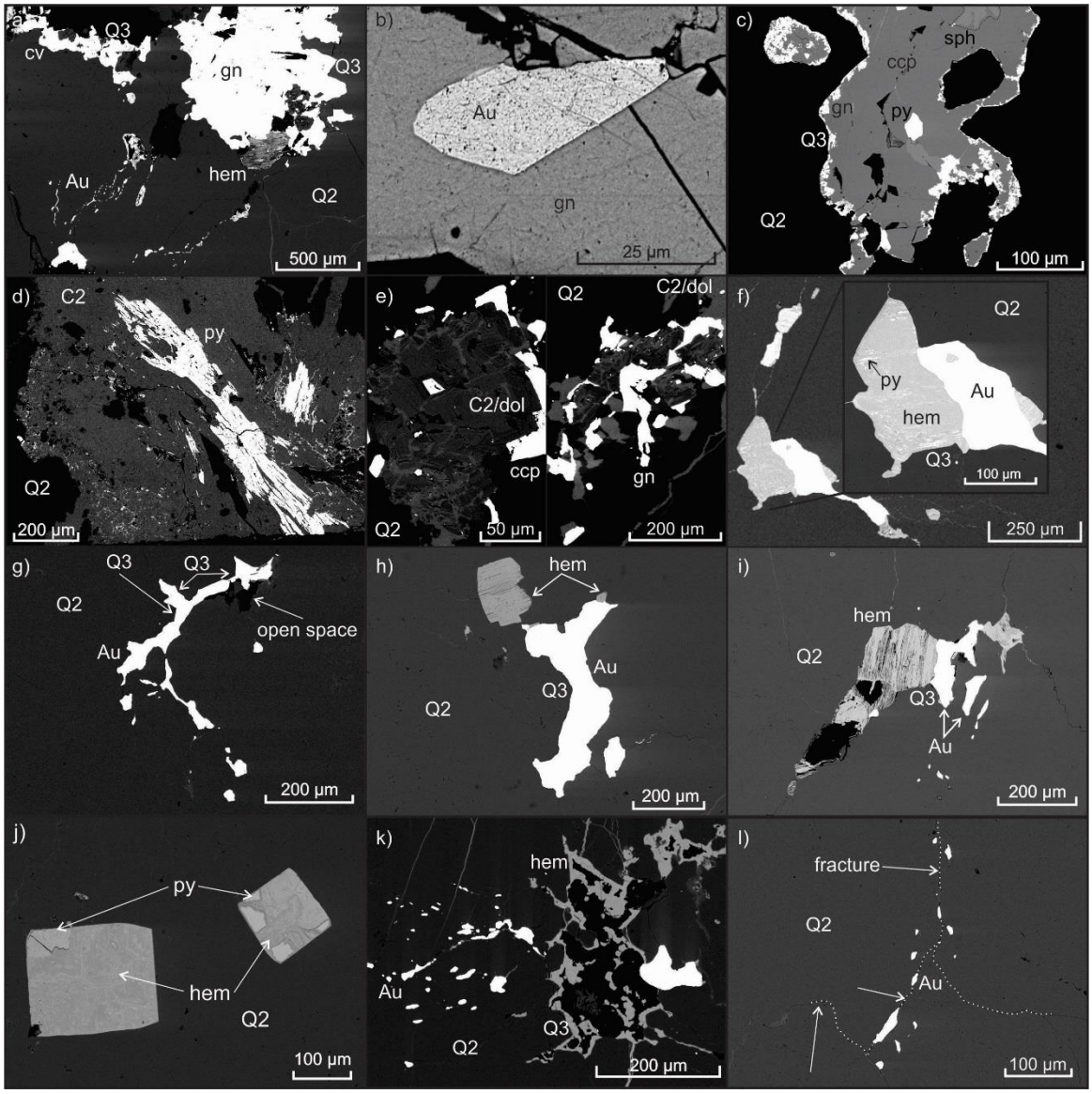
a)
Q3
cv
gn
Q3
Au
hem
Q2
500 µm
b)
Au
gn
25 µm
c)
sph
ccp
gn
py
Q3
Q2
100 µm
d)
C2
py
Q2
200 µm
e)
C2/dol
ccp
Q2
50 µm
Q2
C2/dol
gn
200 µm
f)
Q2
py
Au
hem
Q3
100 µm
250 µm
g)
Q3
Q3
Q2
open space
Au
200 µm
h)
hem
Au
Q3
Q2
200 µm
i)
hem
Q2
Q3
Au
200 µm
j)
py
hem
Q2
100 µm
k)
hem
Au
Q3
Q2
200 µm
l)
fracture
Q2
Au
100 µm

Figure 2.7 previous page – BSE images showing the textural relationships among gold, accessory minerals, and gangue at Maisie and Lavoie. a) Galena hosted in cavity in Q3 and hematite and covellite. Free gold showing fracture infill along with hematite in Q2 (Lavoie). b) Gold grain included in galena (Lavoie). c) Cavity/vug in Q3 containing chalcopyrite grain containing pyrite and sphalerite inclusions, rimmed by galena (Lavoie). d) Porous pyrite replacing host C2 (Maisie). e) Sulfides hosted in carbonate. Left frame: chalcopyrite; right frame: galena. Both sulfides begin infilling C2/dol vugs then intergrow with C2/dol (Lavoie). f) Quartz hosted fracture (Q2) and vug infill (Q3) of pyrite and gold, with shared grain boundary between gold and pyrite. Pyrite is altering to hematite (Maisie). g) Gold showing open space filling texture within Q3 vugs. Multiple euhedral Q3 quartz grain surfaces labeled (Maisie). h) Gold filling open space within Q3, in spatial relation to hematite (Maisie). i) Hematite (after pyrite) and gold filling open space in Q3 (Maisie). j) Pyrite oxidizing to hematite in Q2 (Maisie). k) Gold showing fracture infilling (Q2) and open space filling textures within Q3. Late hematite following Q2 fracture infill, transitioning to open-space filling texture of Q3 (Maisie). l) Fracture infilling gold hosted in massive Q2 quartz. White arrows point to fractures (traced in white dotted line) that host gold (Maisie). Mineral abbreviations: Au=gold; cv=covellite; gn=galena; hem=hematite; Q1=laminated quartz; Q2=massive quartz; Q3=vuggy/lattice-bladed quartz; sph=sphalerite; ccp=chalcopyrite; py=pyrite; C2=massive/polycrystalline calcite; dol=dolomite; brk=brookite.

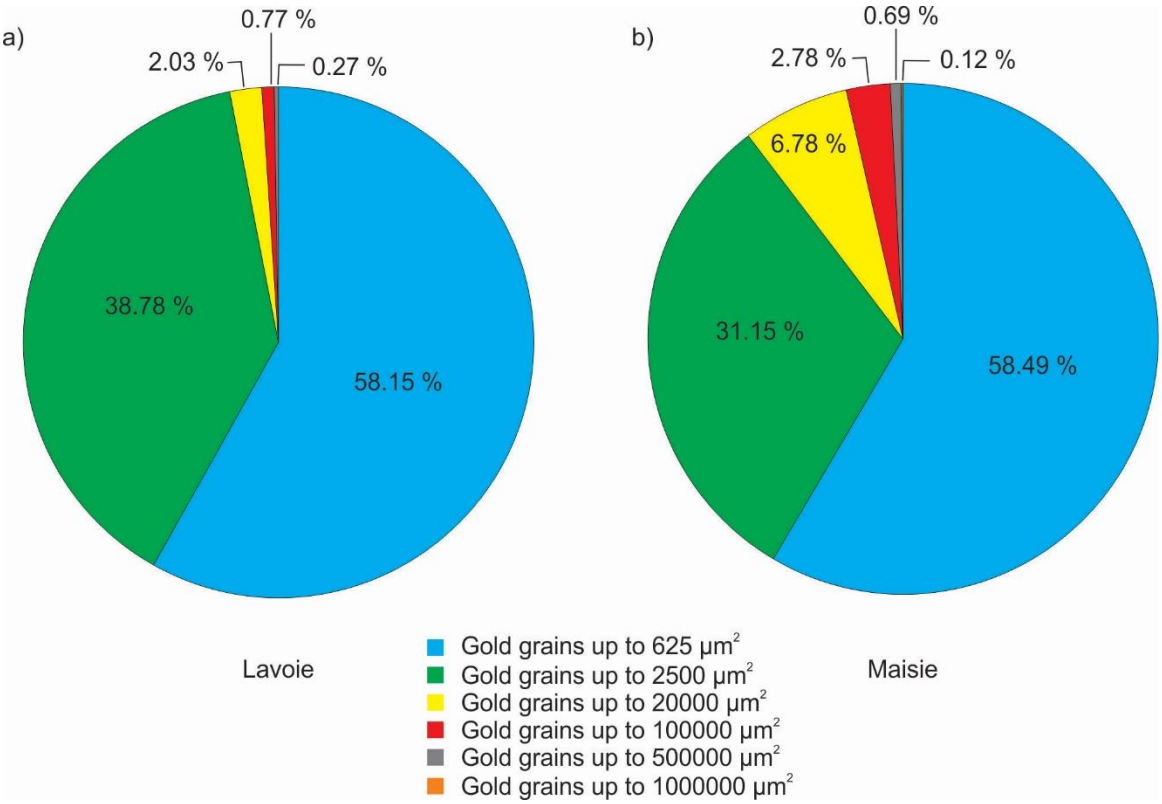

Figure 2.8 – Gold grain size distributions in heavy mineral separates from auriferous veins at a) Lavoie and b) Maisie

2.4.2.2 - Sulfides

Accessory sulfide phases at Maisie and Lavoie comprise the base metal sulfides pyrite, galena, sphalerite, chalcopyrite, and secondary covellite (Fig. 7). Pyrite is the most abundant accessory sulfide phase at both locations (~ up to 2 vol%). At Maisie, pyrite most commonly occurs as 100 – 300µm grains infilling vugs within Q3 and C3 (Fig. 7d, f), and commonly adjoins, or is intergrown with, gold (Fig. 7f). Pyrite grains also occur as inclusions (~ 20 µm) within chalcopyrite (Fig. 7c). Pyrite within Q2 and C2 is less common, occurring as ~ 600 µm long, porous, lathy grains replacing C2, or as euhedral (cubic), 100-300 µm grains included in (Fig. 7d), or along boundaries between, Q2 grains, and less commonly C2. Pyrite is commonly altered to (pseudomorphed by) hematite (Fig. 7f, h-j). Chalcopyrite is the second most abundant "sulfide" phase (trace vol%) at the Maisie occurrence. Chalcopyrite and galena occur in trace vol%, and form anhedral to subhedral 5 – 50 µm long grains, after C2 and dolomite (Fig. 7e), and form partial rims on the carbonate phases.

Pyrite abundances and textural associations are the same at the Lavoie occurrence. Galena is the second most abundant phase (trace vol%) at the Lavoie Au occurrence, and forms euhedral, porous, 200 – 1000 µm grains hosted within cavities or vugs within Q3, enclosed in massive (Q2) quartz (Fig. 7a). Rarely, galena contains inclusions of gold (Fig. 7b), and forms rims on chalcopyrite (Fig. 7c); this provides a key textural constraint on the timing of chalcopyrite (earlier) and sphalerite (later). Sphalerite occurs as anhedral, ~ 50 µm grains, as inclusions within chalcopyrite (Fig. 7c), suggesting that sphalerite and chalcopyrite may be coeval. Chalcopyrite at Lavoie is hosted by vuggy (Q3) quartz, and is sometimes altered to covellite (Fig. 7a).

2.4.2.3 – Oxides

Hematite at both Maisie and Lavoie occurs in massive (Q2) quartz, replacing (pseudomorphing) pyrite (Fig. 7f, h-j) and filling 10 – 100 µm-long fractures. Hematite also infills vuggy (Q3) quartz (Fig. 7k), and has a close textural and spatial association with gold in that setting, with shared grain contacts (Fig. 7f, h,i) and co-infilling vugs with gold (Fig. 7h, k).

Anatase, brookite, and rutile are three titania phases identified by Raman spectrometry at Maisie. Anatase occurs in wall-rock siltstone and delaminated siltstone within Q1. It is a diagenetic phase, occurring as anhedral to euhedral grains 50 to 150 µm long (Fig. 9a). Brookite occurs in Q1 as fractured, blade-like, acicular crystals 50 to 500 µm long (Fig. 9b-e). Brookite also occurs along wall-rock contacts (Q1; Fig. 9d), or within and along the edges of, wall rock septae (Q1; Fig. 9e) as a replacement after anatase. In rare cases the titania phase in this setting is acicular rutile, rather than brookite (Fig. 9f).

2.4.3 – Fluid inclusion petrography, microthermometry, and chemistry

2.4.3.1 – Petrography

Fluid inclusions at the Maisie and Lavoie occurrences were grouped using the fluid inclusion assemblage ("FIA") method (Goldstein and Reynolds, 1994), whereby FIA represent groups of inclusions trapped coevally in secondary trails or planes (healed fractures) or in small clusters of indeterminate origin within quartz and calcite. Three distinct types of fluid inclusion groups (FIAs) were observed in quartz and calcite (Fig. 10). Here, a group "type" refers to the phases observed in inclusions occurring in an FIA. A schematic representation of the relationships among the three FIAs and their host phases, as well as gold and accessory minerals is presented in Figure 11. Observations described

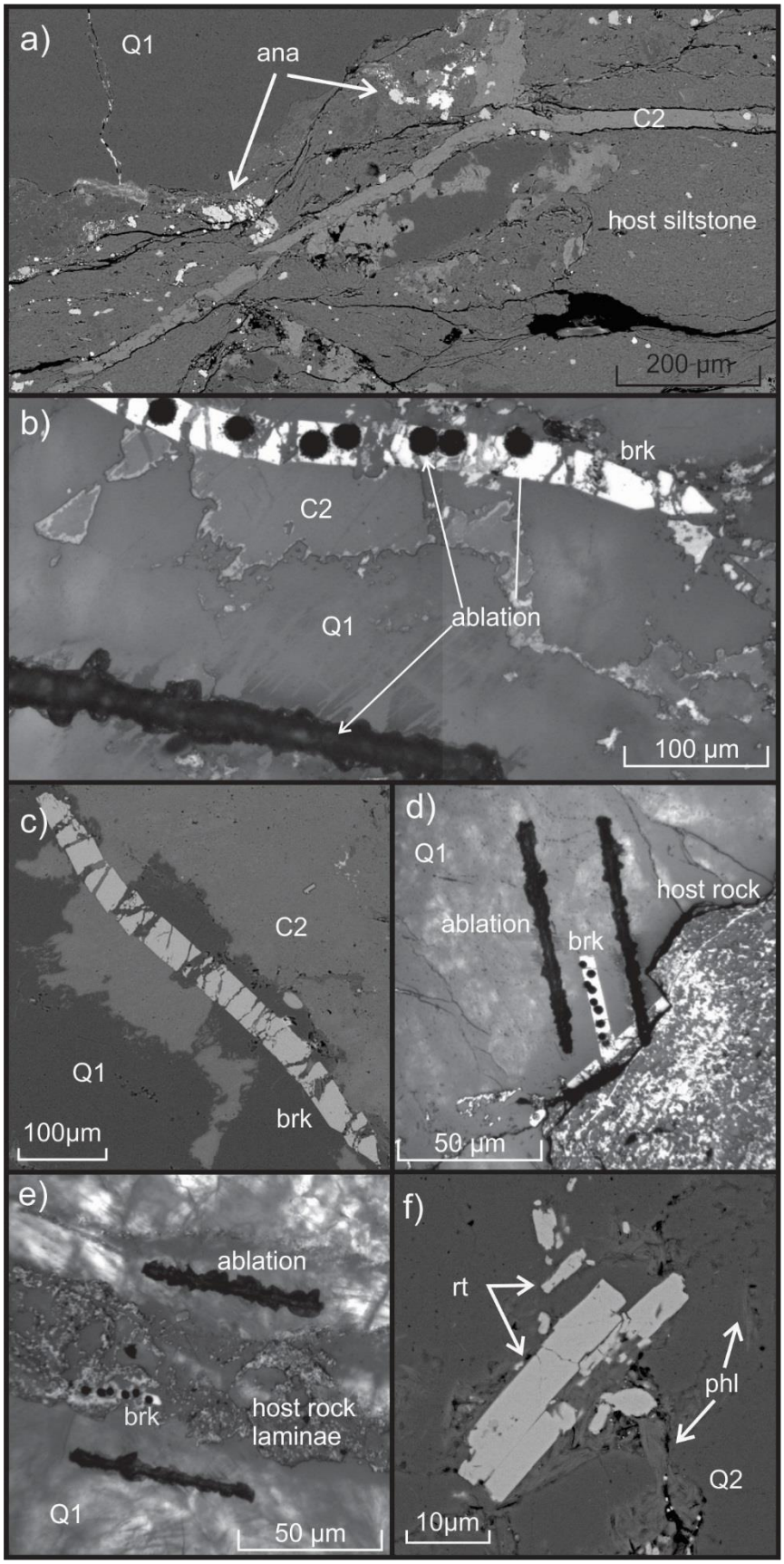
a)
Q1
ana
C2
host siltstone
200 µm
b)
brk
C2
Q1
ablation
100 µm
c)
C2
Q1
brk
100µm
d)
Q1
host rock
ablation
brk
50 µm
e)
ablation
brk
host rock
laminae
Q1
50 µm
f)
rt
phl
Q2
10µm

Figure 2.9 (previous page) – BSE and reflected light images of titania phases from the Maisie gold showing. a) Fractured, anhedral anatase grains at a quartz (Q1) – wall rock contact. b) Brookite hosted in quartz (Q1). Dark lines and spots are ablated areas where the Ti content of quartz was measured, whereas spots in brookite where Zr content was determined. c) Acicular, fractured brookite hosted in Q1. d) Brookite grains hosted in (Q1) quartz growing at wall rock contact. e) Brookite grain hosted in wall rock laminae between Q1 quartz laminations. f) Rutile laths and fragments in close proximity to phlogopite, hosted in Q1. brk=brookite; rt=rutile; ana=anatase; phl=phlogopite; Q1=laminated quartz; C2=massive calcite

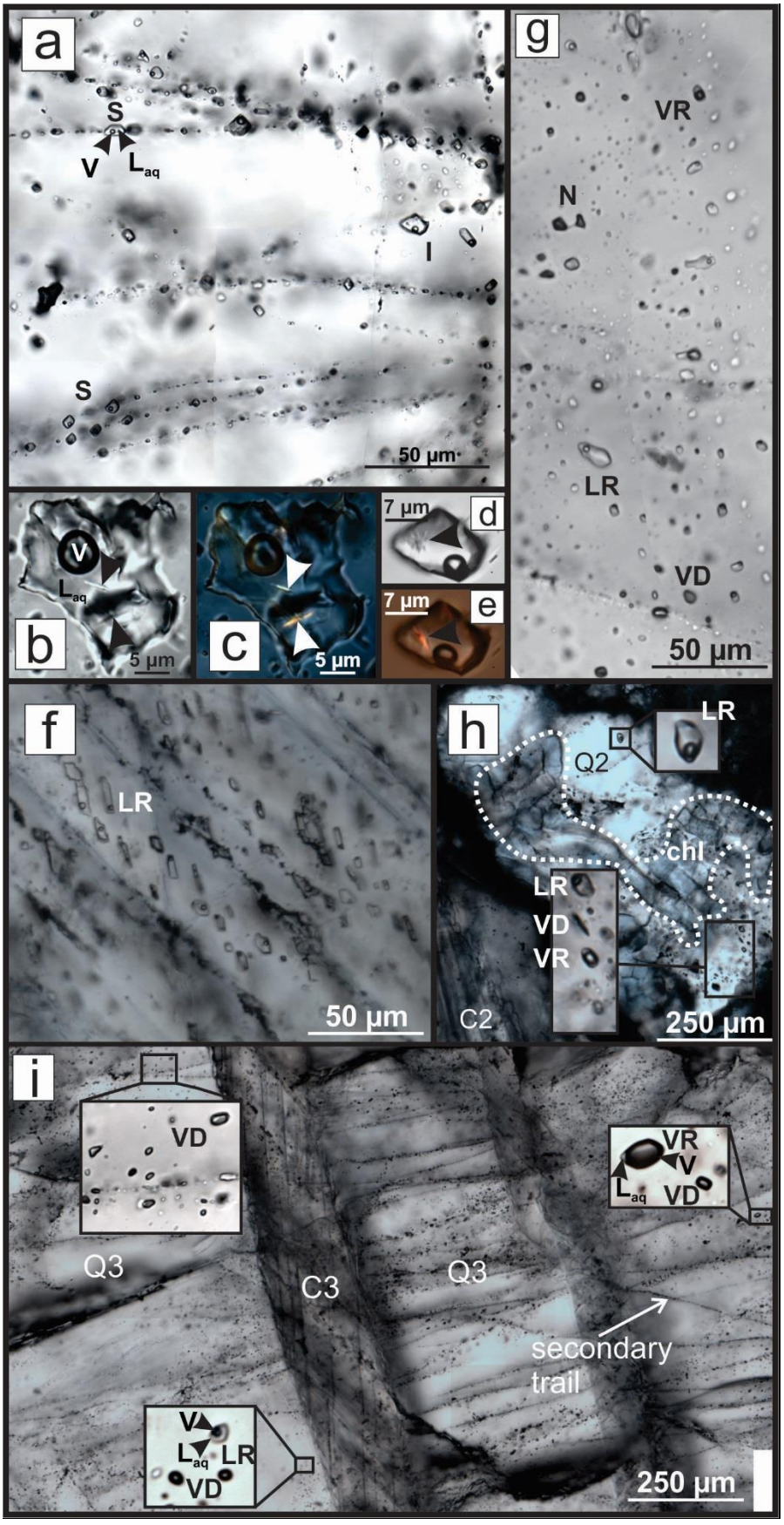
a
S
V
L_{aq}
I
S
50 µm
b
V
L_{aq}
5 µm
c
5 µm
7 µm
d
7 µm
e
g
VR
N
LR
VD
50 µm
f
LR
50 µm
h
LR
Q2
chl
LR
VD
VR
C2
250 µm
i
VD
Q3
C3
Q3
VR
V
L_{aq}
VD
secondary
trail
V
L_{aq}
LR
VD
250 µm

Figure 2.10 previous page – Photomicrographs of fluid inclusions from the Maisie and Lavoie vein systems. All images are in plane-polarized light, except (c) and (e) that are taken in cross-polarized light (analyzer in). (a) Indeterminate (I) and secondary (S), two-phase type 1 FIA inclusions hosted in massive quartz (Q2), many showing negative crystal shape, and containing a vapour bubble (V) and aqueous phase (L_{aq}). (b)-(c) Two phase (L_{aq}+V) type 1 inclusion containing accidentally trapped, birefringent, platy, muscovite crystals (arrows). (d)-(e) Two phase (L_{aq}+V) type 1 inclusion containing accidentally-trapped, birefringent, radiating crystal aggregates of muscovite (arrows). (f) Two-phase (L_{aq}+V) type 1 FIA hosted in (C3). (g) Trail consisting of a type 2 boiling assemblage showing highly variable phase ratios ranging from vapour-dominant (VD) to vapour-rich (VR) to liquid-rich (LR) inclusions. Inclusions trapped along a single, healed fracture, photographed as a mosaic. Inclusions in focus represent a single FIA occurring along a healed fracture plane perpendicular to the viewing direction (flat lying). (h) Two-phase, type 1 fluid inclusion hosted in (Q2), and type 2 FIA hosted in Q2. (i) Bladed quartz and calcite (Q3-C3) showing many fluid inclusion trails across a sample chip. Insets show variability of phase proportions, with "flashing" assemblages depicted, showing small vapour-rich (VR; large vapour bubble) to vapour-dominant (VD; empty-looking) inclusions. In the lower left inset, a rare L-rich inclusion is identified (as would be found in type 1 FIA) together with V-dominant inclusions. qtz=quartz; cal=calcite; chl=chlorite; VD=vapour-dominant; VR=vapour-rich; LR=liquid-rich; V=vapour phase; L_{aq}=aqueous liquid phase; N=necked down

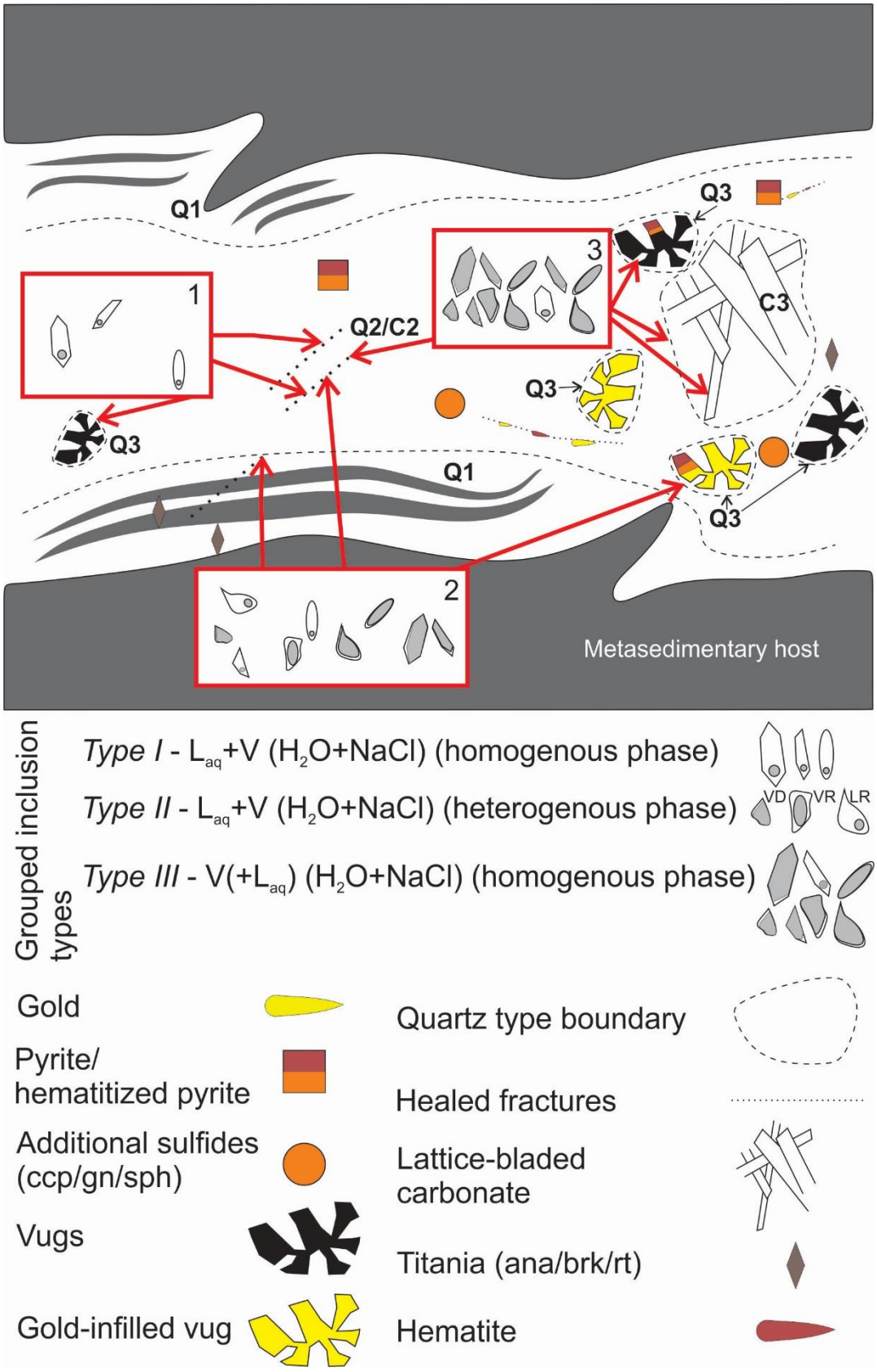
Q1
Q3
3
1
Q2/C2
C3
Q3
Q3
Q1
Q3
2
Metasedimentary host
Grouped inclusion types
Type I - L$_{aq}$+V (H$_2$O+NaCl) (homogenous phase)
Type II - L$_{aq}$+V (H$_2$O+NaCl) (heterogenous phase)
VD
VR
LR
Type III - V(+L$_{aq}$) (H$_2$O+NaCl) (homogenous phase)
Gold
Quartz type boundary
Pyrite/ hematitized pyrite
Healed fractures
Additional sulfides (ccp/gn/sph)
Lattice-bladed carbonate
Vugs
Titania (ana/brk/rt)
Gold-infilled vug
Hematite

Figure 2.11 previous page – Schematic showing the distribution and type of fluid inclusion FIA present in auriferous quartz(-calcite) veins at Maisie and Lavoie quartz types, and gold/accessory mineral textures. FIA types are: type 1, L_{aq} + V (at 20°C) with homogeneous phase ratios; type 2, L_{aq} + V with heterogenous phase ratios; and type 3, V (+ L_{aq}) homogenous phase ratios except with rare L_{aq}-rich inclusions. Type 1 FIA occur as secondary in Q2-C2 and rarely in Q3-C3. Type 2 FIA occur as secondary inclusions in Q1 and Q2 as trails mainy. They also occur indeterminate in Q3-C3. Type 3 FIA occur as indeterminate or secondary inclusions in Q3-C3, but also secondary in Q2The same potentiall healed fractures will contain gold, hematite, and pyrite. Gold and accessory sulfides, and hematite after pyrite pccur in vugs in Q3 and fractures in Q1-C2. Some Q3-vugs are empty, and lined with quartz crystals. Some earlier pyrite occurs in Q2, but the largest crystals showing pyrite II overprinting occur in Q3-vugs and along fractures in Q2. Q1=laminated quartz; Q2=massive quartz; Q3=vuggy quartz; C3=lattice-bladed calcite; ana=anatase; brk=brookite; rt=rutile; hem=hematite; VD=vapour-dominant; VR=vapouor-rich; LR=liquid-rich

below are common to both the Lavoie and Maisie occurrences. Despite their spatial separation there are no discernable differences in terms of fluid inclusion petrography and classification between the two showings.

Type 1 FIA (Fig. 10a-f) consist of rare, two-phase (L_{aq} + V, at room T) inclusions that are most abundant in Q2 and C2, though they also occur in Q3 and C3 (Fig. 11). Type 1 FIA most commonly are of secondary origin, occurring in trails (healed fractures) (Fig. 10a, labelled S; Fig. 11). Less commonly, type 1 FIA are indeterminate in origin, forming clusters of inclusions not associated with healed fractures or growth zones (Fig. 10a, labelled I). The inclusions in type 1 FIA range from ~2 - 30 μm (average = 4 ± 1 μm; 1σ; Tables 2 and 3) in size and show V:L_{aq} ratios that are relatively consistent, with an average phase ratio of 5 ± 2.5 : 95 ± 2.5 (V:L_{aq}; 1σ; Tables 2 and 3). Rarely, birefringent (under cross-polarized light) muscovite (confirmed by Raman spectroscopy; Fig. 12) occurs as fine-grained platy crystals or radiating crystal aggregates within the inclusions (Fig. 10b-f). Muscovite is not present in all fluid inclusions, but when present shows highly variable volumetric proportions and is also seen as included grains in quartz indicating that it is an accidentally trapped solid and not a true daughter phase.

Type 2 FIA contain fluid inclusions have a similar morphology and size range as those in type 1 FIA, but are far more abundant. Type 2 FIA are hosted mainly in secondary trails in Q1, Q2 and C2 (Figs. 10g and 11), and less commonly in Q3 and C3 where they have an indeterminate origin (Fig. 10h). Type 2 FIA show evidence of heterogeneous entrapment, with inclusions in single FIA showing highly variable V:L_{aq} ratios from one inclusion to another, ranging from V-dominant ('VD' – volumetrically a V bubble filling almost all of the inclusion with only a thin film of L_{aq} along the inclusion wall), to V-rich ('VR' –

Table 2 - Fluid inclusion microthermometry data from Maisie quartz(-carbonate) veins

A#	I#	FIA	T_m^1(°C)	T_h^2(°C)	Salinity[3]	Size[4]	V:L[5]	A#	I#	FIA	T_m^1(°C)	T_h^2(°C)	Salinity[3]	Size[4]	V:L[5]	A#	I#	FIA	T_m^1(°C)	T_h^2(°C)	Salinity[3]	Size[4]	V:L[5]
MEN1								e-4	1	s	-2.4	180.2	4.0	4	5	a-4	1	s	-1.3	146.4	2.2	4	7
a-2	1	s	-1.7	157.1	2.9	6	5	f-1	1	s	-1.7	165.0	2.9	4	7	a-5	1	1	-0.4	121.3	0.7	2	7
a-3	1	s	-2.0	161.8	3.4	5	7	f-2	1	s	-1.6	191.2	2.7	3	10	a-5	2	1	-0.2	106.3	0.4	3	5
a-4	1	s	-1.0	185.7	1.7	3	10	f-3	1	s	-1.6	194.5	2.7	4	7	a-7	1	s	-0.8	148.9	1.4	3	7
a-5	1	s	-0.7	204.0	1.2	3	10	f-4	1	s	-1.5	175.6	2.6	4	45	a-8	1	1	-0.3	107.6	0.5	2	5
a-6	1	s	-2.9	150.9	4.8	3	7	MEN6-2b								a-8	2	1	-1.5	108.3	2.6	3	5
a-7	1	s	-1.3	191.0	2.2	4	7	a-1	1	s	-1.0	164.5	1.7	3	10	b-1	1	s	-14.8	95.8	18.5	3	7
b-1	1	3	-2.1	238.1	3.5	4	10	a-2	1	s	-3.0	111.2	4.9	3	10	b-2	1	s	-9.0	136.8	12.9	3	7
b-2	1	3	-1.7	235.7	2.9	3	12	a-3	1	s	-1.0	187.0	1.7	4	12	b-3	1	s	-2.5	152.9	4.2	4	7
b-3	1	s	-1.1	218.5	1.9	4	7	a-5	1	s	-0.2	152.2	0.4	4	12	b-5	1	s	-0.2	174.8	0.4	2	12
b-4	1	s	-1.7	187.3	2.9	4	5	b-1	1	1	-2.9	210.5	4.8	3	7	MEN42-5b							
b-5	1	s	-1.8	217.9	3.0	2	16	b-1	2	1	0.0	186.1	0.0	4	16	a-1	1	s	-0.6	146.1	1.0	2	10
b-6	1	s	-1.9	209.9	3.2	3	10	b-3	1	3	-4.6	139.1	7.3	3	12	a-2	1	s	-0.7	151.4	1.2	2	7
b-7	1	1	-1.6	169.1	2.7	5	10	d-1	1	s	-0.7	136.9	1.2	3	7	a-3	1	s	-0.6	166.1	1.0	2	7
b-7	2	1	-1.6	170.5	2.7	2	7	d-2	1	s	-0.5	130.3	0.9	4	7	a-4	1	s	-1.0	160.8	1.7	3	12
c-1	1	3	-3.0	265.7	4.9	6	12	d-3	1	s	-1.0	128.0	1.7	3	7	a-5	1	s	-1.0	170.0	1.7	4	7
c-2	1	1	-0.7	195.9	1.2	4	10	d-4	1	s	-2.0	144.3	3.4	2	12	a-6	1	s	-1.4	207.8	2.4	3	12
c-2	2	1	-1.2	202.4	2.1	5	10	MEN23-8b								a-7	1	1	-0.7	158.1	1.2	2	7
c-4	1	3	-1.4	217.8	2.4	3	12	a-1	1	s	-4.2	163.1	6.7	3	12	a-7	2	1	-0.6	167.6	1.0	2	10
c-5	1	3	-1.5	194.4	2.6	3	12	a-2	1	s	-3.2	165.6	5.2	5	7	a-7	3	1	-0.1	178.7	0.2	2	7
c-6	1	s	-2.2	241.6	3.7	4	16	a-3	1	s	-5.1	184.3	8.0	3	7	a-7	4	1	-0.8	155.8	1.4	2	7
e-1	1	1	-1.7	182.3	2.9	4	7	a-4	1	s	-3.6	204.4	5.8	3	10	b-1	1	s	-2.1	175.9	3.5	8	7
e-1	2	1	-1.8	167.1	3.0	3	25	b-1	1	1	-1.8	152.3	3.0	3	5	b-2	1	1	-0.2	139.2	0.4	2	10
e-3	1	s	-1.5	172.7	2.6	5	5	b-1	2	1	-1.9	174.8	3.2	3	12	b-2	2	1	-2.7	146.9	4.5	3	15
e-4	1	s	-1.7	180.9	2.9	3	6	b-3	1	s	-1.5	162.6	2.6	7	7	b-2	3	1	-2.2	159.1	3.7	5	10
e-5	1	s	-1.8	209.0	3.0	3	7	b-4	1	3	-0.7	162.0	1.2	4	7	b-5	1	s	-1.6	167.4	2.7	3	10
MEN5								b-5	1	s	-1.9	209.7	3.2	2	10	b-6	1	s	-1.2	187.8	2.1	3	12
a-1	1	3	-1.5	-	2.6	5	10	c-1	1	s	-2.1	206.5	3.5	2	10	b-7	1	s	-1.4	182.1	2.4	4	7
a-3	1	s	-0.2	-	0.4	5	10	c-2	1	s	-0.7	165.3	1.2	3	12	b-8	1	s	-0.8	211.2	1.4	4	10
a-4	1	1	-	136.6	-	4	10	c-3	1	3	-1.7	224.4	2.9	2	10	MEN 47-6c							
a-4	2	1	-4.4	129.0	7.0	3	10	c-4	1	s	-0.2	122.0	0.4	5	7	a-1	1	s	-1.3	162.3	2.2	5	7
a-4	3	1	-	125.6	-	5	10	c-5	1	s	-1.7	185.1	2.9	3	12	a-2	1	s	-2.5	161.2	4.1	3	7
a-7	1	s	-3.5	195.0	5.7	4	12	MEN36-3a								a-3	1	s	-1.6	181.3	2.7	2	10
a-8	1	s	-1.5	138.0	2.6	4	12	a-2	1	s	-0.9	162.2	1.6	4	10	a-4	1	1	0.0	122.0	0.0	2	7
a-9	1	s	-1.1	222.6	1.9	4	12	a-3	1	1	-2.6	234.5	4.3	3	10	a-4	2	1	-0.4	114.3	0.7	3	7
b-1	1	s	-1.2	135.1	2.1	5	7	a-3	2	1	-0.6	177.8	1.0	4	10	a-5	1	s	-0.8	122.4	1.4	5	5
b-3	1	3	-3.2	181.0	5.2	4	12	a-5	1	s	-1.3	180.0	2.2	4	10	b-1	1	1	-1.2	173.1	2.0	3	10
b-4	1	s	-0.5	157.6	0.9	4	12	a-6	1	s	-1.0	196.4	1.7	3	7	b-1	2	1	-1.2	169.1	2.0	3	7
b-5	1	s	-0.9	179.0	1.6	3	10	a-7	1	s	-1.5	187.6	2.6	5	7	b-3	1	s	-1.7	185.1	2.9	3	7
b-6	1	s	-	155.8	-	5	10	a-8	1	s	-1.6	177.7	2.7	3	5	b-4	1	s	-1.2	154.9	2.0	3	7
b-7	1	1	-1.0	179.7	1.7	4	7	a-9	1	s	-0.8	169.7	1.4	5	10	b-5	1	s	-0.1	144.2	0.2	5	7
b-7	2	1	-1.7	186.6	2.9	3	12	a-10	1	s	-0.9	257.2	1.6	11	10	b-6	1	s	-1.8	182.4	3.0	5	7
b-9	1	1	-1.3	187.6	2.2	4	7	a-11	1	s	-0.9	184.5	1.6	3	7	Men 5-5c							
b-9	2	1	-1.5	226.1	2.6	4	16	b-1	1	s	-0.8	176.2	1.4	4	10	a-1	1	1	-2.2	163.6	3.7	-	-
c-1	1	s	-2.1	171.5	3.5	2	10	b-2	1	s	-1.1	181.9	1.9	5	7	a-2	1	1	-2.0	174.5	3.3	-	-
c-2	1	s	-	133.4	-	3	5	b-3	1	s	-1.2	172.1	2.1	3	10	b-1	1	1	-0.9	175.9	1.6	-	-
c-3	1	s	-0.9	170.1	1.6	5	7	b-4	1	s	-1.4	164.9	2.4	3	12	b-2	1	1	-1.1	174.6	1.9	-	-
c-4	1	s	-	190.7	-	4	7	b-5	1	s	-3.4	148.9	5.5	3	12	b-3	1	1	-0.6	181.4	1.0	-	-
d-2	1	s	-2.7	180.2	4.5	2	15	b-6	1	s	-3.0	155.7	4.9	3	10	b-4	1	1	-1.1	186.6	1.9	-	-
d-3	1	s	-1.2	184.4	2.1	4	7	c-1	1	s	-3.7	147.3	6.0	6	5	b-5	1	1	-1.1	188.7	1.9	-	-
d-4	1	s	-	145.6	-	2	12	c-2	1	s	-3.4	202.6	5.5	6	7	c-1	1	1	-0.8	175.6	1.4	-	-
d-5	1	s	-	148.1	-	3	5	c-4	1	s	-1.0	167.0	1.7	5	5	c-2	1	1	-0.8	181.8	1.4	-	-
d-6	1	s	-	127.6	-	4	5	c-5	1	s	-1.3	164.1	2.2	5	5	c-3	1	1	-0.8	183.9	1.4	-	-
d-7	1	s	-	143.2	-	4	7	c-6	1	s	-1.0	172.6	1.7	6	7								
d-8	1	3	-0.9	171.6	1.6	3	10	MEN 40-2b															
e-1	1	3	0.0	150.3	0.0	4	7	a-1	1	s	-0.7	169.7	1.2	5	5								
e-2	1	s	-2.6	176.8	4.3	3	16	a-2	1	1	-0.7	120.3	1.2	2	7								
e-3	1	s	-	143.2	-	3	15	a-2	2	1	-0.6	154.0	1.0	3	10								

[1]T_m^{ice}=Final freezing temperature of fluid phase; [2]T_h=Final homogenization temperature of vapour phase to fluid phase;

[3]- Eq. wt% NaCl; [4]- µm; [5]Ratio of vapour phase to liquid phase; A#=assemblage number; I#=inclusion number; FIA=FIA type (1, 2, 3, or single/non-FIA)

Table 3 - Fluid inclusion microthermometry data from Lavoie quartz(-carbonate) veins

A#	I#	FIA	T_m[1](°C)	T_h[2](°C)	Salinity[3]	Size[4]	V:L[5]
NW1b							
a-1	1	1	-1.3	189.6	2.2	4	10
a-1	2	1	-1.3	165.5	2.2	4	8
a-2	1	1	-1.2	171.8	2.1	4	6
a-2	2	1	1.4	166.9	2.4	4	7
a-5	1	s	-0.8	208.8	1.4	6	10
a-6	1	1	-2.1	170.4	3.5	3	12
a-6	2	1	-1.2	227.1	2.1	3	12
a-8	1	1	-1.0	187.5	1.7	4	8
a-8	2	1	-1.0	193.8	1.7	4	8
b-1	1	1	-0.8	162.6	1.4	2	12
b-1	2	1	-0.8	165.5	1.4	2	12
b-3	1	s	1.6	167.0	2.7	2	9
b-4	1	s	-1.0	192.2	1.7	2	16
b-5	1	3	-0.7	154.7	1.2	2	7
b-6	1	s	-0.5	158.7	0.9	3	7
c-1	1	s	-0.8	178.7	1.4	4	10
c-2	1	s	-0.8	180.2	1.4	4	10
c-3	1	s	-1.0	193.1	1.7	5	12
c-4	1	s	-1.5	195.0	2.6	2	16
d-1	1	2	-1.6	189.3	2.7	4	10
d-1	2	2	0.0	158.1	0.0	3	12
d-1	3	2	-1.2	204.3	2.1	4	10
NW3							
a-1	1	1	-1.4	179.2	2.4	2	16
a-1	2	1	-1.4	179.2	2.4	2	12
a-3	1	1	-1.5	180.3	2.6	3	8
a-3	2	1	-1.3	187.8	2.2	3	8
a-5	1	s	-1.1	195.6	1.9	4	7
NW2a1							
a-1	1	s	-1.8	254.0	3.0	5	10
a-2	1	s	-3.3	223.8	5.4	2	10
a-3	1	2	-2.7	225.3	4.5	3	12
a-3	2	2	-2.5	263.9	4.2	5	20
a-3	3	2	-2.6	249.5	4.3	10	5
a-6	1	s	-1.9	240.2	3.2	7	16
A#	I#	FIA	T_m[1](°C)	T_h[2](°C)	Salinity[3]	Size[4]	V:L[5]
NW2b2							
a-1	1	3	-1.1	162.0	1.9	2	10
a-2	1	s	-2.6	190.7	4.3	2	10
a-3	1	1	-1.3	190.0	2.2	4	10
a-3	2	1	-1.3	184.8	2.2	3	12
b-1	1	s	-1.2	180.1	2.1	4	12
b-2	1	s	-1.0	210.0	1.7	6	16
b-3	1	s	-1.0	187.5	1.7	8	12
b-4	1	s	-1.3	168.3	2.2	4	10
b-5	1	1	-1.8	202.0	3.0	6	12
b-6	1	1	-1.6	204.4	2.7	5	16
b-7	1	s	-1.8	176.7	3.0	6	10
NW2b1							
a-1	1	s	-2.3	188.4	2.4	2	10
a-2	1	1	-1.0	187.7	1.4	3	12
a-2	2	1	-1.0	182.6	1.7	3	12
a-4	1	s	-0.9	178.0	2.1	4	10
a-5	1	s	-0.7	207.5	1.2	2	10
NW1004b							
a-1	1	s	-2.0	202.1	3.4	3	16
a-2	1	s	-1.0	204.9	1.7	4	10
a-3	1	s	-0.9	216.6	1.6	3	9
a-4	1	s	-0.9	210.8	1.6	3	9
a-5	1	s	-1.0	224.9	1.7	2	10
a-6	1	s	-0.7	192.1	1.2	4	12
a-7	1	s	-1.7	246.1	2.9	3	16
a-8	1	s	-0.7	226.5	1.2	3	10
a-9	1	s	-1.3	213.9	2.2	2	9
a-10	1	s	-1.3	227.7	2.2	4	10

[1]T_m^{ice}=Final freezing temperature of fluid phase; 2Th=Final homogenization temperature of vapour phase to fluid phase;
3- Eq. wt% NaCl; 4- µm; 5Ratio of vapour phase to liquid phase;
A#=assemblage number; I#=inclusion number; FIA=FIA type (1, 2, 3, or single/non-FIA)

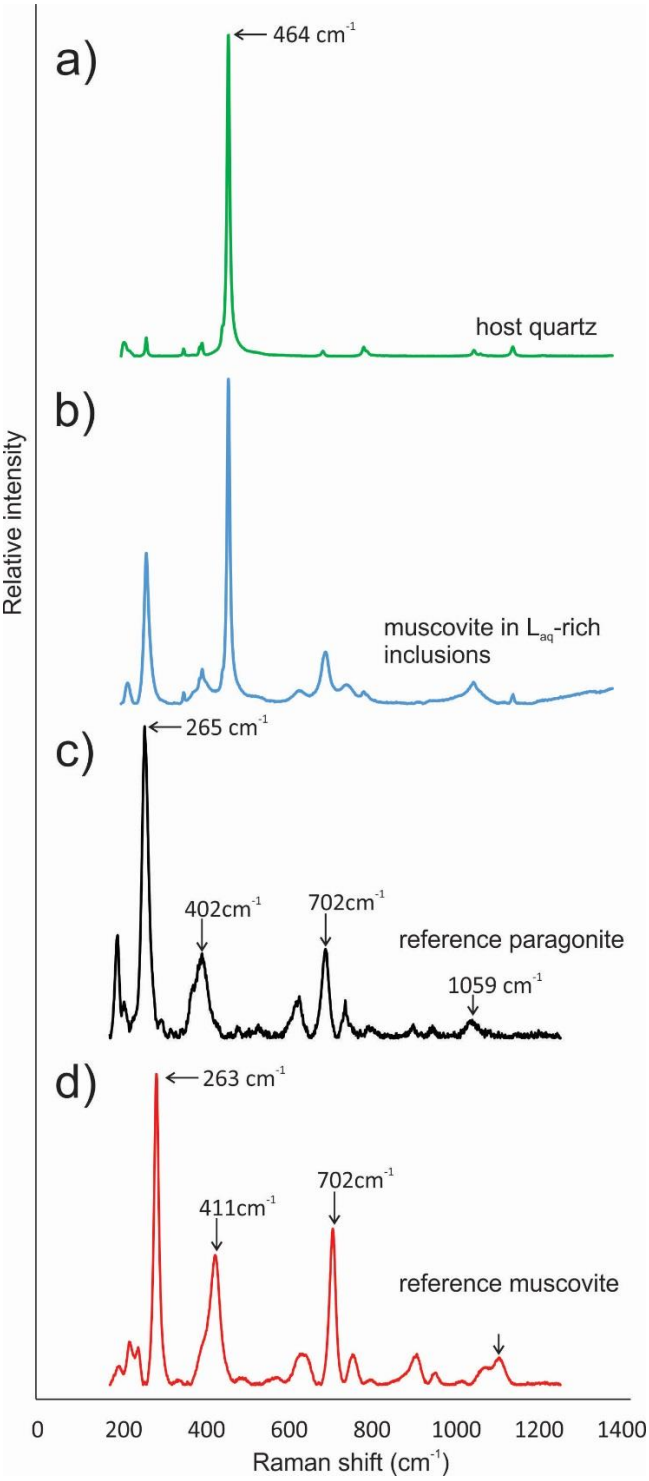

Figure 2.12 – Laser Raman spectra of (a) host quartz to type 1 FIA, (b) birefringent (muscovite) phase, (c) RRUFF database (Lafuente et al., 2016) standard paragonite (reference spectra collected using same laser wavelength source) for comparison, showing characteristic peaks at 265, 402, 702, and 1059 cm^{-1}, and (d) RRUFF database (Lafuente et al., 2016) standard muscovite (reference spectra collected using same laser wavelength source) for comparison, showing characteristic peaks at 2630, 411, and 702cm^{-1}.

vapour-bubble > ~ 50 vol% of inclusion), to L_{aq}-rich ('LR' vapour bubble < ~ 50 vol% of inclusion) (Fig. 10g, h; Fig. 11).

Type 3 FIA are the most abundant type at Maisie and Lavoie, comprised of two-phase ($V+L_{aq}$) inclusions. These FIA have indeterminate or rarely, secondary origin and are hosted mainly in Q3 and C3 (Fig. 11) but also in secondary trails in Q2 and C2 (Fig. 10i). Inclusions in type 3 FIA are similar in both morphology and size to inclusions in type 1 and 2 FIAs, but are consistently V-rich, with little to no visible L_{aq} phase, and have consistent $V:L_{aq}$ phase proportions (when the L_{aq} phase could be observed) among inclusions in a single FIA (indicating homogeneous entrapment). Very rarely, L_{aq}-rich inclusions are found amidst large clusters of V-rich to V-dominant inclusions in type 3 FIA (Figs. 10i).

2.4.3.2 – Microthermometry

2.4.3.2.1 – General microthermometric behaviour

The results of microthermometry for L_{aq}-rich inclusions are reported in Tables 2 and 3, and summarized graphically in Figures 13 and 14 in which data are grouped by sample (e.g. MEN5-5c) and sample chips (e.g. a, b, c), further differentiated by FIA or as individual inclusions (non-FIA) using symbols. Fluid inclusions measured were primarily non-FIA due to the lack of texturally unambiguous FIA in many samples that contain 2-phase, L_{aq}-rich inclusions. Where L_{aq}-rich inclusions were measured in FIA, these FIA were classified as type 1, 2, or 3 at the time of measurements. The majority of FIA containing L_{aq}-rich inclusions that were measured were of type 1 or 3 classification. Some L_{aq}-rich inclusions in type 2 FIA were measured for salinity determination but owing to more widely variable V:L ratios, T_h values were highly variable within single FIA. From the Maisie Au occurrence, 160 L_{aq}-rich fluid inclusions (34 inclusions within 15 FIA, and 126 single

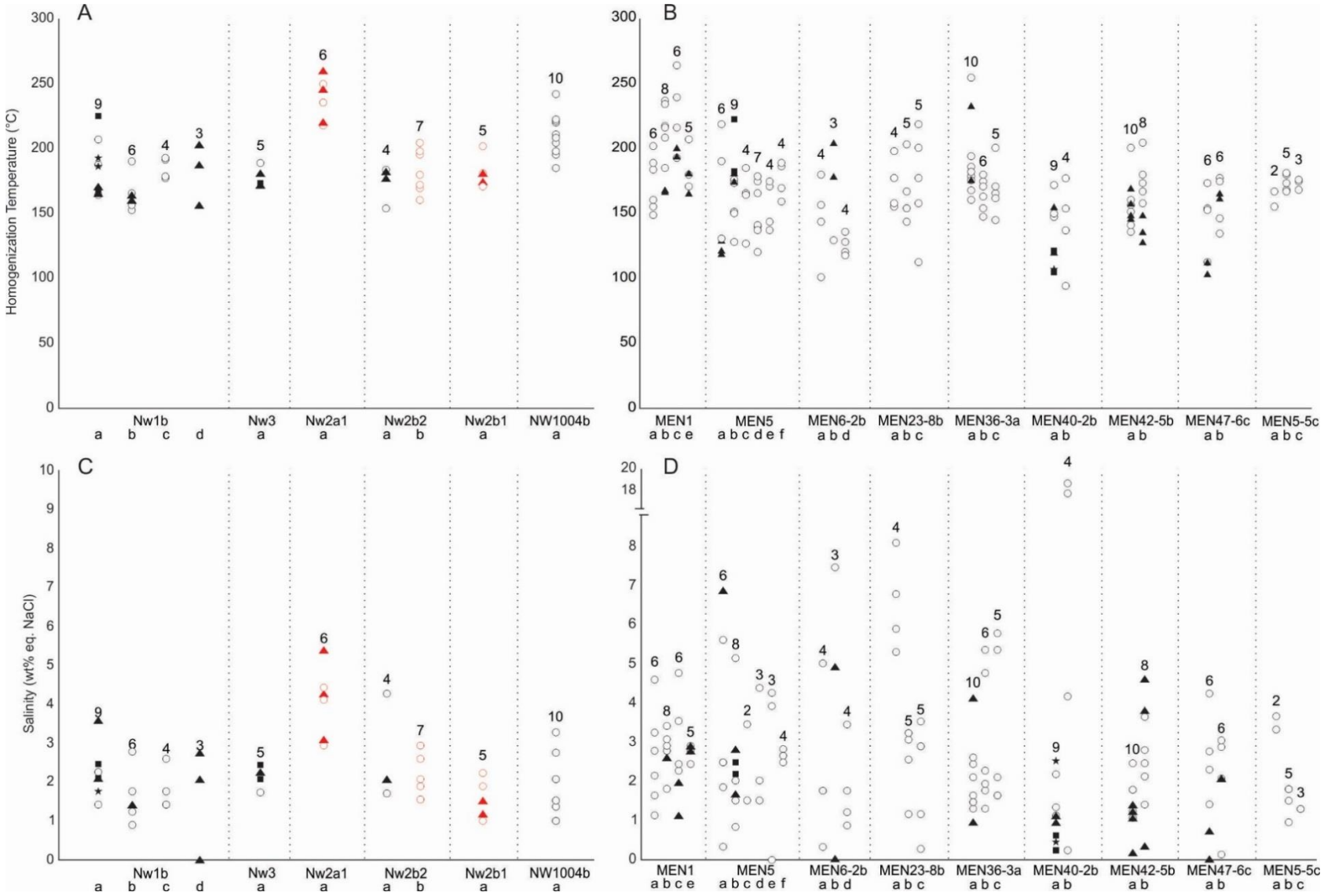
A
B
C
D
Homogenization Temperature (°C)
Salinity (wt% eq. NaCl)
Nw1b
Nw3
Nw2a1
Nw2b2
Nw2b1
NW1004b
MEN1
MEN5
MEN6-2b
MEN23-8b
MEN36-3a
MEN40-2b
MEN42-5b
MEN47-6c
MEN5-5c

Figure 2.13 previous page – Microthermometric data for L_{aq}-rich fluid inclusions type 1 and 3 (FIA and non-FIA) at Lavoie and Maisie. Letter labels represent individual sample chips from single samples (NW and MEN labels). Open circles represent data for single fluid inclusions, whereas filled triangles, stars, and squares are FIA. The number above each sample set shows the number of inclusions measured in each sample chip. Homogenization temperature (A,B) and salinity (C,D) for Lavoie and Maisie are shown side-by-side. Men=Maisie sample, NW=Lavoie sample. Red=carbonate hosted data, Black=quartz hosted data, with variations in symbols representing different FIA (solid symbols) or non-FIA (open symbols).

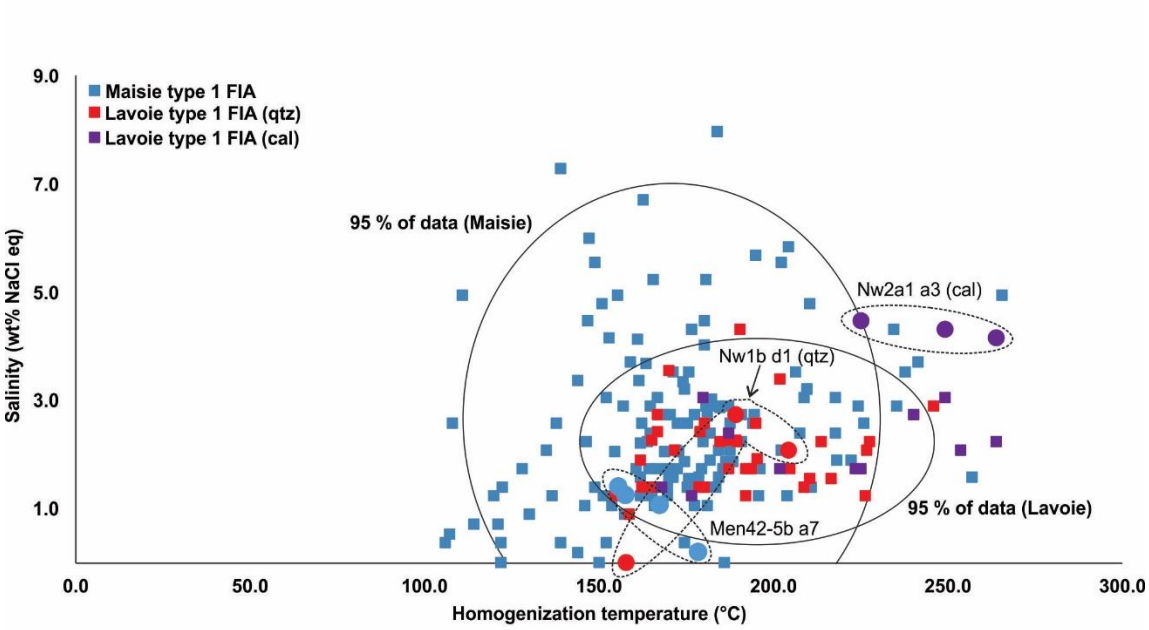

Figure 2.14 – Plot of fluid inclusion temperature of homogenization (T_h; °C) data against inclusion salinity (wt% equiv. NaCl) data. This is an overall comparison of the spread of data (not by FIA or non-FIA), except for few examples to show how they relate to the data. All data for Maisie and Lavoie occurrences are shown, as well representative FIA (i.e. sample Nw2a1, chip a3; Table 3) to illustrate typical variations in values within FIA, between FIA, and between occurrences. Note that the diagram is only valuable as an overall comparison of the ranges in salinity-T_h data for the two occurrences and does not serve as an interpretation tool for fluid or vein evolution. A similar approach is used widely in comparisons of fluid inclusion microthermometric data in different deposits (e.g., Bodnar et al., 2014).

inclusions) were measured, and from the Lavoie Au occurrence, 59 L_{aq}-rich fluid inclusions (20 inclusions within 11 FIAs, and 39 single fluid inclusions) were measured to obtain temperatures of final ice melting (T_m^{ice}) and total homogenization ($T_h^{L+V \rightarrow L}$). Fluid inclusions were modelled in the NaCl-H_2O system. Though not measured routinely, the basis for this approach was the presence of dominantly NaCl determined from observations of eutectic (first) melting which occurred at or slightly below -21.1 °C, later confirmed by LA-ICP-MS (see below). Salinities were calculated using the freezing point depression-salinity relationship of Bodnar (1993).

Final ice melting in L_{aq}-rich inclusions at Maisie occurred between -4.4° and 0.0 °C (n=46) in type 1 FIA, -4.6° and 0.0 °C (n=12) in type 3 FIA, and -5.1° and -0.1 °C (n=103) for single inclusions, except for 2 outliers melting at -9.0 and -14.8 °C. Values of T_m^{ice} correspond to bulk salinities in type 1 FIA ranging from 0.0 – 7.0 wt% NaCl equivalent (n=46), 0.0 – 7.3 wt% NaCl equivalent (n=12) for type 3 FIA, and 0.2 – 8.0 wt% NaCl equivalent (n=103) for single inclusions, with two outliers (12.9 and 18.5 wt% NaCl equivalent).

Final ice melting for L_{aq}-rich inclusions at Lavoie occurs between -2.1° and 1.4 °C (n=20) in type 1 FIA, -2.7° and 0.0 °C (n=7) in type 2 FIA, -1.1° and -0.7 °C (n=2) in type 3 FIA, and -3.3° and 1.6 °C (n=31) in single inclusions. Values for type 1 FIA correspond to a bulk salinity of the aqueous phase ranging from 1.4 – 3.5 wt% NaCl equivalent (n=20), 0.0 – 4.5 wt% NaCl equivalent (n=7) for type 2 FIA, 1.2 – 1.9 wt% NaCl equivalent (n=2) for type 3 FIA, and 0.9 – 5.4 wt% NaCl equivalent (n=31) for single inclusions.

At the Maisie gold occurrence homogenization of the aqueous phase in L_{aq}-rich inclusions occurred by vapour bubble closure ($L_{aq} + V \rightarrow L_{aq}$) between 106.3° and 234.5

°C (n=46) in type 1 FIA, 139.1° and 265.7 °C (n=12) for type 3 FIA, and 111.2° and 257.2 °C (n=103) for single inclusions.

At the Lavoie gold occurrence homogenization of the aqueous phase in L_{aq}-rich inclusions (T_h) also occurred by vapour bubble closure ($L_{aq} + V \rightarrow L_{aq}$) between 162.6° and 227.1 °C (n=20) in type 1 FIA, 158.1° and 263.9 °C (n=7) in type 2 FIA, 154.7° and 162.0 °C (n=2) in type 3 FIA, and 95.8° and 265.7 °C (n=31) for single inclusions.

2.4.3.2.2 – Variability in microthermometric data

Importantly, the total ranges in microthermometric data are much larger than for single samples, sample chips, and FIA (Fig. 13; Tables 2 and 3). Homogenization temperatures at Maisie have a ΔT_h as low as 0.7 °C and as large as 56.7 °C within single FIA (Figs. 13 and 14; Tables 2 and 3), while inter-FIA ΔT_h can range from 1.0 to 100.5 °C (Figs. 13 and 14; Tables 2 and 3), and inter-sample ΔT_h can range from 0.5 to 128.1 °C (Figs. 13 and 14; Tables 2 and 3). Homogenization temperatures at Lavoie have a ΔT_h as low as 0.0 °C and as large as 56.7 °C within single FIA (Figs. 13 and 15; Tables 2 and 3), while inter-FIA ΔT_h can range from 1.1 to 69.0 °C (Figs. 13 and 15; Tables 2 and 3), and inter-sample ΔT_h can range from 0.1 to 105.8 °C (Figs. 13 and 14; Tables 2 and 3).

Salinity values within FIA also show some variation, with Δwt% NaCl equiv. values at Maisie ranging from 0.0 to 4.8 (Figs. 13 and 14; Tables 2 and 3) within single FIA, whereas inter FIA Δwt% NaCl equiv. values range from 0.0 to 4.3 (Figs. 13 and 14; Tables 2 and 3), and inter-sample Δwt% NaCl equiv. values range from 0.0 to 4.8 not including outliers (Figs. 13 and 14; Tables 2 and 3). Salinity values within single FIA at Lavoie have Δwt% NaCl equiv. values ranging from 0.0 to 2.7 (Figs. 13 and 14; Tables 2 and 3), while inter-FIA Δwt% NaCl equiv. range from 0.0 to 2.7 (Figs. 13 and 14; Tables 2 and 3), and

inter-sample Δwt% NaCl equiv. values range from 0.0 to 4.5 not including outliers (Figs. 13 and 14; Tables 2 and 3).

As stated earlier, the rarity of two-phase, L_{aq}-rich inclusions within types 2 and 3 FIA resulted in measurements of no more than 1 – 3 inclusions from many FIA. Not surprisingly single inclusions (non-FIA) generally show a larger range in T_h and salinity within samples/sample chips. Data from single (non-FIA) inclusions commonly overlaps in range with single FIA in the same sample chip. At Maisie ΔT_h inter-inclusion values range from 0.0 to 114.7 °C (Figs. 13 and 14; Tables 2 and 3), and ΔT_h values intra-samples range from 0.2 to 169.9 °C (Figs. 13 and 14; Tables 2 and 3). At Lavoie ΔT_h inter-inclusion values range from 1.1 °C to 54.2 °C (Figs. 13 and 14; Tables 2 and 3), and ΔT_h intra-sample values range from 0.1 to 99.3 °C (Tables 2 and 3).

At Maisie Δwt% NaCl equiv. inter-inclusion values range from 0.0 to 3.5 (Figs. 13 and 14; Tables 2 and 3), and Δwt% NaCl equiv. intra-sample values range from 0.0 to 3.7 (Figs. 13 and 14; Tables 2 and 3). At Lavoie Δwt% NaCl equiv. inter-inclusion values range from 0.0 to 1.6 (Figs. 13 and 14; Tables 2 and 3), and Δwt% NaCl equiv. values intra-sample values range from 0.0 to 3.3 (Figs. 13 and 14; Tables 2 and 3).

2.4.3.3 – Fluid major, minor, and trace element, and volatile composition

The L_{aq} and V phases in L-rich and V-rich inclusions from types 1, 2, and 3 FIA from Maisie and Lavoie were analysed by Raman spectroscopy. Representative signals are shown in Figure 15a. The vapour phase identified in all three inclusion types are water dominated containing trace amounts of CH_4 (2915.93 cm^{-1}; < 1 mole %) and N_2 (2327.71 cm^{-1}; < 1 mole %). The peak intensities for N_2 and CH_4 peaks are highest in the V phase of L-rich and V-rich inclusions. No CO_2 was detected in the inclusions analyzed (Fig. 15a).

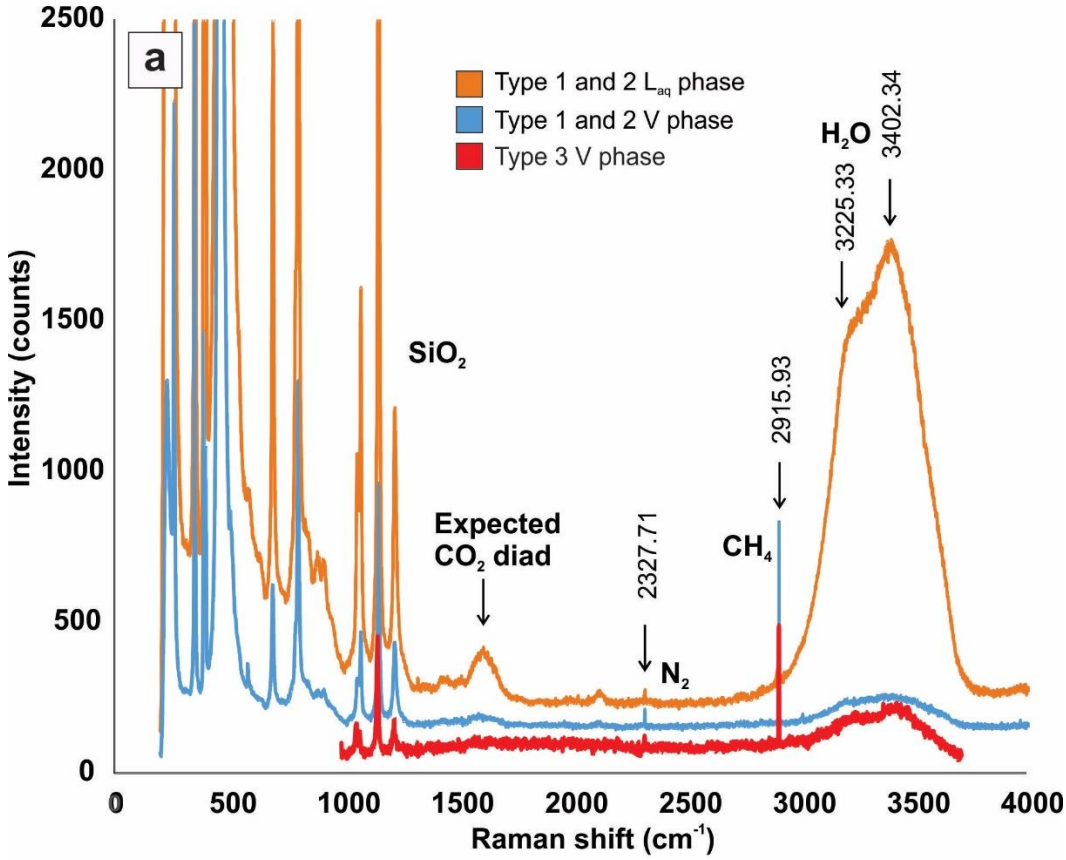
a
Type 1 and 2 L_{aq} phase
Type 1 and 2 V phase
Type 3 V phase
H_2O
3402.34
3225.33
SiO_2
2915.93
Expected
CO_2 diad
2327.71
CH_4
N_2
Intensity (counts)
Raman shift (cm^{-1})

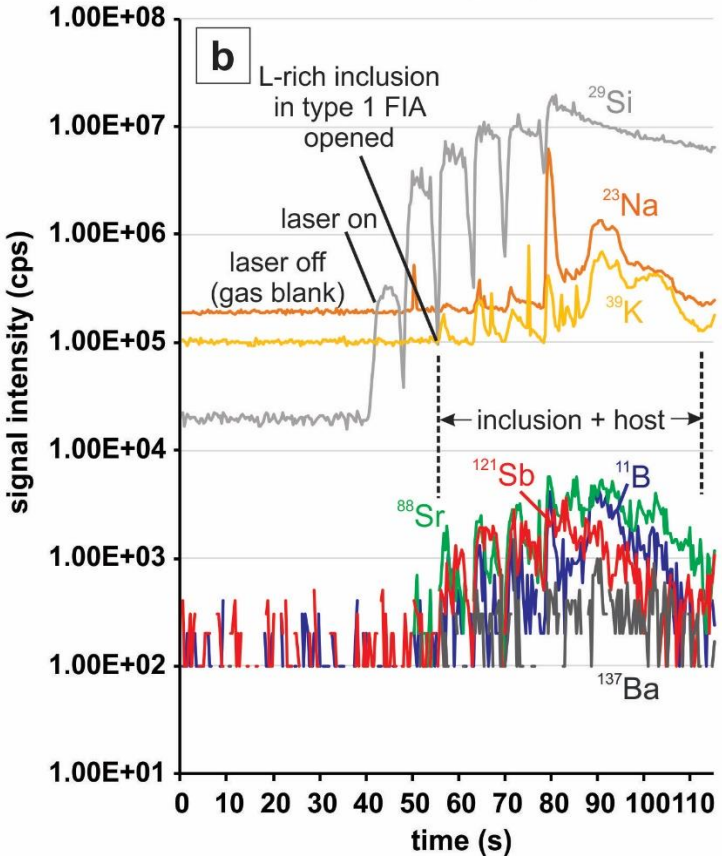
b
L-rich inclusion
in type 1 FIA
opened
laser on
laser off
(gas blank)
^{29}Si
^{23}Na
^{39}K
inclusion + host
^{121}Sb
^{11}B
^{88}Sr
^{137}Ba
signal intensity (cps)
time (s)

Figure 2.15 previous page – Representative Raman and LA-ICP-MS spectra from L-rich and V-rich fluid inclusions. (a) Raman spectra from L_{aq}-rich, types 1 and 2 FIAs fluid inclusions from Maisie. Spectra for L_{aq} in type 1 and 2 FIA are shown in orange and for the V-phase in blue, as well as type 3 (red) vapour phase fluid inclusions. Peak positions of SiO_2, CO_2, N_2, and CH_4 are identified using reference wave numbers from Frezzotti et al. (2012). (b) Transient LA-ICP-MS signal (count rate in counts per second vs. time in seconds) for an ablation of type 1 fluid inclusion. An interval of ~40 s of gas blank (laser off) is collected. The laser is switched on at ~40 s at which point count rate for ^{29}Si increases. Stepped widening of the laser ablation beam diameter is represented by subsequent rises and drops in ^{29}Si. Inclusion is opened at ~55 s with synchronous rise in ^{23}Na, ^{39}K, ^{88}Sr, ^{121}Sb, ^{15b}, and ^{137}Ba count rates.

All L-rich inclusions show an H_2O band shape characteristic of low salinity aqueous fluid (Fig. 15a) as described by Mernagh and Wilde (1989).

LA-ICP-MS results for Q2-hosted L_{aq}-rich inclusions in type 1 FIA from Maisie are reported in Table 4. Figure 15b shows a representative LA-ICP-MS transient signal during ablation of a large, L_{aq}-rich inclusion. Elements consistently detected, and quantified, in 41 inclusions were B, Na, K, Sr, Sb, As, Ba and Cs. Sodium and K reach the highest concentration among these cations (Fig. 15b; ~ 10^5 ppm), followed by Sr, Sb, B, and Ba (Fig. 15b; ~ $10^2 – 10^3$ ppm), and As, Zn, Pb, and Cs (Fig. 15b; ~ 10^1 ppm), and Na/K values averaging 44 ± 68 (1σ). A few inclusions showed anomalous values (897 to 3645 ppm) of Fe indicating pyrite contamination as an accidentally trapped (coevally precipitated) phase. Gold was not above routine detection limits (~ 0.4 ppm).

2.4.4 – Pyrite chemistry

Major, minor, and trace element concentrations in pyrite were determined by LA-ICP-MS (spot) analysis, and are represented graphically in Figures 16 and 17, with data summarized in Table 5. Additionally, entire grains of pyrite were mapped to examine element distributions (Figs. 18 and 19). Pyrite grains analyzed were from massive (Q2) and vuggy (Q3) quartz. Pyrite was analysed with the aim of comparing the chemistry of this vein mineral between occurrences, comparing vein-hosted pyrite to sedimentary (diagenetic) pyrite in the host rocks (as a possible source of Au and affiliated metals), and determining if pyrite records (compositionally and texturally) one or more Au enrichment and Au metal associations.

Table 4 - LA-ICPMS data for L_q-rich fluid inclusions from the Maisie occurrence (ppm)[1]

	^{11}B	^{23}Na	^{25}Mg	^{39}K	^{44}Ca	^{55}Mn	^{56}Fe	^{65}Cu	^{66}Zn	^{75}As	^{85}Rb	^{88}Sr	^{95}Mo	^{107}Ag	^{118}Sn	^{121}Sb	^{133}Cs	^{137}Ba	^{182}W	^{197}Au	^{208}Pb	^{209}Bi
Chip I																						
a03	188.0	4927.9	7.7	331.9	778.7	3.6	284.5	<0.5	<1.5	<2.6	0.8	63.7	<0.08	<0.3	1.0	6.5	1.0	3.6	<0.1	<0.1	<0.1	<0.2
a04	653.1	3594.5	<12.0	217.3	1500.6	<6.2	153.9	<2.4	<7.6	<10.6	<1.0	38.5	<1.1	<1.3	<3.5	<2.7	2.1	5.5	<0.7	<0.5	<0.6	<0.7
a06	540.1	4419.7	<5.2	46.1	538.7	<2.6	<30.0	<1.0	<3.1	<4.4	0.7	51.2	<0.4	<0.5	<1.5	1.9	1.8	3.1	<0.2	<0.2	1.3	<0.3
a21	456.8	4836.6	<8.4	196.9	<185.9	<4.6	<54.7	<2.4	<5.4	<5.5	1.1	43.8	<0.9	<1.3	<2.6	4.6	1.5	3.3	<0.4	<0.1	<0.5	<0.6
a23	68.3	5625.5	<20.3	93.1	<419.8	<10.1	<119.3	<4.2	<9.2	<10.5	<1.9	246.2	<1.5	<2.5	<5.5	<5.1	3.5	24.7	<0.4	<0.2	<0.9	<1.2
b04	101.9	2950.3	<4.2	638.9	4557.9	20.3	390.5	<0.9	<1.8	<2.6	0.8	31.5	<0.1	0.9	<0.8	0.9	0.2	0.5	<0.2	<0.1	0.9	<0.2
b06	179.8	3539.6	17.4	4659.5	366.2	<4.4	250.8	<2.2	<3.9	<5.9	5.4	74.9	<0.8	0.5	<1.9	<1.6	1.8	15.1	<0.2	<0.3	<0.4	<0.3
b07	366.3	3088.0	<22.1	4162.3	840.2	<9.4	<95.5	<4.8	<7.5	<12.4	3.5	33.5	<1.8	<1.2	<4.3	13.5	<0.9	5.1	<0.8	<0.7	<0.9	<0.8
b10	313.8	4491.5	<7.8	1882.9	<191.4	<3.4	<34.1	<1.6	<2.5	<4.1	2.8	28.9	<0.5	<0.5	<1.5	9.2	1.1	8.2	<0.3	<0.2	<0.3	<0.3
Chip II																						
a10	230.6	4272.4	<6.9	603.7	1626.0	10.6	736.0	<1.4	<2.8	5.9	<0.5	66.1	<0.4	<0.6	<1.5	31.9	0.7	4.6	<0.3	<0.2	<0.3	0.3
a12	224.7	4315.3	<19.7	838.6	1389.2	13.1	896.8	<3.6	<8.3	<13.6	<1.6	83.3	<1.0	<1.7	<4.1	31.1	<0.9	19.6	<0.7	<0.5	<0.7	<0.8
a14	440.5	4862.3	<14.0	<33.8	<267.4	<5.5	160.1	<2.7	<5.4	<7.8	<1.0	38.2	<0.9	<1.1	<2.5	3.3	2.4	<1.1	<0.7	<0.5	<0.5	<0.6
a15	353.2	2815.1	181.4	137.6	4177.4	11.6	439.6	<0.5	<1.2	2.2	<0.2	16.3	<0.3	1.0	<0.6	2.4	1.3	0.8	0.3	<0.1	0.2	0.2
b16	310.0	5808.4	<33.9	126.2	<831.3	<13.4	<116.5	<7.4	<9.5	<17.6	<2.6	49.3	<2.1	<2.1	<5.0	21.7	<1.5	5.2	<1.3	<1.0	<1.2	<1.1
b17	312.9	5388.8	<26.6	<69.4	897.6	<9.3	<80.3	<5.6	<7.9	<11.1	<1.9	43.6	<1.3	<1.2	<4.0	<3.6	1.8	16.9	<0.9	<0.7	<0.8	<0.8
b18	324.7	4075.8	35.9	782.6	2764.2	72.2	<68.7	<4.5	<6.7	<10.1	4.8	61.9	<2.1	<1.1	<3.2	3.5	<0.9	13.9	<1.0	<0.8	<0.8	<0.7
b21	595.5	5770.3	<31.1	<77.1	<641.7	<10.5	<85.1	<6.5	<8.7	<11.6	<2.1	19.3	<1.4	<1.4	<4.3	45.0	1.1	1.8	<1.1	<0.8	<1.0	<0.8
b22	311.8	5394.7	<31.2	1180.0	<714.1	<11.3	<93.9	<6.4	<8.7	<13.6	5.5	172.0	<2.1	<1.2	<4.4	13.5	1.6	8.4	<1.0	<0.8	<1.0	<0.9
b23	245.2	5697.4	<14.3	453.7	<302.9	<4.9	<40.4	<3.0	<3.8	<5.8	2.8	86.4	<1.0	<0.6	<1.9	9.8	1.5	8.7	<0.4	<0.4	<0.4	<0.4
Chip III																						
a26	132.3	5145.3	34.3	366.6	509.4	<3.7	<34.7	<1.9	<3.4	<3.3	1.4	141.6	<0.7	<0.5	<1.6	<1.6	1.3	27.6	<0.1	<0.1	<0.3	<0.4
a27	<17.1	5098.6	27.1	271.4	1050.3	<4.8	<44.1	<1.5	<3.7	<3.7	<0.9	258.4	<1.0	<0.6	<2.1	<1.8	1.0	41.1	<0.4	0.1	1.5	<0.4
a30	47.7	4186.9	1049.0	364.2	2697.2	<3.6	<33.6	1.9	<3.5	<2.8	1.8	9.3	<0.6	<0.6	<1.8	<1.4	<0.4	11.7	<0.3	<0.1	0.5	<0.3
a32	46.9	5153.8	307.5	973.3	<490.5	<9.3	<84.6	<4.5	<9.8	<6.8	<2.0	105.5	<1.2	<1.2	<4.0	<3.6	1.3	27.1	<0.7	<0.2	<0.8	<0.8
a33	80.1	5649.3	<27.7	97.7	<521.4	<10.2	<87.6	<4.9	<12.2	<7.9	<2.1	116.5	<2.0	<2.1	<4.9	<4.0	<1.2	8.9	<1.0	<0.2	<1.0	<1.0
b28	<44.0	5634.0	63.3	522.9	<799.1	<12.7	897.2	<7.6	<11.1	<16.1	<2.8	62.3	<2.6	<2.1	<5.2	<5.2	<1.6	10.2	<1.6	<1.1	<1.3	<1.1
b29	558.9	3963.1	<31.5	1978.8	<570.8	25.6	3644.8	<6.0	<7.2	<10.3	<1.9	12.0	<1.2	<1.2	<3.7	<3.4	6.9	<1.7	<0.7	<0.8	<0.7	<0.7
b30	39.0	5345.6	7.3	272.5	507.9	2.7	180.3	<0.8	<0.9	<1.5	0.4	232.9	<0.2	<0.1	<0.5	<0.5	0.3	35.1	<0.1	<0.1	<0.101	0.1
b34	323.2	5151.0	<70.6	<143.6	<1182.5	<19.2	<132.2	<13.3	<14.0	<19.8	<4.1	25.5	<3.0	<2.7	<7.5	<6.9	<2.4	7.0	<1.4	<1.7	<2.0	<1.4
b35	<40.1	5711.7	<45.3	<97.4	<826.2	<12.8	<91.5	<9.7	<8.6	<13.6	<2.9	382.0	2.0	<1.5	<5.2	<4.8	<1.6	47.3	<1.4	<1.0	<1.1	<0.9
b36	29.5	5542.6	<11.0	<23.4	343.0	<3.2	<22.3	<2.0	<2.9	<3.2	0.7	261.0	<0.7	<0.4	<1.2	<1.2	1.2	38.2	<0.3	<0.3	<0.2	<0.2
b41	26.3	4941.5	36.3	187.4	1406.0	<5.7	<42.9	<3.5	<4.4	<5.2	<1.2	176.7	<1.1	<1.2	<2.0	<2.4	<0.6	14.7	<0.4	<0.1	<0.5	<0.5
b42	<52.0	5805.4	<54.4	<115.7	<953.8	<15.8	<114.9	<11.0	<10.6	<12.6	<3.5	200.1	<3.2	<2.4	<5.4	<6.1	<1.8	39.0	<1.8	<0.3	<1.2	<1.3
b43	25.4	4877.1	20.5	99.8	1445.6	<1.9	<13.7	<1.2	<1.3	2.6	0.6	362.8	<0.5	<0.3	<0.7	<0.7	0.9	52.8	<0.2	<0.04	<0.2	<0.1
b44	121.1	5247.6	5.9	1039.0	<92.8	<1.5	<10.9	<1.0	<0.8	3.8	3.3	10.4	<0.3	<0.2	<0.6	1.0	1.1	6.2	<0.1	<0.03	<0.1	<0.1
b45	119.1	5620.7	45.0	<84.5	<697.1	<11.7	<83.1	<8.2	<7.7	7.6	<2.5	62.1	<2.0	<1.8	<4.7	<4.1	1.7	14.5	<0.8	<0.3	<0.9	<0.8
b46	<159.4	3571.8	<144.1	<305.1	3984.5	<43.1	<311.7	<29.8	<39.8	<29.3	<10.1	17.6	<9.3	<8.4	<17.8	<17.0	<5.2	15.1	<4.3	<1.0	<3.8	<3.8
b48	9.8	5332.1	30.1	<15.8	748.9	<2.1	<15.3	<1.5	<1.7	<1.4	0.6	349.2	<0.1	<0.3	<0.7	<0.7	0.9	52.7	<0.3	<0.04	0.2	<0.1

[1]Superscript indicates the isotope measured for each analyte but quantified concentrations are for total analyte not isotope

Table 5 - LA-ICP-MS trace element analyses of vein pyrite, and sedimentary host pyrite (ppm)

	Co	Ni	Cu	Zn	As	Se	Mo	Ag	Sn	Sb	Te	W	Au	Pb	Bi
JC00-137															
1	2870	370	6.13	7.7	420	6	1.75	0.026	0.077	0.136	0.52	bdl	bdl	3.34	0.028
2	3400	99.3	1130	890	176.9	13	6.5	0.153	0.06	0.023	0.18	bdl	bdl	4.35	bdl
3	132.3	183	0.96	0.13	80.9	12	0.012	bdl	0.024	0.05	0.077	bdl	bdl	1.45	bdl
4	7.9	1726	0.113	bdl	401	14	bdl	bdl	0.03	bdl	0.24	bdl	bdl	bdl	bdl
5	472	391	0.3	0.05	49.9	23.7	bdl	bdl	0.021	0.029	0.07	bdl	bdl	0.49	bdl
6	183.6	2057	580	4.6	480	19.3	0.068	0.096	0.125	0.244	0.1	bdl	bdl	6.45	0.081
7	24.2	866	0.057	0.012	710	15.4	bdl	bdl	0.024	0.038	0.14	bdl	bdl	bdl	bdl
8	18.74	1940	bdl	0.09	584	22	bdl	bdl	0.013	bdl	0.11	bdl	bdl	bdl	bdl
9	1.83	447	bdl	0.05	480	17	bdl	bdl	0.018	bdl	bdl	bdl	bdl	bdl	bdl
10	23.9	267	0.126	0.073	64.4	19	bdl	bdl	0.066	bdl	0.042	bdl	bdl	0.16	bdl
11	333	1200	720	1.62	191.6	13	8.1	0.122	0.144	1.19	0.33	0.274	bdl	30.9	0.159
12	26.6	2043	3.26	0.17	921	34	0.166	0.019	0.046	0.282	0.025	bdl	bdl	9.2	0.064
13	57.4	595	39	1.94	205	45	1.8	0.07	0.135	0.95	0.023	0.357	bdl	24.7	0.133
14	170	453	11.7	15	71.6	26	0.6	0.017	0.295	0.55	0.11	0.62	bdl	14.4	0.055
15	8.2	2420	61	1.49	522	10.1	0.08	0.082	0.041	0.171	0.45	bdl	bdl	5.6	0.056
16	172	1247	0.053	bdl	439	6	0.013	bdl	0.055	0.012	bdl	bdl	bdl	0.219	bdl
17	313	1653	0.015	0.012	253	13	bdl	bdl	0.044	0.022	0.11	bdl	bdl	0.016	bdl
18	76.4	1553	139	1.61	423	22	10.4	0.126	0.065	0.7	0.037	0.193	bdl	19.3	0.15
19	1480	285	0.41	0.15	133	10.3	bdl	bdl	0.027	0.042	bdl	bdl	bdl	0.76	bdl
20	33	2630	0.025	0.1	692	20.2	bdl	bdl	0.048	bdl	0.024	bdl	bdl	0.0149	bdl
21	2620	232	136	340	204.2	23	5.5	0.322	0.105	0.767	0.36	0.412	bdl	24.7	0.126
22	656	1453	170	0.18	246.3	14	bdl	bdl	0.009	0.072	bdl	bdl	bdl	2.02	bdl
23	126.7	2000	360	20200	358	22	0.86	0.235	0.265	0.84	0.26	0.487	bdl	23.6	0.127
24	323	438	40	2.03	190	26	3.09	0.091	0.154	1.23	0.11	0.191	bdl	26	0.152
25	98.9	1409	19800	5.29	643	22	3.5	0.125	0.179	0.67	0.16	0.218	bdl	23.8	0.083
26	363	535	22.4	4.7	187.9	16.9	1.4	0.162	0.098	1.11	0.26	0.43	bdl	33.4	0.222
27	436	491	1040	3.5	188	27	3.85	0.264	0.09	0.8	0.052	0.262	bdl	21.3	0.098
28	308	423	18.2	49	79.8	26.5	2.34	0.065	0.111	1.18	bdl	0.54	bdl	27.7	0.169
29	140	2345	0.7	0.07	345	16.2	0.053	bdl	0.041	0.059	0.22	bdl	bdl	0.91	0.017
30	33.2	2470	1240	15.5	609	28	6.9	0.3	0.115	0.98	0.5	0.146	bdl	27.8	0.189
31	1570	1370	2590	75	214.6	15	1.01	0.69	0.144	1.53	0.43	0.77	bdl	35.3	0.182
32	0.083	1627	6.73	0.63	824	15	0.61	0.053	0.176	0.63	bdl	0.42	bdl	12.9	0.116
33	54.8	738	34.8	3.28	143	4	2.48	0.128	0.12	1.35	0.08	0.223	bdl	40	0.248
34	1239	93.7	0.86	0.11	144.5	15	0.151	bdl	0.032	0.044	0.18	bdl	bdl	1.6	bdl
35	417	449	7.5	450	170	18.1	42	0.014	0.048	0.495	0.06	0.095	bdl	11.8	0.051
36	63.9	716	980	324	282	10	1.22	0.293	0.284	1.22	0.45	0.62	bdl	30.3	0.221
37	20.5	1350	11.3	2.5	401	25.6	34	0.058	0.066	0.483	0.29	0.2	bdl	14.81	0.067
38	1950	718	12.2	23	269	21	647	0.058	0.302	0.269	0.26	1.12	bdl	12.33	0.084

Table 5 Cont'd - LA-ICP-MS trace element analyses of vein pyrite, and sedimentary host pyrite (ppm)

	Co	Ni	Cu	Zn	As	Se	Mo	Ag	Sn	Sb	Te	W	Au	Pb	Bi
39	255	343	241	7300	117.3	bdl	0.86	0.063	0.124	0.66	0.064	0.332	bdl	19.8	0.106
40	1.05	384	0.041	0.047	228	21.8	bdl	bdl	0.038	0.008	bdl	bdl	bdl	0.0095	bdl
41	2090	354	139	0.78	240	24	9.8	0.09	0.059	0.43	0.17	0.158	bdl	14.5	0.07
42	227	2417	bdl	0.19	426	19	bdl	bdl	bdl	0.002	0.029	bdl	bdl	0.038	bdl
43	135.1	1236	4730	27200	403	12	bdl	0.172	0.048	0.077	bdl	bdl	bdl	8.46	0.025
44	44.6	1123	1190	3.12	411	26	0.74	0.243	0.39	0.91	0.3	0.81	bdl	27.9	0.146
45	250	743	350	1400	131.8	17	1.73	0.657	0.186	1.88	1.65	0.185	bdl	62	0.438
46	481	307	0.72	0.08	163.2	21.8	0.018	bdl	0.033	0.055	bdl	bdl	bdl	0.87	bdl
47	52.5	1630	460	43	405	35	4.4	0.303	0.218	1.48	1.06	0.44	bdl	45	0.347
48	48.1	1610	2320	57	536	24	2.21	0.347	0.31	1.46	0.27	0.47	bdl	39.4	0.266
49	398	2263	bdl	0.1	486	28.4	bdl	bdl	0.047	bdl	0.056	bdl	bdl	0.0111	bdl
50	78.7	384	5.83	0.38	115.9	19	0.29	bdl	0.039	0.324	bdl	bdl	bdl	8.18	0.055
Men43B[2]															
1	2.08	2170	32.9	0.12	1648	47	bdl	0.414	bdl	74.7	5.9	bdl	0.273	538	3.87
2	7610	9500	36	8	3400	26.5	0.042	1.11	0.028	32.1	3.56	11.8	0.408	1630	3.28
3	30.25	11870	3.9	0.1	68.1	52.9	0.574	0.599	bdl	27.8	0.18	bdl	0.227	67.8	1.273
4	34.9	7960	2.94	0.12	26.6	56.6	0.45	0.219	0.024	13.8	0.17	bdl	0.253	46.1	0.556
5	27.7	8500	3.18	0.18	163	66.8	1.38	0.459	0.054	17.45	0.47	bdl	0.255	50.8	0.598
6	4270	9240	13.2	0.18	142	56.1	0.222	0.476	0.016	26.8	0.36	bdl	0.336	81.8	0.719
7	50.5	9040	2.93	0.16	6.1	63.3	0.318	0.245	bdl	9	0.052	bdl	0.142	20.6	0.353
8	11.91	8770	0.5	0.049	8.6	66.5	0.324	0.057	0.009	3.42	0.08	bdl	0.0178	6.4	0.103
9	500	6750	4.12	0.44	116	56.3	0.245	0.204	bdl	13.5	0.25	0.087	0.158	42.2	0.31
10	34.7	8020	4.42	0.75	354	53	0.47	0.505	0.007	17.55	0.31	bdl	0.158	223	0.464
11	0.051	2154	18.3	0.24	871	32	bdl	0.269	0.016	56.1	0.07	bdl	0.223	417	0.345
12	18.11	12110	37.6	0.57	304	30.4	bdl	0.486	bdl	19.42	0.1	bdl	0.366	90	0.309
13	27.3	16490	3.04	0.15	54.4	29.7	6.1	0.135	0.088	18.1	0.095	bdl	0.445	15	0.031
14	342	11450	10.5	63	2510	53.7	0.328	0.397	0.052	27.9	2.14	0.98	0.354	176	0.784
15	316	11640	20.1	6590	194	63	3.71	0.558	6.4	30.3	1.17	0.98	0.266	500	1.098
16	149	10430	19.4	320	285	47.8	0.78	0.56	0.156	30.7	1.53	bdl	1.09	289	1
17	22500	4370	400	4650	1640	64	3.77	2.43	4.52	135.8	7.99	bdl	1.3	1340	5.12
18	530	13020	256	51	860	39	0.87	1.76	0.15	103.3	4.84	0.002	1.09	1040	3.39
19	5.99	18210	27.4	0.001	2240	13.7	0.006	0.38	bdl	18.73	0.88	2.63	0.439	27.3	0.294
20	0.015	560	18.9	0.1	3.04	6	bdl	0.289	bdl	96.7	0.026	bdl	0.079	467	0.011
21	0.003	356	12.7	bdl	8.04	8	bdl	0.15	bdl	29.3	bdl	0.008	0.020	151	0.009
22	123	5900	1.23	0.68	9.2	37	0.14	0.11	0.013	2.47	bdl	bdl	0.018	11.3	0.027
23	141.9	6340	170	0.37	9.7	56.3	0.078	0.119	0.032	4.99	0.028	bdl	0.0071	21.2	bdl
24	192.7	3640	9.48	33	95.9	64	0.392	0.195	0.002	8.32	bdl	0.025	0.043	111	0.138
25	257	3490	13.9	0.22	17.64	50.7	0.087	0.264	bdl	12.32	bdl	bdl	0.252	61	0.136

[1]JC00-137=Boland Brook pyrite;[2]Men=Maisie gold showing; [3]Pan Concentrates=Lavoie gold showing

bdl=below detection limit

Table 5 Cont'd - LA-ICP-MS trace element analyses of vein pyrite, and sedimentary host pyrite (ppm)

	Co	Ni	Cu	Zn	As	Se	Mo	Ag	Sn	Sb	Te	W	Au	Pb	Bi
26	186.8	5130	12.7	2.39	15.7	44.7	0.329	0.26	bdl	41.5	0.082	bdl	0.167	224	0.035
27	220.7	5050	35.8	43.1	48.2	41.6	0.247	0.201	0.067	13.37	0.025	0.013	0.099	107.9	0.152
28	158.4	4300	1.17	0.21	0.28	36.8	0.205	0.116	bdl	1.7	bdl	0.027	0.041	7.29	0.034
29	1776	67700	4.45	0.17	0.5	40	0.127	0.91	bdl	1.03	0.037	bdl	0.009	27.9	0.151
30	1470	63500	29.4	0.95	1	56.1	0.367	5.79	0.024	1.54	0.075	bdl	bdl	33	0.185
31	63.5	33550	818	5.95	10.2	26.1	0.131	18.35	0.042	7.19	0.11	bdl	0.458	85.5	0.086
32	271	19030	486	7.8	63.6	7.1	0.215	2.05	0.148	26.9	bdl	0.001	0.297	347	0.156
33	183	6520	3.36	1.34	179	27	0.96	0.27	0.054	76	0.23	0.54	0.119	164	0.149
34	411	6720	15.7	1.98	174.6	30.3	3.52	1.85	0.374	64.5	1.4	3.77	0.525	839	1.282
35	1125	18000	8.64	8.5	647	35	9.3	2.67	0.677	108.8	2.23	14.7	0.429	1950	1.15
Men42-5A[2]															
1	20.7	345	1.15	0.014	2244	40.1	0.021	0.022	0.003	1.2	3.74	bdl	0.479	11.5	0.282
2	11.5	260	3.37	0.014	2480	42.7	bdl	0.039	0.001	4.31	4.9	bdl	1.98	29.2	0.78
3	4.98	226	7.8	0.12	4210	46.8	bdl	0.106	bdl	7.88	6.78	bdl	5.35	63.6	1.4
4	182	895	0.54	0.114	2461	43.7	bdl	0.014	bdl	0.75	5.37	bdl	0.613	4.06	0.114
5	39.6	611	2.33	0.079	2556	43.7	bdl	0.032	0.002	3.02	5.33	bdl	1.106	21.1	0.503
Men26C-2[2]															
1	0.003	2.69	4.03	bdl	1444	39.7	bdl	0.029	0.004	4.52	0.65	bdl	0.396	39.8	1
2	0.013	14.9	31	bdl	1624	27.1	bdl	0.042	0.005	1.62	0.74	bdl	0.506	11.4	0.296
3	0.002	7.28	10.54	bdl	1819	29.5	bdl	0.058	bdl	13.8	1.26	bdl	1.24	118.8	3.2
4	1.84	33	0.56	0.17	1217	43.4	bdl	0.002	0.001	0.126	0.76	bdl	0.637	1.01	0.018
5	0.011	51.4	618	bdl	2515	40.7	bdl	0.29	bdl	1.43	1.48	bdl	2.31	12.1	0.25
6	2.03	147.2	2450	152	1836	33.5	0.118	1.06	bdl	7.15	1.68	bdl	0.797	1083	0.377
7	11.35	442	265	11.7	1193	40.5	bdl	0.249	bdl	2.74	2.13	bdl	0.723	89	0.572
Men1004c[2]															
1	12.21	240	0.339	1.75	124.4	44	8.87	0.039	0.121	1.2	bdl	0.017	0.003	2.62	0.010
2	11.12	231	0.46	0.78	527	32	4.69	0.010	0.051	7.95	bdl	bdl	bdl	7.29	0.032
3	29.9	559	0.278	0.24	294	55	6.74	bdl	0.068	5.21	0.027	bdl	bdl	12.26	0.004
4	3.88	110.8	0.156	0.92	1816	32	3.29	bdl	0.071	18.82	0.063	0.001	bdl	6.59	bdl
5	7.45	50.2	194.7	9.67	11.75	35	0.385	0.244	0.121	0.201	bdl	bdl	bdl	9.95	0.005
6	9.6	84.7	199.1	14.12	28.3	21	1.17	0.356	0.281	0.373	bdl	0.002	bdl	100	0.010
7	17.3	134	174.5	17.8	34.6	13	1.23	0.569	0.392	0.86	0.019	0.006	bdl	34	0.017
8	319	2380	2990	8.7	2.3	61	0.267	1.95	0.014	17.5	0.17	bdl	0.316	67.8	5.86
9	640	2900	2180	3.89	4.99	73	0.223	3.55	0.012	37.6	0.35	bdl	0.858	137.4	13.31
10	1038	2850	2630	7.8	2.28	100	0.217	2.63	bdl	24.4	0.22	bdl	0.522	95.1	8.43
NW1004															
1	0.001	1.94	0.032	0.2	1730	10	bdl	bdl	bdl	0.054	0.11	bdl	0.003	0.066	bdl
2	4.7	24.1	2.37	0.54	1553	19	bdl	0.024	0.008	1.83	1.86	bdl	0.15	13.9	2.11

[1]JC00-137=Boland Brook pyrite;[2]Men=Maisie gold showing; [3]Pan Concentrates=Lavoie gold showing

bdl=below detection limit

Table 5 Cont'd - LA-ICP-MS trace element analyses of vein pyrite, and sedimentary host pyrite (ppm)

	Co	Ni	Cu	Zn	As	Se	Mo	Ag	Sn	Sb	Te	W	Au	Pb	Bi
3	0.603	3390	0.73	0.26	80.9	17	bdl	0.001	bdl	bdl	3.34	bdl	bdl	0.022	0.003
4	1.36	1381	1.41	0.33	4430	49	bdl	0.014	0.008	0.024	5.86	bdl	0.19	19	0.39
5	35.4	199	3.69	0.24	2370	14	0.012	0.7	0.074	4.87	5.22	9.7	0.602	510	5.6
6	303	2970	244	12	87	7	bdl	1.51	0.044	36	46.2	bdl	1.8	2130	93.2
7	12.7	334	1.05	0.16	2590	bdl	bdl	0.032	0.025	2.3	9.2	bdl	0.23	18	3.36
8	0.69	506	2.59	0.35	3310	7	0.004	0.027	0.001	0.033	1.47	bdl	0.282	64	1.51
9	0.117	5.29	0.128	0.052	3360	20	bdl	bdl	0.014	0.035	6.15	bdl	0.67	0.37	0.051
10	79	956	28	0.5	549	0.4	0.002	15.1	0.042	6.86	14.9	0.005	0.272	8600	37.5
11	5.5	1110	36.6	6.99	4030	15	0.028	0.361	0.009	4.61	2.6	0.48	2.9	1740	6.2
12	0.011	102.3	0.066	bdl	3320	25	bdl	0.003	bdl	0.029	5.31	0.010	0.561	0.152	0.026
13	6.6	15.4	4.52	0.18	1962	8	bdl	0.07	0.015	6.2	2.08	bdl	0.297	48.2	3.77
14	2.15	1522	0.74	0.017	8.17	23	0.024	0.034	0.012	0.66	0.36	bdl	0.068	4.11	0.152
15	2.02	645	1.88	0.16	9.05	28	0.104	0.017	bdl	1.5	0.22	bdl	0.049	9.54	0.517
16	0.14	415	0.69	0.068	3900	29.8	bdl	0.047	0.009	1.14	8.83	bdl	0.54	8.85	0.685
17	4.33	972	1.33	bdl	11	18.3	0.045	0.03	0.003	1.76	0.21	bdl	0.067	6.2	0.172
18	2.5	849	1.54	bdl	15.56	13	0.012	0.019	bdl	1.73	0.079	bdl	0.052	4.31	0.199
19	2.51	555	6.9	1.1	4430	14.5	bdl	0.178	0.023	6.75	5.12	bdl	0.98	67	2.99
20	4.2	1317	2.71	0.108	15	19.2	0.029	0.053	0.016	2.94	0.47	bdl	0.088	10.7	0.164
21	2.02	1344	7.2	0.91	520	23.7	bdl	0.198	0.003	5.31	2.5	bdl	0.53	87	2.04
22	2.58	1018	18.8	0.83	88.9	19.1	bdl	0.24	0.022	8.04	1.63	bdl	0.66	59.4	2.73
23	990	580	1.21	0.2	14.9	16.6	0.05	0.013	0.006	0.797	0.73	bdl	0.013	5.21	0.294
24	1010	763	2.2	0.24	60.8	10	0.088	0.054	0.005	2.49	1.39	bdl	0.151	21.7	1.38
25	0.185	2830	1.97	0.69	7.74	8	0.132	bdl	0.041	0.098	0.35	bdl	0.039	41	1.6
26	0.994	3080	9.8	3.51	9.14	8	3.31	0.59	0.12	0.405	1.05	0.211	5.4	100	1.96
27	0.171	0.34	0.258	0.16	2690	14.3	bdl	0.004	0.022	0.322	0.88	0.17	0.224	1.62	0.205
28	3.45	1560	380	2.8	101.5	12.7	0.003	4.08	0.022	9.68	6.36	bdl	0.579	2250	12.4
29	3560	2930	5.8	0.68	1100	8.1	bdl	0.3	0.009	1.54	10.9	bdl	0.28	236	3.3
30	0.083	501	5.4	0.59	5720	18	bdl	0.08	0.007	1.58	4.3	bdl	1.26	64	0.84
31	3.51	1930	12	3.23	85	14.8	bdl	0.189	0.004	6.99	1.58	bdl	0.577	240	1.37
32	182.2	1813	6.18	0.21	55.8	9.9	0.010	0.245	0.012	4.78	1.52	bdl	0.486	56	1.33
33	510	3370	23.5	14.1	6070	9.1	bdl	0.94	0.005	9.34	3.64	0.027	1.56	1230	6.4
34	0.006	0.169	0.39	0.19	3010	7.2	0.002	0.013	0.019	0.152	0.107	bdl	0.148	3	0.165
35	2.22	2250	0.13	0.064	0.75	14.8	bdl	0.002	0.021	0.14	1.41	bdl	bdl	0.067	bdl
36	56	547	0.176	0.1	7230	15.1	bdl	0.013	bdl	bdl	0.5	bdl	1.37	0.075	0.011
37	0.129	516	2.05	3.06	4700	14	bdl	bdl	0.015	0.047	0.092	bdl	0.425	144	0.023
38	0.025	0.23	0.146	0.21	19.2	5.4	0.002	bdl	0.002	0.295	0.5	bdl	0.007	3.44	0.002
39	2.96	115	0.13	0.141	3900	6.7	bdl	0.017	0.012	0.24	2.25	bdl	0.25	0.5	0.117
40	9.44	2010	14.3	16	650	9	0.097	0.373	bdl	4.25	2.78	bdl	0.9	577	2.77
41	0.454	104	0.2	0.31	2220	15	bdl	0.027	0.043	0.014	1.97	bdl	0.31	0.66	0.013
42	171	1406	0.111	0.21	3880	14.6	bdl	bdl	0.058	0.057	2.28	bdl	0.152	0.53	0.055

[1]JC00-137=Boland Brook pyrite;[2]Men=Maisie gold showing; [3]Pan Concentrates=Lavoie gold showing

bdl=below detection limit

Table 5 Cont'd - LA-ICP-MS trace element analyses of vein pyrite, and sedimentary host pyrite (ppm)

	Co	Ni	Cu	Zn	As	Se	Mo	Ag	Sn	Sb	Te	W	Au	Pb	Bi
43	0.136	717	6.6	2.2	3920	19.1	0.009	0.193	bdl	6.23	2.84	bdl	1.02	32.4	2.06
44	0.158	2670	0.15	0.21	2.9	14.7	0.008	0.017	bdl	0.078	0.38	bdl	0.002	0.093	0.008
45	2.39	665	18.3	3.77	3520	13.9	bdl	bdl	0.015	0.065	3.89	0.012	0.236	357	3.39
46	300	850	0.076	0.056	5690	4.8	bdl	0.002	0.008	bdl	1.13	bdl	0.152	0.026	bdl
47	0.016	45	3.5	0.45	1429	6.7	bdl	0.026	0.028	2.02	0.24	bdl	0.134	26	0.87
48	1.89	1620	1.46	0.112	9.42	14.6	0.058	0.025	0.004	1.61	0.55	bdl	0.051	7.87	0.401
49	1.88	2120	0.39	0.153	0.58	20.4	bdl	0.005	0.017	0.1	0.27	bdl	0.002	0.35	0.014
50	56.3	1020	3.65	0.08	120.1	11.1	0.068	8.3	bdl	3.55	6.7	bdl	0.129	4150	20
51	0.007	336	1.64	0.015	3350	20.1	bdl	0.06	0.018	1.5	0.86	bdl	0.335	6.23	0.443
52	0.004	286	0.051	0.047	2770	17.8	bdl	0.005	0.011	bdl	0.45	bdl	0.017	bdl	0.004
53	24.2	769	0.123	0.17	2.96	5.8	0.106	0.007	bdl	0.038	0.095	bdl	0.001	0.485	0.029
54	6	1021	36	2.1	840	10.6	0.019	0.247	0.013	7.3	7.3	0.065	0.64	88	4.8
55	1.76	5.41	0.88	0.13	403	15.3	bdl	0.004	0.024	1.83	8.89	bdl	0.033	9.2	0.279
56	1.98	3.78	6.4	0.3	170	25.8	bdl	bdl	0.035	16.4	8.35	bdl	0.38	94	2.83
57	3.73	2410	6.21	0.19	18.48	24.6	0.058	0.113	0.007	5.55	0.54	bdl	0.3	19.7	1.35
58	3.14	1429	7.5	0.49	38	13.3	bdl	0.072	0.0037	4.84	0.43	bdl	0.133	37.7	0.557
59	1.41	1610	70	0.28	9.06	18.4	bdl	0.104	0.005	0.301	0.31	bdl	0.026	1	0.162
60	1.19	1067	22.4	0.9	12.47	27.1	bdl	0.174	bdl	1.66	0.119	bdl	0.034	9.5	0.69
61	222	1285	0.236	0.41	6360	19.8	bdl	bdl	0.001	0.095	3.54	bdl	0.647	11.5	0.122
62	4.79	1582	0.76	0.25	16.7	11.6	bdl	1.55	bdl	1.13	1.29	bdl	0.026	767	4.29
63	10.9	2060	2.3	0.21	23.3	14.5	bdl	0.037	bdl	2.3	1.16	bdl	0.018	24.2	1.72
64	9.01	2090	2880	69	131.1	17.6	0.002	3.34	0.117	6.62	4.75	bdl	0.59	2110	8.6
65	0.007	7.7	4.44	4.22	6530	18.4	bdl	0.005	0.001	bdl	0.58	bdl	0.358	286	0.002
66	6.18	1750	10.1	0.7	229	15.6	bdl	0.146	0.005	8.61	1.73	bdl	0.521	78	2.03
67	6.08	987	220	2.5	9.1	14.8	0.041	0.076	0.034	2.41	0.48	bdl	0.209	56	1.04
68	4.64	3620	5.2	0.44	5.13	16	0.035	0.008	bdl	0.017	1.75	bdl	0.077	53	1.62
69	5.5	1860	9.1	3.66	169	17.2	0.017	0.125	bdl	6.13	2.06	bdl	1.2	127	3.71
70	2.29	2290	6.15	0.25	120.9	26.7	0.004	0.091	bdl	4.23	1.31	bdl	0.263	27.2	2.2
71	0.858	798	0.46	bdl	66.2	8	0.059	bdl	0.016	0.5	0.29	bdl	0.065	2.41	0.118
72	1.15	674	29	0.62	13.7	18.5	0.002	0.041	0.037	0.36	0.23	bdl	0.17	53	1.69
73	11.9	930	34.1	0.37	163	7	bdl	0.325	bdl	13.8	4.26	bdl	2.22	72.1	5.07
74	4.79	1640	8.3	0.175	82.7	15.7	bdl	0.093	bdl	1.19	1.52	bdl	0.064	34	0.94
75	0.162	2.56	0.171	0.124	3020	12.9	bdl	0.001	0.005	0.012	0.108	bdl	0.152	1.2	bdl
76	0.015	38.8	0.296	0.084	3620	10.1	bdl	0.015	0.005	0.408	2.96	bdl	0.525	1.91	0.219
77	639	1690	17.3	1.14	262	14	0.066	2.85	bdl	1.95	5.21	0.047	2.3	1780	8.9
78	78	775	69	3	2500	14.7	0.102	52	0.079	10.74	16.8	4	220	9000	43
79	0.022	84	0.229	0.164	3100	20.5	bdl	0.002	0.015	0.1	8.2	0.133	0.305	0.4	0.066
80	2.23	186	0.9	0.125	3290	22.5	bdl	0.021	0.029	1.2	7.7	4.5	0.669	4.84	0.645
81	7.6	783	25.3	14.4	282	23.6	bdl	0.072	bdl	5.4	6.8	bdl	0.342	760	4.6
82	349	1215	62.9	11	1175	15.8	0.034	10.4	0.029	46	16.9	bdl	55	3370	29.3

[1]JC00-137=Boland Brook pyrite;[2]Men=Maisie gold showing; [3]Pan Concentrates=Lavoie gold showing

bdl=below detection limit

Table 5 Cont'd - LA-ICP-MS trace element analyses of vein pyrite, and sedimentary host pyrite (ppm)

	Co	Ni	Cu	Zn	As	Se	Mo	Ag	Sn	Sb	Te	W	Au	Pb	Bi
83	0.107	28	0.52	0.17	2750	13.3	0.004	bdl	0.029	0.585	0.17	3.52	0.055	2.58	0.261
84	14.4	1759	13.1	0.8	74.2	3.3	0.002	0.141	0.013	7.94	1.15	bdl	0.311	86	2.77
85	1.29	1420	25.7	0.31	27.6	11.8	bdl	0.107	0.022	1.13	1.03	bdl	0.115	59	1.14
86	2.21	1670	0.05	0.021	72.3	17.9	0.021	0.006	0.002	0.033	0.77	bdl	0.004	0.269	0.009
87	134	805	1.13	0.27	5150	24.9	bdl	0.021	0.009	0.051	3.01	bdl	0.363	4.4	0.166
88	59.7	982	10.6	2.08	5150	18.2	0.063	0.031	0.008	0.236	3.95	0.033	0.73	92	0.42
89	27	918	2.2	0.42	5030	9.5	bdl	0.041	0.015	0.304	1.52	bdl	0.206	41	1.48
90	13.8	503	136	27.3	1240	20.7	0.027	0.54	0.024	17.2	38.4	bdl	1.78	420	21.2
Men5-5															
1	0.192	1.928	37.03	10.42	14137	47.2	bdl	0.157	0.105	14.82	1.939	bdl	69.20	58.267	0.387
2	0.224	0.055	42.44	6.779	15456	31.3	bdl	0.172	bdl	8.356	bdl	bdl	68.01	68.775	0.446
3	204.4	671.8	61.57	1.507	15636	54.2	0.095	0.716	0.081	75.15	7.096	bdl	61.47	506.25	12.9
4	185.8	677.8	48.59	0.879	16946	64.7	bdl	0.751	0.041	70.23	7.268	bdl	61.14	536.42	13.67
5	161.9	479.3	51.4	3.078	15552	46.5	0.198	0.499	0.605	46.29	10.21	0.167	60.74	333.6	9.693
6	0.426	0.53	44.75	9.272	17849	72.7	bdl	0.175	bdl	11.26	6.906	bdl	60.38	66.176	0.743
7	180.8	450.6	49.71	3.312	15615	55.4	bdl	0.567	0.087	43.66	5.21	bdl	59.78	340.24	10.09
8	0.23	0.264	33.46	19.46	12699	45.2	bdl	0.069	bdl	7.589	1.035	bdl	58.96	41.785	0.31
9	299.4	971.3	56.94	2.695	17301	74.6	bdl	0.846	bdl	95.62	8.253	bdl	58.92	646.99	14.88
10	272.6	526.4	37.51	1.238	16439	53.2	0.1	0.408	bdl	43.76	6.621	bdl	58.16	378.23	9.014
11	398.3	870.2	61.77	1.787	18460	65	bdl	0.47	bdl	66.5	8.278	bdl	57.70	425.93	9.696
12	0.542	1.653	37.77	5.679	17183	65.6	bdl	0.314	0.371	42.39	6.378	bdl	56.83	204.54	0.809
13	306.3	702	76.92	4.206	18099	79.6	bdl	1.424	0.091	58.58	3.465	bdl	55.20	482.99	12.67
14	176.1	448.1	38.04	2.407	15504	65.7	bdl	0.502	0.282	42.26	4.777	bdl	54.81	326.88	8.383
15	216.5	530	58.86	2.976	16319	39.7	bdl	0.677	0.043	78.49	10.45	bdl	54.11	499.58	12.24
16	396.3	768.4	54.53	0.587	17481	55.9	bdl	0.303	bdl	54.86	6.184	bdl	53.83	438.48	10.23
17	702.9	1352	60.85	1.164	17146	55.7	bdl	0.666	bdl	104.4	12.84	bdl	53.81	668.36	16.09
18	179.1	410.7	44.46	4.044	14582	50.5	bdl	0.605	0.078	57.44	4.001	0.153	53.71	383.57	10.02
19	233.6	655.2	44.76	1.988	14272	64	bdl	0.648	0.040	73.83	10.62	bdl	53.38	609.06	14.98
20	0.307	0.754	28.04	6.038	10137	25.6	bdl	0.171	0.092	20.79	1.695	bdl	53.12	105.75	0.564
21	291.1	601.8	58.86	2.758	16937	71.3	bdl	0.644	bdl	83.02	6.257	bdl	52.45	650.77	15.1
22	272.7	664.5	48.61	1.204	15205	52.8	bdl	0.428	bdl	47.17	2.863	bdl	52.41	322	8.342
23	442.4	984.9	44.15	1.074	16625	19	bdl	0.379	bdl	59.2	3.698	bdl	51.72	515.5	11.43
24	0.786	3.735	45.37	5.978	19316	18	bdl	0.084	bdl	13.42	1.909	bdl	51.66	73.957	0.835
25	309	712.3	53.61	4.266	18825	54.5	bdl	0.69	bdl	88.1	7.426	bdl	51.37	559.32	13.76
26	0.121	0.449	20.45	6.589	12911	37.5	bdl	0.191	0.039	21.56	5.34	bdl	50.94	123.96	0.896
27	1.085	3.97	84.72	6.163	15414	65.2	bdl	0.449	0.195	52	7.081	bdl	50.68	235.26	2.252
28	549.3	1252	58.46	1.905	17189	85.2	bdl	0.92	bdl	96.31	4.049	bdl	50.64	616.38	16.23
29	612.9	1423	57.8	1.709	16293	60.5	bdl	0.717	bdl	61.72	4.784	bdl	50.08	596.87	14.29
30	402.7	1739	67.4	2.984	16422	38.4	bdl	0.667	0.045	45.76	4.806	bdl	49.75	451.33	9.306

[1]JC00-137=Boland Brook pyrite;[2]Men=Maisie gold showing; [3]Pan Concentrates=Lavoie gold showing

bdl=below detection limit

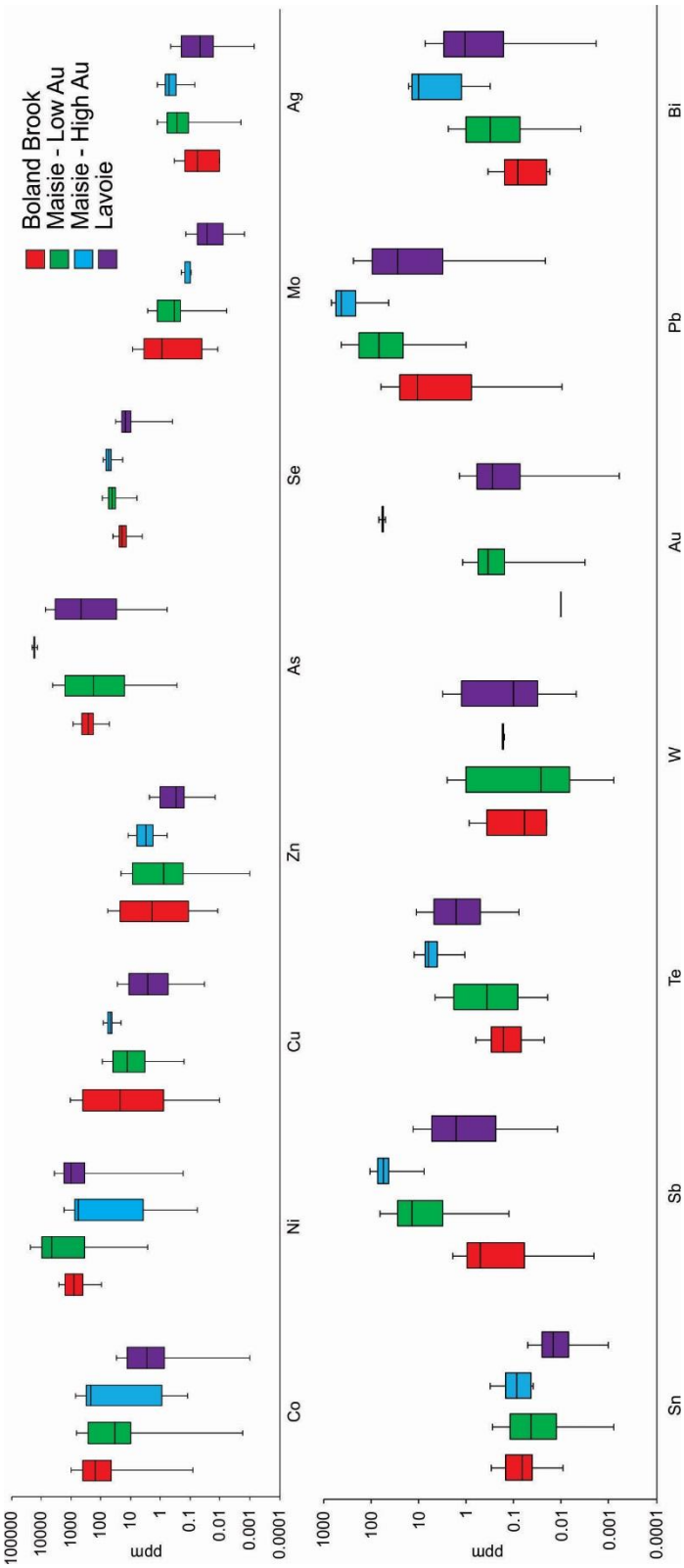

Figure 2.16 – Box-whisker plots of minor and trace element concentrations within pyrite from within the Maisie and Lavoie veins, and from the underlying Boland Brook Formation, with sample numbers listed in Table 5.

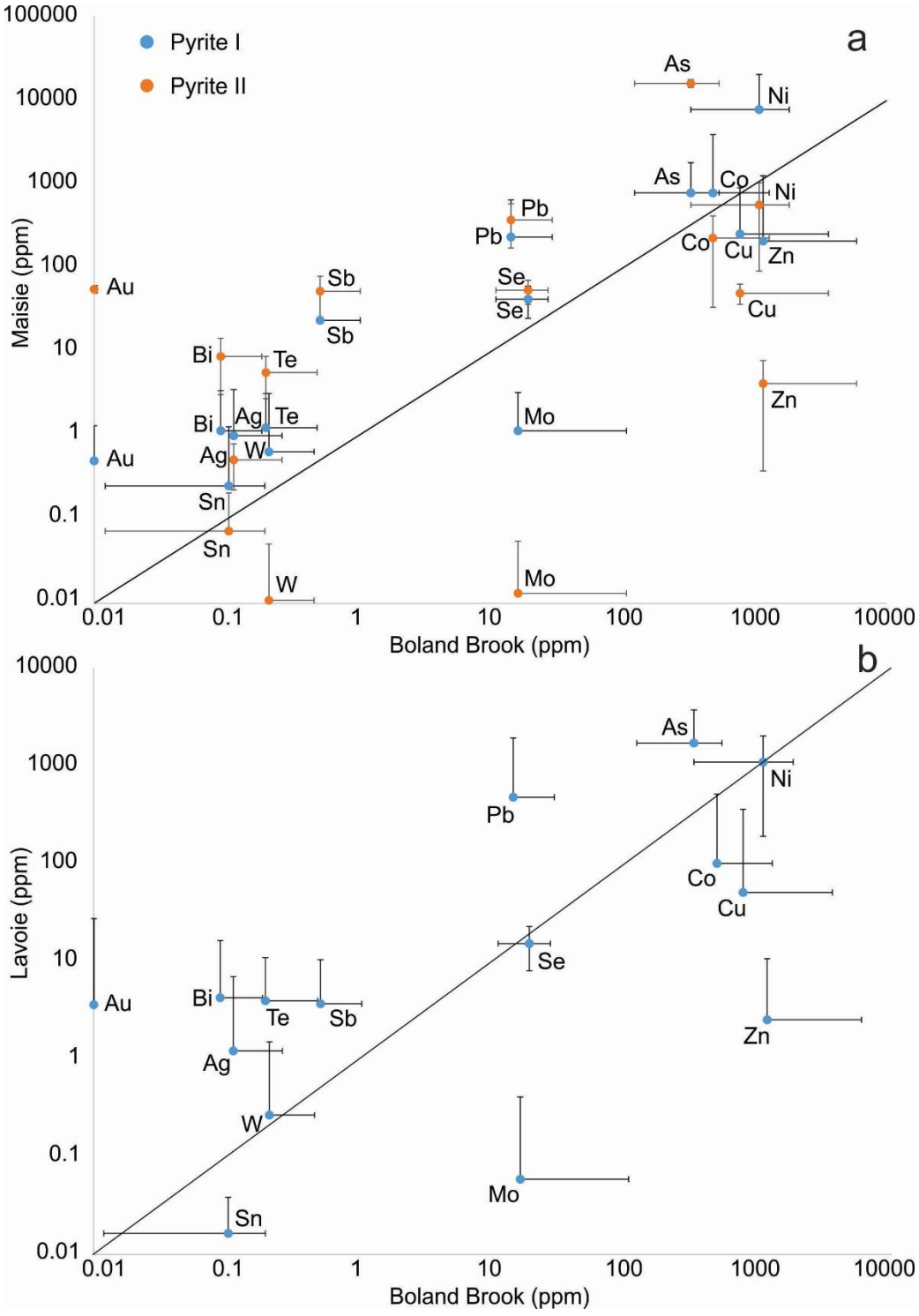

Figure 2.17 – Scatter diagrams comparing pyrite from Au showings (y-axis) and the underlying Boland Brook Formation (x-axis). a) Trace element abundances in pyrite from Maisie, including Au poor (blue) to Au rich (orange) pyrite. A 1-to-1 line differentiates elements enriched in vein pyrite from those enriched in sedimentary pyrite. b) Trace element abundances in pyrite from Lavoie. A 1-to-1 line differentiates elements enriched in vein pyrite from those enriched in sedimentary pyrite.

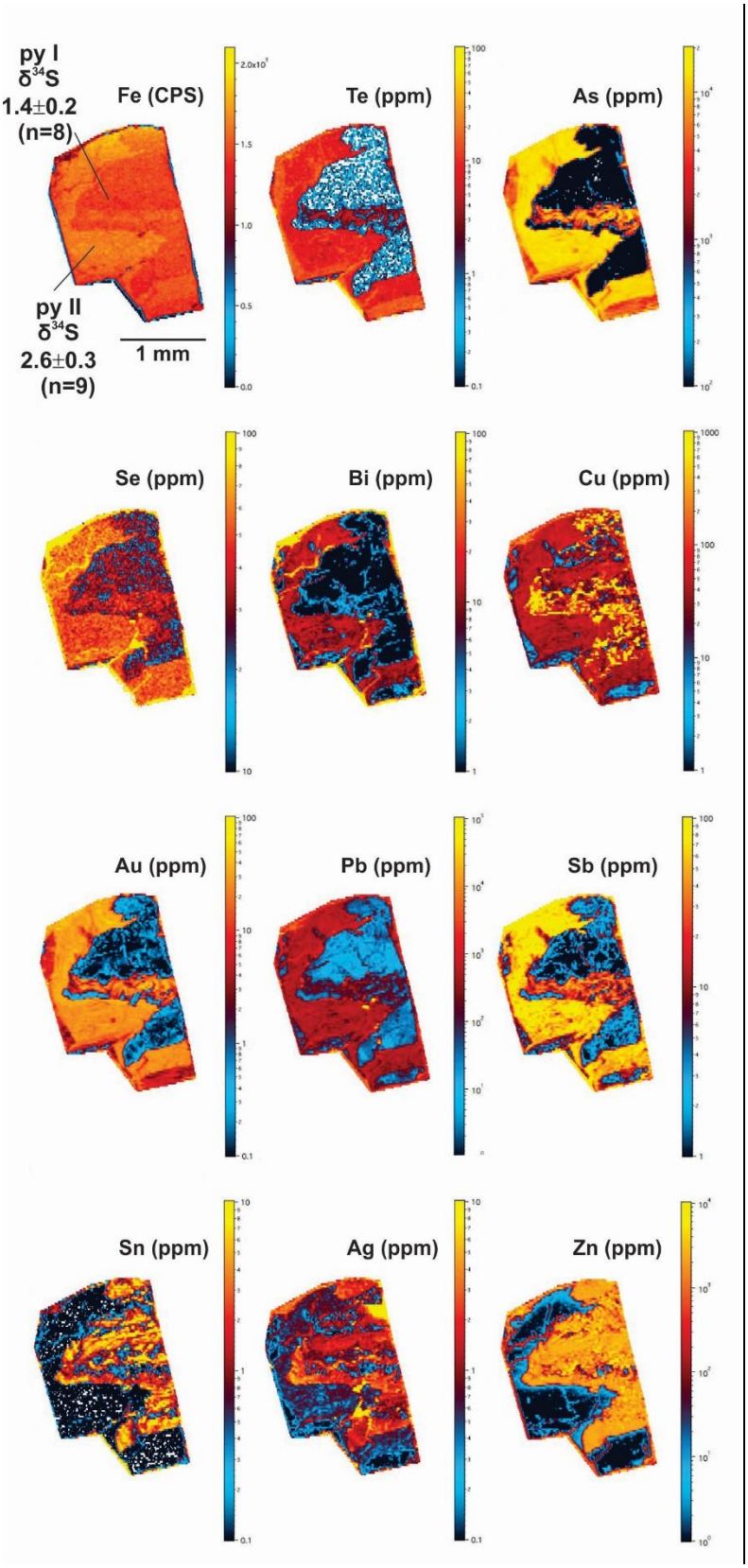
py I
δ34S
1.4±0.2
(n=8)
py II
δ34S
2.6±0.3
(n=9)
1 mm
Fe (CPS)
Te (ppm)
As (ppm)
Se (ppm)
Bi (ppm)
Cu (ppm)
Au (ppm)
Pb (ppm)
Sb (ppm)
Sn (ppm)
Ag (ppm)
Zn (ppm)

Figure 2.18 previous page - Quantitative LA-ICP-MS maps of selected trace metals in a pyrite grain from vein sample Men 5-5c at the Maisie occurrence. The grain shown is ~1.5 x ~2 mm. Scale bars are in units of ppm. Overall these maps show two main compositional domains: an early Zn-Cu-Sn-Ag-enriched generation that is replaced (following partial dissolution) and overgrown by a later Au-As-Pb-Sb-Te-Bi-Se generation. The replacement/overgrowth boundary between the two generations of pyrite is unremarkable aside from an irregular "wispy" fracture network in the central portion of the early domain.

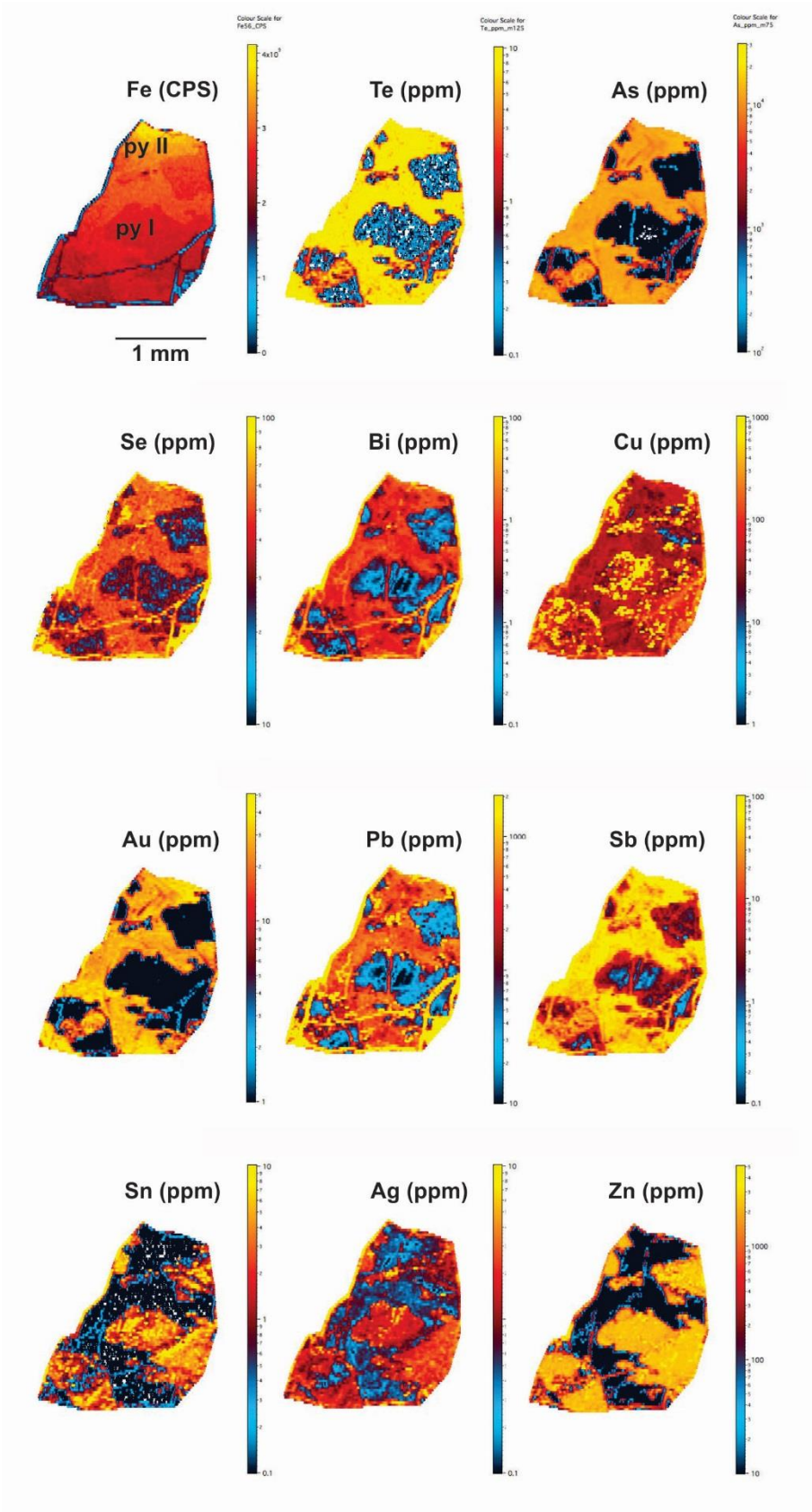
Fe (CPS)
Te (ppm)
As (ppm)
py II
py I
1 mm
Se (ppm)
Bi (ppm)
Cu (ppm)
Au (ppm)
Pb (ppm)
Sb (ppm)
Sn (ppm)
Ag (ppm)
Zn (ppm)

Figure 2.19 previous page - Quantitative LA-ICP-MS maps of selected trace metals in a pyrite grain from vein sample Men 5-5c at the Maisie occurrence. The grain shown is ~1.5 x ~2 mm. Concentration scale bars are in units of ppm. Overall the map series shows two main compositional domains: an early Zn-Cu-Sn-Ag-enriched generation associated with low Au that is replaced (following partial dissolution) and overgrown by a later Au-As-Pb-Sb-Te-Bi-Se generation associated with high Au. Replacement/overgrowth boundaries are unambiguous, showing fracture-controlled replacement and island-mainland textures with remnant patches of the early pyrite generation completely or partly surrounded by the later generation. The lower count rates for Fe (upper left frame) in the early pyrite generation reflects the very high concentrations of Zn in that stage.

2.4.4.1 – Pyrite spot analysis

2.4.4.1.1 – Maisie pyrite

In spot analyses, pyrite shows two levels of Au enrichment; pyrite containing approximately 10^{-1} to 10^{0} ppm Au, and pyrite containing from 10^{1} to 10^{2} ppm by Au. For the high Au domains in pyrite, there is corresponding relatively high concentrations of As, Pb, Ni, and Co (~10^{2}-10^{4} ppm), moderate concentrations of (in decreasing order of abundance) Se, Sb, Cu, Bi, Te, and Zn (~10^{0}-10^{1} ppm), and low concentrations of Ag, Sn, Mo, and W (~10^{-1} ppm) (Figs. 16 and 17). The lower Au domains in pyrite have corresponding high concentration of Ni and As (~10^{2}-10^{3} ppm), moderate Co, Cu, Se, Sb, Pb, and Zn (~10^{0}-10^{1} ppm), and low concentrations of Ag, Bi, Te, Mo, W, and Sn (~10^{-2}-10^{-1} ppm) (Figs. 16 and 17). Higher Au contents in pyrite at Maisie correlate to enrichment in As, Sb, Bi, Te, Se, and Pb (Figs. 16 and 17), and lower Cu, Zn, Sn, Ag and Mo.

2.4.4.1.2 – Lavoie pyrite

Pyrite from Lavoie has Au values ranging from 0.001 ppm to 55 ppm, there is corresponding relatively high concentrations of Ni and As (~10^{2}-10^{3} ppm), moderate concentrations of Pb, Se, Co, Cu, Bi, Te, and Sb (~10^{0}-10^{1} ppm), and low concentrations of Zn, W, Ag, Mo, and Sn (10^{-2}-10^{-1} ppm) (Figs. 16 and 17).

2.4.4.1.3 – Boland Brook Formation sedimentary pyrite

Boland Brook pyrite are hosted in thin-bedded pyritic black carbonaceous mudstone at the top of the Boland Brook Formation (Wilson et al., 2004). Investigation of some of these grains did not detect Au above detection limits (Table 5); however, relatively high concentrations of As, Ni, and Co (~10^{2} ppm), moderate concentrations of Pb, Cu, Se, Zn,

and Mo (~10^0-10^1 ppm), and low concentrations of Bi, Te, Sb, Ag, W, and Sn (~10^{-2}-10^{-1} ppm) were detected (Figs. 16 and 17).

In general, pyrite at Maisie and Lavoie is enriched in Au, Bi, Te, As, Ag, Sb, and Pb relative to the Boland Brook pyrite, whereas the Boland Brook pyrite is enriched in Co, Cu, Zn, Mo, and Sn compared to the pyrite from Maisie and Lavoie. Additionally, the Maisie pyrite is enriched in Ni, Se, and W compared to the Boland Brook and Lavoie. Pyrite at Maisie is enriched in Co, Cu, Zn, Se, Mo, Ag, Sn, Sb, and Pb relative to Lavoie pyrite, whereas Lavoie pyrite is not enriched in any metal relative to the Maisie pyrite.

2.4.4.2 – Pyrite compositional maps

The distribution of, and concentration relationships among, selected major, minor, and trace elements in two large grains of Q3-hosted pyrite from the Maisie vein (sample Men5-5c) is presented in false colour logarithmic concentration maps (Figs. 18 and 19) and scatter plots (Fig. 20) based on ~27,750 ablations extracted from line traverses. Warm colours (orange to red) represent high concentrations, whereas cool colours (blue to black) represent low concentrations in the maps (Figs. 18 and 19).

The maps show complex metal zonation patterns depicting three distinct metal associations involving at least 2 generations of pyrite. Early pyrite ("pyrite I", Fig. 19) shows co-enrichment in Cu, Sn, Ag, Zn, and has relatively low Au concentrations (< 1 ppm). A later generation of pyrite ("pyrite II", Fig. 19) overprints pyrite I with "island-mainland" and fracture-controlled replacement textures outlined by trace element distributions. Pyrite II shows co-enrichment in Te, As, Au, Pb, Sb, Se, Bi, and relatively high Au concentrations, up to ~ 80 ppm. Cobalt and Ni follow a separate (decoupled from all other elements) oscillatory zoning that does not follow the two main zones of high and

low Au (Table 5), though these are not shown in the LA-ICP-MS maps in Figures 18 and 19.

In Figure 20, pyrite I and II generations are discernable in plots of selected trace elements (Au vs. As, Bi, Sb, and Zn). Although positive correlations between Au and As, Bi, Sb are evident, the correlations are not linear, rather they show bimodal distributions comprising (together) the overall correlation and evolution from pyrite I to pyrite II for each x-y plot. Arsenic and Au show the strongest overall positive correlation when both pyrite generations are considered. There is no obvious correlation between Au and Zn (Fig. 20d).

2.4.5 – Stable (O, C, S) and radiogenic (Sr) isotope composition of vein minerals

Stable and radiogenic isotope data were obtained to shed light on fluid sources and hydrothermal processes related to vein formation.

2.4.5.1 – In-situ quartz-carbonate stable oxygen isotope results (SIMS)

SIMS oxygen isotope data for vein quartz and calcite are summarized in Table 6, and depicted graphically in Figure 21a. Data from Maisie were collected from laminated (Q1) quartz, massive quartz(-calcite) (Q2-C2), lattice-bladed quartz-calcite (Q3-C3), and vuggy quartz (Q3) in contact with gold. Data from Maisie are summarized below:

(i) *Early laminated quartz (Q1):* $\delta^{18}O_{V-SMOW}$ values range from 12.3 to 18.8 ‰ (avg. 15.0 ± 2.0 ‰; 1σ; n=14) (Fig. 21a); *Massive quartz (Q2):* $\delta^{18}O_{V-SMOW}$ values range from 12.8 to 19.0 ‰ (avg. 16.8 ± 1.1 ‰; 1σ; n=11) (Fig. 21a);

(ii) *Lattice-bladed quartz (Q3):* $\delta^{18}O_{V-SMOW}$ ranges from 18.4 to 24.9 ‰ (avg. 21.9 ± 1.9 ‰; 1σ; n=22) (Fig. 21a); and

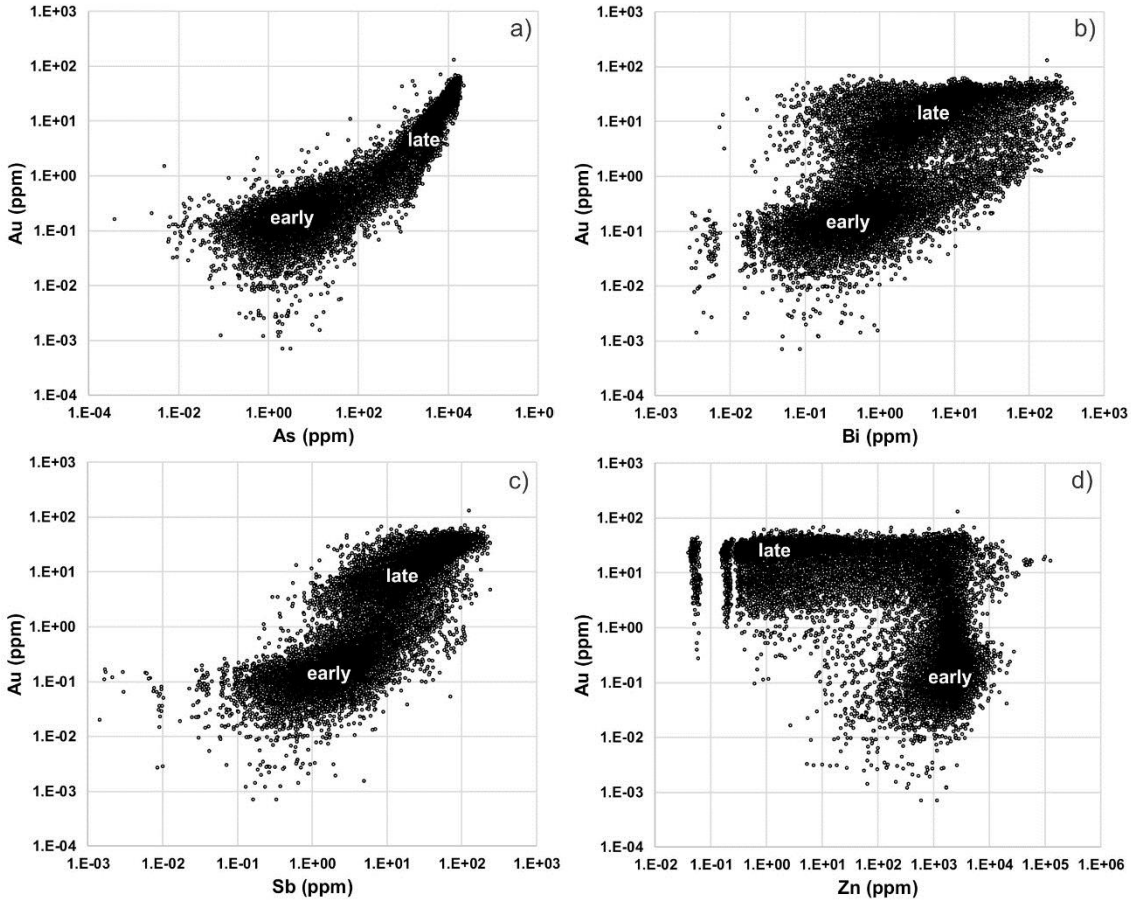

Figure 2.20 - Binary plots of selected trace elements (ppm) in pyrite from vein sample Men 5-5c (Maisie occurrence) created from the results of quantification of 27,750 LA-ICP-MS spectra from line scans obtained during mapping of a ~1.5 x ~2 mm grain. Compositional ranges for early and late pyrite generations are labelled. a) Au vs. As showing strong correlation between the two metals with an increase in the slope of the relationship at around ~ 1 ppm Au; b) and c) Au vs. Bi and Au vs. Sb, respectively showing early and late domains both having similar correlations between the metals but significantly higher Au, Bi and Sb contents in the late pyrite generation. d) Au vs. Zn showing no correlation between the metals. Low Zn concentrations are restricted only to domains with elevated Au.

Table 6 - SIMS O and S isotope data for quartz, calcite, vein sulfides, and host sedimentary pyrite

Quartz site	$\delta^{18}O_{VSMOW}$ (‰)	Calcite site	$\delta^{18}O_{VSMOW}$ (‰)	Quartz site	$\delta^{18}O_{VSMOW}$ (‰)	Calcite site	$\delta^{18}O_{VSMOW}$ (‰)	$\delta^{34}S_{(VCDT)}$ ‰					
Late bladed quartz-calcite intergrowths (syn-gold)(Q3 & C3)				**Early laminated (pre-gold)(Q1) and mid-stage massive quartz (pre-gold)(Q2)**				**St-Quentin**			**Menneval**		**Boland Brook**
Menneval				**Menneval**				*galena*	*sphalerite*	*pyrite*	*chalcopyrite*	*pyrite*	*pyrite*
BG-Men2-2				*Men-1*				2.2	1.0	7.2	2.1	-2.0	-15.6
1	21.7	2	17.3	1	14.4[L]	-	-	1.8	0.4	6.5	3.2	-1.1	-13.9
		2b	16.0	2	13.9[L]	-	-	2.4	3.3	7.6	3.2	1.3	-16.3
2	24.1	1	18.8	3	12.3[L]	-	-	2.6	2.3	8.5	2.6	2.7	-15.3
		2b	16.0	4	16.0[L]	-	-	2.9	1.1	6.1	3.4	2.1	-14.2
3	23.9	3	15.8	5	13.7[M]	-	-	4.3	3.1	6.0	2.9	1.3	-14.9
		6	16.7	6	12.8[M]	-	-	3.7	-0.8	8.7		1.5	-13.0
4	22.9	4	18.0	7	15.1[L]	-	-	4.0	0.2	7.2		1.5	-17.2
		4b	18.1	8	18.8[L]	-	-	2.9	-0.4	7.6		2.4	
5	23.6	5	18.8	9	16.8[L]	-	-	4.0	1.0	8.3		2.4	
6	22.5	7	19.4	10	12.7[L]	-	-	3.4	0.7	5.9		2.8	
		7b	18.8	11	14.6[L]	-	-	3.0	2.8	5.4		3.3	
7	22.9	8	20.0	12	15.9[L]	-	-	3.5	0.7	6.7		2.2	
		8b	17.3	13	18.7[L]	-	-	3.9	0.9	5.0		3.4	
		8c	16.5	14	14.8[L]	-	-	3.4	1.5	6.0		1.8	
8	20.3	9b	15.7	15	17.0[M]	-	-	3.3	0.5	8.7		2.7	
		9c	17.0	16	18.1[M]	-	-		2.1	8.8		2.7	
9	21.6	10b	20.0	17	15.8[M]	-	-		1.2	5.6		3.5	
		10c	18.4	18	16.3[M]	-	-		-0.1	5.4		2.4	
AMen10-2				19	16.5[M]	-	-		3.2	6.7		2.5	
2	20.4	1	20.0	20	16.7[M]	-	-		2.7	8.0		3.1	
3	24.4	2	17.4	21	17.7[M]	-	-			6.1		1.3	
4	23.7	3	17.1	22	19.0[M]	-	-					1.6	
5	19.9	4	18.5	23	14.9[M]	-	-					1.4	
7	20.2	5	15.1	24	17.6[M]	-	-					2.0	
8	20.3	6	16.2	25	15.6[M]	-	-					1.4	
		7	15.1									1.9	
Men47-6b												2.1	
1	18.4	1	23.3	**Vuggy quartz at gold grain boundaries (syn-gold)(Q3)**								2.4	
		2	21.1									3.0	
2	22.3	3	18.4	**Menneval**								2.0	
3	20.5	4	22.6	*Men-2*								2.0[U]	
4	24.9	5	18.3	1	18.5	-	-					2.2[U]	
5	24.5	8	22.6	2	20.0	-	-					3.0[U]	
6	19.3	9	24.4	3	19.8	-	-					2.8[U]	
8	19.3	7	24.8	4	18.0	-	-					2.7[U]	
St-Quentin				5	17.9	-	-					2.6[U]	
NW2c-2				6	19.2	-	-					2.4[U]	
1	18.6	1	18.0	7	18.5	-	-					2.9[U]	
2	18.8	1	18.0	8	20.1	-	-					2.6[U]	
3	18.9	2	18.3	9	18.7	-	-					0.9[L]	
4	18.3	3	16.4	10	18.6	-	-					1.3[L]	
5	20.3	4	17.3	11	20.4	-	-					1.6[L]	
6	17.9	5	18.0	12	18.6	-	-					1.4[L]	
7	18.9	6	18.5	13	19.0	-	-					1.3[L]	
11	19.4	7	19.9	14	18.0	-	-					1.5[L]	
												1.6[L]	
												1.5[L]	

L=laminated, M=massive; A#=analysis number; H=High Au from Men5-5c; L=Low Au from Men5-5c

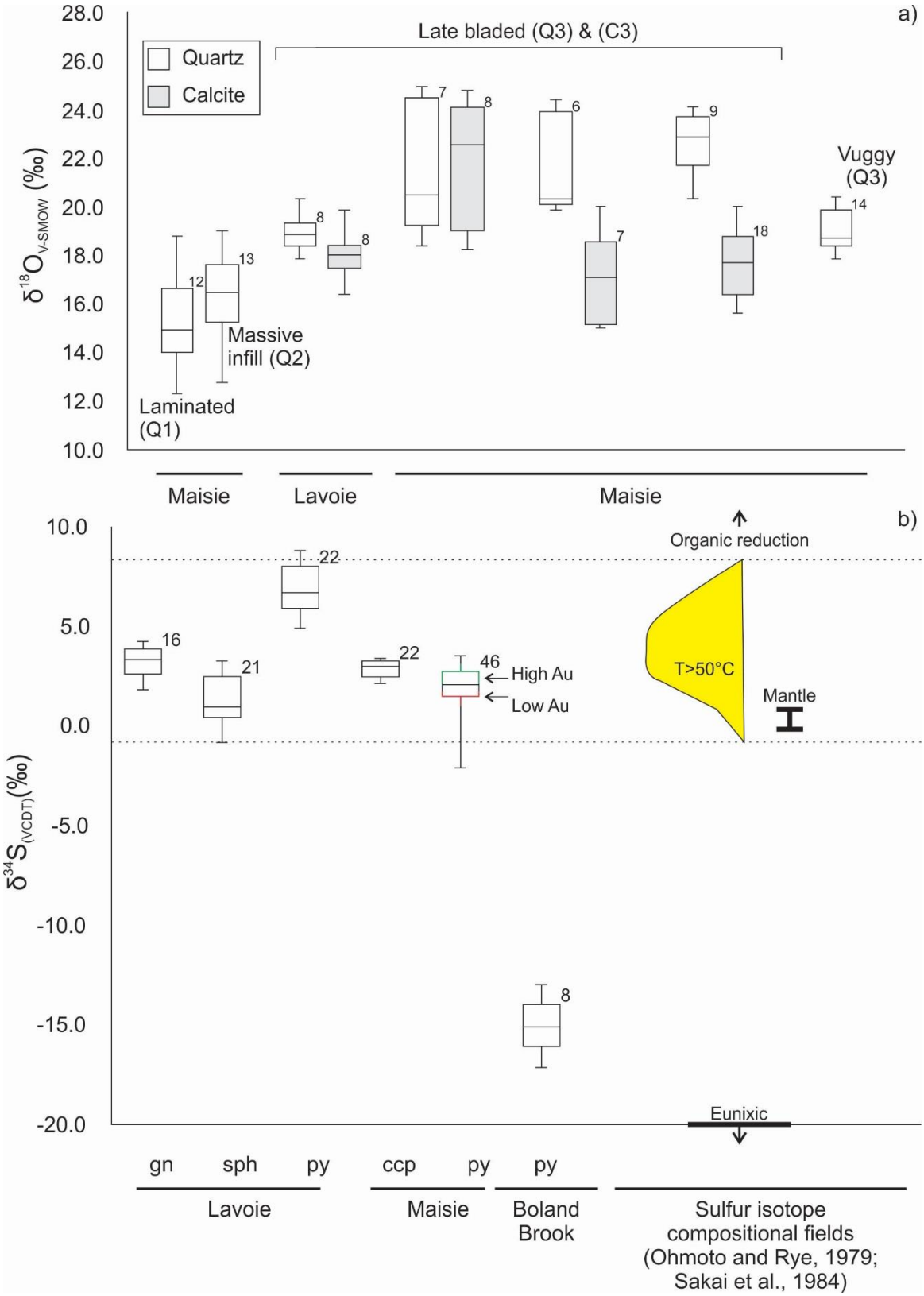
a)
Late bladed (Q3) & (C3)
Quartz
Calcite
$\delta^{18}O_{V\text{-}SMOW}$ (‰)
28.0
26.0
24.0
22.0
20.0
18.0
16.0
14.0
12.0
10.0
Laminated (Q1)
Massive infill (Q2)
Vuggy (Q3)
Maisie
Lavoie
Maisie
b)
Organic reduction
T>50°C
Mantle
High Au
Low Au
$\delta^{34}S_{(VCDT)}$ (‰)
10.0
5.0
0.0
-5.0
-10.0
-15.0
-20.0
Eunixic
gn
sph
py
ccp
py
py
Lavoie
Maisie
Boland Brook
Sulfur isotope compositional fields (Ohmoto and Rye, 1979; Sakai et al., 1984)

Figure 2.21 previous page – Box-whisker diagrams summarizing SIMS data for vein quartz, calcite, and sulfides from the Maisie and Lavoie showings. a) Box-whisker diagram for quartz and calcite oxygen isotopes from the Maisie and Lavoie Au showings. Samples are from lattice-bladed quartz (Q3) and calcite (C3) pairs, a brecciated quartz clast (laminated Q1) hosted within massive quartz (Q2), and vuggy quartz (Q3) in contact with gold grains. b) Box-whisker diagram for S isotope data from Maisie and Lavoie sulfides, including S isotope data for pyrite from the Boland Brook Formation. The yellow field is the range in $\delta^{34}S_{VCDT}$ sourcing S from the decomposition of organics with compounds. Euxinic environments, open to SO_4^{-2}, and closed to H_2S, plot below the vertical axis lower limit, with $\delta^{34}S_{VCDT}$ ranging from -20 to -40 ‰, whereas the organic reduction field plot above the vertical axis upper limits, with $\delta^{34}S_{VCDT}$ ranging from ~ +15 to 25 ‰ in hydrothermal sulfides. $\delta^{34}S$ compositional fields from Ohmoto and Rye (1979), and mantle $\delta^{34}S$ from Sakai et al. (1984).

(iii) *Lattice-bladed calcite (C3):* $\delta^{18}O_{V-SMOW}$ ranges from 15.1 to 24.8 ‰ (avg. 18.6 ± 2.5 ‰; 1σ; n=33) (Fig. 21a).

(iv) *Vuggy quartz sharing gold grain boundaries (Q3):* $\delta^{18}O_{V-SMOW}$ values range from 17.9 to 20.4 ‰ (avg. 19.0 ± 0.8 ‰; 1σ; n=14) (Fig. 21a);

Data from the Lavoie showing are as follows:

(i) *Lattice-bladed quartz (Q3):* $\delta^{18}O_{V-SMOW}$ ranges from 17.9 to 20.3 ‰ (avg. 18.9 ± 0.7 ‰; 1σ; n=8) (Fig. 21a); and

(ii) *Lattice-bladed calcite (C3):* $\delta^{18}O_{V-SMOW}$ ranges from 16.4 to 19.9 ‰ (avg. 18.0 ± 0.9 ‰; 1σ; n=8) (Fig. 21a).

The values of $\delta^{18}O_{V-SMOW}$ in quartz and calcite show that these minerals are strongly enriched in ^{18}O. Overall, the range in $\delta^{18}O_{V-SMOW}$ shifts slightly to higher values from Q1/Q2 (~12 to 19 ‰) to Q3 (~18 to 25 ‰). Q3 calcite mirrors the higher $\delta^{18}O_{V-SMOW}$ seen in Q3 at both locations (~15 to 25 ‰).

2.4.5.2 – Sulfur isotopes

SIMS data ($\delta^{34}S_{VCDT}$) are tabulated in Table 6 and represented graphically in Figure 21b. Data were collected from vein-hosted sulfides to compare the Maisie and Lavoie Au showings, specifically with respect to possible fluid and S sources related to mineralization. Data from the underlying Boland Brook Formation (diagenetic pyrite in black shale layers) was obtained as well, in order to evaluate potential links between sedimentary host rock S and vein sulfides.

The data are summarized below:

(i) *Maisie Au* chalcopyrite $\delta^{34}S_{VCDT}$ values ranges from 2.1 to 3.4 ‰ (avg. 2.9 ± 0.4 ‰; 1σ; n=6) (Fig. 21b); and pyrite $\delta^{34}S_{VCDT}$ values ranges from -2.0 to 3.5 ‰ (avg. 2.0 ± 1.0 ‰; 1σ; n=48) (Fig. 21b).

(ii) *Lavoie Au* galena $\delta^{34}S_{VCDT}$ ranges from 1.8 to 4.3 ‰ (avg. 3.2 ± 0.7 ‰; 1σ; n=16) (Fig. 21b); sphalerite $\delta^{34}S_{VCDT}$ values ranges from -0.8 to 3.3 ‰ (avg. 1.3 ± 1.2 ‰; 1σ; n=21) (Fig. 21b); and pyrite $\delta^{34}S_{VCDT}$ values ranges from 5.0 to 8.8 ‰ (avg. 6.9 ± 1.2 ‰; 1σ; n=22) (Fig. 21b).

(iii) *Boland Brook Formation* pyrite $\delta^{34}S_{VCDT}$ ranges from -17.2 to -13.0 ‰ (avg. -15.0 ± 1.3 ‰; 1σ; n=8) (Fig. 21b).

Overall, sulfides at Maisie and Lavoie have similar ranges in $\delta^{34}S_{VCDT}$ values (~ -2 to 9 ‰). Sulfides from the Boland Brook Formation, in comparison, are far more depleted in ^{34}S (~ -17 to -13 ‰).

Additionally, domains of pyrite I and II recognized in earlier LA-ICP-MS mapping (Figs. 18 and 19) were analysed for $\delta^{34}S_{VCDT}$ to discern any isotopic difference between low and high Au pyrite. Pyrite I has $\delta^{34}S_{VCDT}$ values ranging from 0.9 to 1.6‰ (avg.=1.4 ± 0.2‰; n=8), whereas pyrite II (more Au rich) has $\delta^{34}S_{VCDT}$ values slightly higher, ranging from 2.0 to 3.0‰ (avg.=2.6 ± 0.3‰; n=9).

2.4.5.3 – Bulk carbonate strontium, oxygen, and carbon isotope results

Complimentary (bulk) O and C isotope data, and $^{87}Sr/^{86}Sr_o$ data of vein calcite (C2-C3) are graphically summarized in Figure 22, and listed in Table 7. Values of $\delta^{13}C_{V\text{-}PDB}$ for Maisie vein C2 and C3 range from -8.3 to -6.5 ‰ (avg. -7.2 ± 0.8 ‰; 1σ; n=3), whereas for Lavoie the values range from -6.1 to -5.8 ‰ (avg. -6.0 ± 0.1 ‰; 1σ; n=2). Values of $\delta^{18}O_{V\text{-}SMOW}$ at Maisie range from 14.3 to 15.3 ‰ (avg. 15.0 ± 0.5 ‰; 1σ; n=3), whereas for

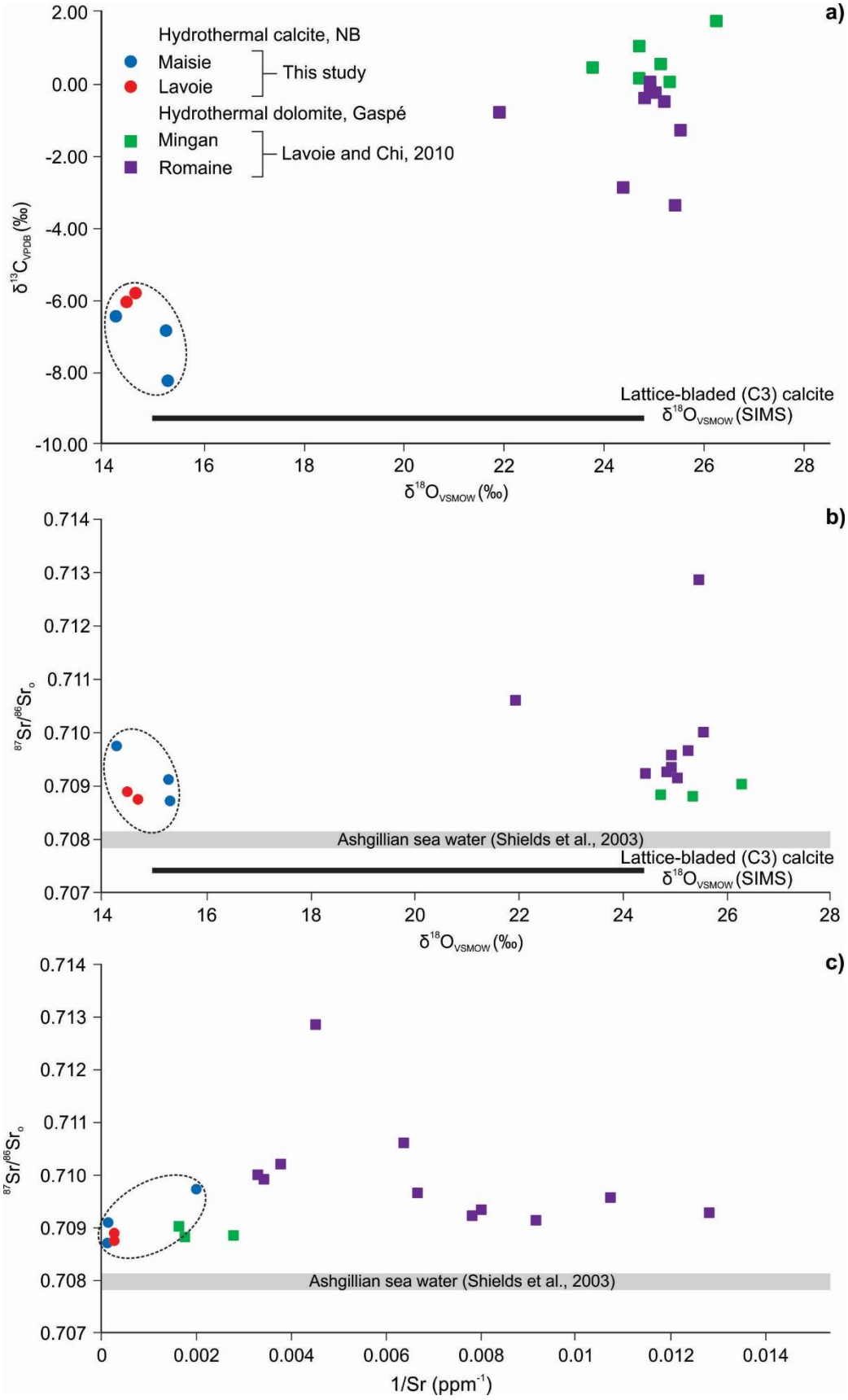
a)
Hydrothermal calcite, NB
Maisie
Lavoie
This study
Hydrothermal dolomite, Gaspé
Mingan
Romaine
Lavoie and Chi, 2010
Lattice-bladed (C3) calcite
δ18OVSMOW (SIMS)
δ13CVPDB (‰)
δ18OVSMOW (‰)
b)
Ashgillian sea water (Shields et al., 2003)
Lattice-bladed (C3) calcite
δ18OVSMOW (SIMS)
87Sr/86Sro
δ18OVSMOW (‰)
c)
Ashgillian sea water (Shields et al., 2003)
87Sr/86Sro
1/Sr (ppm-1)

Figure 2.22 previous page – Plots comparing stable C and O isotope composition, and Sr isotope compositions among hydrothermal calcite samples at Maisie, Lavoie, and regional hydrothermal dolomite samples from the Gaspé Belt (Lavoie and Chi, 2010). Ashgillian sea water (Shields et al., 2003) plotted to compare average sea water $^{87}Sr/^{86}Sr_o$ composition to vein calcite compositions. Lattice-bladed calcite (C3) SIMS values for $\delta^{18}O_{V\text{-}SMOW}$ plotted in comparison to bulk calcite values of C2. a) $\delta^{13}C_{VPDB}$ versus $\delta^{18}O_{V\text{-}SMOW}$ discrimination diagram. b) $\delta^{18}O$ versus $^{87}Sr/^{86}Sr_o$ discrimination diagram. c) $^{87}Sr/^{86}Sr_o$ versus Sr^{-1} discrimination diagram.

Table 7 - Radiogenic strontium, stable oxygen and carbon isotope data for bladed calcite

Sample	$^{87}Sr/^{86}Sr_o$	StdErr (Abs)	$\delta^{18}O$ (‰)	$\delta^{13}C$ (‰)	Rb (ppm)	Sr (ppm)	1/Sr (ppm^{-1})
BG Men 2	0.708720	0.000012	15.32	-8.28	0.181	8179.62	0.000122
Men 5	0.709735	0.000010	14.28	-6.49	0.127	503.83	0.001985
Men 43	0.709112	0.000016	15.29	-6.86	0.132	7799.73	0.000128
NW 2a	0.708761	0.000025	14.68	-5.84	0.168	3631.37	0.000275
NW 2b	0.708902	0.000009	14.49	-6.09	0.144	4078.29	0.000245

Note - Rb and Sr (ppm) were determined by LA-ICP-MS as part of O-C-Sr isotope analytical package.

Lavoie the values range from 14.5 to 14.7 ‰ (avg. 14.6 ± 0.1 ‰; 1σ; n=2). Ratios of $^{87}Sr/^{86}Sr_o$ range from 0.708720 to 0.709735 (± 0.000013; 1σ; n=3), whereas for Lavoie the values range from 0.708610 to 0.708902 (± 0.000017; 1σ; n=2).

The calcite data are compared with data for Ordovician marine (dolomitized) carbonates hosted in siltstone/mudstone overlaying Grenvillian basement in the Gaspé Belt (Lavoie and Chi, 2010) providing a comparison to similarly hydrothermally modified marine sedimentary rocks of the same age as the carbonaceous turbidites of the Grog Brook Group. No data for carbonates in the Grog Brook Group could be obtained owing to the fine grain size (<20 μm) which precludes SIMS analysis.

2.4.6 – Zircon geochronology and REE geochemistry

Zircon was identified in wall rocks (sedimentary rocks and porphyry intrusion), and wall rock laminae within auriferous veins as the only mineral suitable for quantitative geochronology. Zircon was picked from heavy mineral fractionation from laminated vein quartz (Q1; as an inherited phase), and porphyry rock at the Maisie occurrence. The purpose of this work was to (i) characterize the REE chemistry of recovered zircons in order to constrain their origin, and (ii) constrain the maximum age of vein formation, from zircon recovered from the vein. Zircon provenance will be used to determine the relationship, if any, to local magmatic activity during the geologic history of the region, which has been shown to correlate with Au mineralization (McCutcheon & Bevier, 1990).

Rare-earth element (REE)-Y data for zircon from the Maisie Au occurrence (vein and porphyry hosted) is presented in Table 8 and in a normative abundance diagram (Fig. 23). CA-ID-TIMS data for zircon samples is listed in Table 9 and plotted on a concordia diagram (Fig. 24). Three different zircon types were identified in this study:

Table 8 - LA-ICP-MS REE composition of inherited zircon from the Maisie occurrence

Sample	Y	La	Ce	Pr	Nd	Sm	Eu	Gd	Tb	Dy	Ho	Er	Tm	Yb	Lu
MEN-1															
1	2495.8	<0.003	2.3	0.1	1.4	5.3	0.1	40.6	17.9	241.8	90.5	436.0	87.7	765.4	138.7
2	1807.7	<0.003	1.8	0.1	1.5	4.3	0.1	33.2	13.7	182.0	67.2	325.3	67.1	600.7	109.2
3	2027.7	0.0	1.6	0.1	1.4	4.8	0.1	36.6	15.3	206.4	73.3	347.3	69.6	608.0	107.7
4	2201.7	0.0	1.6	0.1	1.9	5.1	0.1	40.0	16.5	224.3	82.3	394.9	80.4	710.8	125.9
5	1991.4	0.0	2.1	0.1	1.5	5.3	0.1	37.7	15.8	209.3	72.1	330.1	65.2	562.9	99.4
6	2759.0	0.0	1.2	0.1	1.7	5.8	0.1	47.3	21.0	283.0	99.8	471.9	93.2	798.9	142.3
7	1847.3	0.0	1.7	0.1	1.2	4.2	0.1	33.3	14.2	188.1	66.4	301.3	59.2	503.8	89.8
8	1954.7	<0.01	2.5	0.1	1.5	5.1	0.1	38.5	16.2	207.0	69.4	304.1	58.8	508.2	89.8
9	2667.9	<0.003	2.4	0.1	1.9	6.0	0.1	46.0	19.6	267.3	96.6	460.8	92.7	807.2	143.4
10	2008.4	<0.01	2.1	0.1	1.7	5.3	0.1	37.9	15.5	204.8	73.6	343.6	69.8	604.1	108.1
11	1689.2	0.1	4.5	0.2	2.6	7.0	0.1	41.6	14.7	181.4	64.3	298.6	60.0	537.9	96.2
12	1921.1	<0.01	1.4	0.0	1.2	4.6	0.1	34.3	14.3	192.2	71.1	346.1	70.3	627.6	113.3
MEN2															
1	1566.5	33.8	223.6	48.2	323.2	127.0	26.4	118.5	20.0	170.8	52.4	218.2	40.0	328.7	57.2
2	872.8	3.6	23.4	3.3	20.0	8.7	2.2	22.1	6.7	84.9	31.0	150.3	31.5	271.7	51.2
3	1398.8	23.3	60.8	8.3	46.1	31.2	4.6	68.9	16.2	156.4	50.7	234.0	46.7	429.9	84.8
4	1433.2	14.6	44.8	5.1	29.9	23.2	3.2	60.7	15.3	156.2	52.6	240.4	48.2	432.5	86.3
5	527.6	16.2	71.4	10.0	46.5	13.7	8.3	22.6	5.9	58.1	18.1	80.5	16.3	148.4	29.4
6	552.2	23.3	86.5	12.1	53.0	12.8	8.0	21.0	5.5	55.5	18.5	88.2	18.3	170.6	34.2
7	1299.9	3.2	32.8	4.4	32.0	17.5	3.7	51.8	14.4	159.2	55.0	251.2	49.2	435.2	82.8
8	1062.0	2.6	29.5	4.2	34.6	18.0	4.7	44.0	12.0	130.3	45.1	204.1	40.3	357.9	66.9
9	756.1	2.4	20.6	1.3	8.6	4.7	1.0	16.7	5.7	74.8	29.8	151.0	32.6	317.4	64.8
10	1088.1	0.5	26.2	0.2	2.3	3.8	1.7	22.3	7.9	107.7	43.7	233.9	56.0	591.8	118.1
11	552.0	4.4	54.6	5.2	38.1	20.4	6.2	33.9	6.7	64.6	20.6	102.4	23.5	250.7	51.3
12	630.7	0.0	6.4	0.1	2.3	3.9	1.3	18.6	5.8	70.3	26.0	128.0	28.6	288.4	57.0
13	885.0	<0.006	9.4	0.1	1.8	2.9	1.1	17.0	6.0	83.5	34.0	179.6	41.5	407.3	84.7
14	438.5	9.5	101.6	12.8	119.2	36.9	7.5	32.7	5.2	46.3	15.3	74.4	17.1	183.0	40.5
15	668.8	23.0	208.1	31.6	275.1	83.7	17.7	70.3	10.1	80.0	23.8	107.4	23.3	238.3	51.4
16	193.6	1.9	17.5	3.5	27.5	18.4	4.3	25.2	3.3	24.3	7.0	33.7	8.0	95.0	23.5
17	753.2	0.4	29.7	0.6	7.9	9.7	2.0	34.9	9.1	96.1	32.3	145.2	29.7	277.9	50.4
18	837.3	0.6	32.3	0.9	9.5	11.6	2.2	39.2	10.5	108.8	36.5	162.5	33.1	305.4	54.5
19	1205.2	0.2	10.6	0.4	3.0	4.2	1.0	27.3	9.6	127.0	50.1	256.2	55.9	548.8	107.3
20	1227.7	0.0	9.4	0.1	1.4	3.0	0.7	22.0	8.2	115.4	48.9	263.1	60.5	597.8	119.1
21	1445.2	48.8	444.2	53.9	226.4	50.7	10.4	90.8	21.5	199.1	58.5	244.9	46.5	406.0	69.7
22	2040.7	109.9	928.6	135.4	615.1	169.0	34.1	208.1	39.3	309.7	76.6	289.1	53.1	453.2	75.8
23	1083.3	0.4	20.9	1.0	9.5	10.2	1.4	38.8	11.7	135.3	46.0	209.1	42.3	372.9	65.8
24	801.0	9.1	59.9	9.3	71.4	41.6	3.8	67.8	12.1	108.3	33.2	149.5	30.3	279.2	49.0

Table 8 - LA-ICP-MS REE composition of inherited zircon from the Maisie occurrence

Sample	Y	La	Ce	Pr	Nd	Sm	Eu	Gd	Tb	Dy	Ho	Er	Tm	Yb	Lu
MEN-19a															
1	1637.9	0.0	17.4	0.2	3.0	5.8	3.0	33.9	13.2	166.3	58.2	262.9	71.0	807.2	88.6
2	2736.8	0.0	41.7	0.4	7.5	21.5	7.7	88.2	30.0	324.6	100.8	414.3	100.9	1100.9	112.6
3	3365.6	0.0	51.8	0.6	11.2	26.6	9.3	104.7	35.9	400.2	125.4	470.8	118.7	1309.2	128.5
4	791.9	0.0	9.1	0.1	1.4	3.7	1.7	18.2	6.5	83.8	29.3	121.2	31.0	366.7	39.7
5	2120.3	0.0	24.0	0.1	3.5	8.7	4.0	43.6	16.9	209.1	75.2	317.6	86.6	965.4	107.4
6	4539.0	0.1	49.8	0.8	16.1	27.5	10.9	113.1	38.7	474.8	163.5	672.5	173.5	1995.0	205.4
7	7133.7	0.2	67.6	2.6	47.1	70.7	25.2	245.3	76.0	809.3	263.3	1039.9	234.7	2237.4	307.5
8	3219.6	0.0	27.9	0.2	5.1	13.6	5.3	66.6	24.8	304.0	111.3	475.5	119.0	1250.1	163.3
9	7579.1	0.0	79.1	0.8	15.6	38.3	15.9	160.6	62.2	738.5	249.9	1030.8	255.5	2716.3	278.9
10	4826.5	0.1	42.1	1.0	20.2	36.3	12.0	139.7	45.8	518.4	173.4	705.6	168.7	1648.3	217.6
11	1554.5	0.0	12.9	0.0	1.6	6.1	2.0	29.4	11.0	145.1	54.1	228.5	55.2	570.4	84.2
12	951.4	0.0	8.2	0.0	1.1	3.4	1.2	19.2	7.0	87.8	32.2	141.3	35.5	350.7	53.5
13	3703.9	0.0	38.9	0.3	8.7	18.4	7.4	86.0	29.1	383.0	132.9	576.0	150.4	1689.1	184.2
14	7724.6	0.1	86.2	0.8	18.7	39.9	16.3	169.4	61.1	749.6	254.2	1065.7	261.4	2815.0	297.3
15	3707.4	0.0	57.3	0.3	7.9	21.8	7.5	94.3	34.5	409.3	130.9	519.3	125.5	1369.2	144.7
16	6827.0	0.0	73.3	0.6	13.8	34.0	12.6	143.6	54.3	638.6	221.5	940.8	240.5	2608.6	259.3
17	8492.8	0.0	118.0	0.8	18.6	47.6	16.3	192.8	69.5	800.4	265.1	1041.6	253.3	2615.2	265.8
18	19148.3	0.4	253.9	4.3	96.3	188.8	51.9	752.5	229.5	2290.0	647.1	2224.4	428.7	3660.8	445.1
19	2641.1	0.0	26.4	0.2	4.9	13.9	5.6	61.5	23.3	279.2	98.5	413.6	105.1	1174.0	120.6
20	6059.4	0.2	53.3	0.5	11.6	28.1	10.2	128.3	49.8	597.7	208.5	899.5	217.8	2168.7	285.4
21	3466.6	0.0	38.2	1.2	24.6	40.2	14.2	125.1	37.9	415.1	129.9	536.1	130.3	1391.7	144.9
22	5175.3	0.5	46.3	0.5	13.1	28.6	10.8	131.4	47.2	540.4	188.8	773.8	181.6	1767.0	240.8
23	7040.6	0.0	64.5	0.7	15.3	34.9	13.9	181.1	60.9	725.7	254.6	1062.7	246.5	2334.6	320.2
24	7912.8	0.0	82.3	0.8	16.0	38.4	16.5	180.4	62.5	765.6	249.6	1032.2	259.3	2716.0	288.5
25	9188.3	0.1	122.3	1.0	19.9	47.8	17.0	202.5	72.2	834.9	284.4	1119.1	273.0	2807.9	291.6
26	7997.5	0.1	86.4	0.7	17.2	40.2	14.7	166.0	62.0	743.7	253.8	1051.4	268.5	2920.9	292.0
27	8933.2	0.1	80.1	0.9	17.2	44.3	15.3	209.0	71.1	865.8	292.3	1198.8	278.5	2652.6	337.2
28	5292.4	0.3	52.8	2.1	41.9	62.4	23.2	209.0	62.5	670.7	200.1	774.4	175.5	1697.7	212.5
29	8900.5	0.1	94.1	1.1	20.5	47.7	19.4	202.7	72.6	871.9	285.1	1143.0	276.3	2842.0	302.7
30	7559.1	0.2	104.8	0.8	15.5	36.6	14.2	174.1	61.1	729.6	244.5	963.3	231.1	2431.4	260.6
31	7489.7	0.1	69.3	0.7	15.4	40.5	14.7	177.1	64.9	773.3	258.8	1087.9	253.7	2474.2	328.1
32	23418.8	0.3	320.2	4.4	96.3	198.6	63.6	856.7	258.7	2622.8	776.8	2762.2	546.3	4660.7	591.2
33	23320.0	0.4	313.6	4.0	91.6	199.9	64.4	816.8	257.6	2594.4	771.0	2674.6	527.8	4478.3	570.2
34	24011.0	0.1	427.2	3.2	75.5	179.4	59.4	857.0	280.4	2825.6	830.0	2766.2	549.4	4645.3	523.5
35	4871.0	0.0	34.0	0.3	8.1	22.9	9.4	117.3	41.4	495.8	175.4	728.1	171.7	1702.2	221.5
36	24085.4	0.1	425.9	3.2	76.2	182.4	56.1	836.1	275.9	2861.4	823.0	2779.9	551.5	4713.1	530.3
37	9948.3	0.1	142.6	1.2	22.6	54.1	20.2	242.2	83.8	955.2	313.0	1199.5	283.3	2879.4	294.0
38	16837.1	0.2	218.5	3.3	73.5	161.7	45.5	646.3	199.4	1971.5	562.3	1942.9	379.5	3164.9	402.1
39	3876.9	0.0	26.4	0.2	8.4	16.8	7.3	86.5	32.8	387.4	138.7	582.5	142.4	1425.8	194.9
40	9309.0	0.2	84.4	1.0	20.3	44.9	17.0	220.0	76.1	905.1	298.5	1227.7	276.0	2663.0	337.8

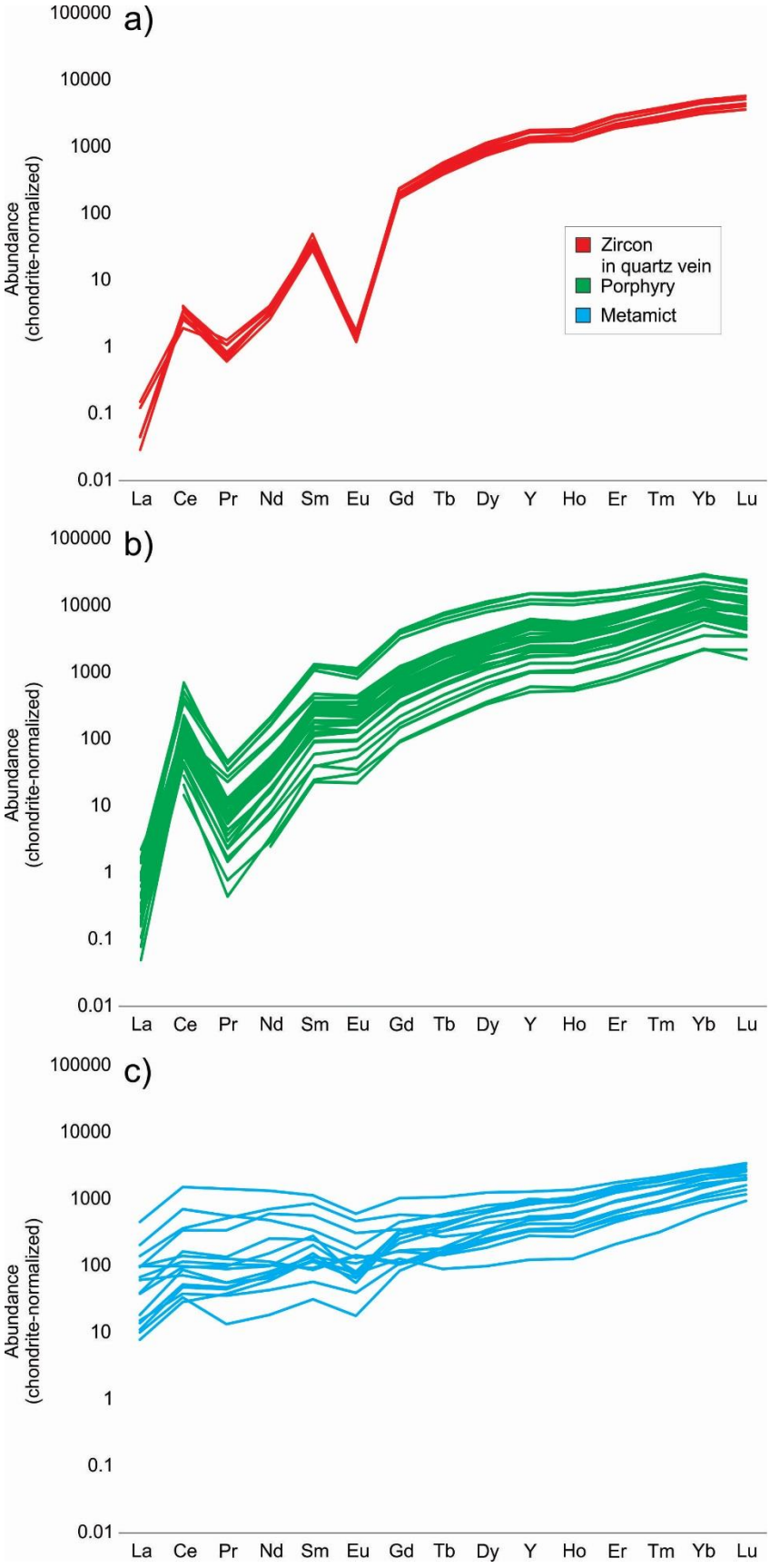
a)
b)
c)
Abundance
(chondrite-normalized)
100000
10000
1000
100
10
1
0.1
0.01
La Ce Pr Nd Sm Eu Gd Tb Dy Y Ho Er Tm Yb Lu
Zircon
in quartz vein
Porphyry
Metamict

Figure 2.23 previous page – REE-Y normative abundance patterns of zircon from the Maisie Au occurrence, chondrite normalized (McDonough and Sun, 1995). a) Zircon from heavy mineral separates recovered from a mineralized, laminated, massive Q1-Q2 vein. b) Zircon inclusion from heavy mineral separates collected from the porphyry dike adjacent to the vein. c) Metamict zircon from heavy mineral separates recovered from massive, vuggy Q2-Q3 vein.

Table 9 - U-Pb isotopic data for zircons

							Radiogenic Isotope Ratios								Isotopic Dates					
Sample	Th/U	$^{206}Pb^*$ x10^{13} mol	mol % $^{206}Pb^*$	Pb^*/Pb_c	Pb_c (pg)	$^{206}Pb/^{204}Pb$	$^{208}Pb/^{206}Pb$	$^{207}Pb/^{206}Pb$	% err	$^{207}Pb/^{235}U$	% err	$^{206}Pb/^{238}U$	% err	corr. coef.	$^{207}Pb/^{206}Pb$	±	$^{207}Pb/^{235}U$	±	$^{206}Pb/^{238}U$	±
(a)	(b)	(c)	(c)	(c)	(c)	(d)	(e)	(e)	(f)	(e)	(f)	(e)	(f)		(g)	(f)	(g)	(f)	(g)	(f)
MEN-1																				
z1a	0.323	2.5167	99.59%	69	0.87	4358	0.102	0.053962	0.125	0.439404	0.187	0.059084	0.092	0.806	368.45	2.82	369.83	0.58	370.05	0.33
z1b	0.386	2.9372	99.92%	366	0.19	22628	0.121	0.054004	0.068	0.439701	0.132	0.059078	0.070	0.957	370.18	1.54	370.04	0.41	370.02	0.25
MEN19a																				
z1	0.868	5.1774	99.96%	791	0.18	43133	0.274	0.053943	0.069	0.435820	0.131	0.058622	0.070	0.948	367.67	1.55	367.30	0.40	367.24	0.25
z2	0.762	5.2275	99.96%	889	0.16	49760	0.240	0.053925	0.067	0.435622	0.130	0.058615	0.070	0.950	366.92	1.51	367.16	0.40	367.20	0.25
z3	0.807	3.6226	99.95%	632	0.15	34984	0.254	0.053916	0.069	0.435437	0.132	0.058600	0.069	0.954	366.54	1.56	367.03	0.41	367.11	0.25
z4	0.848	3.3944	99.93%	465	0.20	25469	0.267	0.053959	0.077	0.435729	0.137	0.058593	0.072	0.921	368.34	1.73	367.24	0.42	367.06	0.26
z5	1.096	5.9076	99.96%	922	0.19	47696	0.345	0.053958	0.067	0.437051	0.130	0.058772	0.071	0.951	368.28	1.50	368.17	0.40	368.15	0.25
z6	1.049	3.9546	99.94%	606	0.19	31686	0.331	0.053956	0.075	0.435599	0.136	0.058578	0.072	0.921	368.22	1.70	367.14	0.42	366.97	0.26

(a) z1, z2, etc. are labels for analyses composed of single zircon grains that were annealed and chemically abraded (Mattinson, 2005). Labels in bold denote analyses used in weighted mean calculations.

(b) Model Th/U ratio calculated from radiogenic 208Pb/206Pb ratio and 207Pb/235U date.

(c) Pb* and Pbc are radiogenic and common Pb, respectively. mol % $^{206}Pb^*$ is with respect to radiogenic and blank Pb.

(d) Measured ratio corrected for spike and fractionation only. Fractionation correction is 0.16 ± 0.03 (1 sigma) %/amu (atomic mass unit) for single-collector Daly analyses, based on analysis of EARTHTIME 202Pb-205Pb tracer solution.

(e) Corrected for fractionation and spike. Common Pb in zircon analyses is assigned to procedural blank with composition of 206Pb/204Pb = 18.04 ± 0.61%; 207Pb/204Pb = 15.54 ± 0.52%; 208Pb/204Pb = 37.69 ± 0.63% (1 sigma). 206Pb/238U and 207Pb/206Pb ratios corrected for initial disequilibrium in 230Th/238U using a D(Th/U) of 0.20 ± 0.05 (1 sigma).

(f) Errors are 2 sigma, propagated using algorithms of Schmitz and Schoene (2007) and Crowley et al. (2007).

(g) Calculations based on the decay constants of Jaffey et al. (1971). 206Pb/238U and 207Pb/206Pb dates corrected for initial disequilibrium in 230Th/238U using a D(Th/U) of 0.20 ± 0.05 (1 sigma).

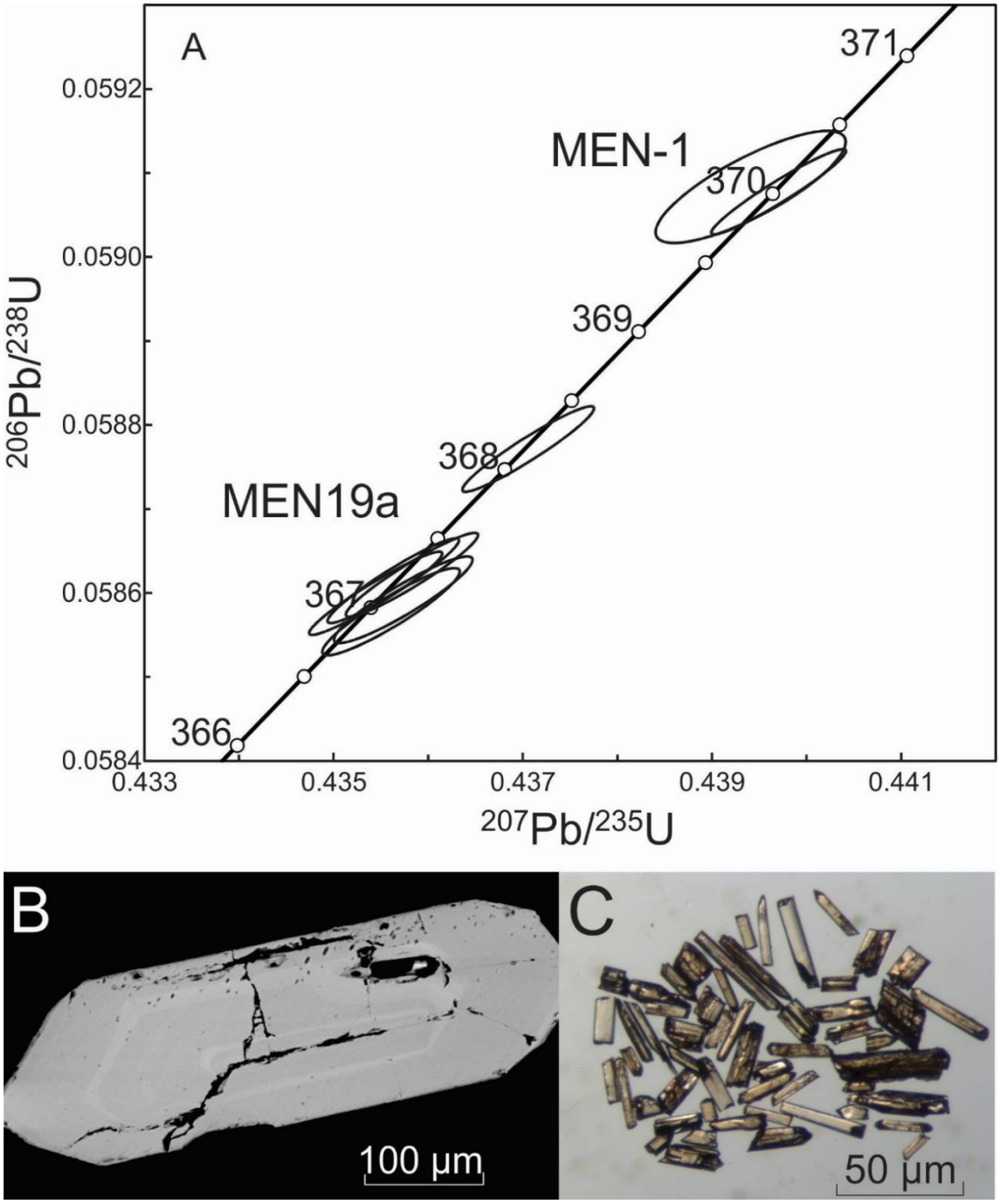

Figure 2.24 – U-Pb zircon geochronology of the Maisie Au veins. A) U-Pb concordia plot of dates from single grains of zircon, Plotted with Isoplot 3.0 (Ludwig, 2003). Error ellipses are at 2 sigma. B) vein-hosted sample Men-1. C) Men19a porphyry dike zircons.

(i) A large (~ 300 µm), euhedral zircon grain was recovered from a laminated auriferous vein sample (MEN-1). Rare earth element (REE)-Y data for this zircon (Table 8) indicate LREE << HREE, and pronounced negative Eu, Pr, and La anomalies, and elevated Sm_N/La_N and Ce/Ce^* values (Fig. 23a). These characteristics collectively are diagnostic of magmatic zircon (Zhong et al., 2018; Roberts et al., 2018). The zircon was broken into three fragments, the two smallest of which yielded a weighted mean age of 370.03 ± 0.20 / 0.23 / 0.45 Ma (MSWD = 0.03, probability of fit = 0.87; Fig. 24). The age is interpreted to be the age of crystallization.

(ii) Six zircon grains, ~ 25 to 50 µm in length, from heavy mineral separates of a porphyry sample MEN19a, immediately adjacent to the mineralized quartz vein at Maisie, were dated. The five youngest dates yielded a weighted mean age of 367.12 ± 0.11 / 0.16 / 0.42 Ma (MSWD = 0.71, probability of fit = 0.58; Fig. 24). This is interpreted as the igneous crystallization age. The other grain yielded an age date of 368.15 ± 0.25 Ma. This grain is interpreted as being inherited, but also magmatic in origin. The rare earth element (REE)-Y compositions of these zircons (Table 8) are very similar to the single zircon from the quartz vein with LREE << HREE but with higher Ce, and a less pronounced Eu anomaly (Fig. 23b).

(iii) The most abundant zircon grains from the vein sample (MEN-1) are detrital metamict based on their morphology and REE geochemistry (Fig. 23c), and have been reported in other clastic sedimentary terrains in this area of New Brunswick (Dokken, 2017). In contrast to magmatic zircons from Men-1 and the porphyry, these grains are small (~ 25 to 50 µm long), anhedral and highly altered, and fractured, and the REE-Y patterns have a more gentle slope (LREE<HREE), with no La, Ce, Pr, or Eu anomalies.

Preliminary U-Pb dating yielded discordant ages of 2.0 – 2.2 Ga (D. Davis, University of Toronto, communication, 2018).

2.4.7 – Mineral thermometry

Further constraints on the T of vein formation were sought using semi-quantitative thermometers based on (i) the Al content of chlorite (Jowett 1991; and Cathelineau 1998), (ii) the Ti content within quartz in contact with titania (Thomas et al., 2010), and (iii) the Zr content of titania (Tomkins et al., 2007). All data are summarized in Figure 25 and in Tables 10 and 11.

2.4.7.1 – Chlorite thermometry

The Al content of chlorite from within siltstone along the margin of the quartz vein at Maisie (n=37) was investigated to obtain a semi-quantitative constraint on temperature of the (retrograde) alteration of mica to chlorite associated with vein formation.

Chlorite major and minor element composition, and calculated Ts are summarized in Table 10. Recalculated chlorite compositions show that chlorite is predominantly ripidolitic, with a few grains of pycnochlorite, and a single grain classified as brunsvigite. Aluminum-in-chlorite Ts calculated using equations from Cathelineau (1998) and Jowett (1991) range from 245 to 387 °C over both analysed samples (Fig. 25). The range between both samples is similar.

2.4.7.2 – Titania thermometry

The Zr content of brookite (identified by Raman spectroscopy) which formed prior to, and at the onset of, Q1 was determined to provide a semi-quantitative T constraint for brookite growth (after anatase) at Maisie. The thermometer calibration used was from Tomkins et al. (2007). Data are summarized in Table 11 for ten brookite grains (each

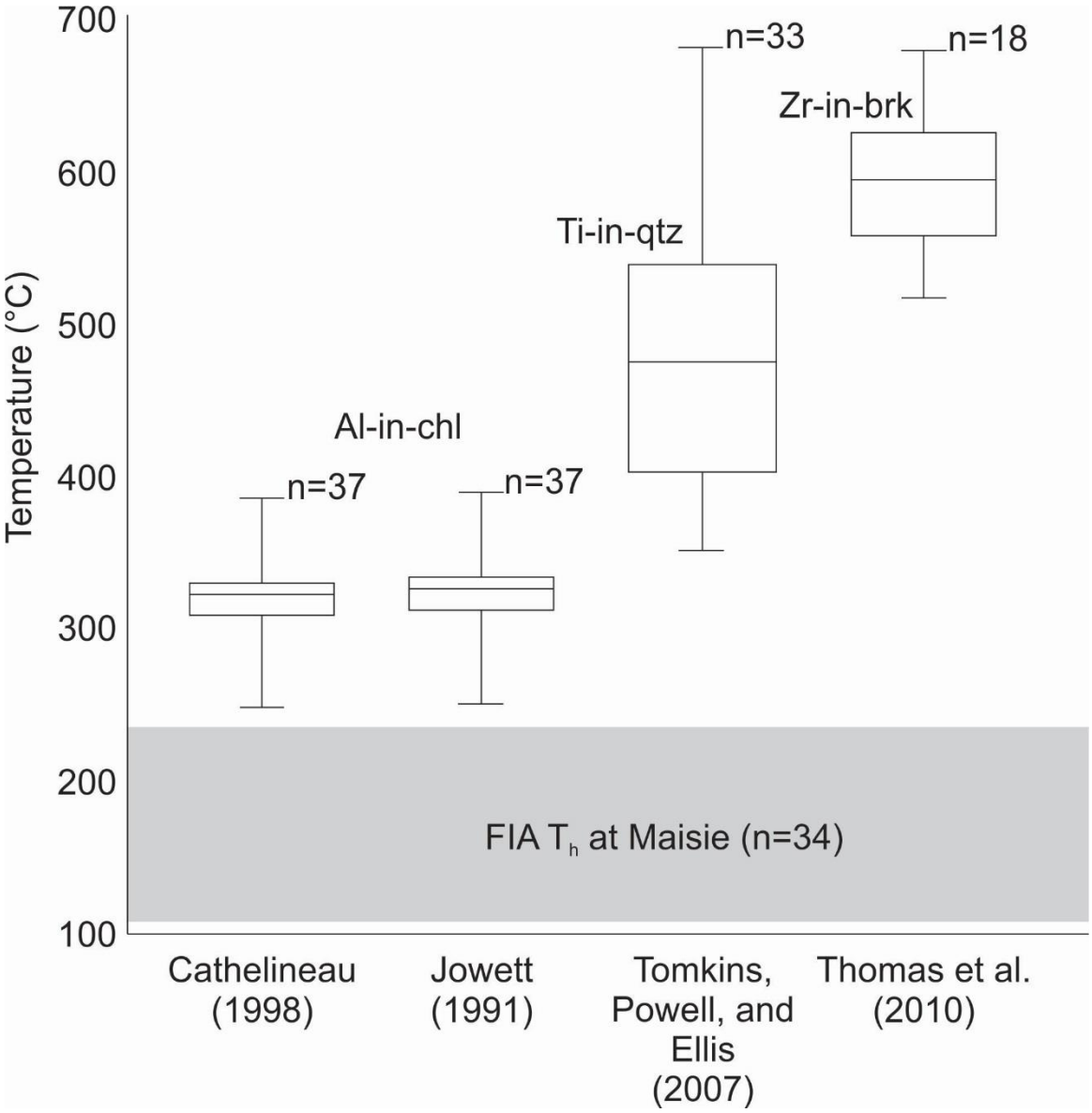

Figure 2.25 – Box-and-whisker plots of semi-qualitative mineral temperatures obtained from mineral chemistry geothermometers. Three mineral thermometers (Al-in-chl, Ti-in-qtz, and Zr-in-brk) were applied to samples from Maisie. Chlorite temperatures were calculated using Al^{iv} (Cathelineau, 1998, and Jowett, 1991). Zirconium-in-brk (Tomkins et al., 2007) and Ti-in-qtz (Thomas et al., 2010) temperatures were calculated assuming a pressure of 1 kbar. The grey field represents the total range of FIA T_h values from Maisie, as all thermometers are calculated using minerals from Maisie for 2 phase L+V inclusions in secondary trails in Q2. chl=chlorite; qtz=quartz; brk=brookite; n=number of analysis; T_h=temperature of homogenization; FIA=fluid inclusion assemblage

Table 10 - Wall rock chlorite composition and thermometry

	S1	S2	S3	S4	S5	S6	S7	S8	S9	S10	S11	S12	S13	S14	S15	S16	S17	S18	S19	S20	S21	S22	S23	S24	S25	S26	S27	S28	S29	S30	S31	S32	S33	S34	S35	S36	S37
SiO_2	25.72	26.35	26.46	26.19	28.74	27.89	26.22	26.91	25.92	26.37	26.87	26.27	26.61	24.73	27.42	26.95	26.79	27.04	25.11	26.26	26.60	27.30	26.91	26.71	26.59	27.17	24.29	26.56	26.32	26.16	27.10	26.17	25.40	25.76	27.58	26.73	26.76
TiO_2	0.02	0.01	0.03	0.00	0.00	0.02	0.00	0.01	0.05	0.00	0.00	0.03	0.00	0.07	0.32	0.09	0.01	0.03	0.06	0.01	0.05	0.04	0.03	0.00	0.02	0.00	0.01	0.02	0.03	0.08	0.00	0.01	0.06	0.02	0.00	0.00	0.04
Al_2O_3	20.00	20.57	18.54	19.93	17.20	17.75	20.28	19.60	20.75	20.41	19.22	20.46	20.25	21.71	18.61	20.17	20.62	19.05	19.68	20.29	17.84	18.00	20.64	20.30	20.72	20.11	22.62	20.18	20.42	19.90	20.40	20.34	20.44	19.89	17.31	20.79	19.79
FeO	22.87	24.36	25.59	24.19	22.26	21.58	24.24	23.51	22.79	24.34	21.68	23.94	23.27	27.55	23.83	22.96	23.28	21.32	25.33	22.72	24.55	22.52	22.65	22.13	22.47	22.30	23.88	22.52	22.86	22.69	22.30	22.84	24.43	22.59	21.44	22.29	22.42
MnO	0.30	0.28	0.44	0.25	0.22	0.21	0.29	0.29	0.29	0.32	0.29	0.28	0.27	0.37	0.25	0.30	0.33	0.39	0.47	0.27	0.33	0.28	0.25	0.25	0.28	0.32	0.13	0.23	0.27	0.24	0.29	0.25	0.33	0.25	0.36	0.27	0.25
MgO	14.32	14.49	13.08	14.30	16.29	17.06	14.18	15.13	15.20	14.08	17.17	14.14	14.54	11.67	15.12	14.39	14.66	17.60	15.19	16.03	16.06	16.18	15.69	15.75	15.69	16.00	13.80	15.86	15.25	15.53	15.70	15.91	12.84	15.60	17.34	15.81	15.62
CaO	0.16	0.14	0.13	0.14	0.16	0.15	0.12	0.13	0.12	0.10	0.12	0.13	0.09	0.03	0.12	0.19	0.11	0.04	0.01	0.06	0.02	0.30	0.10	0.08	0.09	0.11	0.05	0.08	0.09	0.12	0.08	0.06	0.04	0.05	0.09	0.13	0.16
Na_2O	0.09	0.08	0.10	0.06	0.07	0.08	0.06	0.10	0.07	0.08	0.07	0.11	0.12	0.02	0.05	0.18	0.14	0.07	0.05	0.06	0.03	0.14	0.11	0.13	0.10	0.11	0.09	0.11	0.12	0.13	0.09	0.07	0.08	0.06	0.14	0.09	0.10
K_2O	0.08	0.06	0.12	0.10	0.13	0.11	0.09	0.12	0.11	0.06	0.06	0.09	0.12	0.07	0.11	0.11	0.07	0.05	0.03	0.10	0.07	0.16	0.09	0.09	0.06	0.11	0.05	0.09	0.08	0.07	0.08	0.04	0.05	0.05	0.07	0.07	0.11
Cr_2O_3	0.19	0.12	0.02	0.06	0.03	0.09	0.15	0.12	0.06	0.06	0.01	0.07	0.11	0.01	0.03	0.11	0.06	-0.01	0.01	0.12	0.01	0.07	0.05	0.11	0.07	0.08	0.03	0.07	0.11	0.13	0.20	0.04	0.01	0.04	-0.03	0.09	0.11
No. of O	28	28	28	28	28	28	28	28	28	28	28	28	28	28	28	28	28	28	28	28	28	28	28	28	28	28	28	28	28	28	28	28	28	28	28	28	28
Total	83.8	86.5	84.5	85.2	85.1	84.9	85.6	85.9	85.4	85.8	85.5	85.5	85.4	86.2	85.9	85.5	86.1	85.6	86.0	85.9	85.6	85.0	86.5	85.5	86.1	86.3	84.9	85.7	85.5	85.1	86.2	85.7	83.7	84.3	84.3	86.3	85.4
Expected*	85.4	85.4	85.4	85.4	85.4	85.4	85.4	85.4	85.4	85.4	85.4	85.4	85.4	85.4	85.4	85.4	85.4	85.4	85.4	85.4	85.4	85.4	85.4	85.4	85.4	85.4	85.4	85.4	85.4	85.4	85.4	85.4	85.4	85.4	85.4	85.4	85.4
Number of ions based on 28 oxygens (with Fe2+/Fe3+ and OH calculated assuming full site occupancy)																																					
Si	5.60	5.58	5.79	5.63	6.09	5.93	5.61	5.71	5.53	5.62	5.69	5.61	5.66	5.36	5.82	5.71	5.65	5.71	5.42	5.56	5.74	5.84	5.63	5.64	5.59	5.69	5.24	5.62	5.59	5.60	5.68	5.56	5.57	5.57	5.92	5.60	5.68
Al^{IV}	2.40	2.42	2.21	2.37	1.91	2.07	2.39	2.29	2.47	2.38	2.31	2.39	2.34	2.64	2.18	2.29	2.35	2.29	2.58	2.44	2.26	2.16	2.37	2.36	2.41	2.31	2.76	2.38	2.41	2.40	2.32	2.44	2.43	2.43	2.08	2.40	2.32
Al^{VI}	2.75	2.73	2.60	2.70	2.41	2.39	2.74	2.63	2.76	2.77	2.50	2.78	2.78	2.92	2.51	2.79	2.80	2.46	2.44	2.64	2.28	2.40	2.74	2.72	2.75	2.68	3.01	2.67	2.73	2.63	2.74	2.66	2.88	2.64	2.31	2.76	2.66
Ti	0.00	0.00	0.00	0.00	0.00	0.00	0.00	0.00	0.01	0.00	0.00	0.00	0.00	0.01	0.05	0.02	0.00	0.01	0.01	0.00	0.01	0.01	0.01	0.00	0.00	0.00	0.00	0.00	0.00	0.01	0.00	0.00	0.01	0.00	0.00	0.00	0.01
Cr	0.03	0.02	0.00	0.01	0.00	0.01	0.02	0.02	0.01	0.01	0.00	0.01	0.02	0.00	0.01	0.02	0.01	0.00	0.00	0.02	0.00	0.01	0.01	0.02	0.01	0.01	0.01	0.01	0.02	0.02	0.03	0.01	0.00	0.01	0.00	0.01	0.02
Fe^{3+}	0.19	0.16	0.19	0.17	0.26	0.16	0.19	0.17	0.14	0.20	0.08	0.20	0.22	0.15	0.22	0.26	0.23	0.08	0.00	0.10	0.01	0.10	0.19	0.18	0.17	0.18	0.12	0.14	0.16	0.12	0.22	0.11	0.24	0.11	0.09	0.18	0.17
Fe^{2+}	3.98	4.15	4.50	4.18	3.69	3.67	4.15	4.00	3.92	4.14	3.76	4.08	3.93	4.84	4.01	3.81	3.88	3.69	4.63	3.92	4.42	3.93	3.78	3.73	3.78	3.73	4.19	3.85	3.90	3.94	3.68	3.95	4.24	3.98	3.76	3.72	3.81
Mn	0.06	0.05	0.08	0.04	0.04	0.04	0.05	0.05	0.05	0.06	0.05	0.05	0.05	0.07	0.04	0.05	0.06	0.07	0.08	0.05	0.06	0.05	0.04	0.04	0.05	0.06	0.02	0.04	0.05	0.04	0.05	0.04	0.06	0.05	0.07	0.05	0.05
Mg	4.64	4.57	4.27	4.58	5.15	5.40	4.52	4.79	4.83	4.47	5.42	4.50	4.62	3.77	4.79	4.55	4.61	5.54	4.88	5.06	5.16	5.16	4.89	4.96	4.92	5.00	4.44	5.00	4.83	4.95	4.90	5.04	4.20	5.02	5.55	4.94	4.95
Ca	0.04	0.03	0.03	0.03	0.04	0.03	0.03	0.03	0.03	0.02	0.03	0.03	0.02	0.01	0.03	0.04	0.03	0.01	0.00	0.01	0.01	0.07	0.02	0.02	0.02	0.03	0.01	0.02	0.02	0.03	0.02	0.01	0.01	0.01	0.02	0.03	0.04
Na	0.08	0.07	0.08	0.05	0.05	0.07	0.05	0.09	0.06	0.07	0.06	0.09	0.10	0.02	0.04	0.15	0.11	0.06	0.04	0.05	0.02	0.12	0.09	0.11	0.08	0.09	0.07	0.09	0.09	0.11	0.07	0.06	0.07	0.05	0.12	0.08	0.08
K	0.04	0.03	0.06	0.06	0.07	0.06	0.05	0.06	0.06	0.03	0.03	0.05	0.06	0.04	0.06	0.06	0.04	0.03	0.02	0.05	0.04	0.09	0.05	0.05	0.03	0.06	0.03	0.05	0.04	0.04	0.04	0.02	0.03	0.03	0.04	0.04	0.06
OH*	16	16	16	16	16	16	16	16	16	16	16	16	16	16	16	16	16	16	16	16	16	16	16	16	16	16	16	16	16	16	16	16	16	16	16	16	16
Total	35.81	35.83	35.81	35.83	35.72	35.84	35.80	35.84	35.86	35.78	35.93	35.80	35.78	35.83	35.76	35.75	35.77	35.93	36.11	35.91	36.01	35.94	35.81	35.83	35.82	35.83	35.89	35.88	35.85	35.90	35.76	35.89	35.74	35.89	35.94	35.81	35.83
Fe/(Fe+Mg)	0.47	0.49	0.52	0.49	0.43	0.42	0.49	0.47	0.46	0.49	0.41	0.49	0.47	0.57	0.47	0.47	0.47	0.40	0.49	0.44	0.46	0.44	0.45	0.44	0.45	0.44	0.49	0.44	0.46	0.45	0.44	0.45	0.52	0.45	0.41	0.44	0.45
T (°C)[1]	325	328	294	319	245	272	323	307	337	321	310	323	314	363	288	306	316	307	354	331	302	285	320	317	326	310	383	321	326	325	312	331	330	330	273	324	311
T (°C)[2]	329	332	300	324	249	275	328	311	340	326	313	327	318	370	293	310	320	309	359	334	306	289	323	320	329	313	387	324	329	328	315	335	335	333	276	327	315

[1]Temperatures from Cathelineau (1998), [2]Temperatures from Jowett (1991), *Measured Standard Block 53 chlorite

Table 11 - Zr and Ti LA-ICP-MS values and corresponding thermometers from brookite and quartz (Q1), respectively

Sample/ Analysis #	Zr (ppm)	T(°C)[1]	Sample	Ti (ppm)	T(°C)[2]
Men10-2			Men10-2		
1 - 1	120	546	1 - 1	44	482
1 - 2	537	658	1 - 2	59	505
2 - 1	183	575	2 - 1	32	459
2 - 2	194	579	2 - 2	83	533
2 - 3	189	577			
2 - 4	77.5	518			
3 - 1	543	659	3 - 1	99	549
3 - 2	536	658	3 - 2	14.5	406
3 - 3	482	649			
3 - 4	377	629			
4 - 1	74.2	515	4 - 1	9.6	382
4 - 2	102	535	4 -2	45	484
4 - 3	90.1	527			
4 - 4	137	554			
5 - 1	289	608			
5 - 2	283	606			
5 - 3	229	591			
Men40-2a			Men40-2a		
1 - 1	313	614	1 - 1	91	541
1 - 2	142	557	1 - 2	28	449
1 - 3	72.7	514	2 - 0	350	680
1 - 4	319	616			
2 - 1	131	551	2 - 1	100	550
2 - 2	266	602	2 - 2	77	527
2 - 3	579	665	3 - 0	25	441
2 - 4	662	676			
3 - 1	272	603	3 - 1	33	461
3 - 2	231	591	3 - 2	5.1	348
4 - 1	223	589	4 - 1	7.9	371
4 - 2	266	602	4 - 2	6.6	361
4 - 3	233	592			
5 - 1	396	633			
5 - 2	150	561			
5 - 3	188	576			

Temperature calculated with assumed pressure of P=1 kbar

[1]Thermometer from Tomkins, Powell, and Ellis (2007);

[2]Thermometer from Thomas et al. (2010)

confirmed as brookite by Raman spectroscopy) collected from drill core samples. Zirconium concentrations in brookite range from 73 to 662 ppm (n=33), and yield calculated Ts ranging from 514 to 676 °C (average = 592 ± 45 °C; 1σ) (Fig. 25). Temperatures were calculated assuming a P of 1 kbar, though uncertainty in P at low P (< 5 kbar) has negligible effect on calculated T (Tomkins et al. 2007).

2.4.7.3 – Quartz thermometry

The Ti content of quartz (Q1) in apparent textural equilibrium with brookite (fragmented crystals "floating" in Q1) was determined to provide a semi-quantitative temperature constraint on quartz vein growth at Maisie. The thermometer calibration used was Thomas et al. (2010). Data are summarized in Table 11 for eight grains (each of which correspond to previously analysed brookite for Zr-in-brookite) within Q1. Titanium values in quartz adjacent to brookite range from 5 to 350 ppm (n=18), resulting in calculated vein Ts ranging from 348 to 680 °C (average = 474 ± 82 °C; 1σ) (Fig. 25). Temperatures were calculated assuming a pressure of 1 kbar, though uncertainty at low P (< 5 kbar) has negligible effect on calculated T (Thomas et al. 2010).

2.4.7.4 – Limitations of semi-quantitative thermometers

It is important to note that the mineral thermometers have limitations, which must be taken into consideration when interpreting results. With respect to Zr-in-titania the Tomkins et al. (2007) thermometer is calibrated for rutile, but the mineral phase analysed here is brookite. The different crystal structures of rutile vs. brookite may affect the partitioning behaviour of Zr, though no literature has been found to support this. A second limitation of Tomkins et al. (2007) is that SiO_2 activity of quartz must be 1, and a Zr-rich mineral (e.g., zircon, baddeleyite) must be present to fix Zr activity to 1. If these conditions

are not met, the Ts reported will be minimums. At the Maisie occurrence, zircons are hosted in quartz-rich sedimentary wall rock fragments and quartz veins, thus, SiO_2 and Zr activity will be high, likely close to 1. Finally, the Thomas et al. (2010) Ti-in-quartz thermometer will report minimum Ts if Ti activity is less than one. Titania mineral phases are hosted in wall rocks (anatase) and quartz(-carbonate) veins (brookite/rutile) and are thought to be in equilibrium with Q1. Thus, the activity of Ti will be high, likely close to 1.

2.5 Discussion

2.5.1 – Paragenesis of the auriferous quartz(-carbonate) veins

Review of textural, mineralogical, fluid inclusion and isotope data enables a comparison of the styles of mineralization at the Maisie and Lavoie occurrences, specifically to determine if they represent the same type of Au mineralization – a key question posed in this research.

Textural and mineralogical observations show three distinct stages of vein formation that are common to both occurrences. A simple paragenetic sequence and schematic is presented in Figure 26, and detailed descriptions of each vein stage is presented below:

Stage 1 – Laminated veining

An early, laminated vein stage (Q1; Fig. 26) involved the accumulation of fine- to coarse-grained quartz bands/layers, separated by wall-rock septae (some stylolitic; Stage 1; Fig. 4e; Fig. 5a, b). Aside from Q1, no minerals precipitated in the veins. However, at the onset of stage 1 the recrystallization of anatase occurred (in the sedimentary wall-rocks along vein margins; Figs. 9a and 26) to form blades/needles of brookite-rutile at wall rock

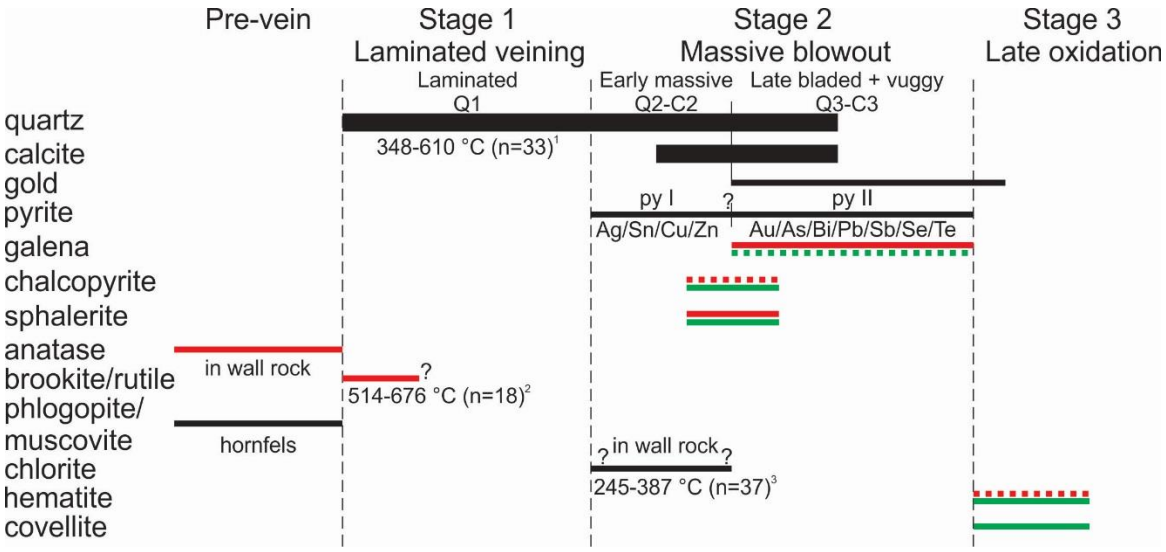

Figure 2.26 – Paragenetic sequence for the Maisie and Lavoie Au showings. A late stage oxidation event related to hematite formation, hematitization of pyrite, and chalcopyrite altering to covellite. Black bars = ubiquitous at both locations, red bars = Maisie exclusive, green bars = Lavoie exclusive, and dashed lines indicate which location contained modally more of a given mineral. Bar thickness is proportional to modal abundance. Elements listed below the pyrite line are the early and late metal associations seen in the LA-ICP-MS data (and corresponding maps). 1-Ti-in-qtz; Thomas et al., (2010); 2-Zr-in-brookite; Tomkins et al., (2007); 3-Al-in-chlorite; Jowett (1991) and Cathelineau (1999).

contacts that are now included in Q1 (Fig. 9d, e; Fig. 26). Gold is not associated with stage 1 veining.

Stage 2 – Massive quartz(-calcite) (Q2-C2) and vuggy/lattice-bladed quartz(-calcite) (Q3-C3)

The most voluminous vein stage (in terms of preserved quartz) was Stage 2. This involved the precipitation of polycrystalline, massive quartz(-calcite) intergrowth (Q2-C2; Figs. 26 and 27). Locally, the brecciation of Q1 occurred and was followed by the cementing of the Q1 fragments by a matrix of Q2-C2 (i.e. fragments of earlier, laminated Q1 material in Q2-C2; *early* Stage 2; Figs. 6 and 26). Later, domains of lattice-bladed calcite (C3)-quartz (Q3) intergrowth formed, and euhedral Q3 quartz crystals grew in vugs (Q3) (*late* Stage 2; Fig. 5c, e, f, i, j; Fig. 26). Whereas Q1 and Q2 occur throughout the vein at Maisie, with domains of Q1 concentrated near vein margins, the occurrence of Q3 along the veins is not pervasive. Rather, discrete zones of Q3, and areas with the thickest intervals of Q2 occur in areas where the vein is (locally) asymmetrically wider (up to ~4.5 m). These dilated areas of the vein were assigned the term "blow-outs" and may be associated with locally higher Au grades (based on review of DDH assay data; M. Taylor, SLAM Resources, communication, 2019).

Stage 2 vein growth was related to the main period of Au precipitation. Specifically, Q2 fracture infilling and Q3 vug infilling by gold provides textural evidence of Au precipitating late in Stage 2 (Fig. 7a, g, h, k, l). Early pyrite I formed euhedral grains hosted in massive Q2 at the onset of Stage 2 vein growth (Figs. 7j and 26); this pyrite contains low concentrations of Au and is enriched in Zn-Cu-Sn. Later pyrite II has a close textural association with gold (Fig. 7f), and likely co-precipitated with Au late in Stage 2 (Fig. 26).

Textural evidence for this includes anhedral pyrite II filling vugs in Q3-C3, or replacing C3 (Fig. 7d), with or without adjoining, or included, gold and other base metal sulfides. Pyrite II is enriched in Au-As-Pb-Bi-Se-Sb-Te, and the paragenetic relationship between pyrite I and II is clear from the replacement textures (Fig. 7c, d, f; Figs. 18 and 19).

Textural evidence indicates that other base metal sulfides (i.e. galena, sphalerite, and chalcopyrite) precipitated syn- to post- Q3 and C3; therefore, they are syn- to post-Au precipitation (Fig. 26). Evidence for this includes chalcopyrite and galena occurring as intergrown grains with, or as partial rims on C3, which is coeval with Au (Fig. 7e). Direct textural evidence of co-precipitation of gold with base metal sulfides comes from the presence of gold sharing grain boundaries with galena at the Lavoie showing (Fig. 7b). Chalcopyrite is rimmed by galena, and may contain inclusions of pyrite and sphalerite (Fig. 7c). This suggests that chalcopyrite and sphalerite precede galena. This is supported by coincident Cu and Zn following Cu, in the pyrite elemental maps (i.e. early pyrite I shows enrichment in Cu-Zn while later pyrite II shows enrichment in Pb; Figs. 18 and 19).

Stage 3 – Late oxidation/alteration

Late alteration of earlier vein minerals at the Maisie and Lavoie occurrences is the final stage of vein development. This stage involved hematitization of pyrite and alteration of chalcopyrite to covellite (Figs. 7a and 26). Hematite is present at both occurrences, however, it is more abundant at Maisie, reflecting a higher original abundance of pyrite (Fig. 7h-j). Only at Lavoie does chalcopyrite show alteration to covellite (Fig. 7a). In many examples hematite pseudomorphs pyrite (Fig. 7f, j) but there are also examples of hematite occurring as fracture infillings, and commonly associate with gold (Fig. 7h, i, k). This suggests that some Au remobilization and precipitation occurred in this last stage of vein

development. The timing of stage 3 relative to stages 1 and 2 is not constrained as it might represent a recent oxidation event related to surface weathering, or the incursion of meteoric water.

2.5.2 – Pressure-temperature constraints on vein formation

Constraining the P-T of vein formation at these occurrences helps to establish (classify) the style of Au mineralization, as well as aid in determining conditions related to Au mineralization. Integration of the results from mineral thermometers (Zr-in-brookite, Ti-in-quartz, and Al-in-chlorite), information concerning local and regional metamorphic conditions, and fluid inclusion microthermometry/petrography are used to estimate the P-T history of vein formation.

2.5.2.1 – Origin of fluid inclusions and discussion of microthermometry

Petrographic observations suggest that the hydrothermal fluids at Maisie and Lavoie varied from 1 (L_{aq})- to 2-phase (L_{aq}+V) during entrapment in fluid inclusions (Fig. 10g-i, top insets). This is observed in type 1 FIA that preserve evidence of homogeneous entrapment (see Fig. 10a, f, i, top 2 insets; showing L_{aq}-rich with consistent phase ratios in FIA at 20°C), transitioning to areas where mixed V-rich/V-dominant and L_{aq}-rich inclusions in type 2 FIA occur with highly variable phase ratios at 20°C (Fig. 10g, h, i, bottom inset). The latter can result from post-entrapment modification (i.e. necking down; Fig. 10g) but is also consistent with a hydrothermal fluid undergoing phase separation, i.e. a boiling system (Browne and Ellis, 1970; Keith et al., 1978; Roedder and Bodnar, 1980; Etoh et al., 2002; Moncada et al., 2012). A single phase fluid in the L field may undergo such rapid boiling (fluid "flashing" to steam; Moncada et al., 2012) that the resulting FIA would consist of groups of abundant V-rich to V-dominant inclusions with consistent phase

ratios and rare, L_{aq}-rich inclusions representing boiling endmember L_{aq} or boiling precursor L_{aq} fluid; type 3 FIA are considered to preserve this condition (Fig. 10i, bottom inset; Fig. 11). Fluid inclusions (types 1-3 FIA) in quartz have a mainly secondary or rarely indeterminate origin where they occur in Q1 and Q2 (Figs. 10a, f, h, and 11). It is considered on the basis of these petrographic observations that the fluid inclusions largely post-date Q1 and Q2. However, all three FIA types commonly have an indeterminate origin in Q3-C3 and, while evidence for primary origin is lacking, the prevalence of type 2 and 3 FIA (preserving boiling-flashing) in Q3-C3 suggests that they may be coeval with this vein stage (Fig. 10g, i, and 11). Flashing can be the result of pressure fluctuations, such as pressure-throttling during vein crack-seal events, for which textural evidence is observed in hand samples (Fig. 4e; Fig. 5a, b; Fig. 6).

Alternatively, the petrographic characteristics (and microthermometric data) of some FIA may be the result of post-entrapment modification (e.g. necking down). Specifically, some of the variability in phase ratios seen in type 2 FIA could result from necking down of a homogeneously trapped, single phase fluid inclusions following the P-T path along the L-V curve (post-entrapment). The absence of visible signs of necking down (i.e. in type 1 FIA), does not preclude the possibility that this process could have occurred thereby explaining variability of up to several tens of degrees in measured T_h within a FIA. Consequently, it may be impossible to differentiate necking down modification from real variations in T and/or P at the time of FIA trapping of non-boiling FIA. However, petrographic observations suggest that in type 2 FIA, rare cases of necking down occurred *after* the inclusions had trapped fluids that were in the 2-phase field (Fig. 10g). Furthermore, necking down cannot account for all of the variation in phase ratios

throughout the system. Specifically, it is unlikely that V-dominant inclusions in type 2 FIA, and dominating type 3 FIA could result from necking down. Such V "end-member" fluid inclusions are too abundant to be post-entrapment related. Thus, while some variation in T_h in type 1 FIA may be attributed to this process, the overall petrographic systematics of types 1, 2, and 3 FIA are consistent with transient boiling/flashing.

Variation in ΔT_h within, and among, FIA range from as little as 0.7 and 1.0 °C, to as much as 56.7 and 100.5 °C at the Maisie occurrence (Figs. 13 and 14). At the Lavoie occurrence variations in ΔT_h within, and among, FIA range from as little as 0.0 and 1.1 °C, to as much as 56.7 and 69.0 °C (Figs. 13 and 14). Microthermometric data and petrographic observations support a number of possible process (boiling, real fluctuations in P and/or T due to decompression or mixing, post-entrapment modification) to explain the range in T_h values.

In a boiling system the T_h values within and FIA would ideally show little variation if the FIA contained inclusions of coexisting, *end-member* V and L_{aq}; V-rich inclusions would homogenize to V, and L-rich inclusions would homogenize to L_{aq} at *same* T; this T_h would be the absolute $T_{trapping}$ (e.g. Roedder and Bodnar, 1980). However, this is seldom the case, as seen at Maisie and Lavoie where there are many occurrences of inclusions within type 2 FIA that show large variability in L_{aq}:V ratios, and correspondingly, a large range in T_h values, representing heterogeneous mixtures of V and L (Figs. 10g-I and 11). Vapour-dominant inclusions (i.e., the end-member V phase associated with boiling) in type 2 and 3 FIA could not be measured as homogenization by dew point transition (L_{aq}+V → V) could not be observed owing to the size of the inclusions and associated optical limitations. However, in boiling and flashing FIA (type 2, variable phase ratios in FIA; and type 3,

consistent phase ratios in FIA dominated by V-rich inclusions except for rare L_{aq}-rich inclusions; Figs. 10g-i and Fig. 11) inclusions with the smallest V bubbles, considered to be at, or close to, end-member composition for the L_{aq} phase associated with boiling, have similar T_h values as inclusions in type 1 FIA showing the lowest T_h which are interpreted to have trapped the single phase fluid that underwent transient boiling/flashing (Bodnar et al., 2014). This suggests that type 1 FIA were trapped close to the boiling point. The trapping of immiscible V in boiling type 2 FIA will result in higher T_h for those inclusions, and a larger ΔT_h (Bodnar et al., 1985). Bodnar et al. (1985) noted that trapping of even a few mole % vapour can raise T_h by tens of degrees, consistent with the spread in T_h observed in both L_{aq}-rich inclusions in type 1 FIA, and in (rare) L_{aq}-rich inclusions measured from type 2 and 3 FIA (Tables 2 and 3; Figs. 13 and 14). Such a situation would mimic the effects on necking-down on phase ratios and microthermometric behaviors. The lower T_h values measured in L-rich inclusions in types 1 and 3 FIA, as well as in single inclusions not associated with FIA (Tables 1 and 2; Figs. 13 and 14) are likely most representative of end-member L_{aq}. Type 1 FIA also show some variation in T_h but are all L_{aq}-rich; this variation in T_h must be related to some other process other than boiling.

Small variations in T_h values may also reflect real variations in P and/or T over the duration of entrapment of inclusions within FIA, or between FIA in single samples. Sufficient variations in confining P evidently took place in order for boiling/flashing to occur, but for type 1 FIA (non-boiling FIA) variations in T_h may simply reflect variations in $P_{trapping}$ at a constant T, with lower T_h values for inclusions trapped at higher P, and vice-versa.

Alternatively, variations in T_h may also result from real variations in T owing to fluid mixing hydrothermal fluid with a cooler fluid such as meteoric water. L_{aq}-rich fluid inclusion salinities within single FIA range from 0 to 4.8 wt.% equiv. NaCl at Maisie, and to 0 to 2.7 wt.% equiv. NaCl at Lavoie (Tables 2 and 3; Figs. 13 and 14), and the overall salinity range observed in L-rich inclusions at both locations considering both FIA and single inclusions (non-FIA) is from ~ 0 to ~8 wt% equiv. NaCl. This salinity range cannot be explained via post-entrapment modification, nor fluctuations in confining P, as neither affect the salinity of a salt-undersaturated fluid after or before entrapment, respectively. Furthermore, while boiling can produce aliquots of end-member, L_{aq}-rich fluid (i.e., trapped in fluid inclusions) with variable salinity depending on the P-T conditions of entrapment along the solvus in the NaCl-H_2O system (Driesner, 2007; Driesner and Heinrich, 2007), the end-member L_{aq} phase salinity will not decrease with decreasing P or T to values ~ 0 wt% equiv. NaCl. Rather, a slightly higher salinity (relative to parental, non-boiling fluid) L_{aq}-rich phase will form during boiling, in equilibrium with a very low salinity vapour. Salinities approaching 0 wt% equiv. NaCl in some L_{aq}-rich inclusions implicate meteoric waters, and by association, cooling. Fluid mixing alone would show as a correlation between T_h and salinity but this is not observed, though the lowest salinity inclusions are associated with the lowest T_h values (Tables 2 and 3; Figs. 13 and 14). Overall, a combination of meteoric water incursion and fluctuations in confining P, large enough to have caused phase separation (boiling/flashing), explain the fluid inclusion petrographic and microthermometric data at Maisie and Lavoie. As mentioned, fluctuations in pressure resulting from fault movements can lead to boiling/immiscibility (Sibson et al., 1988) and this may be inferred from the textures seen in vein stages, from laminated Q1 to massive

Q2 that brecciated the earlier Q1 (Fig. 6), and transitioning locally to boiling/open space textures in areas where veins are locally wider ("blow-outs").

Post entrapment modification (e.g., necking down) was also evaluated as this could also lead to large ΔT_h values within FIA. Petrographic evidence does show that some inclusions were modified by this process (e.g. Fig. 10g) but, as previously mentioned, it is not pervasive. The range in ΔT_h values is relatively large, but not outside an accepted ΔT_h discussed by Fall and Bodnar (2018).

2.5.2.2 – Estimation of P-T

The P-T conditions of vein formation and gold deposition at Maisie and Lavoie are estimated through microthermometric data, mineral thermometers, and also consideration of regional and local constraints on metamorphism. Petrographic evidence suggests that the hydrothermal fluids preserved in fluid inclusions at Maisie and Lavoie were trapped at a late stage in the vein paragenesis (always with secondary origin in Q1 and Q2; so post- Q1 and- Q2), but were possibly timed with the main Au mineralizing event associated with Q3 in late stage 2 vein development. The basis for this includes: (i) types 2 and 3 FIA being commonly indeterminate in origin, and most abundant in Q3-C3 domains, suggesting that they are related to the formation of Q3-C3 domains (and by textural association, gold within Q3 vugs and lattice-bladed calcite); (ii) types 2 and 3 FIA representing boiling/flashing, a known mechanism for Au precipitation (White and Hedenquist, 1995; Taylor et al., 2007; Moncada et al., 2012); and (iii) the occurrence of high Au in pyrite (specifically pyrite II) that overprinted Au-poor pyrite during Q3 formation. The fluids are interpreted to have undergone transient boiling (tending to "flashing"), and were diluted by meteoric water,

driving salinities to approach nil. This model serves as the context for estimations of the P-T window for Au mineralization.

2.5.2.2.1 – Fluid P-T conditions

Figure 27 shows calculated isochores for L_{aq}-rich inclusions in type 1 FIA from Maisie (Fig. 27a; field 1a) and Lavoie (Fig. 27b; field 1a). Field 1a on both figures indicates the P-T region above the L-V surface in which these fluid inclusions were trapped. Type 1 FIA fluid inclusions were trapped above values of T_h which represent minimum $T_{trapping}$. This is in contrast to type 2 and type 3 FIAs (boiling, flashing) for which $T_h = T_{trapping}$, and inclusions were trapped on the L-V curve (Fig. 27a, b; field "1b"). Petrographic and microthermometric evidence, described previously, suggests that types 1, 2, and 3 FIA may be related (i.e. non-boiling vs. boiling). Since values of T_h for L_{aq}-rich inclusions are so similar among types 1, 2, and 3 FIA, it is likely that type 1 FIA was trapped only slightly above the L_{aq}+V curve at low P similar to types 2 and 3 FIA. This suggests that the decrease in P that triggered boiling/flashing was not large. Had type 1 FIA been trapped at much higher P, their T_h values would be much lower than in types 2 and 3 FIA that trapped the equivalent fluid in a boiling state. In that scenario, the drop in P required to boil the fluid would have had to have been much larger, but this is not supported by the microthermometric data, nor the vein textures/ regional metamorphic P-t constraints.

Values of T_h measured through fluid inclusion microthermometry of FIA (Figs. 13, 14, and 27; Tables 2 and 3) at Lavoie shows a T range of 158 to 264 °C for type 2 FIA (average = 215 ± 36 °C; 1σ), and 155 to 254 °C for type 3 FIA (average = 158 ± 4 °C; 1σ). At Maisie, T_h ranges from 139 to 266 °C for type 3 FIA (average = 196 ± 40 °C; 1σ). These T ranges are considered absolute trapping T for these FIA.

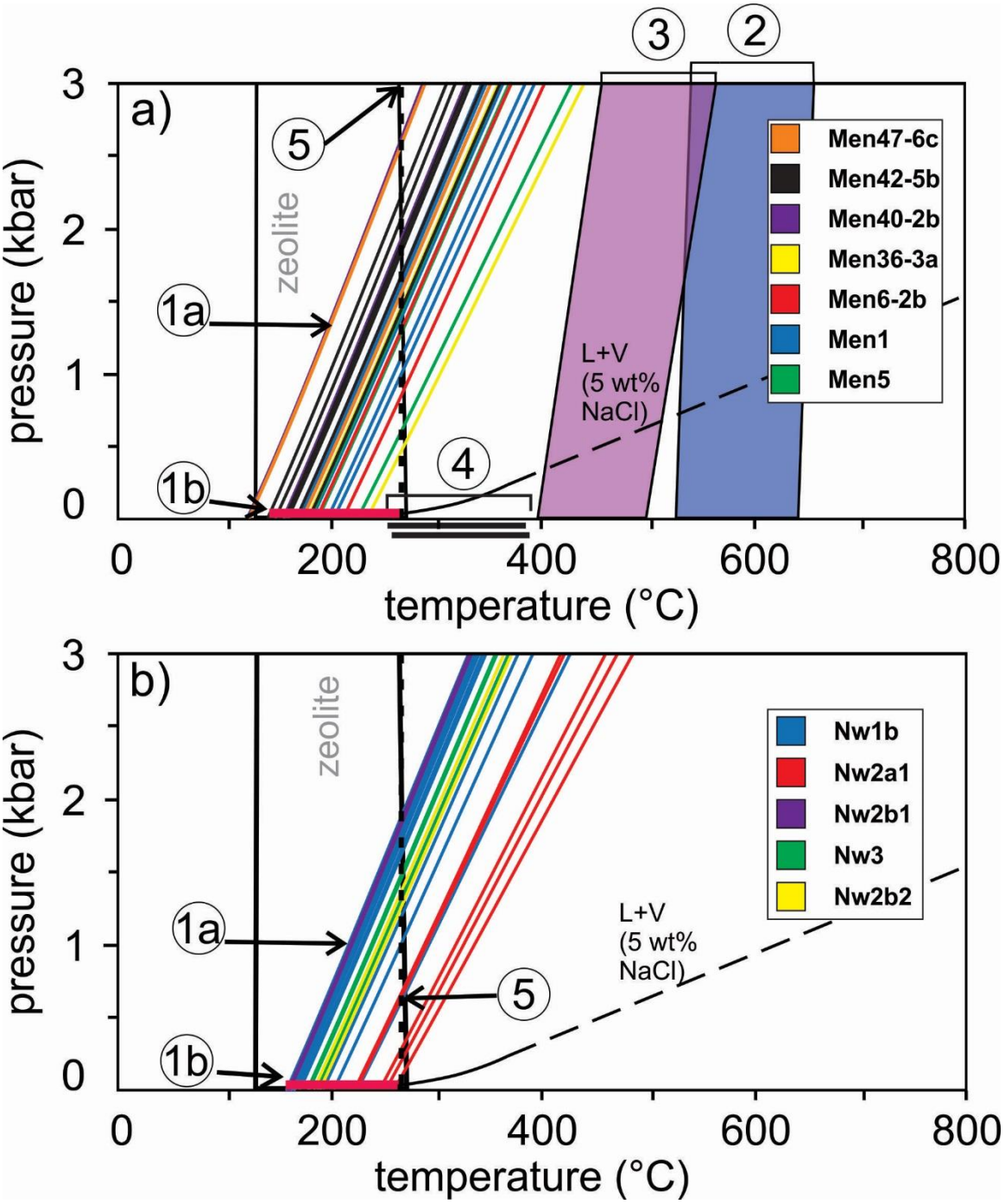
a)
3
2
5
1a
1b
4
zeolite
L+V
(5 wt%
NaCl)
Men47-6c
Men42-5b
Men40-2b
Men36-3a
Men6-2b
Men1
Men5
pressure (kbar)
temperature (°C)
0
200
400
600
800
b)
zeolite
Nw1b
Nw2a1
Nw2b1
Nw3
Nw2b2
1a
1b
5
L+V
(5 wt%
NaCl)
pressure (kbar)
temperature (°C)

Figure 2.27 previous page – P-T constraints for vein and gold formation. Isochores for all Maisie and Lavoie FIA (no single inclusion isochores shown). Numbers in legend (i.e. Nw1b) are FIA # in Tables 2 and 3. Isochores grouped by sample, showing the range of minimum temperatures of entrapment for fluid inclusion. a) fluid inclusion data from the Maisie Au showing. b) fluid inclusion data from the Lavoie Au showing. Field descriptions: 1a – Field of stability for the formation of L_{aq}-rich fluid inclusions during standard entrapment, resulting in the formation of type 1 FIA. 1b – Field of stability for formation of fluid inclusions during boiling/flashing after pressure decrease during crack-seal events, resulting in types 2 and 3 FIA. 2 – Temperature range calculated from Zr-in-brookite (Table 11). 3 – Temperature range calculated from Ti in quartz vein (Table 11). 4 – Temperature ranges from chlorite thermometers (Table 10) applied to wall rock alteration. The lower temperature range is calculated from Cathelineau (1998), and the higher temperature range from Jowett (1991). 5 – Maximum temperature from vitrinite reflectance for the area (Bertrand et al., 2005). The L_{aq}-V curve for a salinity of 5 wt.% equiv. NaCl is shown (Bodnar and Vityk, 1994) as an example; in reality, each inclusion isochore/T_h value is tied to a L-V curve specific to each inclusion's salinity but the overlap of these curves at the scale of the axis makes these L-V curves indistinguishable from one another at low T. Fields 2, 3, and 4 only apply to the samples from Maisie.

The corresponding $P_{trapping}$ calculated from the T_h (=$T_{trapping}$ on L+V curves) values for types 2 and 3 FIA ranges from 2 to 30 bar (average = 10 ± 6 bar) at Maisie corresponding to depths of entrapment of 7 to 111 m (average = 36 ± 24 m; lithostatic pressure; 1σ), or 20 to 302 m (average = 99 ± 66 m; hydrostatic pressure; 1σ). At the Lavoie Au occurrence, the $P_{trapping}$ calculated ranges from 6 to 49 bar (average = 16 ± 12 bar), corresponding to calculated depths of 22 to 184 m (average = 59 ± 45 m; lithostatic pressure; 1σ), or 60 to 498 m (average = 161 ± 121 m; hydrostatic pressure; 1σ).

2.5.2.2.2 – Mineral thermometers

Data from Maisie for the various mineral thermometers are listed in Tables 10 and 11, and graphically summarized in Figure 27a (label 1, 2, and 6), and Figure 25. These data provide semi-quantitative constraints on the T of vein stages prior to fluid inclusion entrapment. Brookite (recrystallized from anatase) is considered to slightly predate the surrounding Q1 in which the brookite/rutile is now included (Fig. 9b-e). Temperatures calculated from Tomkins et al. (2007) from Zr-in-brookite range from 514 – 676 °C (average = 592 ± 45 °C; Figs. 25 and 27a, field 2). Temperatures calculated from Ti-in-quartz using the equation of Thomas et al. (2010), range from 348 – 680 °C (average = 474 ± 82 °C; Figs. 25 and 27a, field 3). Data for chlorite thermometry is listed in Table 10, and on Figure 27 (point 6). Finally, temperatures calculated for Al-in-chlorite using the equations of Cathelineau (1988), yield temperatures ranging from 245 to 383 °C (average = 316 ± 24 °C; Figs. 25 and 27a, field 4), whereas equations from Jowett (1991) yield temperatures ranging from 249° - 387 °C (average = 320 ± 25 °C; Figs. 25 and 27a, field 4). These independent T estimates of vein formation are much higher than regional peak values in the sedimentary host as determined by vitrinite reflectance (Bertrand et al., 2005;

Fig. 27, field 5). Other evidence for locally higher T includes the hornfels along vein margins, and the presence of a porphyry dike located adjacent to the vein at Maisie (Fig. 2b, c). Based on the various thermometric data, significant cooling during vein formation occurred (locally) prior to boiling/flashing and gold deposition.

2.5.3 - Comparison of the Maisie and Lavoie Au occurrences to regional Au deposit styles

A variety of evidence supports the assertion that the Maisie and Lavoie occurrences are the same style of gold mineralization formed under similar condition. The commonalities are: (i) common host sedimentary unit i.e. the Whites Brook Formation; (ii) vein textures and quartz(-carbonate) stages; (iii) similar gold and accessory mineral assemblage paragenesis (Fig. 7), with the exception of minor variations in the relative abundance of accessory base metal sulfides (e.g. higher pyrite abundance at Maisie); (iv) fluid inclusion systematics (CO_2-poor, aqueous NaCl-dominant fluids, T_h and salinity range, non-boiling to transiently boiling/flashing FIA, post-dating Q1-Q2 and requiring a meteoric water contribution) with the exception of a slightly wider overall T_h and salinity at Maisie; (v) S-O-C-Sr isotope compositions for vein minerals; and (vi) pyrite trace element chemistry.

Regionally, there are no other Au occurrences possessing this group of characteristics known. For example, gold-enriched polymetallic sulfides (Cu ± Zn-Pb-Ag-Au) at the Patapedia skarn system (Fig. 1, site 1; Garnier et al., 2007; Malo et al., 2000) are hosted in the White Head Formation, consisting of limestone and calcareous shales. In contrast to Maisie and Lavoie, gold is disseminated within a marble hornfels skarn assemblage and associated stockwork veins. Other skarn deposits in the region include an Fe-Cu ± Au sulfide skarn associated with the McKenzie Gulch intrusions (Fig. 1, site 5) (Lentz et al., 1995).

The Elmtree occurrence (West Gabbro and South Gold Zones; Fig. 1, site 2) (Ruitenberg et al., 1989; Thorne, 2011) is an orogenic Au deposit that consists of quartz veins in which the highest Au grades are associated with sulfide-rich zones (i.e. with pyrrhotite, and infilling fractures in pyrite, arsenopyrite, and pyrrhotite, as well as included within arsenopyrite; Harris, 1986). Whereas a third mineralized zone (the Discovery Zone), contains polymetallic veins that contain Zn-Pb-Ag-Sb-Au mineralization (Bustard and Lentz, 2019).

There is a series of intrusion-related Au deposits close to the study area, including the Upsalquitch Forks, Simpsons Field, and Dalhousie Road occurrences (Fig. 1, site 4) (McCutcheon & Bevier, 1990; Ruitenberg et al., 1989). These occurrences are hosted along the RB-M fault, within Upper to Lower Ordovician sediments that were intruded by mafic and felsic dikes and later mineralized. Alteration is distinct in these low-grade Au showings, dominated by intense carbonitization and quartz-siderite veining.

Overall, when compared to other styles of Au mineralization in the region, the Maisie and Lavoie occurrences are distinct because: (i) Au is present as mainly (free) native gold in veins rather than being disseminated in sulfides, altered intrusions, or wall rocks; (ii) sulfides are scarce, not reaching more than 1 % by volume, and the sulfide assemblages do not include arsenopyrite or pyrrhotite; and (iii) alteration is restricted to chloritization of wall rock phlogopite, oxidation (hematite after pyrite and covellite after chalcopyrite), and trace carbonitization involving calcite not siderite.

2.5.4 – Pyrite mapping and Au enrichment

Characterizing the minor/trace element chemistry of pyrite in Au systems can provide information on metal sources, changes in fluid composition during deposit formation, and

can help to classify deposit types. The application of LA-ICP-MS to map pyrite composition is a more recently adopted technique, providing high resolution textural maps that can greatly assist in understanding more cryptic aspects of Au deposit genesis (Morey et al., 2008; Cook et al., 2009; Deditius et al., 2009, 2014; Large et al., 2009, 2012; Martin, 2012; Winderbaum et al., 2012; Agangi et al., 2015; Franchini et al., 2015; Gregory et al., 2015, 2016, 2017; Reich et al., 2016; Steadman & Large, 2016; Kouhestani et al., 2017; Mukherjee & Large, 2017; Neyedley et al., 2017; Gourcerol et al., 2018a,b; Kerr et al., 2018; Sykora et al., 2018; Wu et al., 2018 and authors therein).

Two generations of pyrite are observed in this study: early, pyrite I that contains low concentrations of Au and shows co-enrichment in Cu-Zn-Sn-W-Ag-Mo, and later pyrite II which has high Au concentrations and shows co-enrichment in Au-Bi-Te-Sb-Pb-As-Se. The assemblage Au, As, Bi, and Te shows the greatest increase in concentration from pyrite I to pyrite II. The Boland Brook Formation, underlying the study area, contains carbonaceous black shale layers hosting diagenetic pyrite enriched in Cu-Zn-Sn-W-Mo and containing very low Au contents (Table 5; Figs. 16 and 17). Early pyrite I has trace metal contents similar to pyrite from the Boland Brook Formation; however, the pyrite II metal association is considerably different and could not have been inherited from the host rocks. The Boland Brook pyrite and pyrite I have trace metal concentration hierarchies of Ni ≈ Zn>Cu>Co>As>Se ≈ Mo>Pb>Sb>Te≈W>Sn>Bi>Au ≈ Ag and Ni>As ≈ Co>Pb ≈ Cu>Zn>Se>Sb>Bi ≈ Ag ≈ Te ≈ Mo>W>Au>Sn, respectively, and are similar to the hierarchy reported for sedimentary/diagenetic pyrite in black shales globally (Gregory et al., 2015). This reinforces the likelihood of sedimentary-linked metals in the early stage

pyrite I with some elements (e.g. Cu, Zn, Sn, Mo, Ag? W?) most likely inherited from hydrothermal fluid interaction with the Boland Brook sulfides.

High Au pyrite II has a trace metal concentration hierarchy of As> Ni>Pb>Co>Au ≈ Sb ≈Se >Cu>Bi ≈ Te>Zn>Ag>Sn>Mo>W, that although similar to diagenetic/sedimentary pyrite (Gregory et al., 2015), also contains atypically elevated Bi, Au, and Te and not characteristic of diagenetic/sedimentary pyrites in other settings globally. Studies of pyrite chemistry in epithermal and intrusion-related Au deposits and in orogenic gold deposits upgraded by magmatic fluids (Cook et al., 2009; Kerr et al., 2018; Sykora et al., 2018) highlight Au-Te-Bi associations in pyrite as having a likely epithermal or intrusion-related provenance. Sykora et al. (2018) also points out that pyrite in porphyry-epithermal deposits tends to contain low Zn, as observed in pyrite II. Elements such as As and Sb have a more ambiguous origin and can be sourced from both black shales (Large et al., 2009, 2012; Gregory et al., 2015), and magmatic vapours in porphyry-epithermal systems (Heinrich et al., 2004).

The slight increase in $\delta^{34}S_{V\text{-}CDT}$ from 1.4 ± 0.2‰ (n=8; pyrite I) to 2.6 ± 0.3‰ (n=8; pyrite II) (Fig. 18) could result from boiling since the lighter S isotope is known to partition into the vapour (McKibben and Eldridge, 1990).

2.5.5 – Stable and radiogenic isotope constraints on fluid/metal source

Stable S-O-C and radiogenic Sr isotope data collected from vein quartz, calcite, sulfides, and host sulfides provides additional constraints on the origin of fluids and metals at the Maisie and Lavoie occurrences (cf. Ohmoto and Rye, 1979; Radtke et al., 1980; Oberthur et al., 1996; Pettke, 1997; Groves et al., 1998; Thébaud et al., 2006; Tornos et al., 2008; Goldfarb et al., 2005, 2015; Sharp, 2017).

2.5.5.1 – S isotopes

Pyrite hosted in black shale layers of the Boland Brook Formation (Carroll, 2002) has very negative $\delta^{34}S_{V\text{-}CDT}$ values (~-17 – -13 ‰), consistent with sulfides that form from bacterial sulfate reduction of marine sulfate in euxinic basins (open to SO_4^{-2} and closed to H_2S; Fig. 21b; Ohmoto and Rye, 1979). Hydrothermal sulfides formed from fluids that dissolved, or equilibrated with, this euxinic S source would have very negative $\delta^{34}S_{V\text{-}CDT}$ values. This is because at the Ts consistent with sulfide formation in the veins (~150-250 °C), fractionation of S isotopes between hydrothermal fluid and pyrite at the source in the Boland Brook Formation, and between fluid and sulfides in the veins would be relatively small. Using fractionation factors for H_2S-sulfide and HS^--sulfide (Sakai, 1968; Li and Liu, 2006; Beaudoin and Therrien, 2009) the calculated hydrothermal sulfide (galena, sphalerite, pyrite, chalcopyrite) $\delta^{34}S_{V\text{-}CDT}$ would be no more than ± 6.5‰ this is significantly less than the variation between pyrite II the Boland Brook Formation pyrite, suggesting that pyrite II at Maisie and Lavoie could not have formed from recycling the $\delta^{34}S_{V\text{-}CDT}$ of pyrite from the Boland Brook Formation with such a large negative $\delta^{34}S_{V\text{-}CDT}$ source (Fig. 21b).

The reduction of marine sulfate by organic compounds in hydrothermal fluids is a second potential pathway to consider with respect to S sources for the vein sulfides. Sulfides formed from H_2S or bisulfide derived from such a process would have large positive $\delta^{34}S_{V\text{-}CDT}$ values (~+15 to +21 ‰; Ohmoto and Rye, 1979). This is because at high T S isotope fractionation between sulfate and bisulfide or H_2O is very small. Subsequent dissolution or equilibration with a high $\delta^{34}S_{V\text{-}}$CDT sulfide will produce hydrothermal sulfide that retain the high positive $\delta^{34}S_{V\text{-}CDT}$ fingerprint. Regionally, there are no major

sources of sulfate minerals, and the host geological units are dominated by siliciclastic rocks and siliciclastic-rich carbonates (Carroll, 2003b) and the range in $\delta^{34}S_{VCDT}$ values in vein sulfides at Maisie and Lavoie are too low to have formed from this S source, regardless (Fig. 21b).

The range in $\delta^{34}S_{V\text{-}CDT}$ values for vein sulfides at Maisie and Lavoie (Figure 21b; pyrite, galena, sphalerite, and chalcopyrite) most closely fits the expected range observed in sulfides that formed from hydrothermal fluids decomposed S-bearing organic compounds (Ohmoto and Rye, 1979; ~0 to 10 ‰). The distribution of data follows a bell curve shape, with the majority of $\delta^{34}S_{V\text{-}CDT}$ values ranging from +3 to +8 ‰. Whereas the pyrite in the Boland Brook Formation did not act as a S source, S-bearing organic compounds in the affiliated carbonaceous rocks (black shales) of this formation may be relevant to this interpretation. The range in vein sulfide $\delta^{34}S_{V\text{-}CDT}$ has some overlap with mantle $\delta^{34}S_{VCDT}$ values, though the vein sulfides have a greater range in positive $\delta^{34}S_{V\text{-}CDT}$ values beyond the mantle range. This does not preclude magmatic input, but it is not resolvable using ^{34}S – ^{32}S systematics.

2.5.5.2 – C isotopes

The negative values of $\delta^{13}C_{V\text{-}PDB}$ in vein calcite are inconsistent with the hydrothermal dissolution of, or equilibration with, solely marine carbonate cements in the host turbidites ($\delta^{13}C_{V\text{-}PDB}$ ~0‰; Sharp 2017). Even hydrothermal carbonates recrystallized from an original marine carbonate source in similar Ordovician rocks have $\delta^{13}C_{VPDB}$ values ~ 0 ‰ (Mingan and Romaine Formations, Anticosti Island; Lavoie and Chi, 2010). The negative $\delta^{13}C_{V\text{-}PDB}$ values observed at Maisie and Lavoie (Fig. 22a) are consistent with vein carbonates being sourced partly from the thermal degradation and breakdown of organic

matter in the host rocks by circulating hydrothermal fluid (cf. Ohmoto and Rye, 1979) which results in highly negative $\delta^{13}C_{V\text{-}PDB}$ values for dissolved bicarbonate which is subsequently inherited by vein calcite when it crystallizes. There is abundant organic material in the surrounding Popelogan arc rocks, specifically the Popelogan Formation which contains carbonaceous shale and underlies the Boland Brook Formation to the east (Carroll, 2003a). These rocks may underlie the Maisie and Lavoie showings at depth. Additionally, there are organic-rich, shale layers in the host rocks (Carroll, 2003a) supporting the argument that the S isotope systematics of vein sulfides were inherited from the thermal decomposition of S-bearing organic compounds in the host sediments.

2.5.5.3 – Sr isotopes

The $^{87}Sr/^{86}Sr_o$ of vein calcite (C3) at Maisie and Lavoie range from 0.708720 to 0.709735. For comparison, the $^{87}Sr/^{86}Sr_o$ values of dolomitized carbonates from the Ordovician Mingan and Romaine Formations (Anticosti Island) range from 0.708815 to 0.712862 (Lavoie and Chi, 2010; Fig. 22b, c). The basis for this comparison is an attempt to evaluate any links between vein calcites and sedimentary carbonate sources in analogous host rocks. Since Sr isotope data is not available for the Grog Brook Group, data for similar deep water Ordovician sedimentary rocks are used for comparison.

The $^{87}Sr/^{86}Sr_o$ values of the Maisie and Lavoie calcite are higher than Late Ordovician (Ashgillian) seawater (Shields et al., 2003; Fig. 22b, c), and very similar to carbonates in the Mingan and Romaine Formations (Lavoie and Chi, 2010; Fig. 22b, c). Calcite from Maisie and Lavoie was not mineralized solely from marine fluids, indicating that the Sr isotope composition of vein calcite is not solely inherited from marine carbonates. Lavoie and Chi (2010) interpreted Sr to have been sourced from hydrothermal fluids circulating

through the Ordovician carbonate-bearing rocks, but also show a more radiogenic Sr contribution indicating that the fluids circulated through Grenvillian basement rocks and dissolved plagioclase. A comparable scenario is not unreasonable for hydrothermal calcite at Maisie and Lavoie, formed from hydrothermal fluids that extracted marine carbonate Sr and radiogenic Sr from basement rocks directly, or recycled Grenville-derived detrital plagioclase within the Grog Brook Group sedimentary rocks (Carroll, 2003a).

2.5.5.4 – O isotopes

The range in quartz $\delta^{18}O_{V\text{-}SMOW}$ values at Maisie shifted to higher positive values from Q1 to Q3. If the source fluid $\delta^{18}O_{V\text{-}SMOW}$ and T remain constant during vein evolution with such an increase in $\delta^{18}O_{V\text{-}SMOW}$ in quartz may result from fluid boiling (Truesdell et al., 1977; Kleine et al., 2018). Evidence of boiling is recorded at Maisie and Lavoie in fluid inclusions and vein textures. However, consideration of the $\delta^{18}O_{V\text{-}SMOW}$ data relative to estimated Ts of quartz crystallization and/or fluid inclusion entrapment allows the $\delta^{18}O_{V\text{-}SMOW}$ of the fluid to be estimated, and when this is done, it can be shown that $\delta^{18}O_{V\text{-}SMOW}$ of the fluid *decreased* from Q1 to Q3. Figure 28 shows isopleths for $\delta^{18}O_{V\text{-}SMOW}$ in the fluid (H_2O) calculated at varying T and $\delta^{18}O_{V\text{-}SMOW}$ for quartz using the quartz-H_2O fractionation factors from Matsuhisa et al. (1979). The results of this exercise (Fig. 28) shows that (i) laminated quartz (Q1), using an estimated crystallization T range from ~350 – 680 °C (Ti-in-qtz), grew from a fluid with $\delta^{18}O_{H2O,\ V\text{-}SMOW}$ ~ +10 ‰ to +18 ‰, and (ii) late-bladed quartz intergrowths (Q3) and vuggy quartz (Q3), using a T range for fluid inclusion entrapment (L_{aq}-rich inclusions) in type 2 and 3 FIA (boiling, flashing; $T_h \approx T_{trapping}$) grew from a fluid with $\delta^{18}O_{H2O,\ V\text{-}SMOW}$ ~ +2‰ to +12 ‰ and ~ +3‰ to +16 ‰ respectively. To form quartz with the $\delta^{18}O_{V\text{-}SMOW}$ values measured, a

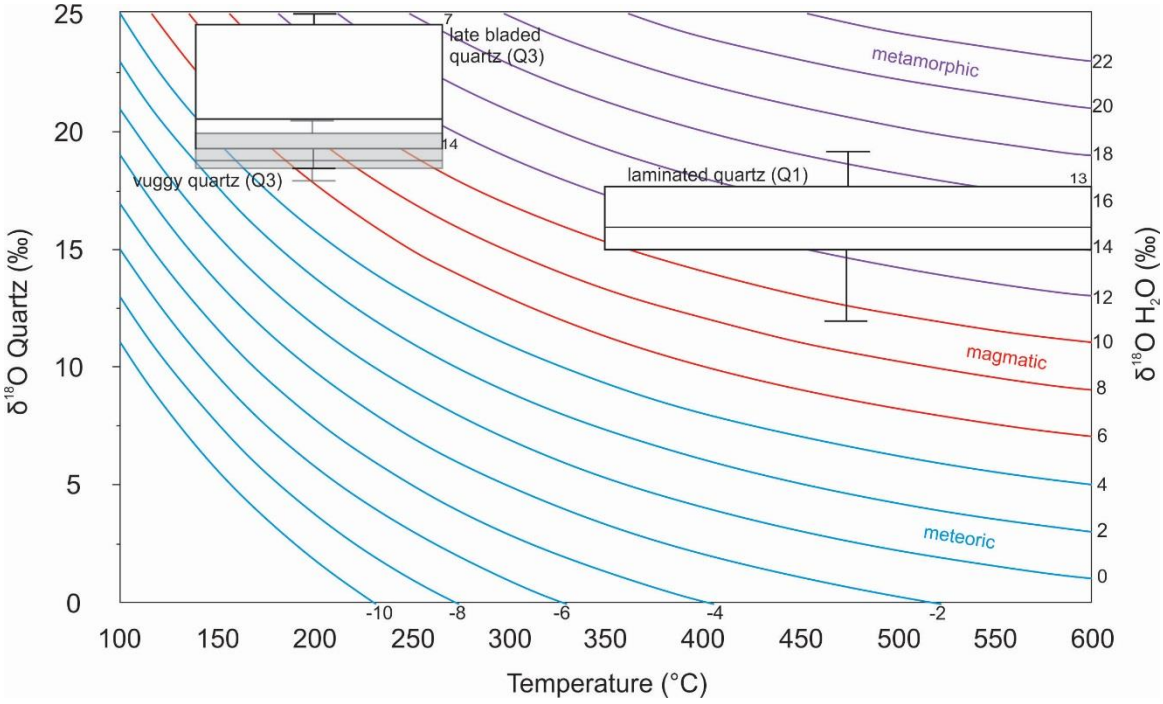

Figure 2.28 – Quartz O-isotope data versus calculated $\delta^{18}O$ isopleths for the equilibrating fluid at variable T. All data are from Maisie. The temperature constraint for laminated quartz (Q1) is from Ti-in-qtz thermometry (Table 11). Late, lattice-bladed and syn-Au vuggy quartz (Q3) are thought to be coeval with types 1, and 3 FIA, with an average T_h (± 1σ) determined from fluid inclusion microthermometry of L_{aq}-rich inclusions in types 2 and 3 FIA ($T_h \approx T_{trapping}$ on L+V curve; Tables 2 and 3).

process capable of shifting the $\delta^{18}O_{V\text{-}SMOW}$ of the equilibrating fluid to a less ^{18}O-rich composition is required.

Mixing of fluids is a likely explanation, and is recorded at Maisie and Lavoie in variations in fluid inclusion salinities. Salinities range from ~ 0 – 8 wt% NaCl equiv., consistent with meteoric water (~ 0 wt% NaCl equiv.) mixing with low grade metamorphic or magmatic fluid that is richer in ^{18}O (Sharp, 2017).

The predicted shift in O-isotope composition from Q1 to Q3 does not clarify the origin of the high salinity end-member fluid/s. While there is no isotopic evidence of a magmatic fluid contribution other considerations, discussed previously, suggest both low grade metamorphic fluid and a magmatic metal source for Au-Bi-Te.

The presence of late hematite (after pyrite) as well as vuggy quartz (Q3) suggests that the system was unroofed (uplifted and/or eroded) a minimum of 7 to 22 m. This and fault reactivation/brecciation would promote incursion of oxidizing meteoric water, as well as open the system up to potential later weathering.

2.5.6 – Deposit style classification of the Maisie and Lavoie veins

Examining all data types from Maisie and Lavoie presented herein, a classification of mineralization type is possible, using global examples of orogenic, epithermal, and intrusion-related Au deposits for comparison:

(i) *General vein morphology* – The Maisie and Lavoie Au showings comprise quartz(-carbonate) hosted, non-refractory Au, with laminated veins transitioning to massive, brecciated, and vuggy/lattice-bladed textures with time. Although laminated veins are present in many orogenic Au deposits (Goldfarb et al., 2005; Groves et al., 2003), they

are not exclusive to orogenic systems. Vuggy and lattice-bladed textures, when resulting from fluid boiling (Browne and Ellis, 1970; Keith et al., 1978; Etoh et al., 2002; Moncada et al., 2012) are consistent with epithermal Au deposits (White & Hedenquist, 1995; Taylor, 2007) and atypical of orogenic Au systems. However, many other epithermal features (e.g. colloform quartz and sinter deposits; Moncada et al., 2012) are not observed. Thus, on the basis of vein textures alone, classification is problematic.

(ii) *Metamorphic grade and hydrothermal P-T conditions* – The host sedimentary rocks of the Grog Brook Group show evidence of localized heating to hornfels facies, and vein minerals record locally very high T (~350 – 680 °C) prior to Au mineralization; however, regional the metamorphic grade is no higher than prehnite-pumpellyite facies, based on vitrinite reflectance data (c.f. Bertrand et al., 2005) and CL colouration of quartz (c.f. Boggs Jr. et al., 2002). The inferred localized high T, early in the vein history at Maisie implies a genetic link to the adjacent porphyry intrusion and raises the possibility that Au mineralization is intrusion-related. On the other hand, the low metamorphic grade of the country rock is inconsistent with the majority of orogenic gold deposits which are hosted within rocks that are commonly metamorphosed from greenschist to amphibolite grade. However, the low metamorphic grade is consistent with relatively uncommon shallow ("epizonal") orogenic gold deposits hosted in very low metamorphic grade rocks (e.g., Telfer mine, Western Australia: Goellnicht et al., 1989; Commoner mine, Zimbabwe: Twemlow and Foster, 1984; Wiluna mine, Western Australia: Hagemann et al., 1992; Donlin Creek, Alaska: Goldfarb et al., 2004). Fluid inclusion systematics constrain late stage vein formation to depths of less

than 300 m at Maisie (hydrostatic), and 500 m at Lavoie (hydrostatic), consistent with an epizonal orogenic or epithermal depth regime.

(iii) *Vein mineralogy* – The mineralized assemblage consists of quartz with minor calcite, gold, and trace base metal sulfides (pyrite, galena, chalcopyrite, sphalerite), with late oxidation (hematitization) of the pyrite, and chloritization of wall rock phlogopite. There are no discrete As, Sb, or Te mineral phases such as arsenopyrite and realgar, stibnite, or hessite, respectively. Thus, the mineralogy is somewhat similar to low-sulfidation epithermal deposits (i.e. pyrite and Pb-Zn sulfides) (Hedenquist et al., 2000; Taylor, 2007; and White & Hedenquist, 1995), but is missing the other mineral phases mentioned. However, importantly, late replacement pyrite II is significantly enriched in Au, As, Sb, Te, Pb, and Bi (Figs. 18 and 19). An epithermal or intrusion-related (magmatic) source of some of these metals (Au, Bi, Te) is likely (Cook et al., 2009; Large et al., 2009, 2012; Kerr et al., 2018; and Sykora et al., 2018). Associated chlorite alteration is not unique to either orogenic or epithermal settings.

(iv) *Fluid inclusion systematics* – Fluid inclusions preserve low salinity (~0 to 8 wt% equiv. NaCl), H_2O-NaCl fluids with trace CH_4 and N_2 and no detectable CO_2. Fluids were trapped at T ~ 150 – 250 °C and at P on, or slightly above, the L_{aq}+V curve (< 50 bars). At the time of FIA entrapment, the hydrothermal systems fluctuated from non-boiling to boiling to flashing. Salinities approaching ~0 wt% equiv. NaCl suggest meteoric water involvement. The overall fluid inclusion characteristics are inconsistent with mesozonal orogenic Au deposits but are consistent with epizonal orogenic or low sulfidation epithermal deposits (Phillips and Groves, 1983; Hagemann et al., 1994; Hedenquist et al., 1994; Groves et al., 1998; Chauvet at al., 2001; Hedenquist et al.,

2000; Neumayr and Hagemann, 2002; Goldfarb et al., 2004; Taylor, 2007; Pudack et al., 2009; Moncada et al., 2012; and Kerr et al., 2018).

In summary, the Maisie and Lavoie occurrences share characteristics of both shallow orogenic (epizonal) and epithermal/intrusion-related Au deposits. Overall, the late stage of vein development related to Au mineralization, combined with the hallmark Au-Bi-Te association in pyrite II, anomalously high T early in vein formation, and the proximity to porphyritic rocks at Maisie suggests that Au endowment may have involved magmatic input/upgrading.

2.5.7 – Gold precipitation mechanisms

Multiple factors control the solubility of Au. Considering the mineralogical, fluid inclusion, and various geochemical and isotopic features of the Maisie and Lavoie Au occurrences as constraints, possible mechanisms for Au precipitation at Maisie are discussed below:

(i) *Boiling* – Textural and fluid inclusion petrography evidence indicate that boiling and rapid boiling (i.e. flashing) occurred at the Maisie and Lavoie vein systems. Boiling is a primary mechanism for Au precipitation in epithermal systems (White and Hedenquist, 1995; Kesler et al., 2003; Taylor et al., 2007; Zoheir et al., 2008; Heinrich et al., 2009). Partitioning of H_2S into the vapour phase during boiling reduces HS^- in the aqueous phase. Rapid boiling of the system will also remove H_2 from the system (McKibben and Eldridge, 1990), which leads to an increase in fO_2 and pH, oxidizing H_2S to SO_2 and SO_4^{-2}, thereby reducing Au solubility (Fig. 29). In accordance with Le Chatelier's Principle, the loss in HS^- and H^+ (to form H_2S or SO_2 gas) results in a shift

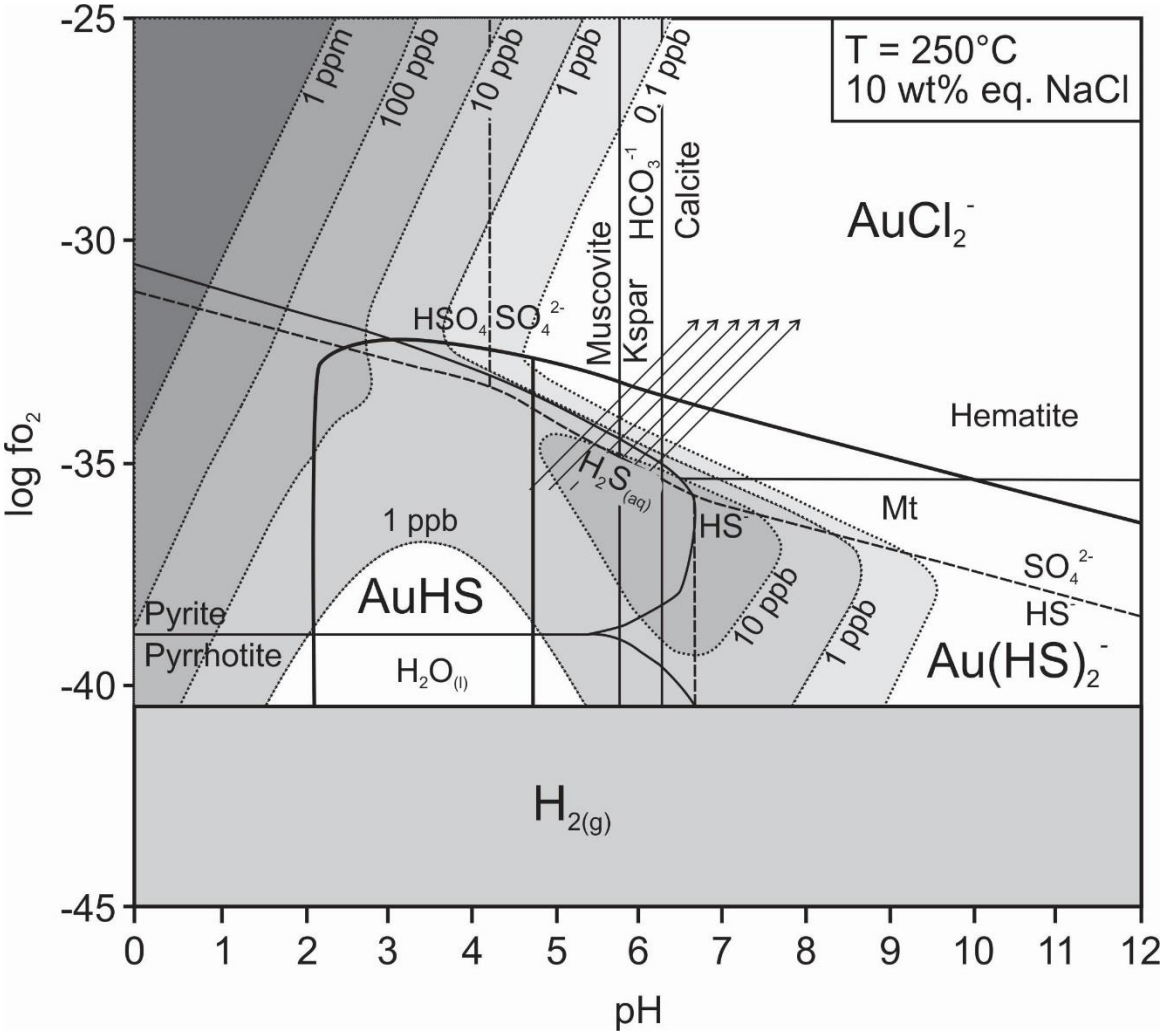

Figure 2.29 – Log fO_2-pH diagram showing Au solubility fields (according to predominant complex) along with stability boundaries for sulfide and oxide minerals and dissolved S species prevailing. Stability boundaries for the muscovite – kspar transition and calcite – HCO_3^{-1} transition are also shown as are contours for Au solubility which decreases sharply towards the upper right quadrant of the diagram. Arrows show proposed evolution of Au-bearing fluids at the Maisie and Lavoie Au occurrences. As the pH and fO_2 increase during meteoric water mixing Au becomes less soluble and precipitates. Diagram modified from Barnes and Czamanske (1967), drawn at ∑S activity = 0.1.

of the mass action expressions (1) and (2) to the left, precipitating Au via decomposition of bisulfide complexes:

$Au_{(s)} + HS^-_{(aq)} + H^+_{(aq)} + ¼\ O_{2(aq)} = Au(HS)°_{(aq)} + ½\ H_2O_{(aq)}$ equation (1)

$Au_{(s)} + 2HS^-_{(aq)} + H^+_{(aq)} + ¼\ O_{2(aq)} = Au(HS)^-_{2(aq)} + ½\ H_2O_{(aq)}$ equation (2)

Evidence of a pH shift due to boiling is the appearance of calcite during Stage 2 of vein formation, and the presence of muscovite only in non-boiling, earlier type 1 FIA.

(ii) *Fluid mixing* – Meteoric water incursion is suggested at Maisie and Lavoie from the range of fluid inclusion salinities (as low as ~0 wt% equiv. NaCl), and $\delta^{18}O_{V\text{-}SMOW}$ data from quartz, used to estimate the shift in fluid $\delta^{18}O_{V\text{-}SMOW}$ with time. This would occur through shallowing of the hydrothermal system, and vein opening/re-opening during crack-seal events related to fluid overpressure and/or fault movement. Mixing of meteoric water with a metamorphic or magmatic fluid would dilute the dissolved concentration of the bisulfide ligand, and drive the reactions (1) and (2) to the left, thereby precipitating Au. The introduction of meteoric water would also raise the fO_2 of the hydrothermal system (Sillitoe, 1994; Groves et al., 2003). In equations (1) and (2) an increase in f_{O2} increases Au solubility (Fig. 29). However, if f_{O2} increases to the point where bisulfide oxidizes to sulfate, and since Au solubility as a chloride complex is so low at neutral to alkaline pH and high fO_2 (Fig. 29) Au will precipitates according to the following reactions:

$Au(HS)^0_{(aq)} + 2O_{2(aq)} = H^+_{(aq)} + SO_4^{2-}_{(aq)} + Au_{(s)}$ equation (3)

$Au(HS)^-_{2(aq)} + 4O_{2(aq)} = 2H^+_{(aq)} + 2SO_4^{2-}_{(aq)} + 2Au_{(s)}$ equation (4)

Both boiling and mixing of hydrothermal fluid and meteoric water likely contributed to Au precipitation at Maisie and Lavoie. A number of other commonly invoked means as Au precipitation mechanisms; however on the basis of a variety of evidence (or absences thereof) from Maisie and Lavoie they can be ruled out as primary Au precipitation mechanisms in this study:

(iii) *Wall rock sulfidation* – This is a common mechanism for Au precipitation in orogenic and epithermal systems (cf. Groves et al., 1998, 2003; Goldfarb et al., 2005; Williams-Jones et al., 2009; Goldfarb and Groves, 2015). Sulfidation reactions in veins and wall rocks, involving the formation of pyrite or arsenopyrite (common in both epithermal and orogenic deposits), will lead to Au mineralization. The formation of pyrite and arsenopyrite from S-rich fluids occurs via reactions 5 and 6:

$$Fe_2O_{3(s)} + 4\ HS^-_{(aq)} = 2FeS_{2(s)} + ½\ O_{2(aq)} + 2H_2O_{(l)} \quad \text{equation (5)}$$

$$2Fe_2O_{3(s)} + 4\ HS^-_{(aq)} + 4\ As_{(aq)} = 4FeAsS_{(s)} + 2\ O_{2(aq)} + 2H_2O_{(l)} \quad \text{equation (6)}$$

Once again, according to Le Chatelier's Principle the formation of pyrite or arsenopyrite will consume bisulfide, shifting equation (7) to the left, thereby favouring Au mineralization:

$$2\ Au(HS)^o_{(aq)} + H_2O_{(l)} + Fe^{2+}\ (\text{wall rock}) \leftrightarrow 2\ Au_{(s)} + FeS_2 + 4\ H^+_{(aq)} + ½\ O_{2(aq)} \quad \text{equation (7)}$$

As the amount of sulfide in the wall rocks adjacent to the veins is negligible (i.e. no sulfidation "halo"), wall rock sulfidation is unlikely to have occurred at Maisie and Lavoie. In order for sulfidation to have occurred the wall rocks would had to have been Fe-rich but the wall rocks (Whites Brook Formation) are mineralogically Fe-poor turbidites (Wilson et al., 2004). However, it is possible that a small proportion of Au

was precipitated in the veins due to "internal" sulfidation (i.e. the formation of trace pyrite in the veins).

(iv) *Cooling* – Thermometric data for the Maisie vein indicates a large decrease in T from Stage 1 to late Stage 2; however, Au precipitation did not occur during Stage 1 or early Stage 2. Gold texturally post-dates both Q1 and Q2, and occurs late with respect to Q3, filling vugs lined with Q3-generation quartz. This is inconsistent with cooling-induced gold precipitation which should occur gradually as T progressively decreases.

2.5.8 – Geochronology

Determining the absolute timing of Au mineralization in orogenic and epithermal systems can be achieved assuming dateable hydrothermal minerals co-precipitated with Au. Such cases provides the opportunity to reconcile the timing of mineralization with the age of causative intrusions and/or other tectonic events. Potassium-bearing minerals such as adularia, illite, and micas are potential candidates but at Maisie and Lavoie these minerals are absent or very rare, and where present (e.g. mica), its textural relationship with Au is ambiguous.

The relative age relationship between vein-hosted mineralization and host rocks are indicated from field observations at Maisie and Lavoie (Fig. 3). Folding of primary bedding (Fig. 3a, b), related to regional deformation during the Taconian and Acadian Orogenies (Wilson 2003; Wilson et al., 2004). Quartz veining occurs suborthogonal (main vein orientation; Fig. 2b inset) or locally subparallel (Fig. 3e) to bedding, cross-cutting locally strongly-folded bedding as well as pencil cleavage (Fig. 3f). Therefore, veining is tentatively late or post- Acadian deformation.

The inherited zircon recovered from quartz vein at Maisie provides a concordant weighted age of 370.03 ± 0.20 Ma. This represents a maximum age for vein mineralization since this zircon was incorporated into the vein during wall rock delamination and constrains Au mineralization to no older than the Late Devonian (Famennian). Magmatic zircon from the adjacent porphyry dike at Maisie gave concordant ages of 368.15 ± 0.15 Ma (inherited) and 367.12 ± 0.11 Ma (crystallization), a few Ma older than the Patapedia River intrusion (Carroll, 2003a; Fig. 30). These ages slightly postdate the vein (inherited) zircon, unlike other regional ages that are much older for mineralization (Schwartz et al., communication; Elmtree, 430 ± 4 Ma; Middle River, 435 ± 3 Ma; and Tetagouche, 436 ± 3 Ma). The inherited zircon in the quartz vein is also distinct from abundant, altered, and recrystallized (metamict) zircon from the quartz vein that gave ages ranging from 2.0 – 2.2 Ga (D. Davis, University of Toronto, communication, 2018), that represent detrital zircons from Laurentia, later sedimented during the closing of the Iapetus Ocean (Pollock et al., 2007; Waldron et al., 2012; Waldron et al., 2014).

In contrast, the large zircon from the quartz vein, yielding the ~370 Ma age, is unaltered, and euhedral, similar to the zircons extracted and dated from the porphyry at Maisie, and has a distinct REE chemistry characteristic of magmatic zircon, with pronounced La, Pr, and Eu anomalies, LREE << HREE, and a high Sm_N/La_N ratio (Fig. 23a; Corfu et al., 2003; Zhong et al., 2018; Roberts et al., 2019). The porphyry zircons have very similar REE chemistry, but with a more pronounced Ce anomaly, and lower Eu anomaly. This similar REE chemistry indicates that the quartz vein-hosted zircon may have a local magmatic origin.

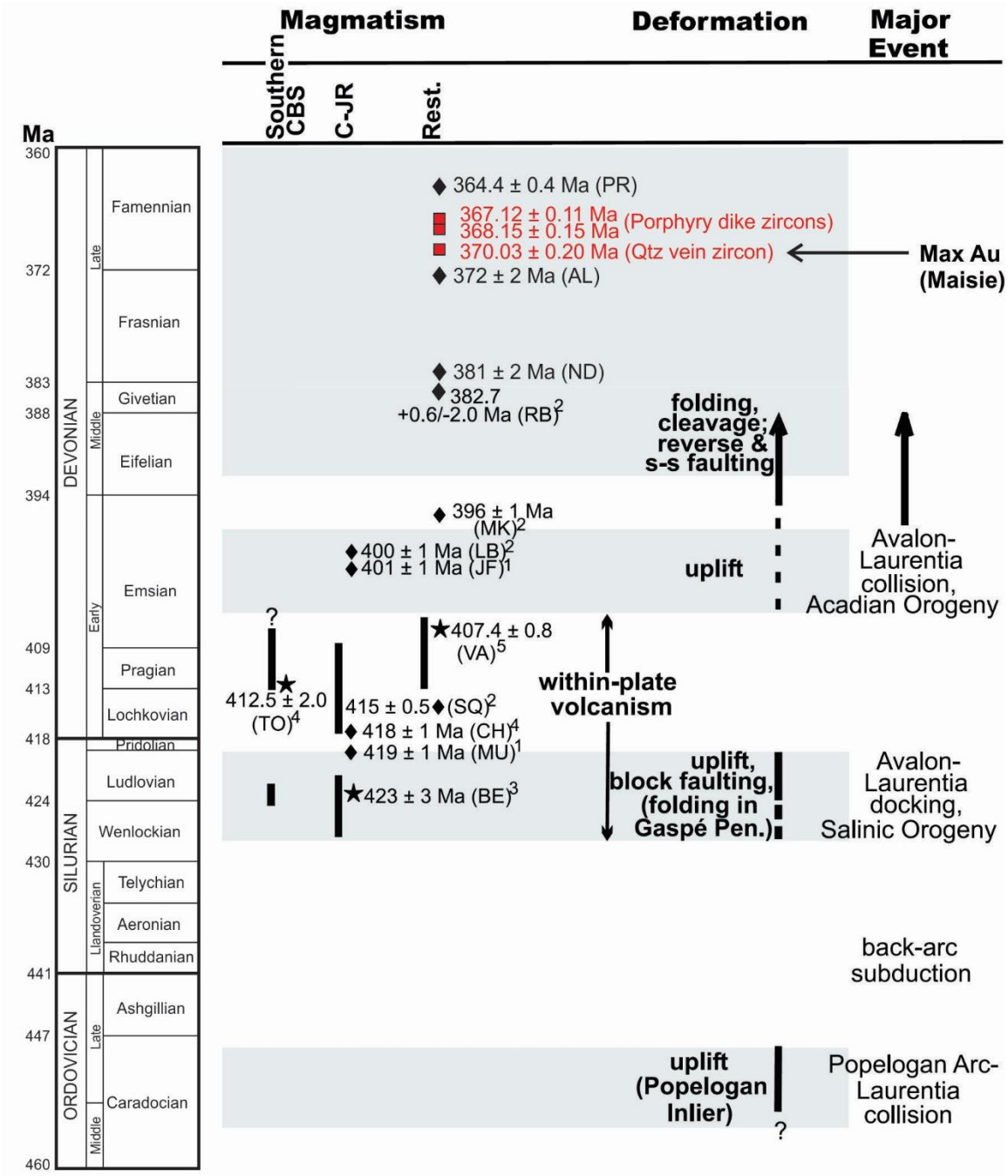

Figure 2.30 – Summary of regional tectonism and magmatism (modified from Wilson et al., 2004). Diagram includes concordant age of magmatic zircon (see Fig. 23a) from a hydrothermal quartz vein and porphyry dike (this study), as well as known felsic and mafic intrusions. Red squares = this study, diamonds = intrusions, stars = volcanic rocks. PR=Patapedia River Intrusion (Carroll, 2003a)

Whereas quartz veining at Maisie has a maximum age of 370 ± 0.20 Ma, the younger ages from the porphyry and other ages for regional magmatism (Fig. 30; the Patapedia River intrusion; Carroll, 2003a) collectively indicate a ~6 Ma window of magmatic activity in the area. If only zircons from the Maisie occurrence (vein and porphyry) are considered, this window is ~3 Ma. The inheritance of suspected magmatic zircon into the vein at Maisie illustrates that at least some magmatism predate vein formation. Together with other evidence, e.g. 1) proximity of the porphyry dike to the vein, 2) mineral thermometric data (suggesting Ts during early vein development stages were very high relative to regional thermal conditions from vitrinite reflectance studies), and 3) anomalous Au-Te-Bi in pyrite formed in a late vein stage, it seems likely that Au mineralization was linked to magmatism (cf. McCutcheon & Bevier, 1990).

2.6 Conclusion

The study concludes that the Maisie and Lavoie Au occurrences are genetically-related, "hybrid" Au systems, with some features consistent with epizonal orogenic Au systems but with an unambiguously late Au-Bi-Te upgrading stage by an epithermal or intrusion-related event. Various vein constituents (C, salts, H_2O, Sr, S, some metals such as Cu-Zn) are consistent with fluids derived from the low metamorphic grade marine metasedimentary rocks that host the veins. Ore, accessory, and gangue minerals were precipitated by low salinity fluids that underwent transient boiling/flashing and mixing with meteoric water. The stages of vein development are summarized (Fig. 31) as follows:

A) Initiation of folding and faulting, and low grade metamorphism of the Grog Brook Group sedimentary rocks during the Taconic, Salinic, and Acadian Orogenies (~440 to 394 Ma; Wilson et al., 2004, 2017).

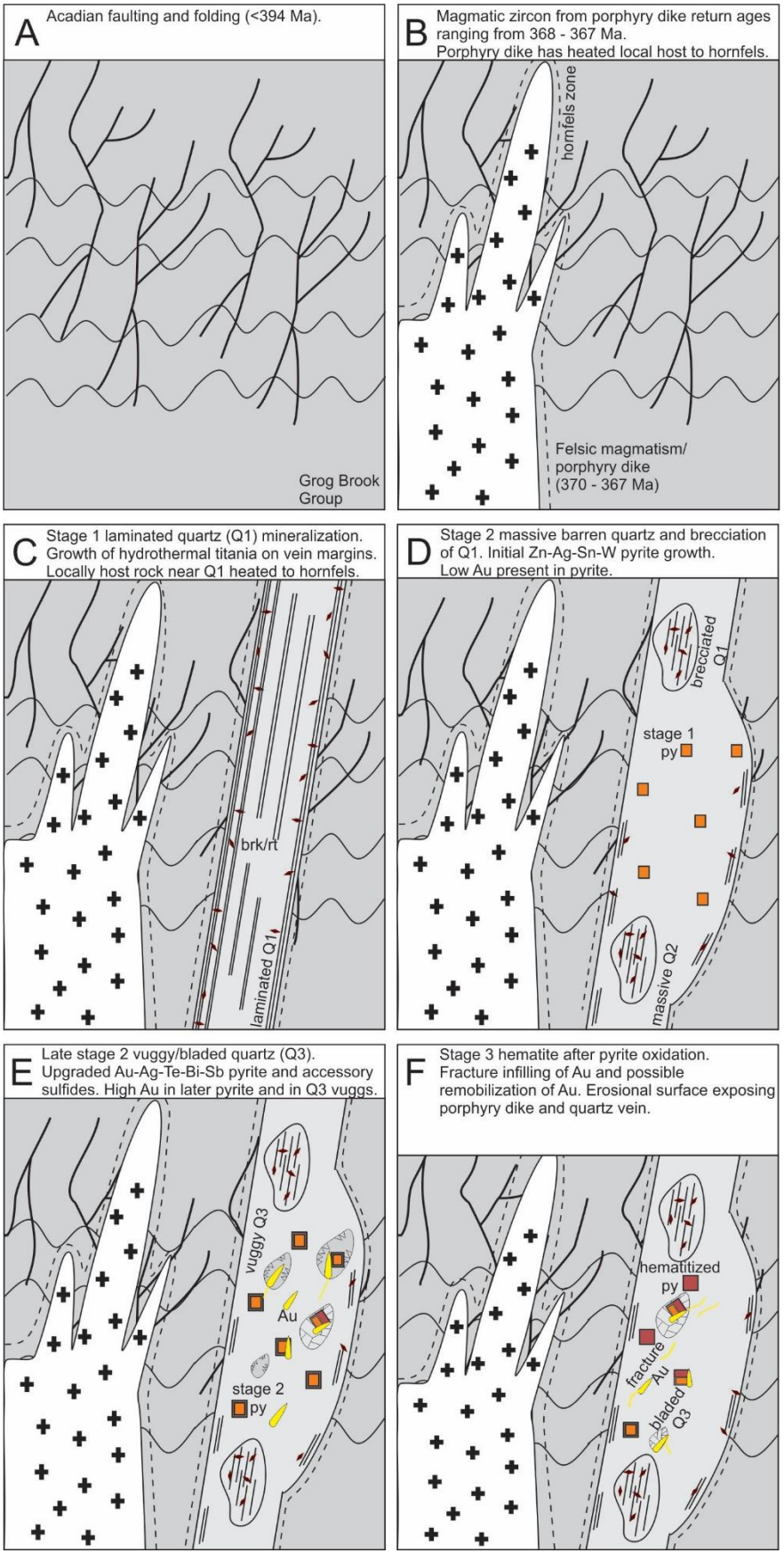
A
Acadian faulting and folding (<394 Ma).
Grog Brook Group
B
Magmatic zircon from porphyry dike return ages ranging from 368 - 367 Ma.
Porphyry dike has heated local host to hornfels.
hornfels zone
Felsic magmatism/ porphyry dike (370 - 367 Ma)
C
Stage 1 laminated quartz (Q1) mineralization.
Growth of hydrothermal titania on vein margins.
Locally host rock near Q1 heated to hornfels.
brk/rt
laminated Q1
D
Stage 2 massive barren quartz and brecciation of Q1. Initial Zn-Ag-Sn-W pyrite growth.
Low Au present in pyrite.
brecciated Q1
stage 1 py
massive Q2
E
Late stage 2 vuggy/bladed quartz (Q3).
Upgraded Au-Ag-Te-Bi-Sb pyrite and accessory sulfides. High Au in later pyrite and in Q3 vuggs.
vuggy Q3
Au
stage 2 py
F
Stage 3 hematite after pyrite oxidation.
Fracture infilling of Au and possible remobilization of Au. Erosional surface exposing porphyry dike and quartz vein.
hematitized py
fracture Au
bladed Q3

Figure 2.31 previous page – Deposit synthesis at Maisie and Lavoie. A) Folding and faulting of host Grog Brook Group sedimentary rocks during the Salinic and Acadian Orogenies (Wilson et al., 2004). B) Intermediate magmatism at depth occurring between ~370 to 367 Ma. Emplacement of a porphyry dike at Maisie heats host rocks (locally) to a hornfels facies. C) Stage 1 vein development occurs. Laminated Q1 and formation of brookite (brk). Vein temperatures cool from 680 to 245 °C. A hornfels develops along vein margins. Magmatic, vein-hosted zircon at Maisie returns a concordant age of ~370 Ma. D) Stage 2 vein development occurs, with massive barren Q2-C2 containing brecciated clasts of Q1. Early, pyrite I mineralization, [low Au and a co-assemblage of Cu-Zn-Sn-W-Ag-Mo]. E) Stage 2 vein development transitions to vuggy Q3, with native gold and sulfides infilling vugs. Pyrite II overprints pyrite I [higher Au than pyrite I, with co-enrichment in Bi-Te-Sb-Pb-As-Se]. Lattice-bladed C3 intergrowth with Q3 forms at the end of Stage 2 vein development. Metal precipitation is driven by transient boiling and rapid boiling (i.e. flashing), and mixing of fluids (incursion of oxidizing meteoric water). F) Stage 3 vein development is characterized by the oxidation of the mineralized veins. Hematite infills fractures and vugs. Pyrite alters to hematite, and chalcopyrite to covellite. An estimated erosional surface is placed, to represent present conditions at Maisie (and Lavoie).

B) Felsic to mafic magmatism at depth, occurring between ~370 – 367 Ma. At Maisie, a nearby plagioclase-biotite dacitic porphyry dike heats the host sedimentary rocks to (locally) hornfels facies.

C) Stage 1 of vein development consisting of laminated Q1 and brookite/rutile (recrystallization of anatase from wall rock). Temperatures in the vein suggests cooling from 680 to 245°C at the onset of vein growth. Hornfels develops along vein margins, which subsequently undergoes retrograde alteration.

D) Stage 2 of vein development begins with the formation of massive, barren Q2-C2 and associated brecciation of Q1. Pyrite I, with low contained Au and a metal assemblage of Cu-Zn-Sn-W-Ag-Mo forms.

E) Stage 2 vein development transitions to the formation of vuggy quartz infilled by native gold and sulfides. Early pyrite I is overprinted by pyrite II exotic metal association of higher Au and enrichment in Bi-Te-Sb-Pb-As-Se with a notable increase in Bi, Te, and As. The formation of lattice-bladed C3 intergrown with Q3 occurs in late Stage 2 vein development. Metal precipitation driven by transient boiling/flashing and meteoric water incursion (mixing/oxidation).

F) Stage 3 vein development is characterized by oxidation. Pyrite alters to hematite and chalcopyrite to covellite. Hematite and remobilized gold infill vugs and fractures. The absolute timing of Stage 3 is unclear, though it's relative timing is determined to be after Stage 2.

2.7 References

Agangi A, Hofmann A, Rollion-Bard C, Marin-Carbonne J, Cavalazzi B, Large R, Meffre S (2015) Gold accumulation in the Archaean Witwatersrand Basin, South Africa – Evidence from concentrically laminated pyrite. Earth-Science Review. 140, p 27-

Annels AE, Roberts DE (1989) Turbidite-hosted gold mineralization at the Dolaucothi gold mines, Dyfed, Wales, United Kingdom. Economic Geology. 84(5), p 1293-314

Barnes HL, Czamanske GK (1967) Solubilities and transport of ore minerals. Geochemistry of hydrothermal ore deposits. p 334-381

Bertrand R, Malo M, Lavoie D (2005) Thermal Maturation and Hydrocarbon Potential of Ordovician to Devonian Rocks in Northwestern New Brunswick. In AAPG Annual Convention. p 1 – 85

Beaudoin G, Therrien P (2009) The updated web stable isotope fractionation calculator. Handbook of stable isotope analytical techniques. 2, p 1120-1122

Bodnar RJ (1993) Revised equation and table for determining the freezing point depression of H2O-NaCl solutions. Geochimica et Cosmochimica acta. 57(3), p 683-684

Bodnar RJ, Vityk MO (1994) Fluid inclusions in minerals: Methods and applications. Pontignano, Siena, short course. p 117-130

Bodnar RJ, Lecumberri-Sanchez P, Moncada D, Steele-MacInnis M (2014) Fluid inclusions in hydrothermal ore deposits. Treatise on Geochemistry, Second Edition. Elsevier, Oxford. p 119-142

Bodnar RJ, Reynolds TJ, Kuehn CA (1985) Fluid inclusion systematics in epithermal systems: Reviews in Economic Geology. (2), p 73 - 97

Boggs Jr S, Young-Ihn K, Goles GG, Rusk BG, Krinsley D, Seyedolali A (2002) Is quartz cathodoluminescence color a reliable provenance tool? A quantitative examination: Journal of Sedimentary Research. 72, p 408–415

Browne PR, Ellis AJ (1970) The Ohaki-Broadlands hydrothermal area, New Zealand; mineralogy and related geochemistry. American Journal of Science. 269(2), p 97-131

Bustard AL, Lentz DR (2019) Gold and polymetallic mineralization, Elmtree property, Alcida area. EMP conference abstract. p 28

Cathelineau M (1988) Cation site occupancy in chlorites and illites as a function of temperature. Clay Minerals. (23), p 471-482

Carroll JI (2002) Lithogeochemistry of Ordovician sedimentary rocks associated with Ni-Co stream-silt anomalies along Ritchie Brook, Kedgwick map area, northern New Brunswick. Natural Resources Canada, Geological Survey of Canada. p 1-15

Carroll JI (2003a) Geology of the Kedgwick, Gounamitz River, States Brook and Menneval map areas (NTS 21 O/11, 21 O/12, 21 O/13, and 21 O/14), Restigouche County, New Brunswick. In: B.M.W. Carroll (ed.), Current Research 2002. New Brunswick Department of Natural Resources; Minerals, Policy and Planning Division, Mineral Resources Report 2003-4. p 23-57

Carroll JI (2003b) Geology of the Menneval area (NTS 21 O/14), Restigouche County, New Brunswick New Brunswick Department of Energy and Mines, Map plate MP 2003-26, 1:50 000 scale

Chauvet A, Piantone P, Barbanson L, Nehlig P, Pedroletti I (2001) Gold Deposit Formation during Collapse Tectonics: Structural, Mineralogical, Geochronological, and Fluid Inclusion Constraints in the Ouro Preto gold Mines, Quadril átero Ferrífero, Brazil. Economic Geology. 96(1), p 25-48

Cook NJ, Ciobanu CL, Mao J (2009) Textural control on gold distribution in As-free pyrite from the Dongping, Huangtuliang and Hougou gold deposits, North China Craton (Hebei Province, China). Chemical Geology. 264(1-4), p 101-121

Cook NJ, Ciobanu CL, Meria D, Silcock D, Wade B (2013) Arsenopyrite-pyrite association in an orogenic gold ore: Tracing mineralization history from textures and trace elements. Economic Geology. 108(6), p 1273-1283

Corfu F, Hanchar JM, Hoskin PW, Kinny P (2003) Atlas of zircon textures. Reviews in mineralogy and geochemistry. 53(1), p 469-500

Crowley JL, Schoene B, Bowring SA (2007) U-Pb dating of zircon in the Bishop Tuff at the millennial scale. Geology. (35), p 1123-1126

Davies JL (1977) Geological Map of Northern New Brunswick. Department of Natural Resources. 1 sheet

Deditius AP, Utsunomiya S, Ewing RC, Chryssoulis SL, Venter D, Kesler SE (2009) Decoupled geochemical behavior of As and Cu in hydrothermal systems. Geology. 37(8), p 707-710

Deditius AP, Reich M, Kesler SE, Utsunomiya S, Chryssoulis SL, Walshe J, Ewing RC (2014) The coupled geochemistry of Au and As in pyrite from hydrothermal ore deposits. Geochimica et Cosmochimica Acta. 140, p 644-770

Dokken RJ (2017) Detrital Zircon Studies in Silurian Basins of Southern New Brunswick. University of Alberta; Thesis. p 1-148

Driesner T (2007) The system H_2O–NaCl. Part II: Correlations for molar volume, enthalpy, and isobaric heat capacity from 0 to 1000° C, 1 to 5000bar, and 0 to 1 X NaCl. Geochimica et Cosmochimica Acta. 71(20), p 4902-4919

Driesner T, Heinrich CA (2007) The system H_2O–NaCl. Part I: Correlation formulae for phase relations in temperature–pressure–composition space from 0 to 1000° C, 0 to 5000bar, and 0 to 1 X NaCl. Geochimica et Cosmochimica Acta. 71(20), p 4880-4901

Eremin RA, Voroshin SV, Sidorov VA, Shakhtyrov VG, Pristavko VA, Gashtold VV (1994) Geology and genesis of the Natalka gold deposit, Northeast Russia. International Geology Review. 36(12), p 1113-1138

Etoh J, Taguchi S, Izawa E. Gas measurement of fluid inclusions from the Hishikari epithermal gold deposit, southern Kyushu, Japan, using Laser Raman microprobe. Resource Geology. 52(4), p 405-408

Fall A, Bodnar RJ (2018) How Precisely Can the Temperature of a Fluid Event be Constrained Using Fluid Inclusions? Economic Geology. 113(8), p 1817 - 1843

Fayek M, Harrison TM, Ewing RC, Grove M, Coath CD (2002) O and Pb isotopic analyses of uranium minerals by ion microprobe and U–Pb ages from the Cigar Lake deposit. Chemical Geology. 185(3-4), p 205-225

Flanagan M (2015) Mineral report of work 477926. New Brunswick Department of Mines and Energy, Minerals and Petroleum Databases. p 1-19

Franchini M, McFarlane C, Maydagán L, Reich M, Lentz DR, Meinert L, Bouhier V (2015) Trace metals in pyrite and marcasite from the Agua Rica porphyry-high sulfidation epithermal deposit, Catamarca, Argentina: Textural features and metal zoning at the porphyry to epithermal transition. Ore Geology Reviews. 66, p 366-387

Frezzotti ML, Tecce F, Casagli A (2012) Raman spectroscopy for fluid inclusion analysis. Journal of Geochemical Exploration. 112, p 1-20

Garnier V, Malo M, Dubé B, Chagnon A, Beaudoin G (2007) Carlin-type gold mineralization at Saint-André-de-Restigouche, Gaspé Peninsula (Québec), Canadian Appalachians. Mineralium Deposita. 42(6), p 639-662

Gerstenberger H, Haase G (1997) A highly effective emitter substance for mass spectrometric Pb isotope ratio determinations. Chemical Geology. (136), p 309-312

Goellnicht NM, Groves DI, McNaughton NJ, Dimo G (1989) An epigenetic origin for the Telfer gold deposit. Econ. Geol. Monogr. 6, p 151-167

Goldfarb RJ, Groves DI (2015) Orogenic gold: Common or evolving fluid and metal sources through time. Lithos. 233, p 2-6

Goldfarb RJ, Groves DI, Gardoll S (2001) Orogenic gold and geologic time: a global synthesis. Ore geology reviews. 18(1), p 1-75

Goldfarb RJ, Ayuso R, Miller ML, Ebert SW, Marsh EE, Petsel SA, Miller LD, Bradley D, Johnson C, McClelland W (2004) The late Cretaceous Donlin Creek gold deposit, Southwestern Alaska: Controls on epizonal ore formation. Economic geology. 99(4), p 643-671

Goldfarb R, Baker T, Dube B, Groves DI, Hart CJ, Gosselin P (2005) Distribution, character and genesis of gold deposits in metamorphic terranes. Society of Economic Geologists. p 407-450

Goldstein RH, Reynolds TJ (1994) Systematics of fluid inclusions in diagenetic minerals. SEPM Short Course Notes. (31), p 213

Gourcerol B, Kontak DJ, Thurston PC, Petrus JA (2018a) Application of LA-ICP-MS sulfide analysis and methodology for deciphering elemental paragenesis and associations in addition to multi-stage processes in metamorphic gold settings. The Canadian Mineralogist. 56(1), p 39-64

Gourcerol B, Kontak DJ, Thurston PC, Petrus JA (2018b) Results of LA-ICP-MS sulfide mapping from Algoma-type BIF gold systems with implications for the nature of mineralizing fluids, metal sources, and deposit models. Mineralium Deposita. 53(6), p 871-894

Gregory DD, Large RR, Halpin JA, Baturina EL, Lyons TW, Wu S, Danyushevsky L, Sack PJ, Chappaz A, Maslennikov VV, Bull SW (2015) Trace element content of sedimentary pyrite in black shales. Economic Geology. 110(6), p 1389-1410

Gregory DD, Large RR, Bath AB, Steadman JA, Wu S, Danyushevsky L, Bull SW, Holden P, Ireland TR (2016) Trace element content of pyrite from the kapai slate, St. Ives Gold District, Western Australia. Economic Geology. 111(6), p 1297-1320

Gregory DD, Lyons TW, Large RR, Jiang G, Stepanov AS, Diamond CW, Figueroa MC, Olin P (2017) Whole rock and discrete pyrite geochemistry as complementary tracers of ancient ocean chemistry: an example from the Neoproterozoic Doushantuo Formation, China. Geochimica et Cosmochimica Acta. 216, p 201-220

Groves DI, Goldfarb RJ, Gebre-Mariam M, Hagemann SG, Robert F (1998) Orogenic Au deposits: a proposed classification in the context of their crustal distribution and relationship to other Au deposit types. Ore geology reviews. 13(1-5), p 7-27

Groves DI, Goldfarb RJ, Robert F, Hart CJR (2003) Au deposits in metamorphic belts: overview of current understanding, outstanding problems, future research, and exploration significance. Economic Geology. 98, p 1-29

Guillong M, Meier DL, Allan MM, Heinrich CA, Yardley BW (2008) Appendix A6: SILLS: A MATLAB-based program for the reduction of laser ablation ICP-MS data of homogeneous materials and inclusions. Mineralogical Association of Canada Short Course. 40, p 328-33

Hagemann SG, Groves DI, Ridley JR, Vearncombe JR (1992) The Archean lode gold deposits at Wiluna, Western Australia; high-level brittle-style mineralization in a strike-slip regime. Economic Geology. 87(4), p 1022-1053

Hagemann SG, Gebre-Mariam M, Groves DI (1994) Surface-water influx in shallow-level Archean lode-Au deposits in Western, Australia. Geology. 22(12), p 1067-1070

Harris DC (1986) Mineralogic report on samples from the Elmtree Deposit, Energy Mines, and Resources, Canada, Unpublished Company Report

Hedenquist JW, Matsuhisa Y, Izawa E, White NC, Giggenbach WF, Aoki M (1994) Geology, geochemistry, and origin of high sulfidation Cu-Au mineralization in the Nansatsu District, Japan. Economic Geology. 89(1), p 1-30

Hedenquist JW, Arribas A, Reynolds TJ (1998) Evolution of an intrusion-centered hydrothermal system; Far Southeast-Lepanto porphyry and epithermal Cu-Au deposits, Philippines. Economic Geology. 93(4), p 373-404

Hedenquist JW, Arribas AN, Gonzalez-Urien E (2000) Exploration for epithermal Au deposits. Reviews in Economic Geology. 13(2), p 45-77

Heinrich CA, Driesner T, Stefánsson A, Seward TM (2004) Magmatic vapor contraction and the transport of gold from the porphyry environment to epithermal ore deposits. Geology. 32(9), p 761-764

Su W, Heinrich CA, Pettke T, Zhang X, Hu R, Xia B (2009) Sediment-hosted gold deposits in Guizhou, China: products of wall-rock sulfidation by deep crustal fluids. Economic Geology. 104(1), p 73-93

Heiss J, Condon DJ, McLean N, Noble SR (2012) $^{238}U/^{235}U$ systematics in terrestrial uranium-bearing minerals. Science. (335), p 1610-1614

Henderson JR, Henderson MN, Wright TO (1990) Water-sill hypothesis for the origin of certain veins in the Meguma Group, Nova Scotia, Canada. Geology. 18(7), p 654-657

Jaffey AH, Flynn KF, Glendenin LE, Bentley WC, Essling AM (1971) Precision measurement of half-lives and specific activities of 235U and 238U. Physical Review 4, p 1889-1906

Jowett E (1991) Fitting iron and magnesium into the hydrothermal chlorite geothermometer. GAC/MAC/SEG Joint Annual Meeting (Toronto). Program with Abstracts 16, A62. p 1-15

Keith TE, White DE, Beeson MH (1978) Hydrothermal alteration and self-sealing in Y-7 and Y-8 drill holes in northern part of Upper Geyser Basin, Yellowstone National Park, Wyoming. US Govt. Print. Off. p 1-25

Kerr MJ, Hanley JJ, Kontak DJ, Morrison GG, Petrus J, Fayek M, Zajacz Z (2018) Evidence of upgrading of Au tenor in an orogenic quartz-carbonate vein system by late magmatic-hydrothermal fluids at the Madrid Deposit, Hope Bay Greenstone Belt, Nunavut, Canada. Geochimica et Cosmochimica Acta. 241, p 180-218

Kerrich R, Wyman D (1990) Geodynamic setting of mesothermal Au deposits: An association with accretionary tectonic regimes. Geology. 18(9), p 882-885

Kesler SE, Fortuna J, Ye Z, Alt JC, Core DP, Zohar P, Borhauer J, Chryssoulis SL (2003) Evaluation of the role of sulfidation in deposition of gold, Screamer section of the Betze-Post Carlin-type deposit, Nevada. Economic Geology. 98(6), p 1137-1157

Klaussen K, Lloyd S (2012) Mineral report of work 477343. New Brunswick Department of Mines and Energy, Minerals and Petroleum Databases. p 1-131

Kleine BI, Stefánsson A, Halldórsson SA, Whitehouse MJ, Jónasson K (2018) Silicon and oxygen isotopes unravel quartz formation processes in the Icelandic crust. Geochemical Perspectives Letters. (7), p 5-11

Kontak DJ, Smith PK, Kerrich R, Williams PF (1990) Integrated model for Meguma Group lode Au deposits, Nova Scotia, Canada. Geology. 18(3), p 238-242

Kouhestani H, Ghaderi M, Large RR, Zaw K (2017) Texture and chemistry of pyrite at Chah Zard epithermal gold–silver deposit, Iran. Ore Geology Reviews. 84, p 80-101

Krogh TE (1973) A low contamination method for hydrothermal decomposition of zircon and extraction of U and Pb for isotopic age determination. Geochimica et Cosmochimica Acta. (37), p 485-494

Lambeck A, Mernagh TP, Wyborn L (2011) Are Iron-Rich Sedimentary Rocks The Key To The Spike In Orogenic Au Mineralization In The Paleoproterozoic? Economic Geology. 106(3), p 321-330

Large RR, Danyushevsky L, Hollit C, Maslennikov V, Meffre S, Gilbert S, Bull S, Scott R, Emsbo P, Thomas H, Singh B (2009) Au and trace element zonation in pyrite

using a laser imaging technique: Implications for the timing of Au in orogenic and Carlin-style sediment-hosted deposits. Economic Geology. 104(5), p 635-668

Large RR, Bull SW, Maslennikov VV (2011) A carbonaceous sedimentary source-rock model for Carlin-type and orogenic gold deposits. Economic Geology. 106(3), p 331-358

Large R, Thomas H, Craw D, Henne A, Henderson S (2012) Diagenetic pyrite as a source for metals in orogenic gold deposits, Otago Schist, New Zealand. New Zealand Journal of Geology and Geophysics. 55(2), p 137-149

Lavoie D, Chi G (2010) Lower Paleozoic foreland basins in eastern Canada: tectono-thermal events recorded by faults, fluids and hydrothermal dolomites. Bulletin of Canadian Petroleum Geology. 58(1), p 17-35

Lafuente B, Downs RT, Yang H, Stone N (2016) The power of databases: the RRUFF project. In: Highlights in mineralogical crystallography, Walter de Gruyter GmbH. p 1-29

Lentz DR, Goodfellow WD, Moore CE (1995) The geological significance of the alkalic gabbro in the immediate hanging wall to the Brunswick No. 12 massive sulphide deposit. Bathurst, New Brunswick: Geological Survey of Canada Paper. p 233-243

Li Y, Liu J (2006) Calculation of sulfur isotope fractionation in sulfides. Geochimica et Cosmochimica Acta. 70(7), p 1789-1795

Lloyd S (2013) Mineral report of work 477434. New Brunswick Department of Mines and Energy, Minerals and Petroleum Databases. p 1-25

Ludwig KR (2003) User's manual for Isoplot 3.00 a geochronological toolkit for Excel. Berkeley Geochronological Center Special Publication. 4, p 1-71

Malo M, Béland J (1989) Acadian strike-slip tectonics in the Gaspé region, Québec Appalachians. Canadian Journal of Earth Sciences. 26(9), p 1764-1777

Malo M, Bourque PA (1993) Timing of the deformation events from Late Ordovician to Mid-Devonian in the Gaspé Peninsula. Geological Society of America Special Papers. 275, p 101-122

Malo M, Moritz R, Dube B, Chagnon A, Roy F, Pelchat C (2000) Base metal skarns and Au occurrences in the southern Gaspé Appalachians: distal products of a faulted and displaced magmatic-hydrothermal system along the Grand Pabos-Restigouche fault system. Economic Geology. 95(6), p 1297-1318

Mao J, Konopelko D, Seltmann R, Lehmann B, Chen W, Wang Y, Eklund O, Usubaliev T (2004) Postcollisional age of the Kumtor Gold Deposit and timing of Hercynian events in the Tien Shan, Kyrgyzstan. Economic Geology. 99, p 1771 – 1780

Martin RD (2012) Syenite-hosted gold mineralization and hydrothermal alteration at the Young-Davidson deposit, Matachewan, Ontario (Master's thesis, University of Waterloo). p 1-133

Massawe RJ, Lentz DR (2020) Evaluation of crystallization and emplacement conditions of the McKenzie Gulch porphyry dykes using chemistry of rock-forming minerals: Implications for mineralization potential. Ore Geology Reviews. 116, p 1-18

Matsuhisa Y, Goldsmith JR, Clayton RN (1979) Oxygen isotopic fractionation in the system quartz-albite-anorthite-water. Geochimica et cosmochimica acta. 43(7), p 1131-1140

Mattinson JM (2005) Zircon U-Pb chemical abrasion ("CA-TIMS") method: combined annealing and multi-step partial dissolution analysis for improved precision and accuracy of zircon ages. Chemical Geology. (220), p 47-66

McClenaghan SH, Goodfellow WD, Lentz DR (2003) Gold in massive sulfide deposits, Bathurst Mining Camp: distribution and genesis. Economic Geology, Monograph. 11, p 303-326

McCutcheon SR, Bevier ML (1990) Implications of field relations and U-Pb geochronology for the age of gold mineralization and timing of Acadian deformation in northern New Brunswick. Atlantic Geology. 26, p 237-246

McDonough WF, Sun SS (1995) The composition of the Earth. Chemical geology. 120(3-4), p 223-253

McKibben MA, Eldridge CS (1990) Radical sulfur isotope zonation of pyrite accompanying boiling and epithermal gold deposition; a SHRIMP study of the Valles Caldera, New Mexico. Economic Geology. 85(8), p 1917-1925

Mernagh TP, Wilde AR (1989) The use of the laser Raman microprobe for the determination of salinity in fluid inclusions. Geochimica et Cosmochimica Acta. 53(4), p 765-771

Mitchell RH (1968) A semiquantitative study of trace elements in pyrite by spark source mass spectrography. Norsk Geologisk Tidsskrift. 48, p 65-80

Moncada D, Mutchler S, Nieto A, Reynolds TJ, Rimstidt JD, Bodnar RJ (2012) Mineral textures and fluid inclusion petrography of the epithermal Ag-Au deposits at

Guanajuato, Mexico: Application to exploration. Journal of Geochemical Exploration. 114, p 20-35

Morey AA, Tomkins AG, Bierlein FP, Weinberg RF, Davidson GJ (2008) Bimodal distribution of gold in pyrite and arsenopyrite: examples from the Archean Boorara and Bardoc shear systems, Yilgarn Craton, Western Australia. Economic Geology. 103(3), p 599-614

Mukherjee I, Large R (2017) Application of pyrite trace element chemistry to exploration for SEDEX style Zn-Pb deposits: McArthur Basin, Northern Territory, Australia. Ore Geology Reviews. 81, p 1249-1270

Neumayr P, Hagemann SG (2002). Hydrothermal fluid evolution within the Cadillac tectonic zone, Abitibi greenstone belt, Canada: relationship to auriferous fluids in adjacent second-and third-order shear zones. Economic Geology. 97(6), p 1203-1225

Neyedley K, Hanley JJ, Fayek M, Kontak DJ (2017) Textural, fluid inclusion, and stable oxygen isotope constraints on vein formation and gold precipitation at the 007 deposit, Rice Lake Greenstone Belt, Bissett, Manitoba, Canada. Economic Geology. 112(3), p 629-660

Oberthuer T, Mumm AS, Vetter U, Simon K, Amanor JA (1996) Gold mineralization in the Ashanti Belt of Ghana; genetic constraints of the stable isotope geochemistry. Economic Geology. 91(2), p 289-301

Ohmoto H, Rye RO (1979) Isotopes of sulfur and carbon. Geochemistry of Hydrothermal Ore Deposits (Barnes, HL, ed.). p 509-567

Parkhill MA (2005) Till geochemistry of the Kedgwick, Gounamitz River, States Brook, and Menneval map areas (NTS 21 O/11, 12, 13, and 14), Madawaska, Restigouche, and Victoria counties, northwestern New Brunswick. New Brunswick Department of Natural Resources, Minerals, Policy and Planning Division, Open File. 199, p 1-31

Paton C, Hellstrom J, Paul B, Woodhead J, Hergt J (2011) Iolite: Freeware for the visualisation and processing of mass spectrometric data. Journal of Analytical Atomic Spectrometry. 26(12), p 2508-2518

Pettke T, Diamond LW (1997) Oligocene gold quartz veins at Brusson, NW Alps; Sr isotopes trace the source of ore-bearing fluid to ore a 10-km depth. Economic geology. 92(4), p 389-406

Phillips GN, Groves DI (1983) The nature of Archaean gold-bearing fluids as deduced from gold deposits of Western Australia. Journal of the Geological Society of Australia. 30(1-2), p 25-39

Pollock JC, Wilton DHC, van Staal CR, Morrissey KD (2007) U-Pb detrital zircon geochronological constraints on the Early Silurian collision of Ganderia and Laurentia along the Dog Bay Line: the terminal Iapetan suture in the Newfoundland Appalachians: American Journal of Science. 307(2), p 399-433

Pudack C, Halter WE, Heinrich CA, Pettke T (2009) Evolution of magmatic vapor to gold-rich epithermal liquid: The porphyry to epithermal transition at Nevados de Famatina, northwest Argentina. Economic Geology. 104(4), p 449-477

Radtke AS, Rye RO, Dickson FW (1980) Geology and stable isotope studies of the Carlin gold deposit, Nevada. Economic Geology. 75(5), p 641-672

Raiswell R, Plant J (1980) The incorporation of trace elements into pyrite during diagenesis of black shales, Yorkshire, England. Economic Geology. 75(5), p 684-699

Ramsay WR, Bierlein FP, Arne DC, VandenBerg AH (1998) Turbidite-hosted gold deposits of Central Victoria, Australia: their regional setting, mineralising styles, and some genetic constraints. Ore Geology Reviews. 13(1), p 131-151

Reich M, Simon AC, Deditius A, Barra F, Chryssoulis S, Lagas G, Tardani D, Knipping J, Bilenker L, Sánchez-Alfaro P, Roberts MP (2016) Trace element signature of pyrite from the Los Colorados iron oxide-apatite (IOA) deposit, Chile: A missing link between Andean IOA and iron oxide copper-gold systems? Economic Geology. 111(3), p 743-761

Riciputi LR, Paterson BA, Ripperdan RL (1998) Measurement of light stable isotope ratios by SIMS:: Matrix effects for oxygen, carbon, and sulfur isotopes in minerals3. International Journal of Mass Spectrometry. 178(1-2), p 81-112

Riva J, Malo M (1988) Age and correlation of the Honorat Group, southern Gaspé Peninsula. Canadian Journal of Earth Sciences. 25(10), p 1618-1628

Roberts NM, Yang QY, Santosh M (2018) Rapid oxygen diffusion during high temperature alteration of zircon. Scientific reports. 8(3661), p 1-10

Roedder E, Bodnar RJ (1980) Geologic pressure determinations from fluid inclusion studies. Annual review of earth and planetary sciences. 8(1), p 263-301

Ruitenberg AA, McCutcheon SR, Watters SE, Mc-Leod MJ, Burton DM, Hoy D (1989) Field guide to gold occurrences in New Brunswick: New Brunswick Department of Natural Resources and Energy. Minerals and Energy Division, Field Guidebook. p 1-63

Ryan RJ, Smith PK (1998) A review of the mesothermal gold deposits of the Meguma Group, Nova Scotia, Canada. Ore Geology Reviews. 13(1-5), p 153-183

Rye DM, Rye RO (1974) Homestake gold mine, South Dakota; I, Stable isotope studies. Economic Geology. 69(3), p 293-317

Sakai H (1968) Isotopic properties of sulfur compounds in hydrothermal processes. Geochemical Journal. 2(1), p 29-49

Sakai H, Des Marais DJ, Ueda A, Moore JG (1984) Concentrations and isotope ratios of carbon, nitrogen and sulfur in ocean-floor basalts. Geochimica et Cosmochimica Acta. 48(12), p 2433-2441

Sangster AL, Smith PK, Goodfellow WD (2007) Metallogenic summary of the Meguma gold deposits, Nova Scotia. Mineral Deposits of Canada: A Synthesis of Major Deposit-Types, District Metallogeny, the Evolution of Geological Provinces, and Exploration Methods. Geological Association of Canada, Mineral Deposits Division, Special Publication No. 5, p 723-732

Schmitz MD, Schoene B (2007) Derivation of isotope ratios, errors and error correlations for U-Pb geochronology using ^{205}Pb-^{235}U-(^{233}U)-spiked isotope dilution thermal ionization mass spectrometric data: Geochemistry, Geophysics, Geosystems (G^3). 8(8), p 1-20

Schwarz S, Lentz D (2009) The Middle River Gold deposit, NE New the B. In International Applied Geochemistry Symposium. p 1-209

Sequin MK, Gahe E (1985) Paleomagnetism of Lower Devonian volcanics and Devonian dikes from northcentral New Brunswick, Canada. Physics of the Earth and Planetary Interiors. 4(38), p 262-276

Sharp Z (2017) Principles of stable isotope geochemistry

Shields GA, Carden GA, Veizer J, Meidla T, Rong JY, Li RY (2003) Sr, C, and O isotope geochemistry of Ordovician brachiopods: a major isotopic event around the Middle-Late Ordovician transition. Geochimica et Cosmochimica Acta. 67(11), p 2005-2025

Sibson RH, Robert F, Poulsen KH (1988) High-angle reverse faults, fluid-pressure cycling, and mesothermal gold-quartz deposits. Geology. 16(6), p 551-555

Sillitoe RH (1994) Erosion and collapse of volcanoes: Causes of telescoping in intrusion-centered ore deposits. Geology. 22(10), p 945-948

Sim MS, Sessions AL, Orphan VJ, Adkins JF (2019) Precise determination of equilibrium sulfur isotopes effects during volatilization and deprotonation of dissolved H_2S. Geochemica et Cosmochimica Acta. (248), p 242-251

Steadman JA, Large RR (2016) Synsedimentary, Diagenetic, and Metamorphic Pyrite, Pyrrhotite, and Marcasite at the Homestake BIF-Hosted Gold Deposit, South Dakota, USA: Insights on Au-As Ore Genesis from Textural and LA-ICP-MS Trace Element Studies. Economic Geology. 111(7), p 1731-1752

Sykora S, Cooke DR, Meffre S, Stephanov AS, Gardner K, Scott R, Selley D, Harris AC (2018) Evolution of pyrite trace element compositions from porphyry-style and epithermal conditions at the Lihir gold deposit: implications for ore genesis and mineral processing. Economic Geology. 113(1), p 193-208

Taylor BE (2007) Epithermal gold deposits. Mineral deposits of Canada: a synthesis of major deposit-types, district metallogeny, the evolution of geological provinces, and exploration methods. Edited by WD Goodfellow. Geological Association of Canada, Mineral Deposits Division, Special Publication. 5, p 113-139

Thébaud N, Philippot P, Rey P, Cauzid J (2006) Composition and origin of fluids associated with lode gold deposits in a Mesoarchean greenstone belt (Warrawoona Syncline, Pilbara Craton, Western Australia) using synchrotron radiation X-ray fluorescence. Contributions to Mineralogy and Petrology. 152(4), p 485

Thomas JB, Watson EB, Spear FS, Shemella PT, Nayak SK, Lanzirotti A (2010) TitaniQ under pressure: the effect of pressure and temperature on the solubility of Ti in quartz. Contributions to Mineralogy and Petrology. 160(5), p 743-759

Thorne KG (2011) Gold. New Brunswick Department of Natural Resources; Lands, Minerals and Petroleum Division, Mineral Commodity Profile No. 8, p 1-8

Tomkins HS, Powell R, Ellis DJ (2007) The pressure dependence of the zirconium-in-rutile thermometer. Journal of Metamorphic Geology. 25(6), p 703-713

Tornos F, Solomon M, Conde C, Spiro BF (2008) Formation of the Tharsis massive sulfide deposit, Iberian Pyrite Belt: geological, lithogeochemical, and stable isotope evidence for deposition in a brine pool. Economic Geology. 103(1), p 185-214

Tremblay A, Dubé B (1991) Structural relationships between some gold occurrences and fault zones in the Bathurst area, northern New Brunswick. Current Research, Part D, Geological Survey of Canada, Paper. p 89-100

Truesdell AH, Nathenson M, Rye RO (1977) The effects of subsurface boiling and dilution on the isotopic compositions of Yellowstone thermal waters. Journal of Geophysical Research. 82(26), p 3694-3704

Twemlow SG, Foster RP (1984) Archaean gold-telluride mineralization of the Commoner mine, Zimbabwe. In Gold. (82), p 469-492

Waldron JWF, McNicoll VJ, van Staal CR (2012) Laurentia-derived detritus in the Badger Group of central Newfoundland: deposition during closing of the Iapetus Ocean. Canadian Journal of Earth Sciences. 49(1), p 207-221

Waldron JWF, Schofeld DI, Murphy JB, Thomas CW (2014) How was the Iapetus Ocean infected with subduction? Geology. 42(12), p 1095-1098

White NC, Hedenquist JW (1995) Epithermal gold deposits: styles, characteristics and exploration. SEG newsletter. 23(1), p 9-13

Wilde AR, Layer P, Mernagh T, Foster J (2001) The giant Muruntau gold deposit: geologic, geochronologic, and fluid inclusion constraints on ore genesis. Economic Geology. 96(3), p 633-644

Williams-Jones AE, Bowell RJ, Migdisov AA (2009) Gold in solution. Elements. 5(5), p 281-287

Wilson RA (2003) Geology of the Upsalquitch Siding area (NTS 21 O/15d). Restigouche County, New Brunswick. New Brunswick Department of Natural Resources, Minerals, Policy and Planning Division; Plate 2003-10

Wilson RA, Burden ET, Bertrand R, Asselin E, McCracken AD (2004) Stratigraphy and tectono-sedimentary evolution of the Late Ordovician to Middle Devonian Gaspé Belt in northern New Brunswick: evidence from the Restigouche area. Canadian Journal of Earth Sciences. 41(5), p 527-551

Wilson RA, Kamo SL (2012) The Salinic Orogeny in northern New Brunswick: geochronological constraints and implications for Silurian stratigraphic nomenclature. Canadian Journal of Earth Sciences. 49, p 222-238

Wilson R.A., 2017. The Middle Paleozoic Rocks of Northern and Western New Brunswick, Canada. New Brunswick Dept. of Natural Resources and Energy, Memoir 4; p 334

Winderbaum L, Ciobanu CL, Cook NJ, Paul M, Metcalfe A, Gilbert S (2012) Multivariate analysis of an LA-ICP-MS trace element dataset for pyrite. Mathematical Geosciences. 44(7), p 823-842

Wu YF, Li JW, Evans K, Koenig AE, Li ZK, O'Brien H, Lahaye Y, Rempel K, Hu SY, Zhang ZP, Yu JP (2018) Ore-forming processes of the Daqiao Epizonal Orogenic gold deposit, west Qinling Orogen, China: constraints from textures, trace elements, and sulfur isotopes of pyrite and marcasite, and Raman spectroscopy of carbonaceous material. Economic Geology. 113(5), p 1093-1132

Yavuz F, Kumral M, Karakaya N, Karakaya MÇ, Yıldırım DK (2015) A Windows program for chlorite calculation and classification. Computers & geosciences. 81, p 101-113

Zhong S, Feng C, Seltmann R, Li D, Qu H (2018) Can magmatic zircon be distinguished from hydrothermal zircon by trace element composition? The effect of mineral inclusions on zircon trace element composition. Lithos. 314, p 646-657

Zoheir B, Akawy A, Hassan I (2008) Role of fluid mixing and wallrock sulfidation in gold mineralization at the Semna mine area, central Eastern Desert of Egypt: Evidence

from hydrothermal alteration, fluid inclusions and stable isotope data. Ore Geology Reviews. 34(4), p 580-596

Chapter 3 – Limitations, future work, and exploration criteria

3.1 – Study limitations

A significant limitation of this study was the lack of exposed vein contacts with wall rocks and other relevant lithologies (e.g. the porphyry) at the study sites. The textural and structural relationships of such contacts, observed at the deposit scale, are critical to elucidating deposit type. In particular, only small and/or partial exposures of veins were available for study.

A second limitation (potentially) is the use of titania minerals for thermometry in hydrothermal environments, specifically in the accuracy of calculated Ts, based in part on assumptions about the activity of Ti and Zr (assumed to be near 1). Few studies of the viability of the thermometers in hydrothermal veins exist (Tomkins et al., 2007; Thomas et al., 2010; Cabral et al., 2014). The problem with titania mineral thermometry applied to hydrothermal systems is that the thermometers are based on experimental systems involving metamorphic and igneous rocks co-saturated in rutile and zircon (i.e. activities of Ti and Zr = 1). Furthermore, the calculated T for each thermometer increases if a_{Zr} and a_{Ti} are <1. In this study the prerequisites for the application of these thermometers are met: i.e. "co-saturated" zircon (present in wall rocks as detrital phases), rutile/brookite (as replacement after anatase along wall rock contacts with vein and in wall rock septae), and quartz (in the vein, and in wall rocks). Thus, calculated Ts are considered to be minimum values, and so the impact of such an uncertainty does not invalidate the high T conditions revealed during early vein development.

As stated, the interpretation of boiling/flashing FIA may not be correct, as this is based on partial microthermometry (of L_{aq} rich inclusions) and petrographic observations.

Additional microthermometric data of suspected V-end member inclusions would help to provide further evidence/constraints for boiling if T_h values are similar to coexisting L_{aq}-rich inclusions; however, this study is limited by the size and optical clarity of the minor L_{aq} phase in such inclusions, in particular near the dew point transition.

Lastly, the models explaining the origin of stable isotope values for minerals makes a number of assumptions that are built upon semi-quantitative evidence provided from petrography, comparison to regional sources for C, O, and S, etc. While it is stated that the models developed are reasonable given the setting and evidence, there are other pathways to yield minerals with the isotope values seen at Maisie and Lavoie. For example, more complicated mixing models, the influence of fluid-wall rock interaction, and Rayleigh fractionation should not be ignored.

3.2 – Future research

Titania minerals (brookite, anatase, and rutile) were recovered from heavy mineral separates during the early stages of this research. Preliminary LA-ICP-MS analyses were done to determine the major-, minor-, and trace-element compositions of these minerals in order to determine if vein titania mineral chemistry could be discriminated from wall rock titania phases, thereby constituting a potential exploration vectoring tool. Interpretation of the trace element compositions of titania phases were ultimately left out of the thesis for future work, as the primary objective of this study was to characterize and classify the Maisie and Lavoie Au occurrences, establish deposit model parameters, and determine how the occurrences compare to other Au showings in northern New Brunswick and adjacent Gaspé Peninsula (PQ). Additionally, the apparent lack of titania minerals at Lavoie

prohibits independent thermometry; a concerted effort to obtain independent T data for Lavoie is encouraged.

Additional geochronological data from the Maisie and Lavoie Au occurrences are needed to constrain the *absolute* timing of vein formation (and Au mineralization). Hydrothermal monazite is present in the Maisie vein and should be dated. Furthermore, the age of the Lavoie mineralization needs to be constrained in order to enable comparisons to the genetically-similar Maisie occurrence.

A structural geology study of the study area would benefit the overall understanding of the region and associated Au mineralization, as differences among Taconic, Salinic, and Acadian Orogenies are not well understood, in particular with respect to preserved structures/fabrics as they relate to structural preparation for, and relative timing of, Au mineralization.

Further analysis, petrography, and mapping of the porphyry dike at Maisie will provide insight into its genetic and spatial relationship (if any) to the mineralized quartz veins including constraining cross cutting relations between vein(s) and igneous rocks.

3.3 – Applications to exploration

Recommendations based on the findings of this study to further exploration in northern New Brunswick for non-refractory Au occurrences in the Grog Brook Group include: (i) Mapping and identification of intrusions similar in age to the vein-derived and porphyry zircon at the Maisie Au occurrence (370.03 ± 0.20 Ma to 367.12 ± 0.11 Ma); (ii) Recognition of quartz veins with similar textural and fluid inclusion characteristics, i.e.: quartz(-calcite) hosted; petrographic evidence of transient boiling and “flashing”; FIA

salinity ranging from 0 – 8 wt.% and T_h values averaging 169 ± 28 °C (1σ; type 1, non-boiling) and 179 ± 30°C (1σ; type 3, flashing); (iii) Recognition of zoned pyrite with overprinting textures and associated *Au, Bi, Te,* As, Pb, Sb, Se, enrichment; and (iv) seeking evidence of locally high Ts, exceeding Ts from regional vitrinite data (~ 265 °C; Bertrand et al., 2005).